NOVA SCHOOL OF SCIENCE & TECHNOLOGY

DEPARTMENT OF MECHANICAL AND INDUSTRIAL ENGINEERING

Methodologies for optimal design and additive manufacturing of metamaterials combining negative property indexes

Cláudia Sofia João de Almeida

Master in Mechanical Engineering

DOCTORATE IN MECHANICAL ENGINEERING

NOVA University of Lisbon

September, 2025

NOVA SCHOOL OF SCIENCE & TECHNOLOGY

DEPARTMENT OF MECHANICAL AND INDUSTRIAL ENGINEERING

Methodologies for optimal design and additive manufacturing of metamaterials combining negative property indexes

Cláudia Sofia João de Almeida

Master in Mechanical Engineering

Adviser: Pedro Samuel Gonçalves Coelho
Associate Professor, NOVA School of Science and Technology, NOVA University Lisbon

Co-advisers: Alexandre José da Costa Velhinho
Assistant Professor, NOVA School of Science and Technology, NOVA University Lisbon

Examination Committee:

Chair: Telmo Jorge Gomes dos Santos,
Full Professor, NOVA School of Science and Technology, NOVA University Lisbon

Rapporteurs: Hélder Carriço Rodrigues,
Full Professor, IST Higher Technical Institute, University of Lisbon
Igor André Rodrigues Lopes,
Principal Investigator, INEGI – Institute of Science and Innovation in Mechanical and Industrial Engineering

Adviser: Pedro Samuel Gonçalves Coelho,
Associate Professor, NOVA School of Science and Technology, NOVA University Lisbon

Members: Maria de Fátima Reis Vaz,
Full Professor, IST Higher Technical Institute, University of Lisbon
Telmo Jorge Gomes dos Santos,
Full Professor, NOVA School of Science and Technology, NOVA University Lisbon
Carla Maria Moreira Machado,
Assistant Professor, NOVA School of Science and Technology, NOVA University Lisbon

DOCTORATE IN MECHANICAL ENGINEERING

NOVA University of Lisbon
September, 2025

Methodologies for optimal design and additive manufacturing of metamaterials combining negative property indexes

Para o meu filho Simão e
o meu marido Pedro, a minha paz.

AGRADECIMENTOS

Com a conclusão deste trabalho encerra-se um capítulo importante da minha vida, que não teria sido alcançado sem o contributo de muitas pessoas às quais deixo o meu profundo agradecimento.

Primeiramente, gostaria de expressar a minha gratidão ao meu orientador, Prof. Dr. Pedro Coelho, pela excecional orientação prestada, não só ao longo deste trabalho, mas durante todo o meu percurso académico e pelas inúmeras trocas de ideias e desafios que sempre impulsionaram o meu crescimento académico e científico. Agradeço também ao meu coorientador, Prof. Dr. Alexandre Velhinho, pela partilha de conhecimento sobre metamateriais; foi um verdadeiro privilégio aprender tanto. Para além dos meus orientadores, gostaria de deixar um agradecimento especial ao Prof. Dr. José Guedes, do Instituto Superior Técnico, pela generosidade com que sempre partilhou o seu conhecimento na área da homogeneização e pelas reuniões profundamente enriquecedoras que tivemos. Assim como à Prof.ª Dra. Ana Luísa Custódio, pela extraordinária capacidade de transmitir conceitos complexos de otimização multiobjectivo de forma clara, direta e acessível. Agradeço ainda ao Prof. Dr. Ole Sigmund pela oportunidade de aprender valiosos conhecimentos com professores pioneiros da otimização topológica, com a participação no curso "*Topology Optimization - Theory, Methods and Applications*", na Universidade Técnica da Dinamarca. Agradeço também ao Prof. Dr. Krister Svanberg, do Instituto Real de Tecnologia, Suécia, pelos códigos de otimização disponibilizados. Aos meus colegas de Doutoramento, em especial ao Fábio Conde, André Mourato e Pedro Fonseca, obrigada pela companhia e colaboração ao longo desta jornada. Agradeço ainda aos alunos do mestrado em Engenharia Mecânica, Rui Silva, Francisco Menezes e Bernardo Santos, e, em especial, à Irina Ribas, do mestrado em Materiais Avançados e Reciclagem Inovadora, pela troca de impressões e alguns contributos básicos que deram para o desenvolvimento da minha tese.

À minha família, a quem dizer um simples obrigado não chega. Mãe, pai, mano, Teté, Marina, avô Raul, Teresa, Joana e Tiago, vocês são o grande pilar da minha vida. Às minhas amigas, Raquel, Anocas, Maggie, Laís, Inês, Carolina, Sofia, Cláudia, Marianas e Matilde,

obrigada pela vossa amizade e leveza, que é das coisas mais bonitas que levo da vida, e aos meus grandes amigos, por serem uma fonte diária de alegria. Obrigada por tudo, sempre. Por último, ao meu marido, Pedro. Obrigada por seres uma fonte de inspiração e orgulho todos os dias, pela paz e amor sereno, pelo lar onde posso crescer e sonhar e pela família que construímos juntos – essa sim, é a verdadeira grande obra da minha vida.

Por último, agradeço à Faculdade de Ciências e Tecnologia da Universidade Nova de Lisboa, em especial ao DEMI e CENIMAT|i3N, por todo o equipamento disponibilizado para realizar o meu trabalho. Agradeço também à Fundação para a Ciência e Tecnologia (FCT – MCTES), pelo financiamento proporcionado através da bolsa de estudos para doutoramento com referência 2021.05360.BD, e através do projeto 2022.06903.PTDC - TOP&AM4FGM (http://doi.org/10.54499/2022.06903.PTDC).

"We especially need imagination in science. It is not all mathematics, nor all logic, but it is somewhat beauty and poetry" (Maria Mitchell).

ABSTRACT

Engineering is evolving alongside technology, demanding new approaches to design materials capable of dealing with growing structural and functional challenges. Metamaterials are artificially engineered materials designed to exhibit unusual properties, often unattainable in natural materials. Among the most counterintuitive behaviors, Negative Poisson's Ratio (NPR) and Negative Thermal Expansion (NTE) stands out, showing unique thermomechanical responses such as lateral expansion under tension and contraction upon heating. These unconventional behaviors are promising for a wide range of engineering applications, from aerospace to biomedical devices.

This thesis presents the development of a computational framework for the systematic design of metamaterials exhibiting both NPR and NTE, incorporating advanced topology optimization techniques, such as multimaterial, multiobjective and multiscale optimization. Two complementary design strategies are explored, to tailor effective properties at the microscale and embed such behavior into structural applications: (1) a microscale approach, focused on investigating the intrinsic trade-off between NPR and NTE using multimaterial and multiobjective topology optimization and different types of microstructure discretizations (truss-like and continuum-like), obtaining Pareto sets; and (2) a multiscale approach, to investigate how the macrostructure geometry and loading conditions influence the performance and design of the microstructures. The proposed methodology incorporates homogenization techniques, material symmetry constraints and uniform and layer-wise material distribution in the structure to bridge the gap between microscale material behavior and macroscale functional requirements.

Through a series of case studies, including multiobjective optimization, the influence of anisotropy, and applications under non-uniform loading such as pure bending, the developed methodology demonstrates its ability to generate functionally graded porous metamaterials with tailored auxetic responses. Regarding the competitive behavior of both indexes, the minimization of the Poisson's ratio depends mostly on the architecture of the unit-cell, while the NTE is due to both architecture and material distribution. So, both can be neg-

ative simultaneously, but extremizing one property results in worsening the other. In the multiscale framework, the concept of auxetic structure is introduced, allowing to formulate the optimization problem using the actual structural response, moving beyond the conventional material design approach. This methodology has proved successful in designing auxetic and thermoauxetic structures, while also evidencing the critical role of macroscale effects, such as loading and geometry, on the optimized microstructural layout. Additionally, a computational cost study is performed, providing insights into the scalability and efficiency of the proposed methods. The present work further explores the integration of optimized designs with additive manufacturing, aiming to bridge the gap between design and manufacture.

Overall, this work contributes to the advancement of functional metamaterial design by enabling the concurrent tuning of mechanical and thermal properties and ensuring their effectiveness at both the material and structural levels.

Keywords: Metamaterials; Multiobjective optimization; Multiscale; Negative thermal expansion; Auxetic; Multimaterial; Homogenization.

RESUMO

A engenharia está a evoluir em paralelo com os avanços tecnológicos, exigindo novas abordagens para projetar materiais capazes de enfrentar desafios estruturais e funcionais cada vez maiores. Os metamateriais são materiais artificialmente concebidos para exibirem propriedades invulgares, muitas vezes inalcançáveis em materiais naturais. Entre os comportamentos mais contraintuitivos, destacam-se o coeficiente de Poisson negativo (NPR) e a expansão térmica negativa (NTE), que resultam em respostas termomecânicas únicas, como expansão lateral sob tração e contração com o aumento da temperatura. Estes comportamentos não convencionais revelam-se promissores para uma vasta gama de aplicações de engenharia, desde o setor aeroespacial até dispositivos biomédicos.

Esta tese apresenta o desenvolvimento de uma abordagem computacional para o projeto sistemático de metamateriais com ambos NPR e NTE, integrando técnicas avançadas de otimização topológica, como a otimização multimaterial, multiobjetivo e multiescala. São exploradas duas estratégias de projeto complementares, com o objetivo de ajustar propriedades efetivas à microescala e incorporar tais comportamentos em aplicações estruturais: (1) uma abordagem à microescala, focada na investigação do conflito intrínseco entre NPR e NTE, utilizando otimização topológica multimaterial e multiescala e diferentes tipos de discretização da microestrutura (do tipo treliça e do tipo contínuo), obtendo frentes de Pareto; e (2) uma abordagem multiescala, para estudar como a geometria da macroestrutura e as condições de carregamento influenciam o desempenho e o projeto das microestruturas de material. A metodologia proposta incorpora técnicas de homogeneização, restrições de simetria de material e estratégias de distribuição de material uniforme e por camadas, de forma a ligar o comportamento do material à microescala com os requisitos funcionais à macroescala.

Através de um conjunto de estudos de caso, incluindo otimização multiobjetivo, influência da anisotropia e aplicações com carregamento não uniforme, como flexão pura, a metodologia desenvolvida demonstra a sua capacidade de gerar metamateriais porosos com gradiente de funcionalidade com respostas auxéticas ajustadas. No que diz respeito ao comportamento competitivo entre os dois índices de propriedades, a minimização do coeficiente

de Poisson depende maioritariamente da arquitetura da célula unitária, enquanto a NTE resulta tanto da arquitetura como da distribuição do material. Assim, ambas as propriedades podem ser simultaneamente negativas, mas a minimização de uma conduz inevitavelmente à degradação da outra. No contexto multiescala, introduz-se o conceito de estrutura auxética, permitindo formular o problema de otimização com base na resposta estrutural real, indo para além da abordagem convencional focada apenas no material. Esta metodologia revelou-se eficaz no projeto de estruturas auxéticas e termoauxéticas, evidenciando também o papel determinante dos efeitos à macroescala, tal como o carregamento e a geometria, na definição da microestrutura otimizada. Adicionalmente, é realizado um estudo de custo computacional, fornecendo perspetivas sobre a escalabilidade e eficiência dos métodos propostos. O presente trabalho explora ainda a integração das soluções ótimas com manufatura aditiva, com o intuito de colmatar a lacuna entre projeto e fabrico.

No seu todo, este trabalho contribui para o avanço do projeto de metamateriais funcionais, ao permitir o ajuste simultâneo das propriedades mecânicas e térmicas, garantindo a sua eficácia tanto ao nível do material como ao nível estrutural.

Palavras chave: Metamateriais; Otimização multiobjectivo; Multiescala; Expansão térmica negativa; Auxético; Multimaterial; Homogeneização.

CONTENTS

LIST OF FIGURES

LIST OF TABLES

GLOSSARY

Additive Manufacturing	Fabrication process, also commonly known as 3D printing, where a 3D object is built, layer by layer, from a digital model.
Anepectic	A material that combines both a negative Poisson's ratio and negative thermal expansion
Auxetic	A material that has a negative Poisson's ratio, exhibiting a unique mechanical behavior by contracting in the transverse direction when compressed and expanding when under tension
Coefficient of Thermal Expansion	Material property that describes how a material's size changes in response to temperature variations
Finite Element Method	Numerical technique used to find approximate solutions to boundary value problems in engineering, by dividing a complex structure into smaller elements.
Homogenization	A process that transforms a heterogeneous medium into a homogeneous one to determine its equivalent (effective) behavior
Metamaterials	Artificially engineered materials with properties not found in nature, arising from the arrangement and geometry of their microstructure
Multiobjective optimization	A field of optimization that deals with problems where multiple, often conflicting, objective functions need to be optimized simultaneously.
Multiscale structures	Structures characterized by two distinct scale levels: the macroscale, referring to the structural level, and the microscale, referring to the material scale

Poisson's ratio	Material property that describes how a material deforms in directions perpendicular to an applied load
Structural optimization	Set of theory and methods aimed at finding the optimal solution for minimizing (or maximizing) a structural performance, subject to a set of constraints or requirements.
Topology optimization	Optimization method used to determine the optimal material distribution within a design domain
Unit-cell	The smallest periodic heterogeneity that is repeated throughout the domain

ACRONYMS

AM	Additive Manufacturing
AH	Asymptotic Homogenization
BC	Boundary Conditions
CTE	Coefficient of Thermal Expansion
DMO	Discrete Material Optimization
DOF	Degree Of Freedom
EBH	Energy-Based Homogenization
FDM	Finite Difference Method
FE	Finite Element
FEA	Finite Element Analysis
FEM	Finite Element Method
FFF	Fused Filament Fabrication
FGM	Functionally Graded Material
GA	Genetic Algorithm
GCMMA	Globally Convergent Method of Moving Asymptotes
GS	Ground Structure
LC	Load Cases
LSM	Level-set Method
MMA	Method of Moving Asymptotes
MMTO	Multi Material Topology Optimization
NPR	Negative Poisson's Ratio

NTE	Negative Thermal Expansion
OC	Optimality Criteria
PBC	Periodic Boundary Conditions
PFM	Phase-Field Method
PR	Poisson's Ratio
RAMP	Rational Approximation of Material Properties
RMMI	Recursive Multiphase Materials Interpolation
RVE	Representative Volume Element
SFP	Shape Function Parametrization
SIMP	Solid Isotropic Material with Penalization
SLA	Stereolithography
SLP	Sequential Linear Programming
SQP	Sequential Quadratic Programming
TO	Topology Optimization
UC	Unit-Cell
UMMI	Uniform Multiphase Materials Interpolation

SYMBOLS

Latin

A_e	Area of the bar element
a_e	Size variable of the bar element
a_0, a_i, d_i	MMA parameters
$\mathbf{B}_e, \mathbf{B}_{e^M}$	Strain-displacement matrix of micro element e or macro element e^M
$b_i, \mathbf{b}$	Body forces
$\langle b_i \rangle$	Homogenized body loads
c_i	Constraint violation parameter in MMA
C	Compliance value
C^+	Maximum admissible compliance value
ca	Continuation approach parameter for compliance
$C^H_{ijkl}, \mathbf{C}^H$	Homogenized compliance tensor
$\mathbf{d}$	Optimization search direction
d	Characteristic dimension of the microscale
D	Characteristic dimension of the macroscale
e, e^m	Micro finite element
e^M	Macro finite element
E	Young's modulus of an isotropic material
E^1	Young's modulus of the stiffest (isotropic) material phase
E_{ijkl}	Stiffness tensor
E^ϵ_{ijkl}	Stiffness tensor including microstructure heterogeneities

$E^e_{ijkl}, \mathbf{E}_e$	Stiffness tensor of finite element e
$\mathbf{E}^m$	Stiffness tensor of a given (isotropic) material phase m
$E^H_{ijkl}, \mathbf{E}^H$	Homogenized stiffness tensor
$\mathbf{E}^H_{e^M}$	Homogenized stiffness tensor of macro element e^M
$\mathbf{E}^H_l$	Homogenized stiffness tensor of layer l
E^{RVE}_{ijkl}	Stiffness tensor computed through the RVE method
$\mathbf{F}$	Load vector
$\mathbf{F}^m$	Mechanical load vector
$\mathbf{F}^{th}$	Thermal load vector
f	Objective function
$f_0, \tilde{f}_0$	Original and approximating objective functions
$f_i, \tilde{f}_i$	Original and approximating constraint functions
f_i^{max}	Maximum value of an objective function i
f_i^{min}	Minimum value of an objective function i
f_ν	Poisson's ratio objective function
f_α	Coefficient of thermal expansion objective function
G	Shear modulus
G^1	Shear modulus of the stiffest (isotropic) material phase
g_i	Inequality constraints
h_k	Equality constraints
$\mathbf{I}$	Identity matrix
i	Number of iterations
k	Iteration step
$\mathbf{K}$	Global stiffness matrix
$\mathbf{K}_e, \mathbf{k}_e$	Element stiffness matrix

K	Bulk modulus
K^+	Maximum admissible bulk value
K^-	Minimum admissible bulk value
l	Layer
L, L_e	Length of the bar element
$L_j^{(k)}, U_j^{(k)}$	MMA lower and upper moving asymptote
LC	Number of load case
m	Total number of design constraints
m^{crit}	Total number of critical or active constraints
n	Total number of design variables
N, N^m	Number of micro finite elements
N^M	Number of macro finite elements
N_c	Number of coupled finite elements
N_e	Neighborhood of element e
N_f	Number of material phases
N_i	Shape function of a given finite element
nl	Number of layers
$ndof$	Number of degrees of freedom
p, p_1, p_2	Power-law penalty exponents
$q_i, \mathbf{q}$	Applied traction forces
R, r_{min}	Filter radius
$\mathbf{s}$	Vector of the design variables
$\mathbf{s}^{(k)}$	Design variable vector in iteration k
$\mathbf{s}^0$	Starting point in the optimization process
$\mathbf{s}^1$	Updated point in the optimization process

s_i^+, s_i^{max}	Upper bound on the design variable i
s_i^-, s_i^{min}	Lower bound on the design variable i
S_A	Dimensional scale factor of the bar element
$\mathbf{t}, z$	MMA artificial variables
$\mathbf{T}_e$	Transformation matrix of bar element e
t^{mi}	Time spent solving the microscale analysis
t^{MA}	Time spent solving the macroscale analysis
t^{ε}	Time spent computing the strain field
$t^{\partial\varepsilon}$	Time spent computing the sensitivities of the strain field
$u_i, \mathbf{u}, \mathbf{U}$	Displacement solution
$\mathbf{U}^m$	Mechanical displacement solution
$\mathbf{U}^{th}$	Thermal displacement solution
$\mathbf{U}_e^{A(kl)}$	Element displacement solution
$\mathbf{U}_{e^M}$	Displacement solution of macro element e^M
$u_i^{\epsilon}, \mathbf{u}^{\epsilon}$	Asymptotic expansion of the displacement field
$\mathbf{u}^i$	i^{th} term of the asymptotic expansion of the displacement field
V, V^{mi}	Volume of the microstructure (UC)
V^+	Maximum admissible volume value
V_i	Total volume of the ground structure
V_e	Volume (or area in 2D) of micro element e
V_{e^M}	Volume (or area in 2D) of macro element e^M
V_l	Volume (or area in 2D) of layer
$v_i, \mathbf{v}$	Virtual periodic displacement
$w_{m,e}$	Weight functions
$x_1, x_2, \mathbf{x}$	Macroscopic spatial coordinates

x_i, x_e	Spatial location of macro element i or e
$y_1, y_2, \mathbf{y}$	Microscopic spatial coordinates
y_i, y_e	Spatial location of micro element i or e
$Y, \lvert Y \rvert$	Microscopic domain and area (in 2D)
¥	Solid part of the microscopic domain
$Y_{e^m}, \lvert Y_{e^m} \rvert$	Micro element domain and area (in 2D)
$\mathbf{z}$	Dummy-load vector

Greek

α	Optimal step size
α^*	Normalization factor of the CTE objective function
α^1	Coefficient of thermal expansion of the first (isotropic) material phase
α_{ij}	Coefficient of thermal expansion tensor
$\bar{\alpha}_{ij}$	Average CTE tensor of the macrostructure
$\boldsymbol{\alpha}_e$	CTE tensor of finite element e
$\boldsymbol{\alpha}^m$	CTE tensor of a given (isotropic) material phase m
$\alpha_{ij}^H, \boldsymbol{\alpha}^H$	Homogenized coefficient of thermal expansion tensor
$\alpha_j^{(k)}, \beta_j^{(k)}$	MMA move limits
β_{ij}	Thermal stress tensor
β_{ij}^{ϵ}	Thermal stress tensor including microstructure heterogeneities
$\beta_{ij}^H, \boldsymbol{\beta}^H$	Homogenized thermal stress tensor
$\boldsymbol{\beta}_{e^M}^H$	Homogenized thermal stress tensor of macro element e^M
$\boldsymbol{\beta}_l^H$	Homogenized thermal stress tensor of layer l
β_{ij}^{RVE}	Thermal stress tensor computed through the RVE method
δ	Percentage of imbalanced load

δ_{ij}	Kronecker delta
Γ_q	Applied traction boundary
Γ_u	Applied displacement boundary
ΔT	Temperature differential
ϵ	Characteristic inhomogeneity dimension
$\epsilon_1, \epsilon_2^-, \epsilon_2^+, \epsilon_3$	Constraint functions parameters
$\varepsilon_{ij}^{e^M}$	Strain tensor of macro element e^M
ε_{ij}^{GP}	Strain tensor in each Gauss point of the macro element e^M
$\varepsilon_{ij}^{\epsilon}$	Strain tensor including microstructure heterogeneities
$\varepsilon_{ij}, \boldsymbol{\varepsilon}$	Strain tensor
$\varepsilon_{ij}^m, \boldsymbol{\varepsilon}^m$	Mechanical strain tensor
$\varepsilon_{ij}^{th}, \boldsymbol{\varepsilon}^{th}$	Thermal strain tensor
$\bar{\varepsilon}_{ij}, \bar{\boldsymbol{\varepsilon}}, \langle \boldsymbol{\varepsilon} \rangle$	Average strain tensor
$\bar{\varepsilon}_{ij}^m, \bar{\boldsymbol{\varepsilon}}^m$	Average mechanical strain tensor
$\bar{\varepsilon}_{ij}^{th}, \bar{\boldsymbol{\varepsilon}}^{th}$	Average thermal strain tensor
$\varepsilon_{ij}^0, \boldsymbol{\varepsilon}^0$	Uniform strain tensor
$\varepsilon_{pq}^{0(kl)}, \boldsymbol{\varepsilon}^{0(i)}$	Superimposed homogeneous macroscopic unit strain
$\varepsilon_{pq}^{*(kl)}, \boldsymbol{\varepsilon}^*$	Fluctuation strain field
$\varepsilon_{pq}^{A(kl)}$	Induced strain field
$\varepsilon_{pq}^{0\alpha}, \boldsymbol{\varepsilon}^\alpha$	Superimposed homogeneous macroscopic thermal unit strain
$\varepsilon_{pq}^{*\alpha}, \boldsymbol{\varepsilon}^{*\alpha}$	Fluctuation thermal strain field
$\varepsilon_{pq}^{A\alpha}$	Induced thermal strain field
$\boldsymbol{\lambda}$	Adjoint vector
ν^*	Normalization factor of the PR objective function
ν	Poisson's ratio of isotropic material

ν_{ij}	Poisson's ratio
$\overline{\nu}_{ij}$	Average Poisson's ratio of the macrostructure
ρ_e	Artificial density variable of element e
$\tilde{\rho}_e$	Filtered artificial density variable of element e
$\rho_{1,e}, \boldsymbol{\rho}_1$	Topological density variable
$\rho_{2,e}, \boldsymbol{\rho}_2$	Material selection density variables
$\tilde{\rho}_{1,e}, \tilde{\boldsymbol{\rho}}_1$	Filtered topological density variable
$\tilde{\rho}_{2,e}, \tilde{\boldsymbol{\rho}}_2$	Filtered material selection density variables
ρ_{min}	Lower bound of the artificial density variable
$\rho^1_{e^m,l}$	Topological density variable of micro element e^m, in layer l
$\rho^2_{e^m,l}$	Material selection density variables of micro element e^m, in layer l
σ^{ϵ}_{ij}	Stress tensor including microstructure heterogeneities
$\sigma_{ij}, \boldsymbol{\sigma}$	Stress tensor
$\bar{\sigma}_{ij}, \overline{\boldsymbol{\sigma}}$	Average stress tensor
σ^0_{ij}	Uniform stress tensor
σ^{VM}	Von-Mises stress
$\Upsilon_k, \boldsymbol{\Upsilon}$	Micro thermal displacement vector
φ	Step function
ϕ_1, ϕ_2	Continuation approach parameters for constraints
Φ	Arbitrary Y- periodic function
X	Arbitrary function with explicit and implicit dependence on a variable
$\chi^{pq}_k, \boldsymbol{\chi}^{pq}, \boldsymbol{\chi}^{(i)}$	Micro elastic displacement vector
ψ_1, ψ_2, ψ_3	Objective functions parameters
$\Psi, \lvert\Psi\rvert$	RVE domain and area (in 2D)
ω	Weight of multiobjective optimization

Ω^{ϵ}	Macroscopic domain including microstructure heterogeneities
Ω	Macroscopic design domain
Ω_{e^M}	Design domain of the macro element
Ω_l	Design domain of the layer
Ω_{mat}	Subdomain with material
Ω_{void}	Subdomain with void

Mathematical

$\partial\Omega^{\epsilon}$	Boundary of the macroscopic domain

1

INTRODUCTION

In recent years, the advancements of computational methods and manufacturing technologies has allowed to explore novel materials capable of addressing increasingly complex design challenges. These challenges highlight the need for hybrid materials that can sustain demanding temperature conditions, given the critical role of thermal loads in engineering applications. Metamaterials have emerged as a class of engineered materials, which, in many cases, can be described as composite materials with a periodic porous microstructure, as considered in the context of this thesis. Such materials can be systematically designed and additively manufactured to exhibit customized physical properties [1], being perfect candidates for addressing emerging engineering challenges. This new class of artificially materials has enabled the development of innovative multifunctional composites that exhibit exceptional properties, typically absent in natural materials [2]. The name metamaterial derives from the Greek word μετά (*meta*), meaning beyond and the Latin word *materia*, meaning material.

A particularly promising subset of metamaterials exhibits unconventional effective properties such as Negative Poisson's Ratio (NPR) and Negative Thermal Expansion (NTE). Materials with NPR expand in the lateral direction when stretched axially and contract laterally when compressed axially, while NTE materials shrink when heated, which are phenomena rarely found in nature. These behaviors open the door to cutting-edge engineering applications in fields such as aerospace (e.g., thermally stable optical mounts), biomedical devices (e.g., auxetic meshes for hernia repair, dental fillers), and precision engineering [3,4].

Typically, NPR arises from reentrant, chiral, or rotational geometries in metamaterials made from a single material [4], while NTE metamaterials combine at least two materials

with contrasting (and positive) thermal expansion coefficients [5]. Although both phenomena have been studied independently, combining them into the same material design solution remains a complex challenge requiring advanced modeling strategies.

In structural mechanics, a composite material is often characterized by small-scale periodic heterogeneities (solids and voids), referred to as unit-cell (UC), that is repeated throughout the structure. When the heterogeneities are regular enough to be assumed periodic and their dimensions are very small in comparison to the macroscopic body, the material is commonly called *composite with periodic microstructure* [6], and metamaterials are often categorized as such. Full modeling and simulation of the entire heterogeneous domain would lead to an extremely complex computational model with millions of degrees of freedom. This would make the problem computationally prohibitive, highlighting the need for alternative approaches to efficiently capture the material's overall behavior without modelling every microscopic detail. One approach to computing macroscopic behavior is through homogenization methods, which treats the heterogeneous medium as an equivalent homogeneous one by typically analyzing its representative microstructure [7]. Nevertheless, the homogenization method is not restricted to the periodic medium, being a very efficient tool in modelling complex heterogeneous media [8].

Most designs of metamaterials with both NPR and NTE found in the literature rely on empirical or intuitive approaches [9]. However, to fully explore the design space and achieve functional properties, systematic methods such as topology optimization are essential to establish a framework of conceptual design. When combined with homogenization theory, this strategy – known as inverse homogenization method [10] – has proven effective in designing metamaterials with NPR or NTE. Nonetheless, the simultaneous optimization of both negative indexes remains largely unexplored. Moreover, the fine-tuning of competing property indexes becomes important to find functional solutions in engineering applications.

1.1 Context and Motivation

This PhD thesis is focused on the analysis and optimization of metamaterials, proposing a systematic design methodology, aiming to generate complex microstructures with both NPR and NTE, based on a multimaterial topology optimization framework. The exploration of these two indexes, both negative, places the design problem on a multimaterial, multiphysics, multiobjective, and multiscale level. The term *Anepectic*, derived from the Greek word

“Επέκταση” (*Epéktasi*), meaning *expansion*, was proposed by Raminhos [32] to describe such materials. It further explores the integration of such optimized designs with additive manufacturing, aiming to bridge the gap between design and fabrication.

The multiscale optimization approach excels in comparison to the classical microscale approach based on inverse homogenization, usually used to systematically design metamaterials. A material obtained by microstructural optimal design, without modelling a structure at macroscale, is merely optimum in terms of equivalent mechanical properties, which may not perform optimally in real structural applications with complex loading and boundary conditions [11]. This motivates pursuing a hierarchical optimization framework, based on a multiscale approach, that considers broader physical and practical constraints.

Over the past decades, Additive Manufacturing (AM) has experienced significant growth and it has been increasingly used to fabricate a wide range of components and novel materials. As AM technologies continue to advance, they enhance product quality and expand their applicability across demanding industries such as aerospace, biomedical engineering, and defense [12]. AM also enhances design freedom, supports material efficiency, and contributes to sustainable manufacturing practices.

Another main motivation for this work is the integration of computational design with AM. Due to their geometric complexity, most optimized microstructures cannot be produced using traditional fabrication methods. AM, however, unlocks the potential for producing optimized structures and materials, as it is inherently suited for fabricating highly customized and intricate components, allowing the physical realization of complex microstructures [13]. There is a strong interdependency between AM and structural optimization, as many optimized designs only became viable with the advent of AM, while the evolution of AM technologies continues to expand the possibilities of what can be achieved through optimization. Together, they form an engineering cycle that begins with optimal design and culminates in manufacturable, functional prototypes [14].

Despite the promising synergy between computational design and AM, a significant gap still exists between theoretical optimization results and their practical manufacturability, particularly in density-based approaches, which often produce fine-scale or jagged features that are difficult to fabricate. Many optimization studies on mechanical metamaterials remain purely theoretical, without addressing the constraints and opportunities of real-world production. Therefore, there is a pressing need to develop multidisciplinary methodologies that effectively bridge the gap between design and fabrication [15]. Establishing an engineer-

ing cycle, from the systematic and optimal design of metamaterials to the fabrication and experimental validation of physical prototypes, is essential for translating these advanced materials into practical applications [9].

In summary, this thesis contributes to the development of a computational framework for the design and analysis of metamaterials with tailored effective properties. It focuses primarily on the use of topology optimization to design materials exhibiting NPR and NTE, addressing both microscale and multiscale design paradigms. Numerical homogenization methods are employed to evaluate and validate the effective behaviour of the optimized microstructures. Prototype fabrication is conducted here, to contribute to a full design-to-manufacture cicle, from the computational optimization of microarchitectures and material distributions using topology optimization, to their potential fabrication using AM. Nevertheless, the core emphasis of this thesis lies on the computational and theoretical problem.

1.2 Approach and Objectives

The primary objective of this research is to advance the state of the art in the optimal design of structural metamaterials with NPR and NTE. Although microstructural optimization is a widely investigated research topic, studies on the combined effect of anepectic materials are quite scarce. In this regard, the thesis proposes two complementary optimization paradigms: one at the microscale, focused on tailoring the effective properties of a UC; and another at the multiscale level, addressing both material and structural scales simultaneously. Both approaches involve solving complex multiphysics, multimaterial, and multiobjective topology optimization problems. Their development contributes to pushing the boundaries of computational design and materials engineering and provides a robust framework for tailoring metamaterials with precise and functional effective properties. To accomplish the objectives set forth in this thesis, five core tasks were developed and executed.

Firstly, a comprehensive understanding of the state of the art on auxetic and anepectic metamaterials, whether designed through analytical models or systematic methods was carried out. This task involved a thorough literature review and synthesis of various models exhibiting both negative indexes. It served as a learning and benchmarking stage, focused on analyzing existing geometries and material compositions of metamaterials with NPR and NTE. This process helped develop critical insight and sensitivity to the problem under study. In parallel, finite element models were also developed to simulate the effective behavior of

such microstructures, either modeled with continuum (based on quadrilateral finite elements) or discrete (based on truss or beam elements forming a ground structure) discretizations.

Secondly, Asymptotic Homogenization (AH) techniques, used to compute the equivalent behavior of a composite material, are implemented and solved using finite element-based numerical methods. This implementation required the application of key concepts from continuum mechanics, including the enforcement of periodic boundary conditions on the microstructure domain, and incorporating coupled thermomechanical effects into the problem equilibrium equation. With optimization in mind, a multiphase interpolation scheme is adopted, involving void and two distinct solid phases, an essential setup to enable NTE, which arises from the interaction between materials with different values of both elastic moduli and coefficients of thermal expansion. This task provides the necessary background to formulate the optimization problem.

The next two major tasks involve the formulation and computational implementation of two key optimization problems: one at the microscale and another at the multiscale level. At the microscale, the full optimization framework is implemented in a structured and modular computational code (in MATLAB ®), with consideration for parallel computing techniques to handle the high computational demands. Efficient algorithms such as the Globally Convergent Method of Moving Asymptotes (GCMMA) [16] are explored to solve the problem. At the multiscale level, the optimization integrates both the material's microstructure and the macroscopic structural domain it belongs to, such as optical mounts or thermal dampers, enabling the use of realistic boundary conditions in the design process [17,18]. Together, these tasks aim to advance the development of optimized metamaterials with tailored thermomechanical responses within application-relevant settings. These tasks resulted in significant original code-level contributions, including the development of multiscale analysis algorithms, the implementation of an isoparametric finite element, and the complete implementation of sensitivity analysis for the proposed optimization framework.

Lastly, the final task of this thesis concerns the transition from computational design to physical realization through additive manufacturing. However, before fabrication can occur, it is essential to establish a robust workflow capable of converting optimized design solutions into manufacturable designs. This involves addressing key challenges such as geometric regularization or smoothing, and adapting the design to the constraints of specific AM technologies. The goal is to ensure that the complex architectures resulting from optimiza-

tion can be accurately and efficiently fabricated, preserving their intended thermomechanical properties. This step lays the foundation for future prototyping and functional experimental testing.

1.3 Structure of the Thesis

This thesis is structured into four main sections. Chapter 2 presents the scientific framework necessary to contextualize this work. First a literature review on metamaterials with both NPR and NTE is presented, followed by the theoretical principles on linear thermoelasticity, homogenization theory and structural optimization.

The following three chapters reflect the main tasks of the thesis, with the microscale topology optimization presented in Chapter 3, the multiscale topology optimization in Chapter 4 and finally, in Chapter 5, the workflow to bridge design and fabrication. With the problem posed at the microstructural level, a multiobjective topology optimization framework is developed, to investigate the influence of having both indexes negative in the metamaterial design. Furthermore, the UC is discretized using a ground structure approach and a discrete anepectic metamaterial is also presented in chapter 3. The optimization of metamaterials using a multiscale approach is rather novel, and so, Chapter 4 is focused on gaining insight into the influence of the structure and boundary conditions on the optimized material. Additionally, in the beginning of Chapter 4, some results from the microscale optimization are revisited to fully explore the potential offered by the multiscale model proposed here. Finally, Chapter 5 introduces a methodology developed to convert the optimized solutions into manufacturable designs, presenting some samples fabricated using 3D printing. Lastly, along with the conclusions presented in each chapter, the main remarks of this work and possible future research avenues are presented in Chapter 6.

2

SCIENTIFIC FRAMEWORK

In this chapter, the fundamental concepts regarding the work developed in this thesis are covered, providing the necessary scientific background and context. Firstly, a comprehensive review of the state of the art of metamaterials is presented in Section 2.1, with a particular focus on mechanical metamaterials exhibiting negative Poisson's ratio and negative thermal expansion. Both empirically and systematically designed metamaterials are discussed to illustrate different approaches found in the literature. This first subsection is based on the conference paper "Architectured and additively manufactured double-negative index metamaterials", that covers the tasks developed in the beginning of the present thesis and was published in the proceedings of the Eccomas congress 2022 [9]. Section 2.2 provides an overview of thermoelasticity theory, which forms the basis for understanding the coupled thermal and mechanical behavior of materials. Subsequently, the principles of homogenization theory are introduced, as they are essential for characterizing the effective properties of periodic materials. The chapter concludes with a section on structural optimization, which outlines basic concepts, such as topology optimization, multimaterial design, and multiscale modeling, that are directly applied throughout this thesis.

2.1 Metamaterials: A Brief Story

The term metamaterial refers to engineered materials that do not occur naturally but are artificially designed to exhibit properties that conventional materials do not possess [19]. Many such unusual properties arise not from the composition of the constituent materials, but from

the internal architecture, i.e., the specific way in which different material phases are arranged and interconnected [20].

Among the distinctive characteristics of metamaterials, one of the most appealing is their ability to exhibit negative effective properties. These negative properties are of particular interest due to their counter-intuitive behaviour. The term "auxetic," used to describe materials that exhibit Negative Poisson's Ratio (NPR), was first introduced by Evans et al. [21], in 1991. The word derives from the Greek αὐξητικός (*auxetikos*), meaning "tending to increase," reflecting the counterintuitive expansion of these materials when stretched. The atypical deformation mechanism of NPR is usually linked to the architecture of the UC, mainly categorized as re-entrant, chiral, or rotational structures [2,4]. Materials exhibiting NPR where first known through the pioneer publications of Lakes in 1987 [22], and Prall and Lakes [23], in 1997.

This type of behavior holds great potential for a wide range of applications across various fields, including aerospace, biomedical engineering, sports [24], defense, and smart systems [3] due to their effectiveness in absorbing sound, vibrations and energy absorption [25]. In aerospace and defense, for instance, they are particularly promising for use in protective equipment [26], while in the biomedical field, they have been explored for the development of prosthetic devices [27]. In addition to their auxetic properties, these materials enhance other mechanical properties such as shear resistance, indentation resistance [28,29], fracture toughness [30], and energy absorption capability [31].

Another interesting negative property is the Coefficient of Thermal Expansion (CTE), that enables a wide range of applications, including thermally stable mirrors for space telescopes, microchips, dental composites, optical fibers, spacecraft components, and the production of biomedical devices such as surgical meshes for hernia repair or compression garments [32]. Other relevant applications include semiconductors, biomedical sensors, solar energy systems [33], satellite antennas, precision instruments, and thermal sensors [34]. Controlling the CTE of a material is crucial for structural safety, minimizing thermal stress, extending the service life of devices and measuring accurately, especially in environments with significant temperature fluctuations [35,36]. Naturally occurring materials exhibiting Negative Thermal Expansion (NTE) are very rare; the behaviour has been shown to occur in some complex metal oxides, polymers, and zeolites [37]. However, the tunability of the coefficient of thermal expansion (CTE) in composite materials is achieved not only by carefully designing the microstructure's architecture but also by selecting the appropriate constituent mate-

rials [38]. This results from the relation of the deformation mechanism of NTE and the relative expansion of the constituent materials, which have positive (yet dissimilar) CTE values.

Metamaterials can display thermoauxetic behaviour either under mechanical or thermal loading, corresponding respectively to a NPR or a NTE coefficient. Materials exhibiting a negative Poisson's ratio expand laterally when subjected to tensile loading and contract laterally under compressive loading. In the case of NTE, the material contracts when exposed to an increase in temperature. This unconventional behaviour is illustrated in Fig. 2.1.

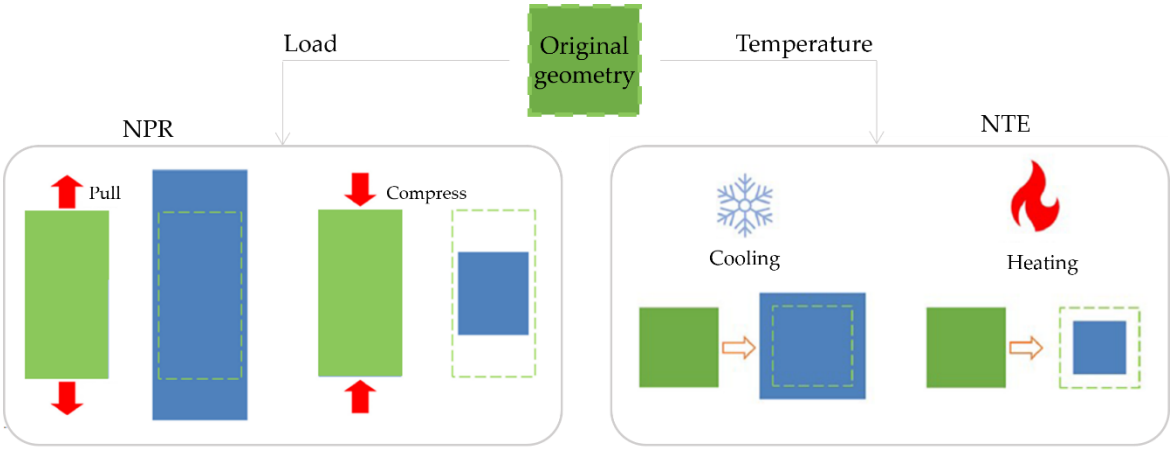

Figure 2.1 – Schematic representation of the structural behaviour of negative Poisson's ratio (NPR) and negative thermal expansion (NTE). Adapted from [39].

Recently, the search for multifunctional metamaterials has gained increasing interest due to their potential for allowing novel research directions in the fields of material design and engineering, targeting a wider range of applications [3]. In particular, mechanical metamaterials presenting both NPR and NTE, coined as 'anepectic' by Raminhos et al. [32], can potentially offer improved performance in fields such as aerospace and medicine, due to the combination of both effects.

The empirical design has been the most common approach to obtain and tune these double-negative index metamaterials. The first model of a structure combining both NPR and NTE was proposed by Grima et al., in 2007 [40]. The authors achieved this by adding a second material to an existing auxetic microstructure composed of interconnected beams forming triangles. Their work highlighted the tunability of the Poisson's Ratio (PR) and thermal properties by adjusting geometric parameters and material selection. This approach of starting with a known auxetic structure and modifying its geometry and materials has since become a common method for developing anepectic microstructures. Following this, in 2015, Ha et al. [41] developed a chiral bi-material lattice structure with NTE and a constant

NPR of -1. Ng et al. [42], in 2017, further advanced this field by modifying a re-entrant triangle auxetic structure to incorporate two materials, demonstrating that this bi-material design can achieve both auxetic properties and NTE. Similarly, Ai and Gao [43], also in 2017, proposed a star-shaped re-entrant lattice structure capable of achieving tunable NPR and NTE, with their work later extended to three-dimensional structures [36]. Wei et al. [44], in 2018 introduced a triangle-arrow metastructure combining a re-entrant triangle with a bi-material triangle to achieve both NPR and NTE, expanding the work to three-dimensions in 2021 [45]. Li et al. [46] employed a similar strategy, starting from a typical NTE structure to achieve NPR behaviour, successfully fabricating a star-square lattice metastructure using 3D printing. Fong et al. [47], in 2020, optimized the geometric parameters of the metamaterial proposed in [43], demonstrating how optimization can be used to amplify the range of NTE and NPR values. In the same year, Fu et al. [48], developed a 3D metamaterial composed of two chiral honeycomb layers capable of exhibiting a wide range of Poisson's ratio (PR) and thermal expansions. In 2021, Peng and Bargmann [49] proposed a hybrid-honeycomb structure with tuneable thermoelastic properties. Li et al. [50] also extended their work on composite metamaterials to both two-dimensional and three-dimensional designs, further refining the relationship between NPR, CTE, and geometric parameters. In 2023, Tian et al. [51] designed and fabricated a metamaterial with controllable PR and CTE. Recently, in 2024, Dong et al. [52] analysed the impact resistance of a metamaterial featuring NPR and tailorable CTE, Liu et al. [53] design a 3D metamaterial with adjustable CTE, PR and bandgap and Wang and Liu [54] proposed a 3D metamaterial with zero PR and programmable CTE and Young's modulus. Notably, most of these studies have focused on analytical and numerical approaches. However, in 2019, Raminhos et al. [32] conducted an experimental study by 3D-printing a star-shaped re-entrant mesh and testing it under thermal conditions. The metamaterials proposed in these studies are summarized in Fig. 2.2.

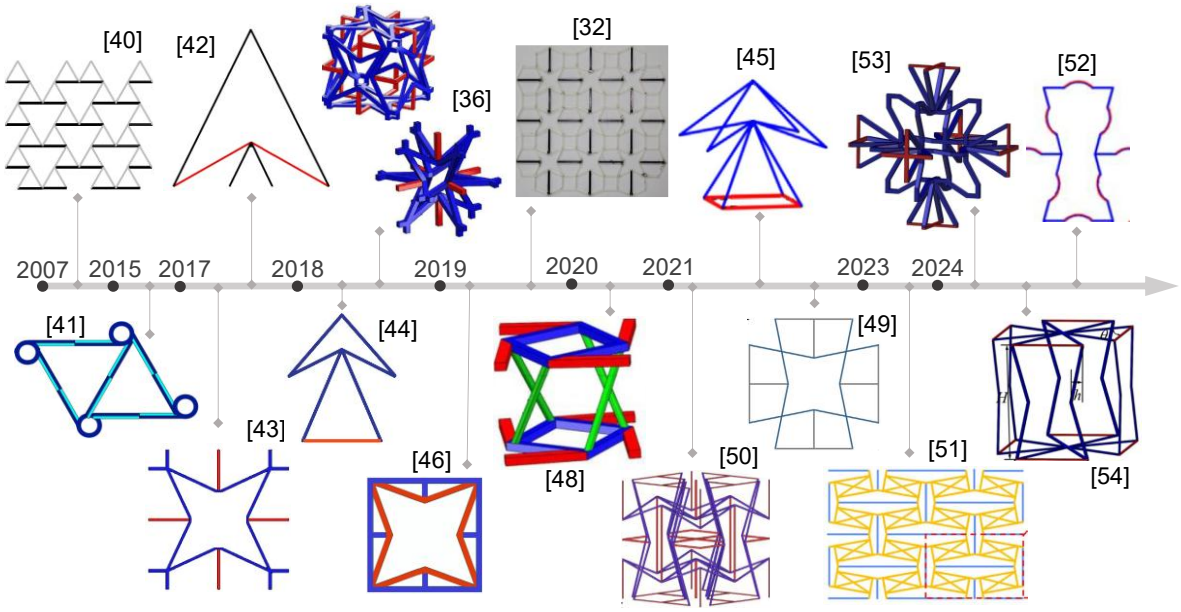

Figure 2.2 – Contributions from 2007 to the present on anepectic microstructure achieved via empirical design.

The effective properties of composite materials with periodic microstructure can be tailored by carefully designing the geometry and strategically distributing constituent materials within the design domain, called the Unit-Cell (UC). A UC is the smallest periodic heterogeneity repeated throughout the space, i.e., the microstructure. The empirical approach to design the UC relies solely on the designer's intuition and previously shared experience. However, to fully explore the potential of metamaterials, systematic design methods are demanded. Topology Optimization (TO) has proved to be a promising breakthrough on material design tools [55]. It allows to establish a framework of conceptual design without prior knowledge or bias of the optimal design, fully exploring design freedom. This can be achieved by means of a density-based approach [56], as addressed in the present work, supported on the Solid Isotropic Material with Penalization (SIMP) method [57]. Homogenization methods, such as the Asymptotic Homogenization (AH) [7,58] and the Energy-Based Homogenization (EBH) [59–62] are used to compute the effective properties of the periodic composite material, by analysing a single UC [7,63]. While AH has long been used in the optimization of both elastic and thermoelastic properties, the EBH method was limited to elastic properties optimization until recently Guo et al. [64] extended this method to optimize thermoelastic properties as well. Homogenization-based TO plays a key role on the determination of the optimal material distribution within the UC's design domain, which became known as the inverse homogenization method [10].

In the optimization of metamaterials, the literature extensively investigates their remarkable extreme thermoelastic properties. Gibiansky and Sigmund [65] first investigated the maximization of the bulk modulus and successfully attained three-phase composites that possess bulk moduli close to the Hashin-Shtrikman-Walpole bounds [66], revealing the potential of TO applied to composites design. Since then, other studies emerged on the use of TO to enhance mechanical properties [62,67,68]. Obtaining auxetic structures via TO has also been a widely covered research topic [69–72]. In [5] the first composite with NTE obtained systematically through TO was presented, using a three-phase composite material (two solids plus void). Other studies emerged afterwards, pursuing the same three-phase TO approach [73–76].

Despite these advances, most of the existing work on anepectic metamaterials, with both NPR and NTE, has relied on predefined auxetic topologies, exploring the effects of modifying geometric parameters and material combinations (see Fig. 2.2). This contrasts with the scarcity of contributions based on emerging systematic design methods. with only a few recent works found in the literature [9], as summarized next. Wang et al. [77] used a level-set based TO method to design the first optimal 2D metamaterial exhibiting both negative indexes and used a target-based objective function subject to individual material volume fraction constraints. Vineyard and Gao [78] used the level-set method to design 2D and 3D metamaterials with positive, zero or negative CTE and NPR, using the ε-constraint multi-objective method in the optimization problem formulation. Han and Wei [79] and Han et al. [80,81], used a density-based method to optimize bi and tri-material 2D metamaterials. To achieve both negative indexes, the authors resort to an Alternating Active Phase & Objective algorithm based on the dynamical switch of the objective functions. Li et al. [75] used density based TO to optimize 3D multi-material auxetic microlattices, with zero thermal expansion, by considering stiffness, isotropy, PR, and CTE in the objective function, through a combination of weights. Li et al. [39] presented 3D isotropic lattice metamaterials exhibiting NPR and NTE. The authors also weighted four design criteria in the objective function: isotropy, PR, CTE, and geometry penalizations. The problem was stated using mixed integer programming and solved by a genetic algorithm. The authors also use a multiobjective genetic algorithm to obtain a set of Pareto fronts, allowing to perceive the influence of both negative indexes on each other as conflicting design criteria. However, this last problem, solved in the objective function space, is only stated as a microstructural sizing optimization problem, i.e.,

the microstructure topology remains unchanged. The metamaterials proposed in these studies are presented in Fig. 2.3.

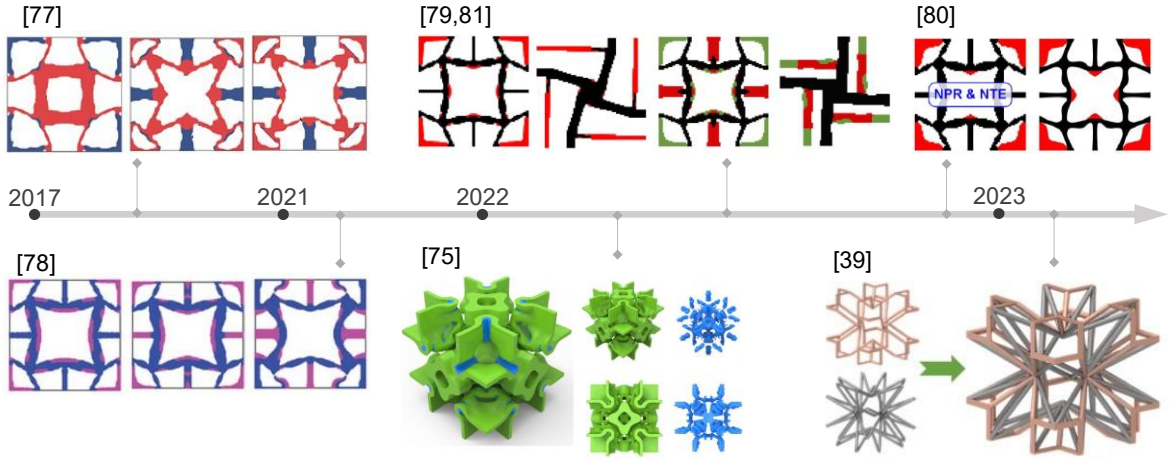

Figure 2.3 – Contributions from 2017 to the present on anepectic microstructure achieved via systematic design.

Recalling [78], these authors puzzlingly affirm that CTEs and PRs are not competing, i.e., each of them can change without affecting the other. However, in the seminal work by Sigmund and Torquato [5] it is only concluded that there is no mechanistic relationship between NTE and NPR, i.e., isotropic materials with effective NTE exist with positive value of PR and they can be obtained by mixing two base materials with positive thermal expansion coefficients amidst voids. Therefore, the combined influence of having both indexes negative remains understudied. The previous attempt in [39] of generating Pareto fronts is developed further in this thesis to include topology changes, to gain insight into the conflicting nature of designing for NPR and NTE. Although only NTE is sensitive to material selection, both CTE and PR are topology sensitive, and the same topology is not equally optimal for both negative indexes, as shown later by plotting several nondominated (Pareto) design solutions.

From the reviewed literature, it is evident that most contributions on the optimal design of metamaterials focus on the continuous design domain setting (see Fig. 2.3). Notably, truss-like microstructures present the prominent characteristic of being lightweight while also being able to achieve tailorable properties [82,83]. However, many studies on truss-like microstructures emphasize simple configurations (i.e., not optimal), often with analytical solutions of the elastic properties [84,85]. The existing body of research, vital as it is, still exhibits a gap in the exploration of lattice metamaterials obtained through TO using the Ground Structure (GS) method. On this topic, the pioneer work of Sigmund [10] is highlighted, which used the EBH method to design auxetic materials modelling the base cell with the

GS method. In 2015, Hirota and Kanno [86], solved a TO problem involving three material phases, using the GS method, to design a planar structure with NTE. Muños-Rojas et al. [87] designed truss-like periodic materials with enhanced simultaneous stiffness and heat transfer homogenized properties. Li et al. [88] and Li et al. [89] design mechanical metamaterials through TO proposing a new method to generate a three-dimensional GS with geometric cubic symmetry. The first work proposed a pentamode lattice metamaterial while the latter proposed a metamaterial exhibiting extreme isotropy and NPR. In 2023, Li et al. [39] proposed a multi-material GS to develop a truss-like metamaterial with both NPR and NTE. Recently, in 2024, Yang et al. [90], developed a methodology to design multifunctional metamaterials, based on the GS approach, combining stiffness criteria, high thermal conductivity and zero or negative CTE. The authors also fabricated a bimetallic specimen to demonstrate the manufacturability of the optimized design solutions.

The homogenization methods mentioned above, which analyse a single UC to predict the effective properties, assuming infinite periodicity, whereas in practice, composite materials comprise only a finite number of UC repetitions. This raises awareness about the importance of studying scale-size effects on the effective thermoelastic properties of periodic metamaterials as addressed in the present framework. As an alternative to the homogenization method, the Representative Volume Element (RVE) method allows for full-size characterization of composite materials, avoiding the need for geometric periodicity when the RVE is sufficiently large [91,92]. Pecullan et al. [93] numerically showed that as the number of UC repetitions increases, the results obtained through the RVE method, under the Dirichlet and Neumann boundary conditions, converged toward those predicted by the AH method, representing the upper and lower bounds, respectively. In Coelho et al. [94], a similar methodology was applied for microstructures designed by the inverse homogenization method, and similar conclusions were established. However, these contributions solely focus on the elastic effective properties.

While the RVE-based approach allows for evaluating scale-size effects and verifying whether the properties predicted by homogenization theory truly reflect macroscopic behaviour, it does not inherently ensure that the optimized microstructure performs well at the structural scale. To directly account for macroscopic performance during material design, a multiscale optimization strategy can be adopted. When considering a multiscale model, the loading conditions of the structure are taken into account when designing the material's microstructure. These conditions, both mechanical and thermal, play a crucial role in the design

process of the material's microstructure, ensuring that the microstructural features are tailored to withstand the specific loads applied at different scales [95–98].

While most of the past multiscale research has focused on enhancing structural performance at the macroscale, the use of multiscale topology optimization to design metamaterials by tailoring their microstructure for specific macroscale properties remains sparsely explored. In 2014, Wang et al. [95] optimized a material to achieve prescribed properties, using a nonlinear material model and evaluating the material performance in the macroscale with longitudinal and transversal tensile tests under finite deformation. Similar work was proposed by Zhang and Khandelwal [99], using nonlinear homogenization method. Li et al. [100], used level set to design a layer-wise Functionally Graded Material (FGM)-based composite, with auxeticity and improved stiffness by means of a multiobjective function. Zheng et al. [101], in 2024, pioneered the incorporation of thermoelastic principles into the multiscale optimization problem by designing a metamaterial thermal actuator. In these studies, a multiscale optimization approach is used to account for the interaction between scales, enabling the determination of the optimal microstructure and material distribution [11]. Multiscale optimization has also been used to design metamaterials in various fields, such as acoustic [102] and mechanical cloaking [103]. Further methods and approaches on multiscale modeling and optimization of metamaterials can be found in the review article by Lee et al. [104] and by Kochmann et al. [105].

2.2 Theory of Linear Thermoelasticity

The stress-strain relation for a linear thermoelastic problem is given by the generalized Hooke's law:

$$\sigma_{ij} = E_{ijkl}\varepsilon_{kl}^{m} = E_{ijkl}\varepsilon_{kl} - E_{ijkl}\alpha_{kl}\Delta\mathrm{T} \tag{2.1}$$

where E_{ijkl} is the stiffness tensor, α_{ij} the coefficient of thermal expansion tensor and ΔT is the temperature differential.

The mechanical strain, ε_{ij}^{m}, is defined by the difference between the total and thermal strain, i.e., $\varepsilon_{ij}^{m} = \varepsilon_{ij} - \varepsilon_{ij}^{th}$. As the infinitesimal strain theory is assumed, ε_{ij} is the linear strain tensor, also called Cauchy's strain tensor, defined by Eq. (2.2):

$$\varepsilon_{ij} = \frac{1}{2}\left(\frac{\partial u_i}{\partial x_j} + \frac{\partial u_j}{\partial x_i}\right) \tag{2.2}$$

where ε_{ij}^{th} is the thermal stress tensor, defined by (2.3):

$$\varepsilon_{ij}^{th} = \alpha_{ij}\Delta\mathrm{T} \tag{2.3}$$

Using the definition of the thermal stress tensor, $\beta_{ij} = E_{ijkl}\alpha_{kl}$, the reduced stress-strain relation expressed in Eq. (2.1) can be rewritten for a plane stress deformation state, in a compact matrix form, as:

$$\begin{bmatrix}\sigma_{11}\\ \sigma_{22}\\ \sigma_{12}\end{bmatrix} = \begin{bmatrix}E_{1111} & E_{1122} & E_{1112}\\ & E_{2222} & E_{2212}\\ sym & & E_{1212}\end{bmatrix}\begin{bmatrix}\varepsilon_{11}\\ \varepsilon_{22}\\ 2\varepsilon_{12}\end{bmatrix} - \begin{bmatrix}\beta_{11}\\ \beta_{22}\\ \beta_{12}\end{bmatrix}\Delta\mathrm{T} \tag{2.4}$$

The fourth order tensor that characterize the elastic properties of a given material (E_{ijkl}), and the second order thermal stress tensor (β_{ij}) as well as stress and strain tensors, satisfy the following symmetries:

$$E_{ijkl} = E_{jikl} = E_{ijlk} = E_{klij};\ \beta_{ij} = \beta_{ji};\ \sigma_{ij} = \sigma_{ji};\ \varepsilon_{ij} = \varepsilon_{ji} \tag{2.5}$$

In a general 3D anisotropic linear case, considering the tensor symmetries, the stiffness tensor has twenty-one independent elastic coefficients (instead of eighty-one). This number reduces for six different elastic coefficients in 2D. As for the thermal coefficients, considering tensor symmetries, there are six distinct thermal coefficients in 3D and three in 2D. The number of independent elastic coefficients decreases as material symmetry increases. Anisotropic materials, with the least symmetry level, have the highest number of independent elastic coefficients, resulting in the general tensors in Eq. (2.4).

An orthotropic material has, in 2D, two symmetry planes, resulting in a material with four distinct elastic coefficients and two thermal coefficients. The stress-strain relation for orthotropic behaviour is thus given by Eq. (2.6):

$$\begin{bmatrix}\sigma_{11}\\ \sigma_{22}\\ \sigma_{12}\end{bmatrix} = \begin{bmatrix}E_{1111} & E_{1122} & 0\\ & E_{2222} & 0\\ sym & & E_{1212}\end{bmatrix}\begin{bmatrix}\varepsilon_{11}\\ \varepsilon_{22}\\ 2\varepsilon_{12}\end{bmatrix} - \begin{bmatrix}\beta_{11}\\ \beta_{22}\\ 0\end{bmatrix}\Delta\mathrm{T} \tag{2.6}$$

If a material is isotropic, then its physical properties at any point are invariant under a rotation of axes, i.e., are the same in any direction, resulting in three independent elastic coefficients and one thermal coefficient. The stress-strain relation for an isotropic, linear thermoelastic solid, is thus given by Eq. (2.7):

$$\begin{bmatrix}\sigma_{11}\\ \sigma_{22}\\ \sigma_{12}\end{bmatrix}=\begin{bmatrix}E_{1111} & E_{1122} & 0\\ & E_{1111} & 0\\ & & E_{1212}\end{bmatrix}\begin{bmatrix}\varepsilon_{11}\\ \varepsilon_{22}\\ 2\varepsilon_{12}\end{bmatrix}-\begin{bmatrix}\beta_{11}\\ \beta_{11}\\ 0\end{bmatrix}\Delta\mathrm{T} \tag{2.7}$$

For this case, the previous relation Eq. (2.7) can be written as a function of the material properties, given in Eq. (2.8):

$$\begin{bmatrix}\sigma_{11}\\ \sigma_{22}\\ \sigma_{12}\end{bmatrix}=\frac{E}{1-\nu^2}\begin{bmatrix}1 & \nu & 0\\ & 1 & 0\\ & & (1-\nu)/2\end{bmatrix}\begin{bmatrix}\varepsilon_{11}\\ \varepsilon_{22}\\ 2\varepsilon_{12}\end{bmatrix}-\frac{E\alpha}{1-\nu}\begin{bmatrix}1\\ 1\\ 0\end{bmatrix}\Delta\mathrm{T} \tag{2.8}$$

where E, α and ν are the Young's modulus, coefficient of thermal expansion and Poisson's ratio of the isotropic material, respectively.

The thermoelastic properties of any material can be derived from its defining tensors. For orthotropic materials, the bulk and shear modulus are given by $K=\frac{1}{4}(E_{1111}+E_{2222}+2E_{1122})$ and $G=E_{1212}$, respectively [106]. The Poisson's ratio is given by $\nu_{12}=E_{1122}/E_{1111}$ (defined from an applied vertical load) and $\nu_{21}=E_{2211}/E_{2222}$ (from an applied horizontal load) [62], which leads to $\nu_{12}=\nu_{21}=\nu$ in the isotropic case. These ratios derive from the PR definition, i.e., $\nu_{12}=-\varepsilon_{11}/\varepsilon_{22}$, with the stiffness tensor having the coefficients E_{1122} and E_{2212} null, see Eq. (2.6). For an anisotropic material, see Eq. (2.4), any measures depending on the stiffness tensor coefficients must be interpreted as an approximate measure of the deformation in the principal directions. Therefore, for anisotropic materials, the properties must be referred to as quasi-effective Poisson's ratio and quasi-effective bulk modulus. The effective shear modulus is evaluated the same way for the anisotropic case [107].

2.3 Homogenization Theory

Consider the classical problem of thermoelasticity applied to a heterogeneous medium $\epsilon\Re^n$ such as a composite material. The homogenization method correlates two spatial scales, namely microscopic (i.e., UC) and macroscopic (i.e., full composite) scales, by assuming infinite periodicity of the UC. The characteristic length of the UC (microscale) d, is assumed to be several orders of magnitude bellow the characteristic length of the periodic medium (macroscale) D, i.e., $d \ll D$. The proportion between these dimensions defines the parameter $\epsilon = d/D$ known as the *characteristic inhomogeneity dimension* [6]. To satisfy one of the assumptions of the homogenization theory, the separation of scales, this dimension must be sufficiently small (i.e., $\epsilon \ll 1$). It can also be seen as an association between the scales, with the

quantity $1/\epsilon$ representing the amplification factor of the macroscale that enlarges the dimension of the UC, Y, to be comparable with the dimensions of the periodic material, Ω^ϵ.

Another assumption of the homogenization method for periodic medium is that the functions denoting some properties of the heterogeneous medium must be periodic through the macroscale. For a given physical or geometric property, Φ, to be periodic, it must satisfy the condition $\Phi(\mathbf{x}+\mathbf{y}) = \Phi(\mathbf{x})$, where $\mathbf{x} \in \Omega^\epsilon$ and $\mathbf{y} \in Y$ are the position variables of the macroscale and microscale, respectively. The properties of the macroscopic domain (e.g., strains, stresses, displacements, …) are periodically repeated with period ϵY and slowly vary at the macroscopic level, from point to point with $\mathbf{x}$. However, due to the high level of heterogeneity at the microscopic level, these properties will rapidly vary within a small neighborhood ϵ of a point $\mathbf{x}$, i.e., rapidly vary at the microscopic level with $\mathbf{y}$. So, all the properties of the macroscopic domain are assumed to depend on both scales and the relation between the position variables is $\mathbf{y} = \mathbf{x}/\epsilon$. Consequently, an arbitrary function Φ that satisfies $\Phi(\mathbf{x}) = \Phi(\mathbf{x},\mathbf{y}) = \Phi(\mathbf{x},\mathbf{x}/\epsilon)$ is said to be Y-periodic in $\mathbf{y} \in Y$ for each $\mathbf{x} \in \Omega^\epsilon$. Moreover, Periodic Boundary Conditions (PBC) and uniformity of the macroscopic applied mechanical load, e.g., stress or strain, are considered [6,108,109].

In the development of this subsection, the following material model is considered: A body of domain Ω^ϵ, regular and limited by boundary $\partial\Omega^\epsilon$, characterized by the parameter ϵ, considering traction forces $\mathbf{q}$ in Γ_q, imposed displacement $\mathbf{u}$ in Γ_u and body loads due to temperature $\Delta T \neq 0$, represented in Fig. 2.4.

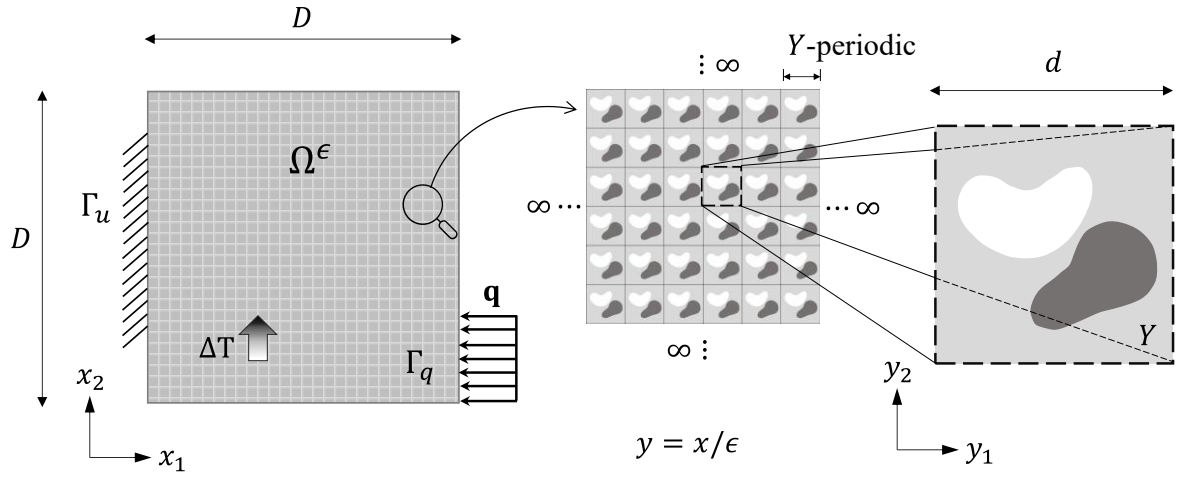

Figure 2.4 – Arbitrary equivalent homogeneous medium of a thermoelastic composite (i.e., macroscale, with size D), composed of periodic heterogeneous medium with periodic microstructure through an UC with size d.

2.3.1 Asymptotic Homogenization

The general thermoelastic problem for a material with periodic microstructure is formulated as a boundary value problem, defined in Eq. (2.9), which consists of determine the displacement field, $\mathbf{u}^{\epsilon}$. Solving this boundary value problem allow the estimation of the effective properties of the equivalent homogeneous material by the homogenization method. The development of the thermoelastic equations presented in this section is based on the formulation introduced in [58].

$$\begin{cases} \dfrac{\partial \sigma_{ij}^{\epsilon}}{\partial x_i} + b_j = 0, & \mathbf{x} \in \Omega^{\varepsilon} \\ \sigma_{ij}^{\epsilon} n_i = q_i & \text{in } \Gamma_q \\ u_i^{\epsilon} = 0 & \text{in } \Gamma_u \end{cases} \tag{2.9}$$

where σ_{ij}^{ϵ} are the components of the Cauchy stress tensor and u_i^{ϵ} are the components of the displacement vector. The superscript ϵ in Eq. (2.9) and in the following equations indicates that the variable is a function of total material, including microstructure heterogeneities.

The stress-strain relation given by the generalized Hooke's law for a classical linear thermoelastic problem, recall Eq. (2.1), can be rewritten using the definition of the thermal stress tensor as:

$$\sigma_{ij}^{\epsilon} = E_{ijkl}^{\epsilon} \varepsilon_{kl}^{\epsilon} - \beta_{ij}^{\epsilon} \Delta \mathrm{T} \tag{2.10}$$

where E_{ijkl}^{ϵ} are the components of the fourth-order stiffness tensor, α_{kl}^{ϵ} are the coefficients of thermal expansion and $\beta_{ij}^{\epsilon} = E_{ijkl}^{\epsilon} \alpha_{kl}^{\epsilon}$ are the components of the thermal stress tensor. As the infinitesimal strain theory is assumed, $\varepsilon_{ij}^{\epsilon}$ is the linear strain tensor, also called Cauchy's strain tensor, recall Eq. (2.2).

Applying the virtual displacement principle for linear elasticity, the problem defined in Eq. (2.9) is formulated as:

$$\int_{\Omega^{\epsilon}} \sigma_{ij}^{\epsilon} \frac{\partial v_i}{\partial x_j} \mathrm{d}\Omega = \int_{\Omega^{\epsilon}} b_i^{\epsilon} v_i \mathrm{d}\Omega + \int_{\Gamma_t} q_i v_i \mathrm{d}\Gamma \ , \qquad \forall \mathbf{v} \in V_{\Omega^{\epsilon}} \tag{2.11}$$

$V_{\Omega^{\varepsilon}} = \{\mathbf{v} \text{ defined in } \Omega^{\varepsilon}, \text{ regular enough: } \mathbf{v}|_{\Gamma_u} = 0\}$

Substitution Eq. (2.10) into Eq. (2.11) yields:

$$\int_{\Omega^\epsilon}\left(E^\epsilon_{ijkl}\frac{\partial u^\epsilon_k}{\partial x_l}-\beta^\epsilon_{ij}\Delta\mathrm{T}\right)\frac{\partial v_i}{\partial x_j}\mathrm{d}\Omega=\int_{\Omega^\epsilon}b^\epsilon_i v_i\mathrm{d}\Omega+\int_{\Gamma_t}t_i v_i\mathrm{d}\Gamma\,,\qquad\forall\mathbf{v}\in V_{\Omega^\epsilon}\tag{2.12}$$

Using the two-scale asymptotic expansion, the solution of the problem stated in Eq. (2.9), $\mathbf{u}^\epsilon$, can be written as:

$$\mathbf{u}^\epsilon(\mathbf{x})=\mathbf{u}^0(\mathbf{x},\mathbf{y})+\epsilon\mathbf{u}^1(\mathbf{x},\mathbf{y})+\epsilon^2\mathbf{u}^2(\mathbf{x},\mathbf{y})+\cdots=\sum_{i=0}^{\infty}\epsilon^i\mathbf{u}^i(\mathbf{x},\mathbf{y}),\quad\mathbf{y}=\frac{\mathbf{x}}{\epsilon}\tag{2.13}$$

where the displacement functions $\mathbf{u}^i(\mathbf{x},\mathbf{y})$ are Y-periodic in $\mathbf{y}$.

Considering that the spatial derivatives w.r.t. $\mathbf{x}$, of an arbitrary function Φ that depend on two scales, are given by Eq. (2.14).

$$\frac{\partial\Phi^\epsilon(\mathbf{x})}{\partial x_j}=\frac{\partial\Phi(\mathbf{x},\mathbf{y})}{\partial x_j}+\frac{1}{\epsilon}\frac{\partial\Phi(\mathbf{x},\mathbf{y})}{\partial y_j},\qquad\forall\Phi(\mathbf{x})=\Phi(\mathbf{x},\mathbf{y})\tag{2.14}$$

And substituting Eq. (2.13) up to the ϵ^2 term in Eq. (2.12), while considering Eq. (2.14), yields:

$$\begin{aligned}\int_{\Omega^\epsilon}\Bigg\{\Bigg[E^\epsilon_{ijkl}\Bigg(\frac{\partial\left(u^0_k+\epsilon u^1_k+\epsilon^2u^2_k\right)}{\partial x_l}+\frac{1}{\epsilon}\frac{\partial\left(u^0_k+\epsilon u^1_k+\epsilon^2u^2_k\right)}{\partial y_l}\Bigg)-\beta^\epsilon_{ij}\Delta\mathrm{T}\Bigg]\Bigg(\frac{\partial v_i}{\partial x_j}\\+\frac{1}{\epsilon}\frac{\partial v_i}{\partial y_j}\Bigg)\Bigg\}\mathrm{d}\Omega=\int_{\Omega^\epsilon}b^\epsilon_i v_i\mathrm{d}\Omega+\int_{\Gamma_t}t_i v_i\mathrm{d}\Gamma\,,\qquad\forall\mathbf{v}\in V_{\Omega^\epsilon}\end{aligned}\tag{2.15}$$

After some mathematical manipulation and development of Eq. (2.15), the following result is verified:

$$\begin{aligned}\int_{\Omega^\epsilon}\Bigg\{&E^\epsilon_{ijkl}\Bigg[\frac{1}{\epsilon^2}\Bigg[\frac{\partial u^0_k}{\partial y_l}\frac{\partial v_i}{\partial y_j}\Bigg]+\frac{1}{\epsilon^1}\Bigg[\frac{\partial u^0_k}{\partial y_l}\frac{\partial v_i}{\partial x_j}+\left(\frac{\partial u^0_k}{\partial x_l}+\frac{\partial u^1_k}{\partial y_l}\right)\frac{\partial v_i}{\partial y_j}\Bigg]\\&+\epsilon^0\Bigg[\left(\frac{\partial u^0_k}{\partial x_l}+\frac{\partial u^1_k}{\partial y_l}\right)\frac{\partial v_i}{\partial x_j}+\left(\frac{\partial u^1_k}{\partial x_l}+\frac{\partial u^2_k}{\partial y_l}\right)\frac{\partial v_i}{\partial y_j}\Bigg]+\epsilon^1(\cdots)+\epsilon^2(\cdots)\Bigg]\\&-\beta^\epsilon_{ij}\Delta\mathrm{T}\frac{\partial v_i}{\partial x_j}-\frac{1}{\epsilon^1}\beta^\epsilon_{ij}\Delta\mathrm{T}\frac{\partial v_i}{\partial y_j}\Bigg\}\mathrm{d}\Omega=\int_{\Omega^\epsilon}b^\epsilon_i v_i\mathrm{d}\Omega+\int_{\Gamma_t}t_i v_i\mathrm{d}\Gamma\,,\\&\forall\mathbf{v}\in V_{\Omega^\epsilon}\end{aligned}\tag{2.16}$$

$V_{\Omega^\epsilon\times¥}=\{\mathbf{v}(\mathbf{x},\mathbf{y});(\mathbf{x},\mathbf{y})\in\Omega^\epsilon\times¥;\mathbf{v}(.,\mathbf{y})Y\text{-periodic};$
regular enough and $\mathbf{v}|_{\Gamma_u}=0\}$

Note that ¥ represent the solid part of the base UC's domain, Y. Considering once again a Y-periodic and regular function, the result in Eq. (2.17) is verified.

$$\lim_{\epsilon\to 0^+}\left(\int_{\Omega^\epsilon}\Phi(\mathbf{x},\mathbf{y})\mathrm{d}\Omega\right)=\int_{\Omega^\epsilon}\frac{1}{|Y|}\left(\int_{¥}\Phi(\mathbf{y})\mathrm{d}Y\right)\mathrm{d}\Omega \tag{2.17}$$

That is, the material behavior can be regarded as a volumetric average $\langle\Phi\rangle$, given through a function Φ, withing the UC domain, i.e., when $\epsilon\to 0$:

$$\langle\Phi\rangle=\frac{1}{|Y|}\int_{¥}\Phi(\mathbf{y})\mathrm{d}Y \tag{2.18}$$

Rewriting each term with the same power ϵ of Eq. (2.16) and applying the results in Eqs. (2.17) and (2.18), Eqs. (2.19)-(2.21) are obtain. Note that only the first three terms, ϵ^{-2}, ϵ^{-1} and ϵ^{0}, are considered.

$$\epsilon^{-2}:\int_{\Omega^\epsilon}\left(\frac{1}{|Y|}\int_{¥}E_{ijkl}\frac{\partial u_k^0}{\partial y_l}\frac{\partial v_i}{\partial y_j}\mathrm{d}Y\right)\mathrm{d}\Omega=0 \tag{2.19}$$

$$\epsilon^{-1}:\int_{\Omega^\epsilon}\left(\frac{1}{|Y|}\int_{¥}\left(E_{ijkl}\left[\frac{\partial u_k^0}{\partial y_l}\frac{\partial v_i}{\partial x_j}+\left(\frac{\partial u_k^0}{\partial x_l}+\frac{\partial u_k^1}{\partial y_l}\right)\frac{\partial v_i}{\partial y_j}\right]-\beta_{ij}\Delta\mathrm{T}\frac{\partial v_i}{\partial y_j}\right)\mathrm{d}Y\right)\mathrm{d}\Omega=0 \tag{2.20}$$

$$\begin{aligned}\epsilon^{0}:\int_{\Omega^\epsilon}\left(\frac{1}{|Y|}\int_{¥}\left(E_{ijkl}\left[\left(\frac{\partial u_k^0}{\partial x_l}+\frac{\partial u_k^1}{\partial y_l}\right)\frac{\partial v_i}{\partial x_j}+\left(\frac{\partial u_k^1}{\partial x_l}+\frac{\partial u_k^2}{\partial y_l}\right)\frac{\partial v_i}{\partial y_j}\right]\right.\right.\\ \left.\left.-\beta_{ij}\Delta\mathrm{T}\frac{\partial v_i}{\partial x_j}\right)\mathrm{d}Y\right)\mathrm{d}\Omega=\int_{\Omega^\epsilon}\left(\frac{1}{|Y|}\int_{¥}b_i v_i\mathrm{d}Y\right)\mathrm{d}\Omega+\int_{\Gamma_t}t_i v_i\mathrm{d}\Gamma\end{aligned} \tag{2.21}$$

Note now that the stiffness tensor only depends on the microscopic variable, **y**, within the UC domain, Y. This tensor characterizes the base material of the UC. Typically, and here as well, the base material is a linear isotropic solid.

Solving Eqs. (2.19)-(2.21) results in local problems, i.e., in the UC domain. From the 1st term results the following local problem:

$$\frac{1}{|Y|}\int_{¥}E_{ijkl}\frac{\partial u_k^0}{\partial y_l}\frac{\partial v_i}{\partial y_j}\mathrm{d}Y=0 \tag{2.22}$$

The arbitrary displacement can be considered to only dependent on the macroscopic design variable, i.e., $\mathbf{v} = \mathbf{v}(\mathbf{x})$, and Eq. (2.22) is then satisfied. It follows that the first term of the asymptotic expansion depends only on the macroscopic variable and $\frac{\partial u_k^0}{\partial y_l} = 0$:

$$\mathbf{u}_k^0(\mathbf{x}, \mathbf{y}) = \mathbf{u}_k^0(\mathbf{x}) \tag{2.23}$$

Considering Eq. (2.23) in the 2nd term of Eq. (2.20), leads to:

$$\frac{1}{|Y|}\int_{¥} \left[E_{ijkl}\left(\frac{\partial u_k^0}{\partial x_l} + \frac{\partial u_k^1}{\partial y_l}\right) - \beta_{ij}\Delta\mathrm{T}\right]\frac{\partial v_i}{\partial y_j}\mathrm{d}Y = 0 \tag{2.24}$$

where $\mathbf{u}^1(\mathbf{x}, \mathbf{y})$ represents the microscopic displacement, obtained by involving the characteristic displacement vectors. Microscopic displacement $\mathbf{u}^1$ can be written as follows:

$$\mathbf{u}_k^1(\mathbf{x}, \mathbf{y}) = -\chi_k^{pq}(\mathbf{y})\frac{\partial u_p^0}{\partial x_p} + \Upsilon_k(\mathbf{y})\Delta\mathrm{T} \tag{2.25}$$

where χ_k^{pq} and Υ_k are the characteristic displacement vectors for the elastic and thermal problem, respectively. Introducing Eq. (2.25) in Eq. (2.24), with some mathematical manipulation, gives:

$$\frac{1}{|Y|}\int_{¥} \left[\left(E_{ijkl} - E_{ijpq}\frac{\partial \chi_p^{kl}}{\partial y_k}\right)\frac{\partial u_k^0}{\partial x_l} - \left(E_{ijpq}\frac{\partial \Upsilon_p}{\partial y_p} - \beta_{ij}\right)\Delta\mathrm{T}\right]\frac{\partial v_i}{\partial y_j}\mathrm{d}Y = 0 \tag{2.26}$$

Uncoupling Eq. (2.26) into two equations representing the local elastic, Eq. (2.27), and local thermal, Eq. (2.28), problems, respectively, allows the calculation of the characteristic displacement vectors.

$$\int_{¥} E_{ijpq}\frac{\partial \chi_p^{kl}}{\partial y_q}\frac{\partial v_i}{\partial y_j}\mathrm{d}Y = \int_{¥} E_{ijkl}\frac{\partial v_i}{\partial y_j}\mathrm{d}Y \tag{2.27}$$

$$\int_{¥} E_{ijpq}\frac{\partial \Upsilon_p}{\partial y_q}\frac{\partial v_i}{\partial y_j}\mathrm{d}Y = \int_{¥} \beta_{ij}\frac{\partial v_i}{\partial y_j}\mathrm{d}Y \tag{2.28}$$

Once the microscopic equilibrium equations, Eqs. (2.27) and (2.28), are solved, and substituting the solutions of $\mathbf{u}_k^0$ (Eq. (2.23)) and $\mathbf{u}_k^1$ (Eq. (2.25)) into Eq. (2.21), the local problem of the ϵ^0 order term is obtained:

$$\begin{aligned}&\int_{\Omega^\epsilon}\left[\left(\frac{1}{|Y|}\int_{¥}\left(E_{ijkl}-E_{ijpq}\frac{\partial\chi_p^{kl}}{\partial y_k}\right)\mathrm{d}Y\right)\frac{\partial u_k^0}{\partial x_l}\right.\\&\left.-\left(\frac{1}{|Y|}\int_{¥}\left(\beta_{ij}-E_{ijpq}\frac{\partial\Upsilon_p}{\partial y_p}\right)\mathrm{d}Y\right)\Delta\mathrm{T}\right]\mathrm{d}\Omega\\&=\int_{\Omega^\epsilon}\left[\frac{1}{|Y|}\int_{¥}b_i\mathrm{d}Y\right]v_i\mathrm{d}\Omega+\int_{\Gamma_t}t_iv_i\mathrm{d}\Gamma\end{aligned}\tag{2.29}$$

Finally, this leads to the equivalent equilibrium problem, previously defined in Eq. (2.12), homogenized, expressed in terms of the homogenized constitutive parameters:

$$\int_{\Omega^\epsilon}\left[E_{ijkl}^H\frac{\partial u_k^0}{\partial x_l}-\beta_{ij}^H\Delta\mathrm{T}\right]\mathrm{d}\Omega=\int_{\Omega^\epsilon}\langle b_i\rangle\mathrm{d}\Omega+\int_{\Gamma_t}t_iv_i\mathrm{d}\Gamma\tag{2.30}$$

Where the homogenized stiffness tensor, the homogenized thermal stress tensor and the homogenized vector of the volumetric forces are given by Eq. (2.31), Eq. (2.32) and Eq. (2.33), respectively.

$$E_{ijkl}^H=\frac{1}{|Y|}\int_{¥}\left(E_{ijkl}-E_{ijpq}\frac{\partial\chi_p^{kl}}{\partial y_k}\right)\mathrm{d}Y\tag{2.31}$$

$$\beta_{ij}^H=\frac{1}{|Y|}\int_{¥}\left(\beta_{ij}-E_{ijpq}\frac{\partial\Upsilon_p}{\partial y_q}\right)\mathrm{d}Y\tag{2.32}$$

$$\langle b_i\rangle=\frac{1}{|Y|}\int_{¥}b_i\mathrm{d}Y\tag{2.33}$$

The homogenized properties can also be written in their symmetrical form as:

$$E_{ijkl}^H=\frac{1}{|Y|}\int_{¥}E_{rspq}\left(\delta_{pk}\delta_{ql}-\frac{\partial\chi_p^{kl}}{\partial y_q}\right)\left(\delta_{ri}\delta_{sj}-\frac{\partial\chi_r^{ij}}{\partial y_s}\right)\mathrm{d}Y\tag{2.34}$$

$$\beta_{ij}^H=\frac{1}{|Y|}\int_{¥}E_{rspq}\left(\alpha_{pq}-\frac{\partial\Upsilon_p}{\partial y_q}\right)\left(\delta_{ri}\delta_{sj}-\frac{\partial\chi_r^{ij}}{\partial y_s}\right)\mathrm{d}Y\tag{2.35}$$

where δ_{ij} is the Kronecker delta.

2.3.2 Energy-based Homogenization

An alternative method to compute the effective properties of a material is the EBH, which employs average stress and strain theorems. Consider, in Eq. (2.36), the effective stiffness tensor in the symmetrical form, expressed in terms of the element mutual energies [10,59]:

$$E^H_{ijkl} = \frac{1}{|Y|}\int_Y E_{rspq}\left(\varepsilon^{0(kl)}_{pq} - \varepsilon^{*(kl)}_{pq}\right)\left(\varepsilon^{0(ij)}_{rs} - \varepsilon^{*(ij)}_{rs}\right)\mathrm{d}Y \tag{2.36}$$

where $\varepsilon^{0(kl)}_{pq}$ is a superposition of a homogeneous macroscopic unit strain and $\varepsilon^{*(kl)}_{pq}$ is the fluctuation strain field, induced by the inhomogeneities of the unit cell, related to $\boldsymbol{\chi}$ by Eq. (2.37):

$$\varepsilon^{*(kl)}_{pq} = \frac{1}{2}\left(\frac{\partial \chi^{kl}_p}{\partial y_q} + \frac{\partial \chi^{kl}_q}{\partial y_p}\right) \tag{2.37}$$

According to Hashin [110], both the AH and the EBH are equivalent approaches to predict effective elastic material properties. The only difference between the two methods lies in the test strain fields. The EBH imposes three-unit test strains, $\varepsilon^{0(kl)}_{pq}$, directly on the boundaries of the UC, inducing $\varepsilon^{A(kl)}_{pq}$. This latter strain field corresponds to the superimposed strain field in the AH, i.e., $\varepsilon^{A(kl)}_{pq} \equiv \left(\varepsilon^{0(kl)}_{pq} - \varepsilon^{*(kl)}_{pq}\right)$, see [10]. The strain fields $\varepsilon^{A(kl)}_{pq}$ are determined through the solution of the UC equilibrium problem, subject to the unit test strain $\varepsilon^{0(kl)}_{pq}$, and assuming periodicity. Thus, Eq. (2.36) can be rewritten as:

$$E^H_{ijkl} = \frac{1}{|Y|}\int_Y E_{rspq}\varepsilon^{A(kl)}_{pq}\varepsilon^{A(ij)}_{rs}\mathrm{d}Y \tag{2.38}$$

In fact, the term "energy-based homogenization" is often used improperly. While referring to the effective elastic property, written in equivalent form in terms of element mutual energies, see Eq. (2.36). However, solving the local problems of the UC, see Eqs. (2.27) and (2.28), to compute the strain fields $\varepsilon^{*(kl)}_{pq}$, results in the AH approach. The advantage of the EBH method lies in the fact that it allows us to compute the elastic effective properties by directly imposing the Dirichlet-type BCs in the finite element model [111], avoiding the need to solve local problems, thus making this method less computationally expensive.

Let us now analyze the effective thermoelastic properties, given in terms of the element mutual energies, i.e.,

$$\beta_{ij}^{H} = \frac{1}{|Y|}\int_{Y} E_{ijpq}\left(\varepsilon_{pq}^{0\alpha} - \varepsilon_{pq}^{*\alpha}\right)\mathrm{d}Y \tag{2.39}$$

where $\varepsilon_{pq}^{0\alpha}$ is a superposition of a homogeneous macroscopic unit thermal load and corresponds to the thermal expansion considering a unit applied temperature, i.e., $\varepsilon_{pq}^{0\alpha} = \alpha_{pq}$.

Here, $\varepsilon_{pq}^{*\alpha}$ is the fluctuation strain field, induced by the inhomogeneities of the unit cell, related to $\boldsymbol{\Upsilon}$ through Eq. (2.40):

$$\varepsilon_{pq}^{*\alpha} = \frac{1}{2}\left(\frac{\partial \Upsilon_p}{\partial y_q} + \frac{\partial \Upsilon_q}{\partial y_p}\right) \tag{2.40}$$

The equivalence between EBH and AH methods can easily be used to predict the effective elastic properties of the material, i.e., E_{ijkl}^{H}. However, to predict the thermoelastic properties, the question whether it is possible to calculate a unit test strain field equivalent to $\left(\varepsilon_{pq}^{0\alpha} - \varepsilon_{pq}^{*\alpha}\right)$ arises. Firstly, it is important to notice that, to design a material with tailorable thermoelastic properties, at least two solid materials must be considered. If only one solid material (or one material and void) is considered, the thermal expansion coefficient α_{kl} remains constant throughout the microstructure, resulting in the effective thermoelastic property $\beta_{ij}^{H} = E_{ijkl}^{H}\alpha_{kl}$ [6]. In this scenario, considering the thermal unit-test strain field $\varepsilon_{pq}^{0\alpha} = [1\ 1\ 0]^{\mathrm{T}}$ imposed directly on the boundaries of the UC, the strain field induced, $\varepsilon_{pq}^{A\alpha}$, is, in fact, equivalent to $\left(\varepsilon_{pq}^{0\alpha} - \varepsilon_{pq}^{*\alpha}\right)$. This results from α_{kl} being constant throughout the microstructure design domain, Y. Therefore, imposing the strain field $\varepsilon_{pq}^{0\alpha}$ corresponds to apply a unit thermal load. However, when α_{kl} is no longer constant across Y, it means that applying a unit thermal load is no longer equivalent to the strain field $\varepsilon_{pq}^{0\alpha} = [1\ 1\ 0]^{\mathrm{T}}$, since different material choices per design element, in Y, are associated to different CTEs. Consequently, to be able to apply this method to compute the thermoelastic properties, the Maxwell-Betti reciprocal theorem is invoked [59], and the homogenized thermal stress tensor is now given by Eq. (2.41):

$$\beta_{ij}^{H} = \frac{1}{|Y|}\int_{Y} \alpha_{pq}E_{pqkl}\left(\varepsilon_{kl}^{0(ij)} - \varepsilon_{kl}^{*(ij)}\right)\mathrm{d}Y \tag{2.41}$$

In this way, the aforementioned equivalence on the elastic unit-test strains can be used to rewrite Eq. (2.41) as:

$$\beta_{ij}^{H} = \frac{1}{|Y|}\int_{Y} \alpha_{pq} E_{pqkl} \varepsilon_{rs}^{A(ij)} \mathrm{d}Y \tag{2.42}$$

The elastic, Eq. (2.34) and Eq. (2.38), and thermal, Eq. (2.35) and Eq. (2.42), effective properties computed either by the AH method or the EBH, are equivalent and yield the same result.

Furthermore, note that the present work assumes a regime of linear thermoelasticity and thermal loads small enough that no coupling effect exists between the homogenization for mechanical and thermal properties.

2.4 Structural Optimization

Structural optimization is, in its essence, a set of theory and methods that aim to obtain an *optimal* design. In this context, optimal design refers to the solution that best optimize a given performance measure of a structure. Usually, the performance measure to optimize is called **objective function**, and the structure is altered by manipulation of a given set of parameters that define the structure, known as **design variables**. Usually, the optimization problem is defined by a set of requirements, known as **constraints**, that define the admissible design space for the design variables. The optimal solutions are then obtained by resorting to optimization algorithms.

In the last decade of the XIX century the pioneer works about structural optimization were firstly published, by Maxwell, in 1890 [112] and Michell, in 1904 [113]. However, significant developments were done only from 1950 upwards, mainly due to the development of three factors: (1) Emergence of the first digital computers, (2) development of numerical methos of mathematical programing and (3) development of the Finite Element Method (FEM). The development of this method traces back to the work of Courant [114], initiated as early as 1943. However, the method only became known by its current name through the work of Clough [115], who popularized the term.

Regarding the numerical methods of non-linear programming, during the 1970s and 1980s, some advances stand out like the Sequential Quadratic Programming (SQP) [116] or the Method of Moving Asymptotes (MMA) [117], that allow the resolution of more complex optimization problems. However, these methods were gradient-based, being only applied to continuum and differentiable problems. The Meta-heuristic methods [118], such as the Ge-

netic Algorithms (GA), appear as a tool to deal with discrete and mixed integer structural optimization problems.

In general, the different structural optimization methods relate to one of the four main categories: (1) Dimensional or sizing optimization; (2) shape optimization; (3) topology optimization and (4) material optimization. Depending on the problem to be solved, the design variables can be continuum, discrete, mixed or even Boolean. In Fig. 2.5 is schematized the first three categories, applied to the known MMB beam problem.

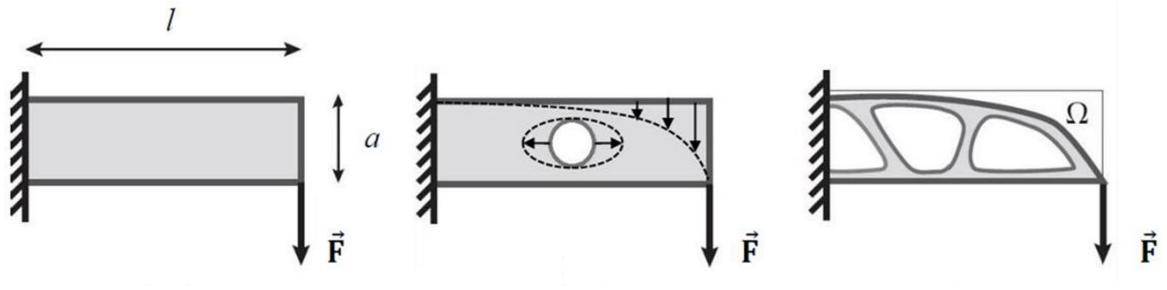

(a) (b) (c)

Figure 2.5 – Structural optimization categories. (a) Dimentional or sizing optimization; (b) shape optimization; (c) topology optimization. Retrived from [119].

In the sizing optimization problem, the design variables are typically responsible for modifying geometric parameters, such as the cross-sectional area of a beam. In contrast, shape optimization focuses on altering the overall form of the structure, with design variables that are associated with the definition of the boundary that define the domain. Among the various approaches, topology optimization is the more recent and offers the highest degree of design flexibility. It seeks to determine the best material layout within a given design domain, Ω. Unlike sizing and shape optimization, topology optimization does not rely on predefined assumptions about the geometry, such as its size or shape. As a result, it allows for more innovative and unrestricted design solutions. The material optimization category, or multimaterial, is defined as the process of determining the optimal distribution of more than one solid material within a given structure. This category can be integrated in any of the previous categories, and is usually used with topology optimization, also called Multimaterial Topology Optimization (MMTO).

Topology Optimization (TO) is, in its essence, a discrete problem, with Boolean design variables, that define the presence (1) or absence (0) of material. Dorn et al. [120], in 1964, introduced a methodology dedicated to the TO of discrete truss structures, called the Ground Structure Approach. The idea of this method is to define a structure by the connec-

tion of nodes with bar or beam elements, using Boolean variables, with 0 representing the absence of connectivity and 1 connectivity. Depending on the desired complexity of the structure, different levels of connectivity can be considered. The simplest configuration maintains connections within the same square element, while the most complex allows for all possible connections, as illustrated in Fig. 2.6.

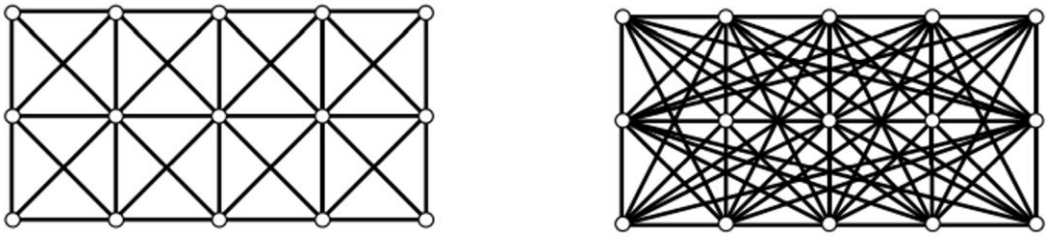

Figure 2.6 – Examples of Ground Structures with different levels of connectivity. Adapted from [121].

In 1988, Bendsoe and Kikuchi [122] extended TO to continuum structures, introducing the homogenization approach, detailed in the previous subsection. This pioneer work originated a whole new research field of continuum topology optimization methods, such as density-based, also known as Solid Isotropic Material with Penalization (SIMP) [56], Rational Approximation of Material Properties (RAMP) [123], level-set method (LSM) [124], phase-field method (PFM), topological derivatives [125], among others. A meaningful review on methods for continuum topology optimization can be found in [126].

In general, an optimization problem with a single objective can be defined with the following standard formulation:

$$\min_{\mathbf{s}} \quad f(\mathbf{s})$$
$$s.t. \begin{cases} g_j(\mathbf{s}) \leq 0; & j = 1, \dots, m \\ h_k(\mathbf{s}) = 0; & k = 1, \dots, p \\ s_i^- \leq s_i \leq s_i^+; & i = 1, \dots, n \end{cases} \tag{2.43}$$

where $\mathbf{s} = [s_1, \dots, s_n]$ is the vector of the n design variables, $f(\mathbf{s})$ is the objective function, $g_j(\mathbf{s})$ the m inequality constraints and $h_k(\mathbf{s})$ the p equality constraints. s_i^- and s_i^+ are the lower and upper bound of the design variables, respectively.

Table 2.1 presents some examples of structural optimization problems that can be formulated accordingly to the category, objective, and constraints.

Table 2.1 – Examples of structural optimization problems.

Category	Design variables	Objective function	Constraints
Sizing	Cross-sectional area	Structural weight	Displacement
Shape	Nodal coordinates	Natural frequency	Buckling load
Topology	Node connectivity	Cost	Volume
Material	Artificial density	Stiffness	Stress

2.4.1 Topology Optimization

The classical topology optimization problem is, conceptually, a discrete problem, as it aims to find, within a given design domain, Ω, a clear distribution of subdomains with material, Ω_{mat}, and with void, Ω_{void} (where $\Omega = \Omega_{mat} \cup \Omega_{void}$). To find the optimal solution that minimizes a given objective, it is necessary to find the subdomain, Ω_{mat} or Ω_{void}, to which each point in the domain, $\mathbf{s}$, belongs. The resolution of this material distribution problem is typically done by discretizing the design domain into N finite elements. A step function is thus introduced to define a discrete variable, to attribute the existence or absence of material to each finite element, e:

$$\varphi(\mathbf{s}) = \begin{cases} 1, & \mathbf{s} \in \Omega_{mat} \\ 0, & \mathbf{s} \in \Omega_{void} \end{cases} \tag{2.44}$$

Therefore, the stiffness tensor of the optimal solution in each element of the design domain, $E^e_{ijkl}(\mathbf{s})$, vary from point to point depending on the value of the step function in the element e, φ_e, according to:

$$E^e_{ijkl} = \varphi_e \mathbf{E}^1 \tag{2.45}$$

where $\mathbf{E}^1$ is the stiffness tensor of a given, usually isotropic, base material, to be distributed over Ω.

To address this problem, optimization algorithms designed for discrete problems, such as meta-heuristics [118], are required. Meta-heuristic algorithms can find good solutions, however, the evaluation of the objective function across the domain often results in high computational costs, and reaching the global optimum is never guaranteed. Tabu Search, Simulated Annealing, Genetic Algorithms, Evolutionary Methods, Scatter Search, Neural Networks, Variable Neighborhood Search and Ant Colonies are some examples of meta-heuristic methods found in the literature. So, given that it is more efficient to use gradient-

based optimization algorithms to solve topology optimization problems, the design variables must be continuous.

The step function previously defined Eq. (2.44) is thus replaced by a continuous variable. In 1989, Bendsøe [56] proposed the SIMP method. This strategy is a *power-law approach*, where the material property in each element of the domain is now interpolated according to:

$$E_{ijkl}^{e} = \rho_e^p \mathbf{E}^1, \qquad p \geq 1 \wedge \rho_e \in]0,1] \tag{2.46}$$

This new variable ρ_e, known as artificially density, takes values between 0 and 1. However, intermediate values of density correspond to intermediate values of material stiffness, that does not belong to the discrete conceptualization of the TO problem. The power law exponent, p, guarantee that the continuous solution is analogous to the discrete one. The penalty exponent p takes values higher than 1 (usually $p = 3$ or 4) to ensure that the intermediate values of density are less advantageous. The penalization leads to solutions near the discrete one, rendering "black-white" designs, as the intermediate densities represent a small gain of stiffness compared to the cost of material. In Fig. 2.7 is observed the relation between the material properties and the artificial density, depending on the penalization, for the power law defined in Eq. (2.46):

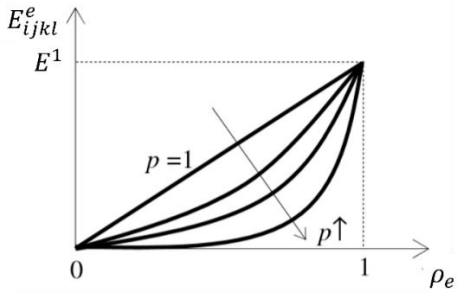

Figure 2.7 – Relation between material properties and the artificial density design variable, depending on the penalization p.

2.4.1.1 Filtering Schemes

Density-based topology optimization often suffers from issues such as checkerboarding and mesh dependency. Checkerboarding refers to patterns of alternating solid and void elements that resemble a checkerboard, while mesh dependency refers to the problem of obtaining significantly different optimal solutions depending on the mesh size or discretization used. To address these challenges, filtering techniques are commonly employed to smooth the density distribution and regularize the design. Two popular filtering methods are (1) the

density filtering and (2) the **sensitivity filtering**. Density filtering involves recalculating the density of each element as a weighted average of the densities of its neighboring elements, and its concept was introduced by Bruns and Tortorelli [127], in 2001. This adjustment is applied before the Finite Element Method (FEM) analysis is performed, and then the sensitivities are updated accordingly, to ensure consistency. In contrast, sensitivity filtering, proposed in 1994 by Sigmund [59], takes a more heuristic approach by modifying the sensitivities after the standard finite element analysis, using the weighted average of neighboring sensitivities. In the context of this thesis the density filtering method is adopted, which is described below.

The neighborhood of an element e includes all elements i, whose centers fall within a specified filter radius, R, from the center of e, i.e.:

$$N_e = \{i | \|x_i - x_e\|\} \tag{2.47}$$

where x_i is the spatial (center) location of element i, and $i \in N_e$ [128].

Since the density filter modifies the element density based on the neighbourhood elements, the modified, or filtered, density becomes a function of the neighbourhood, i.e., $\tilde{\rho}_e(\rho_i)$, computed as follows:

$$\tilde{\rho}_e = \frac{1}{\sum_{i \in N_e} H_{ei}} \sum_{i \in N_e} H_{ei} \rho_e \,, \qquad H_{ei} = \max\{0, R - \|x_i - x_e\|\} \tag{2.48}$$

Note that the filtered density represents the physical density and is used to compute all properties associated with the FEM analysis and optimization problem (e.g., material properties, volume, objective function, constraints, …). This will also impact the sensitivity analysis, as detailed further on, as the design variables that are optimized by the algorithm are the non-filtered densities.

Within the scope of this thesis, this filtering technique is applied to microstructures. Since the microstructure is assumed to be periodically repeated, the filtering of densities at each element located at the UC border implies resetting the neighbourhood structure for averaging, to also consider the densities of elements located at the UC opposite sides. To illustrate this, Fig. 2.8 shows an UC discretized into 9 elements, where filtering element 1 requires including not only the densities of element 2 and 4 (that would suffice in periodicity absence), but also 3 and 7 to maintain periodicity. This procedure was implemented in the

optimization codes developed in the context of this thesis and can be regarded as an extension of the work originally proposed by Xia and Breitkopf [62].

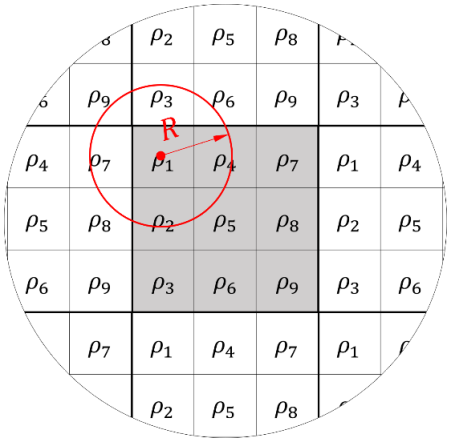

Figure 2.8 – Density filter application to an illustrative UC (3×3 mesh), considering periodicity, unitary elements, and filter radius R slightly above 1.

2.4.2 Multimaterial Topology Optimization

The approach of topology optimization, that determines whether a point in the domain is solid or void, can be extended to distributing different materials within the domain [129]. Multimaterial Topology Optimization (MMTO) has emerged as a powerful strategy to further enhance the mechanical performance of structures by allowing greater flexibility in material distribution. Recent studies have demonstrated its potential in real-world applications. For instance, Lu et al. (2019) [130] applied a multi-material approach to the structural optimization of a bus, simultaneously optimizing material selection, topology, and cross-sectional dimensions under stiffness and natural frequency constraints, with the goal of minimizing mass. Their approach, which split the problem into two sequential subproblems, multi-material topology optimization followed by dimensional optimization, led to an impressive mass reduction of 39.65% in the first step and a further 39.47% reduction in the second. Similarly, Jung et al. [131], in 2019, optimized the roof structure of an electric bus to support battery systems, achieving an 8% lighter design when using a combination of steel and aluminum instead of a single material. Beyond structural applications, recent research has also emphasized that compliance minimization, though widely used in academic settings, lacks physical relevance in industrial design. As highlighted in [129], a more practical approach consists of minimizing total weight under performance constraints, thus allowing the optimizer to determine the optimal balance between materials without the need for pre-

defined volume fractions. In the present study, MMTO plays a crucial role, not only in enhancing structural performance but also in enabling the design of materials with NTE which can only be achieved through the combination of at least two materials with distinct thermal behaviors.

To determine the material in each point of the domain, multimaterial interpolation schemes are used. These mathematical expressions allow to obtain the distribution of two of more base materials within the structure. Examples of such interpolation laws include the extension of SIMP, proposed by Sigmund & Torquato [5], in 1997, and later by Gibiansky & Sigmund [65], in 2000, as well as the Discrete Material Optimization (DMO) method introduced by Stegmann [132] and Lund and Stegmann [133,134], in 2005. In 2011, Gao & Zang [135] made, for the first time, a distinction between Recursive Multiphase Materials Interpolation (RMMI), under which SIMP-based laws are classified, and Uniform Multiphase Materials Interpolation (UMMI), under which DMO-based laws fall. These interpolation schemes select the material based on the value of an artificial density variable. Ideally, this variable is discrete in nature, thereby selecting the properties of one of the available (candidate) materials. However, in continuous approaches, material selection is enforced through penalization, pushing the variable towards one of its bounds, either 0 or 1. Without such penalization, the algorithm would assign properties of a fictitious material, i.e., essentially a mixture of two or more materials. Typically, the number of design variables increases with the number of material phases to be interpolated, although this also depends on the interpolation law being used.

2.4.2.1 SIMP Extensions

Among density-based topology optimization methods, SIMP remains the most widely adopted approach. In 1997, Sigmund and Torquato [5] extended the classical SIMP method, in Eq. 2.46, to consider two solid phases plus void. Considering only two material phases, the SIMP interpolation law is extended to:

$$E_{ijkl}^{e} = \rho_e^p \mathbf{E}^1 + \left(1 - \rho_e^p\right)\mathbf{E}^2, \qquad p \geq 1 \wedge \rho_e \in]0,1] \tag{2.49}$$

Note that, if the second phase is void, i.e., $\mathbf{E}^2 = \mathbf{0}_{3\times3}$, Eq. (2.49) becomes the classic SIMP interpolation in Eq. (2.46). To interpolate between two solid phases there is no need of adding a second design variable. However, to also consider void, i.e., three material phases, Eq. (2.49) is extended as:

$$E_{ijkl}^{e} = \rho_{1,e}^{p}\left(\rho_{2,e}^{p}\mathbf{E}^{1} + \left(1-\rho_{2,e}^{p}\right)\mathbf{E}^{2}\right), \qquad p \geq 1 \wedge \rho_{1,e}, \rho_{2,e} \in]0,1] \tag{2.50}$$

In this case, two design variables per element are needed. The first, $\rho_{1,e}$ is the topological variable, that defines whether the element is void ($\rho_{1,e} = \rho_{min}$) or solid ($\rho_{1,e} = 1$). Note that the design variables cannot be exactly zero, as this would lead to numerical instability or singularity. Nonetheless, it should be set to a sufficient small value to ensure that its contribution to the overall stiffness is negligible. Usually, $\rho_{min} = 10^{-3}$, and for, e.g., $p = 3$, the stiffness of a void element would be $E_{ijkl}^{e} = 10^{-9}\left(\rho_{2,e}^{p}\mathbf{E}^{1} + \left(1-\rho_{2,e}^{p}\right)\mathbf{E}^{2}\right)$, so independently of $\rho_{2,e}$, the stiffness is negligible. Fig. 2.9 presents the graphical representation of the SIMP interpolation law for three material phases (two solid plus void), for different values of the penalization exponent, p.

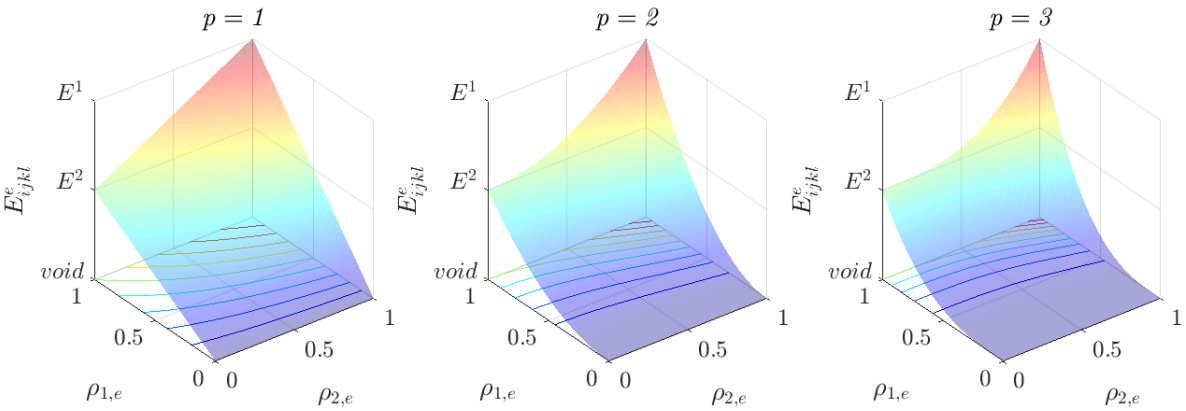

Figure 2.9 – Graphical representation of the SIMP power law, Eq. (2.50), to interpolate three material phases, with (a) $p = 1$, (b) $p = 2$ and (c) $p = 3$.

For any number of candidate materials plus void, i.e., N_f material phases, the interpolation law in Eq. (2.50) is generalized as:

$$\begin{aligned} E_{ijkl}^{e} &= \sum_{m=1}^{N_f}\left[\left(1-\xi_{m,e}\rho_{m,e}^{p}\right)\left(\prod_{i=1}^{m-1}\rho_{m,e}^{p}\right)\mathbf{E}^{N_f-m+1}\right], \\ p \geq 1 \wedge \rho_{m,e} &\in]0,1]; \xi_{m,e} = \begin{cases} 1, m \neq N_f \\ 0, m = N_f \end{cases} \end{aligned} \tag{2.51}$$

Easily it comes that to interpolate between N_f material phases, $(N_f - 1)$ design variables are needed. As the number of phases increase, the interpolation law in Eq. (2.51) becomes quite complex, and the problem tends to get stuck in local minimum [134]. Further-

more, in the void elements, where the design variables are in their lower bound, numerical instabilities may easily appear. For a relative low number for material phases (say around 4), this law is quite easily to implement and widely used in TO problems. However, for more material phases there are other interpolation laws that may be more appropriate.

2.4.2.2 DMO – Discrete Material Optimization

In 2005, Stegmann and Lund [134] presented a new interpolation law, that, similarly to SIMP, is based on an artificial density design variable. This new methodology was first applied to determine the optimal fibre orientation in composite laminated materials, in a compliance minimization problem. At its core, the DMO method originates from multi-material optimization approaches, such as SIMP. In these methods, a property like stiffness, assigned to a finite element, E^e_{ijkl}, is typically obtained through a weighted sum of the properties of each available material phase. In its most generalized way, the DMO interpolation law is given as:

$$E^e_{ijkl} = \sum_{m=1}^{N_f-1} w_{m,e}\mathbf{E}^m = w_{1,e}\mathbf{E}^1, \dots, w_{N_f-1,e}\mathbf{E}^{N_f-1} \tag{2.52}$$

For the properties resulting from Eq. (2.52) to have physical meaning, the weight functions, $w_{m,e}$, must take values of 0 or 1. It is therefore essential that, similarly to the SIMP approach, penalization strategies are applied to ensure that the solution to the continuous problem closely approximates the discrete one. From this general formulation, different versions of the DMO method have been developed, which vary according to the weighting functions adopted. Compared to the SIMP model, these approaches offer the advantage of being generalized to any number of material phases without significantly increasing the mathematical complexity of the formulation.

The DMO 1 [133] approach presents the simpler weight function, with only one design variable for each weight, i.e., $w_{m,e} = \rho^p_{m,e}$, that translates in the generalized law:

$$E^e_{ijkl} = \sum_{m=1}^{N_f-1} \rho^p_{m,e}\mathbf{E}^m = \rho^p_{1,e}\mathbf{E}^1, \dots, \rho^p_{N_f-1,e}\mathbf{E}^{N_f-1} \tag{2.53}$$

Since each weighting function is influenced by only one design variable, this results in a straightforward computational implementation of the model and simplifies the sensitivity analysis. It should be noted that, in the absence of any constraint on the sum of the weighting

functions, multiple material phases could be assigned to the same element, resulting in a mixed or meaningless effective property. To prevent this, it is necessary to constrain the sum of the weighting functions, in each element, so that it does not exceed unit, i.e., $\sum_{m=1}^{N_f-1} \rho_{m,e}^{p} \leq 1$. This inequality constraint allows the identification of the void phase, and thus, the topology, when all design variables are zero.

In Fig. 2.10 is shown the graphical representation of the DMO interpolation law for three material phases (two solid plus void), i.e., Eq. (2.53) with $N_f = 3$, for different values of the penalization exponent, p.

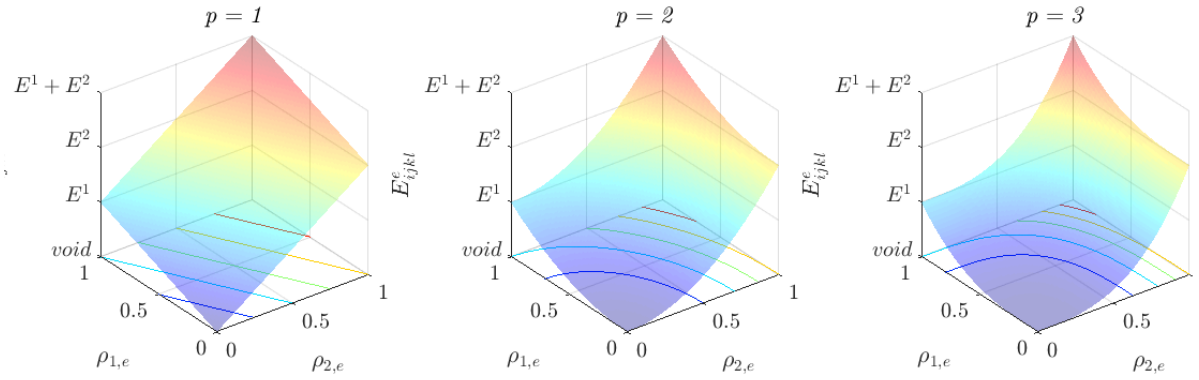

(a) (b) (c)

Figure 2.10 – Graphical representation of the DMO power law, Eq. (2.53), to interpolate three material phases, with (a) $p = 1$, (b) $p = 2$ and (c) $p = 3$.

2.4.2.3 SFP – Shape Function Parameterization

In 2011, Bruyneel [136] proposed a new interpolation law based on the shape functions of a linear quadrilateral element. This methodology has the advantage of being able to interpolate a given number of material phases using fewer design variables than the previously presented approaches. Nevertheless, it is still necessary to penalize the design variables so that they tend toward their discrete values, 0 or 1. The penalization strategy is implemented using the exponent p, similarly to what was described before.

A quadrilateral isoperimetric element in its natural and global referential is represented in Fig. 2.11a and Fig. 2.11b, respectively. The element in Fig. 2.11b) corresponds to the translation of the element in the natural referential, so that ξ and η now varies from 0 to 1 and can be related to $\rho_{1,e}$ and $\rho_{2,e}$.

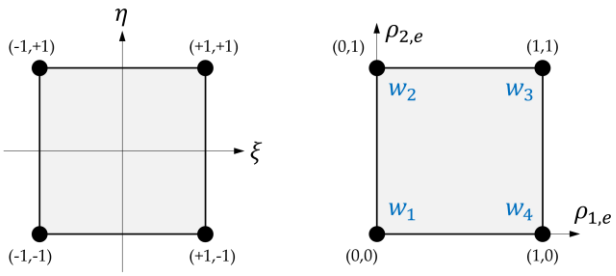

Figure 2.11 – Isoparametric FE in the (a) natural and (b) global coordinate system.

Now, re-writing the shape functions of a linear quadrilateral in the new referential $0_{\rho_{1,e},\rho_{2,e}}$, gives:

$$\begin{cases} w_{1,e} = (1-\rho_{1,e})(1-\rho_{2,e}) \\ w_{2,e} = \rho_{1,e}(1-\rho_{2,e}) \\ w_{3,e} = \rho_{1,e}\rho_{2,e} \\ w_{4,e} = \rho_{2,e}(1-\rho_{1,e}) \end{cases} \tag{2.54}$$

Considering that each function $w_{m,e}$ correspond to the property m to be interpolated, it is possible to select a different property according to the values of the pair $(\rho_{1,e}, \rho_{2,e})$, i.e., to the vertices of the element. Note that in each vertex, the corresponding function is one while the remaining are null. Therefore, the resulting property of an element can be obtained by summing the shape functions, each multiplied by the material property associated with its corresponding phase, i.e.,:

$$\begin{aligned} E^e_{ijkl} = {} & \rho_{1,e}\rho_{2,e}\mathbf{E}^1 + \rho_{1,e}(1-\rho_{2,e})\mathbf{E}^2 + \rho_{2,e}(1-\rho_{1,e})\mathbf{E}^3 \\ & + (1-\rho_{1,e})(1-\rho_{2,e})\mathbf{E}^4 \end{aligned} \tag{2.55}$$

The advantage of this law is that with only two design variables, four material phases (here including void) can be interpolated. The graphical representation of the SFP interpolation law, Eq. (2.55), for different of the penalization exponent, is shown in Fig. 2.12.

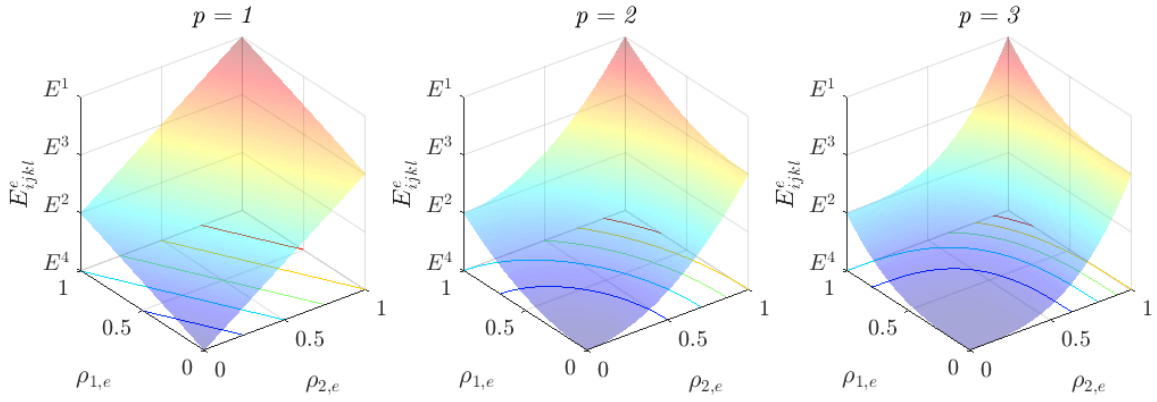

(a) (b) (c)

Figure 2.12 – Graphical representation of the SFP power law, Eq. (2.55), to interpolate three material phases, with (a) $p = 1$, (b) $p = 2$ and (c) $p = 3$.

2.4.2.4 Comparative analysis

The selection of each material phase is strongly influenced by the interpolation surface defined by the chosen material law. Fig. 2.13 illustrates the progression of material property variations when interpolating among the available material phases. It is particularly relevant to observe the "path" taken when interpolating between any two material phases, as this can affect the quality of the solutions obtained, as discussed below. In cases involving multiple solid phases, the filtering process leads to intermediate densities (grey regions) which correspond to phase transitions. These transitions should ideally occur gradually between only two neighbouring phases. For instance, the SFP law can produce physically meaningless results. As shown in Fig. 2.13c, in the transition between phase 2 and phase 3, the black interpolation path results in a stiffness reduction compared to the red one. Consequently, an algorithm aiming for maximum stiffness might opt to transition from phase 2 to 3, through phase 1 (red path), a stiffer material phase, which lacks physical justification. This leads to poor modelling of the material interface between two materials and compromises the physical accuracy of the solution. Therefore, the SFP law may be ill-suited for topology optimization of continuous structures using density-based approaches with filtering.

Regarding the DMO law, the interpolation surface shown in Fig. 2.13b only utilizes the lower half due to the imposed constraint on the sum of the weighting functions. Nevertheless, the path between two material phases still passes through intermediate densities (diagonal path in Fig. 2.13b), and a local minimum may occur depending on the penalization exponent p. When applying a continuation approach, starting from $p = 1$, corresponding to a flat interpolation surface (see Fig. 2.10), this minimum only becomes relevant when $p \geq 1$,

beyond which the interpolation surface becomes non-monotonic. However, since density variables are driven toward their bounds, the likelihood of the algorithm being trapped in such local minima is reduced.

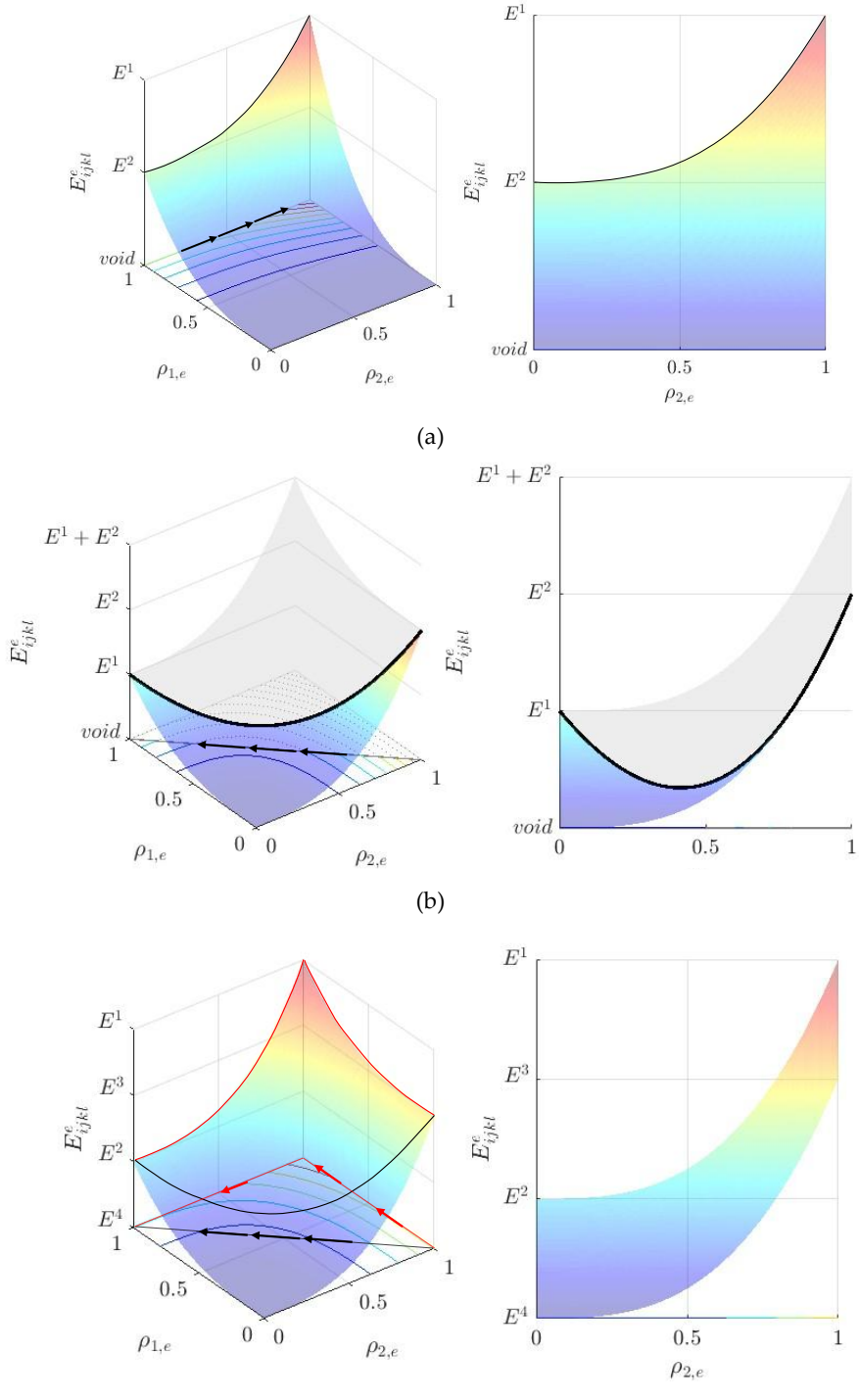

(a)

(b)

(c)

Figure 2.13 – Comparation of interpolation surface, with $p = 3$, for the interpolation law (a) SIMP; (b) DMO and (c) SFP.

Similar to the SFP law, using the DMO law in problems involving density filtering can also yield meaningless intermediate density values. It is worth noting that in most applications of the DMO law reported in the literature, the goal is to determine optimal fibre orientations in laminated composites, a context where filtering is generally avoided, precisely to circumvent the issues described here. Essentially, when using the DMO or SFP laws, it is particularly important to adopt a continuation approach to gradually increase the penalization exponent p, thereby minimizing the influence of local minima on the optimization outcome. In contrast, the SIMP law offers a more favourable interpolation surface, as it inherently provides a monotonic transition between material phases, avoiding the issues seen in the DMO and SFP laws. It is also important to note that the initial design point significantly influences the optimization trajectory, especially when more than two material phases are considered. For example, starting from $\left(\rho_{1,e}, \rho_{2,e}\right) = (0.5,0.5)$ with $p = 3$, the interpolation of the stiffness by the SIMP law yield $E^e_{ijkl} = 0.0156\,\mathbf{E}^1 + 0.1094\,\mathbf{E}^2$ which inherently favours one phase over the others.

In conclusion, the SIMP law was selected here due to its robustness and physically consistent behaviour in problems involving filtering and multiple solid material phases. Its monotonic interpolation path and straightforward implementation for a few material phases make it widely adopted in the literature that deals with the type of TO problems addressed in this thesis.

2.4.3 Multiscale Topology Optimization

In multiscale structures, two distinct level of scales can be typically observed: the **macroscale**, often referred to as the structural scale, and the **microscale**, associated with the material scale. These structures are commonly found in nature, e.g., bone and bamboo, exhibiting exceptional mechanical performance while remaining inherently lightweight and robust.

The concept of multiscale structures is already present in the seminal work of Bendsøe and Kikuchi [122], where the mechanical properties of a material were modeled by numerically homogenizing an infinitesimally small representative UC. However, it was only with the technological progress in additive manufacturing that these multiscale structures moved from being purely theoretical concepts to physically manufacturable structures. In Fig. 2.14 are presented some examples of 3D multiscale structures design by topology optimization, some of which are produced by 3D printing.

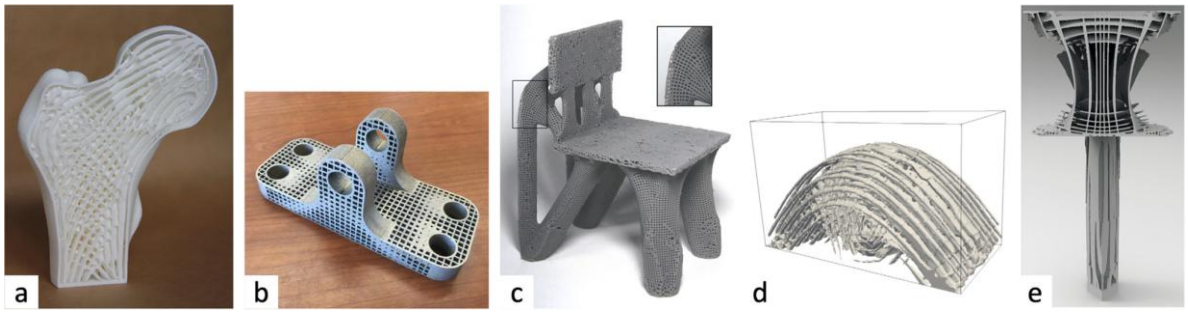

Figure 2.14 – Examples of 3D multiscale structures design by topology optimization. Reproduced from [137].

Rodrigues et al. [138] presented a hierarchical optimization model to simultaneous optimize both structure and microstructure, varying the configuration of the UC from point to point on the macroscale. Following this work, pioneer results were achieved in three-dimensional structures by Coelho et al. [139] and in multimaterial structures by Conde et al. [140]. Concurrent multiscale optimization to minimize mechanical compliance was proposed by Liu et al. [11], with independent micro and macro design variables to improve the possibility of practical applications and manufacturability. Deng et al. [141], further developed the methodology to encompass thermoelastic loads, with similar work presented by Yan et al. [96]. Yan et al., further expanded the multiscale optimization field for thermoelastic lattice structures [98,142,143]. Building on these pioneering studies and approaches, many additional multiscale approaches for structure optimization have emerged [97,137,144,145].

The multiscale optimization procedure can thus be implemented in either hierarchical or concurrent form, as explained in [146]: In the **hierarchical** implementation the optimization procedure consists of two separate problems, the inner and outer problem. In the inner problem, the geometry of the UC is optimized for a fixed structural domain. In the outer problem, the geometry of the structural domain is optimized for a fixed periodic UC. Thus, at every optimization step, the inner and outer problems are solved hierarchically, providing each other with new geometries. In the **concurrent** optimization procedure, the geometries of the micro and macro-scales are updated simultaneously, by augmenting the TO problem with the two sets of design variables representing the two different scales. The first set of design variables consists of the relative material densities of the finite elements discretizing the structural domain, whereas the second set of design variables consists of the relative material densities of the finite elements discretizing the periodic UC.

Conde et al. [147], in 2024, presented two algorithmic strategies to address the coupling between global and local design variables in multiscale topology optimization. In their work, the authors distinguish between **implicit** and **non-implicit** strategies, depending on

how the macroscale design variables (macro-densities) are related to the microscale ones (micro-densities). These strategies reflect different ways of handling the multiscale coupling and are aligned with a hierarchical implementation, where the macro- and micro-problems are solved in a coordinated yet decoupled manner.

The term *multiscale* is widely used in the literature to describe both physical structures and modelling or design strategies. While many multiscale design approaches rely on the assumption of scale separation, typically referred to as multiscale modelling, other approaches, known as mono-scale methods, do not require this assumption and often result in uniform material distributions. Interestingly, mono-scale formulations can still give rise to multiscale-like features when very fine meshes are used, especially in the absence of regularization techniques. In the mono-scale approach, the analysis is performed in the full resolution of the domain and the local control is done by either (1) pattern repetition [148], which enforces periodicity across subdomains or (2) and local volume constraints [149], which limit the amount of solid material locally.

For a comprehensive overview of multiscale design and modelling strategies, the reader is referred to the excellent review paper by Wu et al. [150], which thoroughly discusses the evolution, classification, and implementation of multiscale approaches in topology optimization. Further details on the multiscale topology optimization framework developed in the context of this thesis will be given in Section 4.

2.4.4 Gradient-based Optimization Algorithms

Numerical methods, such as the FEM, empowered by the advent of digital computers, enable the solution of complex optimization problems that are highly relevant in engineering practice. Optimization combined with the FEM is a powerful tool for the automatic design of structures. This means that an optimization process involves performing a series of Finite Element (FE) analyses in which an algorithm iteratively modifies the values of the design variables associated with the numerical model, aiming to improve a structural performance measure. Optimization algorithms are generally divided into two main categories: (1) gradient-based and (2) non-gradient-based (or gradient-free) methods, but only the gradient-based are detailed here, as they are used in this thesis.

Gradient-based optimization algorithms are commonly referred to as mathematical programming methods. They require the design space to be convex, closed, and bounded, and that both the objective function and the constraints are continuous and differentiable (at

least once), which limits their applicability to some real-world problems, particularly those of a discrete or non-continuous nature. However, these methods are highly efficient at locating the optimal point. Typically, these methods begin by identifying a starting point in the design space, $\mathbf{s}^0$, that serves as an initial estimate of the optimum. Then, a search direction, **d,** is calculated using the gradient information, and an optional step, α, in the search direction. This information is then used to select a new design point, $\mathbf{s}^1 = \mathbf{s}^0 + \alpha\mathbf{d}$, within the feasible solution space that improves the objective function. The objective and constraint functions are evaluated, and the algorithm iterates until the convergence conditions are met. In each iteration, the algorithm analyses a neighbourhood around the current design point, evaluating the objective and constraint functions, along with their gradients and curvature. Some well-known examples of gradient-based mathematical programming methods include Steepest Descent Method, Conjugate Gradient Method; Newton's Method; Sequential Linear Programming (SLP); Optimality Criteria (OC); Sequential Quadratic Programming (SQP); Feasible Directions Method, Method of Moving Asymptotes (MMA) and Global Convergence MMA (GCMMA). The MMA and GCMMA was the algorithm chosen to solve the optimization problems addressed in this thesis, due to the capability of dealing with a large number of design variables and moderate number of constraints and will therefore be described in greater detail below.

2.4.4.1 MMA – Method of Moving Asymptotes

In 1987, Svanberg [117] proposed the Method of Moving Asymptotes (MMA). This algorithm solves the original optimization problem by approximating it with a sequence of simpler subproblems that exhibit attractive properties of convexity and separability. Therefore, MMA is a Sequential Convex Programming method, that combines the concepts of approximation and dual solution. As the iterations progress, the solution of these subproblems converges to the solution of the original problem.

To describe the MMA more precisely, the optimization subproblem it solves is presented in Eq. (2.56) and can also be found in [151]. The problem includes m constraints and n design variables, denoted as $\mathbf{s} = (s_1, \dots, s_n)^T, \mathbf{t} = (t_1, \dots, t_m)^T$ and z.

$$
\begin{aligned}
&min \qquad f_0(\mathbf{s}) + a_0 z + \sum_{i=1}^{m} \left(c_i t_i + \frac{1}{2} d_i t_i^2 \right) \\
&s.t \qquad \begin{cases} f_i(\mathbf{s}) - a_i z - t_i \leq 0 & ; i = 1, \dots, m \\ s_j^{min} \leq s_j \leq s_j^{max} & ; j = 1, \dots, n \\ t_i \geq 0 & ; i = 1, \dots, m \\ z \geq 0 \end{cases}
\end{aligned} \tag{2.56}
$$

The functions $f_0(\mathbf{s})$ and $f_i(\mathbf{s})$ represent the objective and constraint functions of the original problem, continuous and differentiable. $\mathbf{s}$ is the design variable vector of the original problem, and $\mathbf{t}$ and z are artificial variables, introduced to prevent the optimization process from producing infeasible solutions. Additionally, by assigning a suitable "penalty" or cost to these variables, the method encourages the final solution to remain as close as possible to the feasible region. The parameters a_0, a_i, c_i e d_i are real values and must satisfy the conditions $a_0 > 0, a_i \geq 0, c_i \geq 0, d_i \geq 0$ and $c_i + d_i > 0$.

In topology optimization it may be impossible to obtain the solution of the problem directly, due to the computational cost of the structural and sensitivity analysis. To deal with this, in each iteration k, MMA replaces the primary optimization problem by a subproblem where the original functions, $f_0(\mathbf{s})$ and $f_i(\mathbf{s})$, are replaced by approximating convex functions, $\tilde{f}_0^{(k)}(\mathbf{s})$ and $\tilde{f}_i^{(k)}(\mathbf{s})$, respectively. These new functions are asymptotic and are defined based on the gradient information of the original functions at the current iteration, while also considering data from previous iterations (optimization history). Starting from the point $\left(\mathbf{s}^{(k)}, \mathbf{t}^{(k)}, z^{(k)}\right)$, the subproblem is solved, and the optimal solution of iteration k becomes the starting point for the next iteration, $\left(\mathbf{s}^{(k+1)}, \mathbf{t}^{(k+1)}, z^{(k+1)}\right)$, and so on.

$$
\begin{aligned}
&min \qquad \tilde{f}_0^{(k)}(\mathbf{s}) + a_0 z + \sum_{i=1}^{m} \left(c_i t_i + \frac{1}{2} d_i t_i^2 \right) \\
&s.t \qquad \begin{cases} \tilde{f}_i^{(k)}(\mathbf{s}) - a_i z - t_i \leq 0 & ; i = 1, \dots, m \\ \alpha_j^{(k)} \leq s_j \leq \beta_j^{(k)} & ; j = 1, \dots, n \\ t_i \geq 0 & ; i = 1, \dots, m \\ z \geq 0 \end{cases}
\end{aligned} \tag{2.57}
$$

The parameter c_i penalizes the objective function to enforce constraint satisfaction. However, an excessively high penalty may cause numerical instabilities, hindering the convergence of the algorithm. Therefore, the choice of c_i values must be made carefully, typical-

ly starting with a low value ($c_i \simeq 10^3$) and increasing it only if necessary to satisfy the constraints.

In Eq. (2.57), the bounds $\alpha_j^{(k)}$ and $\beta_j^{(k)}$, also known as *move limits*, ensure that the design variables remain within an interval that does not include any asymptotes of the approximation function. To avoid the possibility of any "division by zero", when solving the subproblem, the move limits values should be chosen such that:

$$L_j^{(k)} \leq \alpha_j^{(k)} \leq s_j \leq \beta_j^{(k)} \leq U_j^{(k)} \tag{2.58}$$

where $L_j^{(k)}$ and $U_j^{(k)}$ are the *moving asymptotes*. A more detailed implementation of the MMA optimization algorithm can be found in [117].

In 1995, Svanberg [152] introduced an extension of the MMA algorithm known as the Globally Convergent Method of Moving Asymptotes (GCMMA). This approach incorporates both asymptotes simultaneously to construct a non-homogeneous approximation function $\tilde{f}_i$, enabling it to be non-monotonic. Later, in 2002, Svanberg [16] presented an enhanced version of GCMMA, which guarantees that each iteration point is a feasible solution with lower objective value than the previous one. This is achieved by considering *outer* and *inner* iterations in this method, where each outer iteration generates a new solution by solving a convex subproblem based on local approximations; if the solution is not sufficiently conservative, i.e., meaning the approximations are greater or equal to the original functions, inner iterations refine the approximations until this condition is met. A major advantage of this method is that it can deal with a very large number of variables ($\sim 10^4 - 10^5$), however the inner iteration loop implies a major increase in computational time.

2.4.5 Sensitivity Analysis

The sensitivity analysis consists of calculating the sensitivity (or variation) of a function with respect to changes in the design variables. When using gradient-based optimization algorithms this analysis is necessary to guide the algorithm's evolution direction. Essentially, two methods can be used to calculate the gradient of a function: analytical (exact) or numerical. Since evaluating sensitivities often dominates the computational cost of solving an optimization problem, it is crucial to carefully select an appropriate sensitivity analysis method for each specific case. The numerical method most widely used is the Finite Difference Method (FDM), which is very simple to implement, but computational expensive. The analytical

methods are more mathematically elaborated but they are more accurate and require a lower computational cost compared to the numerical methods. The development of this subsection is based on the book by Haug et al [153].

2.4.5.1 Analytical Methods

Most optimization problems consider that the structure is discretized by FE, and the analysis is solved resorting to the FEM, where the static equilibrium equation is given by Eq. (2.59):

$$\mathbf{K}(s)\mathbf{u} = \mathbf{F}(s) \tag{2.59}$$

where s is the design variable, $\mathbf{K}$ and $\mathbf{F}$ are the stiffness matrix and the load vector, respectively, and $\mathbf{u}$ the displacement vector. Consider now a generic function, X, that represent an objective or constraint function in the optimization problem. This function is, in fact, a functional, as it depends on the design variable implicitly and explicitly, through the displacement, i.e., $\mathrm{X}\big(s, \mathbf{u}(s)\big)$. The total derivative of such function w.r.t s, i.e., $\mathrm{d}\mathrm{X}/\mathrm{d}s$, cannot be calculated directly, and so the chain rule in applied:

$$\frac{\mathrm{d}\mathrm{X}}{\mathrm{d}s} = \frac{\partial \mathrm{X}}{\partial s} + \frac{\partial \mathrm{X}}{\partial \mathbf{u}}\frac{\mathrm{d}\mathbf{u}}{\mathrm{d}s} \tag{2.60}$$

The **explicit** part (first parcel) of Eq. (2.60), i.e., $\partial \mathrm{X}/\partial s$, is usually easy to obtain, and computed by derivative rules. The major challenge resides in the computation of the **implicit** part (second parcel), i.e., $\mathrm{d}\mathbf{u}/\mathrm{d}s$. Differentiating both sides of the equilibrium equation (Eq. 2.59), yields:

$$\frac{\mathrm{d}\mathbf{K}(s)}{\mathrm{d}s}\mathbf{u} + \mathbf{K}(s)\frac{\mathrm{d}\mathbf{u}}{\mathrm{d}s} = \frac{\mathrm{d}\mathbf{F}(s)}{\mathrm{d}s} \tag{2.61}$$

Substituting the derivative $\mathrm{d}\mathbf{u}/\mathrm{d}s$ from Eq. (2.61) into Eq. (2.60), results in:

$$\frac{\mathrm{d}\mathrm{X}}{\mathrm{d}s} = \frac{\partial \mathrm{X}}{\partial s} + \frac{\partial \mathrm{X}}{\partial \mathbf{u}}\left(\mathbf{K}^{-1}(s)\left[\frac{\partial \mathbf{F}}{\partial s} - \frac{\partial \mathbf{K}(s)}{\partial s}\mathbf{u}\right]\right) \tag{2.62}$$

However, the direct computation of the inverse of the stiffness matrix, $\mathbf{K}^{-1}(s)$, is impractical, invalidating the use of Eq. (2.62). To overcome this problem, two different analytical methods may be used: (1) Direct method and (2) adjoint method.

In the **direct method**, the derivative of both sides of the equilibrium equation, Eq. (2.59), is done, obtaining the solution $\mathrm{d}\mathbf{u}/\mathrm{d}s$ by solving the following system of equations:

$$\mathbf{K}\left(\frac{\mathrm{d}\mathbf{u}}{\mathrm{d}s}\right) = \mathbf{q}, \qquad \text{where } \mathbf{q} = \left(\frac{\partial \mathbf{F}}{\partial s} - \frac{\partial \mathbf{K}}{\partial s}\mathbf{u}\right) \tag{2.63}$$

However, it is necessary to solve Eq. (2.63) for each design variable, often resulting in a high computational cost. For a problem with n design variables, the system of equations in Eq. (2.63) is solved n times.

In the **adjoint method**, an adjoint vector, $\boldsymbol{\lambda}$, is defined as $\boldsymbol{\lambda}^{\mathrm{T}} = \frac{\partial \mathrm{X}}{\partial \mathbf{u}}\mathbf{K}^{-\mathbf{1}}$, and is solution of the following system of equations:

$$\mathbf{K}(s)\boldsymbol{\lambda} = \mathbf{z}, \qquad \text{where } \mathbf{z} = \left(\frac{\partial \mathrm{X}}{\partial \mathbf{u}}\right)^{\mathrm{T}} \tag{2.64}$$

where $\mathbf{z}$ is the known *dummy-load vector*. Each entry of this vector corresponds to the derivative of the function X w.r.t the displacements, u_i. By solving equation (2.64) for the adjoint variable and substituting its result into (2.62), the derivative is finally given as:

$$\frac{\mathrm{dX}}{\mathrm{d}s} = \frac{\partial \mathrm{X}}{\partial s} + \boldsymbol{\lambda}^{\mathrm{T}}\left[\frac{\partial \mathbf{F}}{\partial s} - \frac{\partial \mathbf{K}(s)}{\partial s}\mathbf{u}\right] \tag{2.65}$$

In this context, in terms of computational cost, the adjoint method requires the definition of an adjoint vector and, consequently, the solution of one adjoint problem for each X-type function included in the formulation of the optimization problem. Assuming the problem involves m constraints defined by such functions, a total of m adjoint problems (or systems of equations) of the type (2.64) must be solved.

Therefore, it can be concluded that when the number of design variables n is smaller than the number of constraints m, the direct differentiation method is generally more efficient. Conversely, when n exceeds m, the adjoint method becomes more advantageous. In cases where $n \simeq m$, both methods show comparable performance. Nevertheless, from a practical standpoint, a design engineer may choose to consider only the critical constraints, i.e., those that are active or close to being active, among all X-type constraints in the formulation. In such cases, the adjoint method is justified, as the number of critical, or active, constraints, m^{crit}, is typically smaller than $m \simeq n$. When multiple load cases (LC) are being considered, the computational cost of both methods increases proportionally with LC. However, focusing again only on the critical constraints, even in the presence of $LC \times m$ constraints, the condition $m^{crit} \ll LC \times m \simeq LC \times n$ still favors the adjoint method.

Finally, selecting multiple materials for the structure leads to a significant increase in the number of design variables, while the number m of constraints remains unchanged. This clearly supports the use of the adjoint method in the context of topology optimization with material selection, as explored in this thesis.

2.4.5.2 Numerical Methods

The FDM computes the approximation $\Delta X/\Delta s$ of the derivative of a given function $X(s)$ w.r.t s, dX/ds. The finite difference can be computed in three different ways: (1) Forward-difference approximation; (2) backward-difference approximation; and (3) central-difference approximation, given by Eq. (2.66), Eq. (2.67) and Eq. (2.68), respectively.

$$\frac{dX}{ds} \approx \frac{\Delta X}{\Delta s} = \frac{X(s+\Delta s) - X(s)}{\Delta s} \tag{2.66}$$

$$\frac{dX}{ds} \approx \frac{\Delta X}{\Delta s} = \frac{X(s) - X(s-\Delta s)}{\Delta s} \tag{2.67}$$

$$\frac{dX}{ds} \approx \frac{\Delta X}{\Delta s} = \frac{X(s+\Delta s) - X(s-\Delta s)}{2\Delta s} \tag{2.68}$$

Where the displacement in $s + \Delta s$ is computed solving:

$$\mathbf{K}(s+\Delta s)\mathbf{u}(s+\Delta s) = \mathbf{F}(s+\Delta s) \tag{2.69}$$

This means that, to compute the derivatives of a function w.r.t n variables, Eq. (2.69) needs to be solved n additional times for the forward and backward-difference, and $2n$ for the central-difference. So, although the methods previously mentioned require solving the systems of equations (2.63) and (2.64), the computational cost associated with additional analysis is higher. Therefore, this method is only advantageous when the number of design variables is relatively small, which is not the case here. Noteworthy is the fact that all derivatives implemented in the scope of this thesis were confirmed by the FDM.

3

MICROSCALE OPTIMIZATION PARADIGM

The present chapter addresses a Multimaterial Topology Optimization problem, using a density-based approach and homogenization methods to compute the effective properties of the periodic composite materials. It is also pursued a comprehensive and critical analysis between the asymptotic homogenization and energy-based homogenization methods, regarding the viability of computing not only the thermoelastic effective properties, carried on in Section 2.3, but also their sensitivities, needed in the thermoelastic microstructural optimization problem. Furthermore, both continuum and truss-like microstructures are presented. For the continuum microstructures, the optimization problem is formulated as a multiobjective optimization problem to investigate the influence of coexisting negative indexes in the Pareto sense. The investigation in the continuum setting is based on the scientific paper by Almeida et al. [154], entitled "Multiobjective topology optimization of metamaterials to analyse the conflicting nature of negative Poisson's ratio and negative thermal expansion", published in Structural and Multidisciplinary Optimization in 2025.

This chapter is structured as follows. Firstly, the material model is introduced in Section 3.1. Section 3.2. presents the topology optimization framework to design metamaterials with extreme thermoelastic properties, followed by the formulation for truss-like microstructures, presented in Section 3.3. The results obtained are presented in Section 3.4. Finally, the main conclusions of this chapter are drawn in Section 3.5.

3.1 Material Model

The material model, outlined in Fig. 3.1, consists of a 2D thermoelastic composite material with periodic porous multimaterial microstructure. The microstructure design square domain, Y, corresponds to the UC, i.e., is the smallest periodic heterogeneity within the composite domain, Ω^{ϵ} (see Fig. 2.4). The behaviour of the periodic composite is extracted from the UC analysis through numerically solving the homogenization equations, applying Periodic Boundary Conditions (PBCs).

The domain of the UC is discretized by a square-grid of $\sqrt{N} \times \sqrt{N}$ Finite Elements (FE) mesh, with a total of N FE. As a multimaterial setting is considered, per each design FE, a density design variable and a material selection design variable are considered, i.e., $\rho_{1,e}$ and $\rho_{2,e}$, respectively. The vector of density variables, $\boldsymbol{\rho}_1$, defines the optimal topology, i.e., it determines void or solid phases, where $\rho_{1,e} = \rho_{min}$ means void and $\rho_{1,e} = 1$ means solid in element e. The lower value, $\rho_{min} = 10^{-3}$ is used to prevent the stiffness matrix from becoming singular. The vector of material selection variables, $\boldsymbol{\rho}_2$, defines the material distribution within the solid part of the design domain, i.e., it identifies whether solid phase 1 ($\rho_{2,e} = 1$) or solid phase 2 ($\rho_{2,e} = \rho_{min}$) exist in element e.

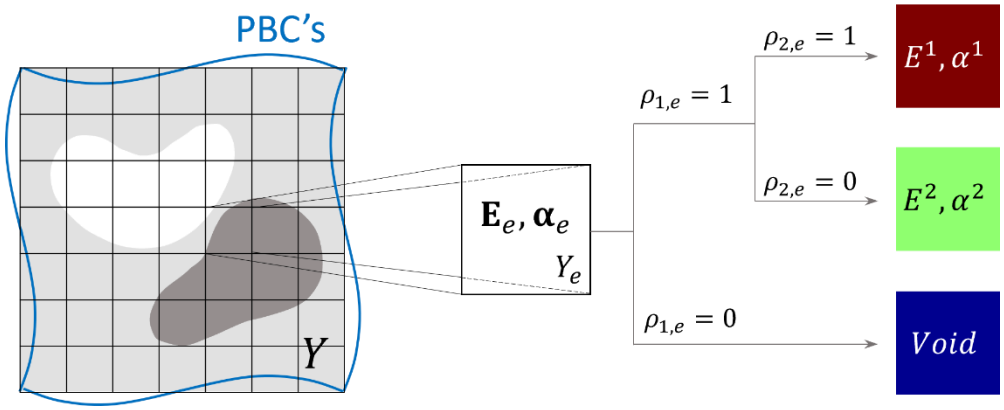

Figure 3.1 – Microscale material model considering a multimaterial periodic microstructure.

The extended SIMP scheme is used here to interpolate the stiffness tensor, $\mathbf{E}_e$, and the CTE tensor, $\boldsymbol{\alpha}_e$, of each element e, according to (3.1) and (3.2):

$$\mathbf{E}_e(\tilde{\rho}_{1,e}, \tilde{\rho}_{2,e}) = \tilde{\rho}_{1,e}^{p_1}\left(\tilde{\rho}_{2,e}^{p_2}\mathbf{E}^1 + \left(1 - \tilde{\rho}_{2,e}^{p_2}\right)\mathbf{E}^2\right) \tag{3.1}$$

$$\boldsymbol{\alpha}_e\left(\tilde{\rho}_{2,e}\right) = \tilde{\rho}_{2,e}^{p_2}\boldsymbol{\alpha}^1 + \left(1 - \tilde{\rho}_{2,e}^{p_2}\right)\boldsymbol{\alpha}^2 \tag{3.2}$$

where $\mathbf{E}^1$, $\mathbf{E}^2$, $\boldsymbol{\alpha}^1$ and $\boldsymbol{\alpha}^2$ are the stiffness and the CTE tensors of the base material phases 1 and 2, respectively, both assumed isotropic, recall Eq. (2.8), and $\tilde{\rho}$ are the filtered densities. The CTE in Eq. (3.2) does not depend on the density variable $\tilde{\rho}_1$. For comprehension, notice that in the homogenization equations $\boldsymbol{\alpha}$ multiplies by $\mathbf{E}$ ($\tilde{\rho}_1$ dependent) and thus it is only its distribution in the UC solid region that eventually matters. Also, bear in mind that only the combination of two or more solid materials differing in CTE allows to design metamaterials with tailorable CTE, mainly aiming its negative values. Otherwise, having a single-material microstructure, the corresponding CTE would simply be that of the selected base material. The exponents p are the penalization parameters. Parameter p_1 is set to penalize densities such that distinct solid/void phases are obtained, while p_2 is set to interpolate between the two solids, enabling their distinction. Since the final designs consist only of discrete values (ρ_{min} or 1), with no intermediate densities, the optimal solutions correspond to well-defined material phases, and the penalization effectively prevents non-physical mixtures, regardless of p_1 and p_2. On the contrary, in [155,156] the exponents and interpolation law must be carefully selected to ensure that interpolated properties are consistent with the physics of solid mixtures, as the goal is to design FGMs.

3.1.1 Prediction of Thermoelastic Effective Properties

The FEM is applied to numerically solve the continuous AH equations, detailed in Section 2.3.1. First, the local equilibrium problems of the UC are solved to obtain the micro displacements, $\boldsymbol{\chi}$ and $\boldsymbol{\Upsilon}$. The equilibrium problems defined in (2.27) and (2.28), are here given in the discretized form as:

$$\mathbf{K}\boldsymbol{\chi}^{(i)} = \mathbf{F}^{m(i)}, i = 1, \dots, 3 \tag{3.3}$$

$$\mathbf{K}\boldsymbol{\Upsilon} = \mathbf{F}^{th} \tag{3.4}$$

where $\mathbf{K}$ is the global stiffness matrix, that corresponds to the discretization of the left of (2.27) and (2.28) and is given by (3.5):

$$\mathbf{K} = \sum_{e=1}^{N} \mathbf{K}_e = \sum_{e=1}^{N} \int_{V_e} \mathbf{B}_e^{\mathrm{T}} \mathbf{E}_e \mathbf{B}_e \mathrm{d}V_e \tag{3.5}$$

The mechanical and thermal load vectors, $\mathbf{F}^{m(i)}$, with $i = 1,2,3$ and $\mathbf{F}^{th}$, corresponding to the discretization of the right side of (2.27) and (2.28), are defined as (3.6) and (3.7), respectively.

$$\mathbf{F}^{m(i)} = \sum_{e} \mathbf{B}_e^{\mathrm{T}} \mathbf{E}_e \boldsymbol{\varepsilon}^{0(i)} \mathrm{d}V_e \,, i = 1, \dots, 3 \tag{3.6}$$

$$\mathbf{F}^{th} = \sum_{e} \mathbf{B}_e^{\mathrm{T}} \mathbf{E}_e \boldsymbol{\varepsilon}^{\alpha} \mathrm{d}V_e \tag{3.7}$$

where V_e is the domain of element e (area in 2D). The unit strain fields, $\boldsymbol{\varepsilon}^{0(i)}$, are $\boldsymbol{\varepsilon}^{0(1)} = [1\ 0\ 0]$, $\boldsymbol{\varepsilon}^{0(2)} = [0\ 1\ 0]$, and $\boldsymbol{\varepsilon}^{0(3)} = [0\ 0\ 1]$. In Eq. (3.7) $\boldsymbol{\varepsilon}^{\alpha}$ is the thermal strain test that corresponds to a unit applied temperature, i.e., $\boldsymbol{\varepsilon}^{\alpha} = \boldsymbol{\alpha}_e$. $\mathbf{B}_e$ denotes the strain-displacement matrix of element e. Finally, $\mathbf{E}_e$ and $\boldsymbol{\alpha}_e$ are the stiffness and the CTE tensors of element e, respectively. In the TO setting, these tensors depend on the element-wise density-based design variables, see (3.1) and (3.2).

The homogenized stiffness tensor, $\mathbf{E}^H$, and homogenized thermal stress tensor, $\boldsymbol{\beta}^H$, corresponding to (2.34) and (2.35), can be numerically computed through (3.8) and (3.9), respectively.

$$\mathbf{E}^H = \frac{1}{|Y|} \sum_{e=1}^{N} \int_{V_e} \left(\boldsymbol{\chi}_e^{0(ij)} - \boldsymbol{\chi}_e^{(ij)} \right)^{\mathrm{T}} \mathbf{K}_e \left(\boldsymbol{\chi}_e^{0(kl)} - \boldsymbol{\chi}_e^{(kl)} \right) \mathrm{d}V_e \tag{3.8}$$

$$\boldsymbol{\beta}^H = \frac{1}{|Y|} \sum_{e=1}^{N} \int_{V_e} (\boldsymbol{\Upsilon}_e^0 - \boldsymbol{\Upsilon}_e)^{\mathrm{T}} \mathbf{K}_e \left(\boldsymbol{\chi}_e^{0(ij)} - \boldsymbol{\chi}_e^{(ij)} \right) \mathrm{d}V_e \tag{3.9}$$

Instead of using the AH, the equivalent EBH can be used to compute the thermoelastic properties (recall Section 2.3.2). Since the EBH allows to compute elastic effective properties by directly imposing the Dirichlet-type BCs in the FE model, it is no longer necessary to compute the load vector in (3.6) and (3.7), which makes this method more practical to implement [62]. The thermoelastic effective properties, corresponding to (2.38) and (2.42), can now be written in the discretized form as:

$$\mathbf{E}^H = \frac{1}{|Y|} \sum_{e=1}^{N} \int_{V_e} \mathbf{U}_e^{A(ij)^{\mathrm{T}}} \mathbf{K}_e \mathbf{U}_e^{A(kl)} \mathrm{d}V_e \tag{3.10}$$

$$\boldsymbol{\beta}^H = \frac{1}{|Y|} \sum_{e=1}^{N} \int_{V_e} \boldsymbol{\alpha}_e^{\mathrm{T}} \mathbf{E}_e \mathbf{B}_e \mathbf{U}_e^{A(ij)} \mathrm{d}V_e \tag{3.11}$$

where $\mathbf{U}_e^{A(kl)}$ are the element displacement solutions corresponding to the unit-test strain fields $\boldsymbol{\varepsilon}^{0(kl)}$, imposed directly on the boundaries of the UC.

The homogenized thermal stress tensor, computed through (3.9) and (3.11), is the same. However, when sensitivity analysis is required, the EBH method cannot be used. This results from the Maxwell-Betti reciprocal theorem being used to compute (3.11). Hence, for a given element e, the quantity inside the integral in (3.9) and (3.11) differs, although the integral over the full Y domain renders the same result. As sensitivities are element-wise quantities, there is no consistency between EBH and AH methods when it comes to computing derivatives of β_{ij}^H coefficients. To sum up, to compute the homogenized thermal stress tensor, both methods can be used, as they are equivalent, but for gradient-based optimization of thermoelastic metamaterials, sensitivities can only be provided by the AH method.

3.2 Topology Optimization Framework

To perform TO an algorithm was developed in Matlab language, by building upon code available in educational papers, such as homoge.m [67] and topX.m [62]. The homoge.m code computes the homogenized tensors using the AH method and, in the context of this thesis, the sensitivities of the homogenized coefficients were implemented. The computation of the thermal homogenized properties, through the EBH method, was added to the topX.m code. Only the AH method is used for microstructure optimization. The optimization cycle is schematically described in Fig. 3.2.

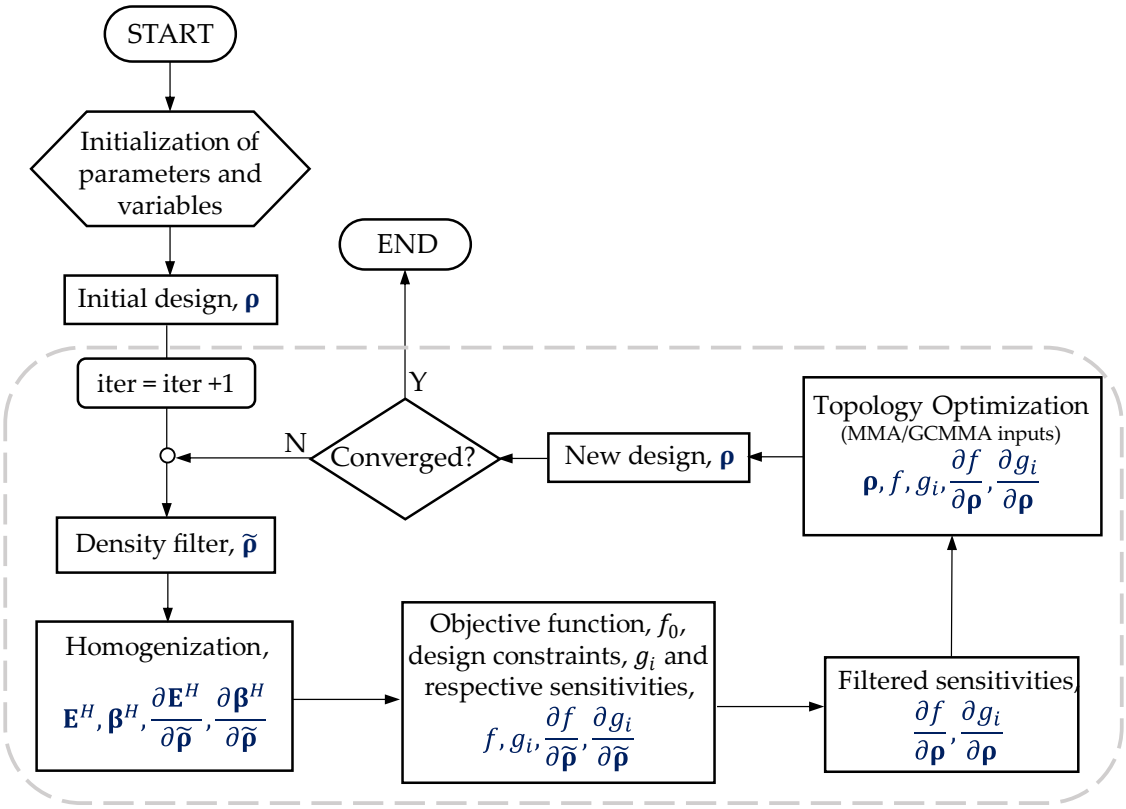

Figure 3.2. – Flowchart illustrating the optimization algorithm for microstructure MMTO with extreme thermoelastic properties.

3.2.1 Problem Formulation

The density fields $\tilde{\boldsymbol{\rho}}_1$ and $\tilde{\boldsymbol{\rho}}_2$ are filtered to avoid mesh-dependency and checker-board patterns. Using a density filter [127], they are given by:

$$\tilde{\rho}_{m,e} = \frac{1}{\sum_{i\in N_e} H_{ei}} \sum_{i\in N_e} H_{ei}\rho_{m,e}\,, H_{ei} = \max\{0, r_{min} - \|y_e - y_i\|\} \tag{3.12}$$

where N_e is the set of elements i, neighbours of element e, r_{min} is the filter radius, and $\|y_e - y_i\|$ is the center-to-center distance between element i and e. Index $m \in [1,2]$ is used to identify the variable type, either to define the topology ($m = 1$) or to select material ($m = 2$). The filtered densities represent the physical design and are used to compute material properties, the objective, and constraint functions.

Since it is assumed that the microstructure is periodically repeated, the filtering of densities at each element located at the UC border also consider the densities of elements located at the UC opposite sides, see Fig. 2.8.

Material symmetry is conveniently enforced by grouping every design element that are opposite toward the symmetry axes, allowing computational savings. Although the time spent computing homogenized properties (and their sensitivities) is only slightly reduced by symmetry, important computational savings exist when the optimizer runs. Solving the MMA subproblem is comparatively about 10 times faster by having, for instance, one quarter of the design variables in 100 × 100 meshes. This approach contrasts with the method of modelling only a portion of the microstructure, as the entire UC domain is modelled for FE analysis. However, it requires only a quarter or half of the design variables for orthotropic designs, depending on the number of symmetry axes considered (two or one, see Figs. 3.3a and 3.3b, respectively). For the anisotropic case, all design variables are included (see Fig. 3.3c). Finally, notice that this grouping approach has an impact on the sensitivity analysis, as it will be later detailed in Section 3.2.3.

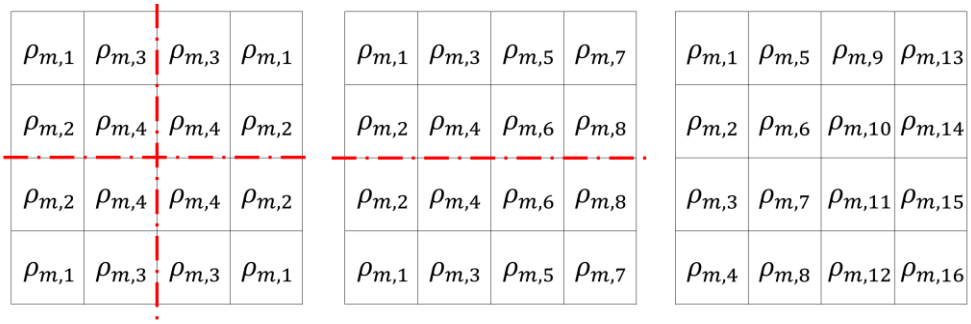

Figure 3.3 – Discretization of an illustrative UC (4×4 mesh): (a) with grouping of variables with two symmetry axes, (b) one symmetry axis and (c) without the grouping of variables, no symmetry is enforced.

Two objective functions are individually presented in this section, with the goal of attaining NPR and NTE, respectively. Each one depends on the coefficients of either the effective stiffness tensor or the CTE tensor. These objective functions will be then considered together in the next section as part of a multiobjective formulation.

The objective function that favours the PR minimization, f_v, to attain the desired auxetic behaviour, is presented as:

$$f_v = E^H_{1122} - \psi_1 0.8^i (E^H_{1111} + E^H_{2222}) - \psi_2 0.95^i (E^H_{1212}) \tag{3.13}$$

Noteworthy is the fact that several objective functions have been tested and reported in the literature to minimize PR [67,100], but this type of objective function in Eq. (3.13) has become known by its good convergence properties and effectiveness, e.g., see [62]. The index

i here is the design iteration number. Since i is used as a power of either 0.8 or 0.95 coefficients, it means that either bulk or shear stiffness maximization, respectively, is to be prioritized during the first design iterations. This strategy helps preventing excessive compliance or even collapse/absence of the microstructure. As i increases, the minimization of the first term E^H_{1122} becomes dominant, being expected that design changes lead to NPR. The present framework takes advantage of this commonly used strategy to obtain auxetics, but it adds novelty in the way that the proposed objective function in Eq. (3.13) may impart either bulk or shear stiffness by setting ψ parameters to 0 or 1. When $\psi_1 = 1$ and $\psi_2 = 0$ bulk-driven designs are favoured, while shear-driven designs are obtained by setting $\psi_1 = 0$ and $\psi_2 = 1$. The 0.95 factor in Eq. (3.13) is proposed here, based on prior numerical experience in obtaining shear resistant auxetics.

The objective function that minimizes the CTE, f_α, is given by Eq. (3.14).

$$f_\alpha = \sum_{i=1}^{\psi_3} \alpha^H_{ii} \tag{3.14}$$

Here, α^H_{ii} are the components of the homogenized CTE, easily obtained from the tensor product $\alpha^H_{ij} = \left(E^H_{ijkl}\right)^{-1}\beta^H_{kl}$. Index ψ_3 can be 1 or 2 depending on the problem to be solved, as it will be detailed in Section 3.4.1. For example, the objective defined in Eq. (3.15) is used to enhance thermoauxeticity specifically along the horizontal direction.

$$f_\alpha = \alpha^H_{11} \tag{3.15}$$

As for the constraints considered in the optimization problem, these can be grouped into three different categories as follows: (1) volume, (2) stiffness; and (3) homogenized coefficients, as detailed bellow.

Firstly, the volume constraint is defined according to Eq. (3.16)

$$g_1 = \frac{\frac{1}{|Y|}\sum_{e=1}^{N} V_e \tilde{\rho}_{1,e}}{V^+} - 1 \tag{3.16}$$

where, the numerator is the total volume V_e of the FE, here considered unitary, and V^+ is the upper bound fixed for the global volume fraction of the UC solid part, regardless of the amount of each material phase. Although individual base material volume fractions could be constrained, as often seen in the related previous works [75,77–81], doing so unduly limits

design freedom. The proportions between the two solids to attain NTE should be optimized rather than fixed, as achieved in the present work.

Regarding the stiffness constraints, these are usually activated when extremizing thermoelastic properties of composites, as the auxetic and thermoauxetic behavior is due to the mechanism-like deformation of the microstructure, associated with lower density. Here two distinct paradigms regarding the stiffness requirements are explored. One is bulk-driven, where the emphasis is placed on ensuring considerable bulk modulus to the metamaterial. Another is shear-driven, where the metamaterial is designed to be stiffer in shear. Depending on the paradigm, constraints are applied to either bulk or shear stiffness to guide the optimization process after the initial stage of design iterations.

The constraint functions g_2 and g_3, shown in Eq. (3.17), are used to impose a lower bound, K^-, and an upper bound, K^+, on the bulk modulus, K, respectively.

$$g_2 = 1 - \frac{K}{K^-} \;\; ; \; g_3 = \frac{K}{K^+} - 1 \tag{3.17}$$

where K^- is set as 1% of the Young's modulus of the stiffest material phase, E^1. As regards K^+, it is set as $\phi_1 K^-$. The bulk modulus for the 2D case is defined as $K = \frac{1}{4}(E^H_{1111} + E^H_{1122} + E^H_{2211} + E^H_{2222})$. For anisotropic materials, the use of this measure has been interpreted as quasi-effective bulk modulus, see [107].

On one hand, the lower bound in Eq. (3.17) is active when the CTE is minimized. On the other hand, minimizing the objective function in Eq. (3.13) means maximizing stiffness during the first design iterations, as previously explained. However, the more such stiffness increases, the less negative is the PR. This is the motivation for using an upper bound constraint on bulk stiffness, which is active when PR is minimized. The results shown later in Section 3.4.1 will confirm this trend. Furthermore, having bulk stiffness limited to a relatively small range, i.e., $K \in [K^-, K^+]$, ensures a fairer comparison among the solutions present in the approximated Pareto front.

For the shear-driven design, the stiffness measure is simply replaced by the shear modulus, given by $G = E^H_{1212}$ for both orthotropic and anisotropic metamaterials [106]. The respective constraint function presents a lower bound, $\phi_2 G^1$, i.e.,

$$g_4 = 1 - \frac{G}{\phi_2 G^1} \tag{3.18}$$

where G^1 is the shear modulus of the stiffest material phase. In this case, unlike the bulk-driven design, only a lower bound is required because this constraint is active for both PR and CTE minimizations. Subsequently, this also ensures a consistent comparison of the solutions present in the approximated Pareto front. For the sake of smooth convergence and initial design feasibility, a continuation approach for both parameters ϕ_1 and ϕ_2, is adopted and detailed in the results subsection.

Thirdly, the constraints applied on homogenized coefficients are detailed. Constraints involving specific homogenized coefficients, from either $\mathbf{E}^H$ or $\boldsymbol{\alpha}^{\mathrm{H}}$ tensors, are here used, in part to impose tensor symmetries (cubic, orthotropy, and isotropy) in conjunction with the strategy for grouping density design variables, as described in Fig. 3.3.

Regarding the elasticity tensor, $\mathbf{E}^H$, cubic and orthotropic symmetries are considered in the results of Section 3.4.1, besides an anisotropic case. In cubic symmetry there is a unique PR, as $E^H_{1111} = E^H_{2222}$. In the orthotropic case, where $E^H_{1111} \neq E^H_{2222}$, two Poisson's ratios can be calculated, i.e., the transverse strain measured in the 2D metamaterial differs, depending on the applied load direction (horizontal or vertical). Recalling Section 2.2, the PR's are defined as: $\nu_{12} = E^H_{1122}/E^H_{1111}$ (defined from an applied vertical load) and $\nu_{21} = E^H_{2211}/E^H_{2222}$ (from an applied horizontal load).

The constraint function in Eq. (3.19) is used to impose cubic symmetry. This ensures that E^H_{1111} and E^H_{2222} differ by 1% (maximum), by setting $\epsilon_1 = 0.01$. The normalization constant E^1 is set as the Young's Modulus of material phase 1.

$$g_5 = \frac{(E^H_{1111} - E^H_{2222})^2}{E^1} - \epsilon_1 \tag{3.19}$$

In the orthotropic case studied here, the goal is to obtain a metamaterial offering different auxetic responses depending on the applied load direction (horizontal or vertical). As an example, here it is considered that ν_{21} must be 40% of ν_{12}. Since symmetry requires $E^H_{2211} = E^H_{1122}$, the needed constraint on homogenized elastic coefficients would be $E^H_{1111} = 0.4E^H_{2222}$. However, an equality constraint is here treated as two inequalities to be handled by the optimizer chosen. Accordingly, the constraint functions g_6 and g_7 are defined in Eq. (3.20), with a lower and an upper bound properly relaxed, i.e., $\epsilon_2^- = 0.39$ and $\epsilon_2^+ = 0.41$, respectively.

$$g_6 = \frac{E^H_{1111}}{\epsilon_2^+ E^H_{2222}} - 1 \; ; \; g_7 = 1 - \frac{E^H_{1111}}{\epsilon_2^- E^H_{2222}} \tag{3.20}$$

Here, the thermoelastic tensor, $\boldsymbol{\alpha}^{\mathrm{H}}$, is considered to be orthotropic or isotropic. CTE minimization of metamaterials is a highly non-linear problem and, when $\boldsymbol{\alpha}^{\mathrm{H}}$ is left anisotropic, poor microstructural connectivity is obtained, making design interpretation difficult or impractical [76]. Interestingly, an optimized metamaterial design may have E_{ijkl}^{H} anisotropic with α_{ij}^{H} isotropic, as shown later for a chiral design. Therefore, to impose $\boldsymbol{\alpha}^{\mathrm{H}}$ isotropic ($\alpha_{11}^{H} = \alpha_{22}^{H}$ and $\alpha_{12}^{H} = 0$), constraint functions g_8 and g_9 are defined in Eq. (3.21) and Eq. (3.22), respectively.

$$g_8 = \frac{(\alpha_{11}^{H} - \alpha_{22}^{H})^2}{\alpha^1} - \epsilon_1 \tag{3.21}$$

$$g_9 = \left(\frac{\alpha_{12}^{H}}{\epsilon_3}\right)^2 - 1 \tag{3.22}$$

Constraint function g_8 is equivalent to g_5, using also $\epsilon_1 = 0.01$ and the normalization constant is α^1 (CTE of material 1). Constraint function g_9 ensures that the component α_{12}^{H} does not exceed ϵ_3. Poor convergence was observed when using ϵ_3 values close to zero. Therefore, $\epsilon_3 = 1$ is chosen, which is already a very small quantity comparing to the CTE of the base materials. Notice that when symmetries are imposed by grouping design variables, as seen in Fig. 3.3, it warrants $\alpha_{12}^{H} = 0$ and thus constraint g_9 can be omitted.

Allowing $\boldsymbol{\alpha}^{\mathrm{H}}$ to be orthotropic, it was observed that the CTE in one direction, say horizontal α_{11}^{H}, can be "hugely" minimized at the expense of turning the CTE in the orthogonal direction α_{22}^{H} a very large positive number. Even though the metamaterial could respond with α_{11}^{H} negative, hardly it would be appealing having a positive α_{22}^{H} greater than the positive CTE of the base material 1 or 2. Therefore, in the present framework a reasonable upper limit of α^1 (material 1 CTE) is imposed to α_{22}^{H}, see Eq. (3.23):

$$g_{10} = \frac{\alpha_{22}^{H}}{\alpha^1} - 1 \tag{3.23}$$

Finally, it is worth mentioning that, in the previous constraint functions, there was the concern of skipping any coefficient α_{ij}^{H} from figuring as denominator because it might be zero.

3.2.2 Multiobjective Optimization

The design of anepectic materials can be posed as a multiobjective TO problem, which appears as novelty here, leading to an original wide range of results shown later. The very essence of this problem statement is searching for nondominated solutions or points in the objective function space, defined by the vector of functions $\mathbf{f}(\boldsymbol{\rho}) = [f_\nu(\boldsymbol{\rho}) \quad f_\alpha(\boldsymbol{\rho})]$, meaning that is not possible to improve one function, without deteriorating the other. Here, a scalarization method is used to combine these two objective functions into one, enabling the problem to be solved using a single-objective optimization algorithm, namely GCMMA [16]. In particular, the weighted sum method is adopted due to the large number of variables involved in the problem definition, the availability of derivatives and, of course, its simplicity. Consequently, the objective function for single-objective associated with the optimization problem is given by Eq. (3.24):

$$f = \omega \frac{f_\nu}{\nu^*} + (1 - \omega) \frac{f_\alpha}{\alpha^*} \tag{3.24}$$

where each objective function is weighted by setting a ω value between 0 and 1, and ν^* and α^*, are normalization factors, defined as explained bellow.

When using a scalarization method, both objectives should be first scaled or normalized, so that both have similar value ranges, and only then weights should be applied, allowing a direct interpretation of these weights. This is particularly important here, as f_ν is several orders of magnitude higher than f_α. Normalization is used to scale the objective functions, such that they have values approximately between 0 and 1 [157]. Generally, in this normalization, the amplitude between the maximum, f_i^{max}, and the minimum, f_i^{min}, values of a function i is used. Since this is a biobjective problem, the value of f_i^{max} corresponds to the value of function i for the point that minimizes function f_j, i.e., $f_i^{max} = f_i(\mathbf{x}_j^*)$, being $\mathbf{x}_j^*$ the point of the design space that minimizes function j, also interpreted as an extreme point of the Pareto optimal set. To determine all the needed data for normalization, each objective function is minimized separately, see Eq. (3.25) and Eq. (3.26). For comprehension, Fig. 3.4 highlights the evaluated amplitudes of interest as blue and green line segments.

$$\min f_\nu \rightarrow \mathbf{x}_\nu^* \text{ such that } f_\nu^{min} = f_\nu(\mathbf{x}_\nu^*) \text{ and } f_\alpha^{max} = f_\alpha(\mathbf{x}_\nu^*) \tag{3.25}$$

$$\min f_\alpha \rightarrow \mathbf{x}_\alpha^* \text{ such that } f_\nu^{max} = f_\nu(\mathbf{x}_\alpha^*) \text{ and } f_\alpha^{min} = f_\alpha(\mathbf{x}_\alpha^*) \tag{3.26}$$

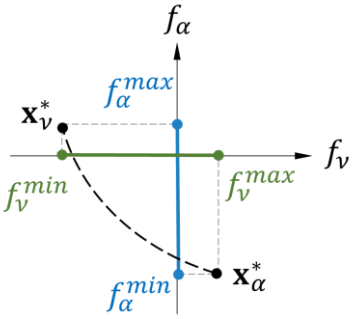

Figure 3.4 – Adopted normalization scheme, based on the amplitude between maximum and minimum function values.

The guidelines given to GCMMA users include, for example, the objective function and constraint values lying in the interval between 1 and 100. Taking this into account, the problems in Eq. (3.25) and Eq. (3.26) are solved resorting to the following normalization factors: 1×10^6 and 10, respectively. Consistently, to ensure that Eq. (2.24) also follows this recommendation, the factors used to normalize the function, ν^* and α^*, are also scaled through division by 100, i.e., $\nu^* = \left(f_\nu^{max} - f_\nu^{min}\right)/100$ and $\alpha^* = \left(f_\alpha^{max} - f_\alpha^{min}\right)/100$.

Finally, the optimization problem formulation to design microstructures with anepectic behavior can be stated as:

$$\begin{aligned} &\min_{\rho_{m,e}} f \\ &s.t.: \begin{cases} g_i \leq 0, & \text{with } i \in \mathbb{N}: 1 \leq i \leq 10 \\ \rho_{min} \leq \rho_{m,e} \leq 1 & m = 1,2;\ e = 1,2,\dots,N; \rho_{min} = 10^{-3} \end{cases} \end{aligned} \tag{3.27}$$

where f is the objective function, defined in Eq. (3.24), according to the weight sum method.

The problem constrains g_i are defined from a set of 10 possible constraints, detailed in the previous subsection. Depending on the problem solved, different sets of constraints may be considered, as later clarified in Table 3.2 of Section 3.4.1.

3.2.3 Sensitivity Analysis

GCMMA requires the first derivatives of the objective and constraints functions, which depend on the derivatives of the homogenized properties w.r.t. the filtered densities, $\tilde{\boldsymbol{\rho}}_1$ and $\tilde{\boldsymbol{\rho}}_2$, i.e, $\frac{\mathrm{d}E_{ijkl}^H}{\mathrm{d}\tilde{\rho}_{m,e}}$ and $\frac{\mathrm{d}\beta_{ij}^H}{\mathrm{d}\tilde{\rho}_{m,e}}$. These sensitivities can be obtained through the adjoint method, and the detailed development is presented in Appendix A. The final expressions for such derivatives are the following (e.g., see [5,158]):

$$\frac{\mathrm{d}E^H_{ijkl}}{\mathrm{d}\tilde{\rho}_{m,e}} = \frac{1}{|Y|}\int_Y \frac{\partial E_{rspq}}{\partial \tilde{\rho}_{m,e}}\left(\delta_{pk}\delta_{ql} - \frac{\partial \chi_p^{kl}}{\partial y_q}\right)\left(\delta_{ir}\delta_{js} - \frac{\partial \chi_r^{ij}}{\partial y_s}\right)\mathrm{d}Y \tag{3.28}$$

$$\begin{aligned}\frac{\mathrm{d}\beta^H_{ij}}{\mathrm{d}\tilde{\rho}_{m,e}} = &\frac{1}{|Y|}\int_Y \frac{\partial E_{rspq}}{\partial \tilde{\rho}_{m,e}}\left(\alpha_{pq} - \frac{\partial \Upsilon_p}{\partial y_q}\right)\left(\delta_{ir}\delta_{js} - \frac{\partial \chi_r^{ij}}{\partial y_s}\right)\mathrm{d}Y \\ &+ \frac{1}{|Y|}\int_Y E_{rspq}\frac{\partial \alpha_{pq}}{\partial \tilde{\rho}_{m,e}}\left(\delta_{ir}\delta_{js} - \frac{\partial \chi_r^{ij}}{\partial y_s}\right)\mathrm{d}Y\end{aligned} \tag{3.29}$$

where $\frac{\partial E_{rspq}}{\partial \tilde{\rho}_{m,e}}$ and $\frac{\partial \alpha_{pq}}{\partial \tilde{\rho}_{m,e}}$ are trivially obtained through the direct differentiation of the interpolation law in (3.1) and (3.2). Since densities, $\tilde{\rho}_{1,e}$ or $\tilde{\rho}_{2,e}$, are assumed uniform over each FE discretizing the UC domain, $|Y|$, the index $e \in [1, \dots, N]$ goes through all densities/elements. Indexes $i, j, k, l, r, s, p, q \in \{1,2\}$ are related to the coordinate system directions, considering 2D problems.

The derivative of the homogenized coefficient of thermal expansion, α^H_{ij}, w.r.t. $\tilde{\boldsymbol{\rho}}$ is given by:

$$\frac{\mathrm{d}\alpha^H_{ij}}{\mathrm{d}\tilde{\rho}_{m,e}} = -C^H_{ijrs}\frac{\mathrm{d}E^H_{rszn}}{\mathrm{d}\tilde{\rho}_{m,e}}C^H_{znkl}\beta^H_{kl} + C^H_{ijkl}\frac{\mathrm{d}\beta^H_{kl}}{\mathrm{d}\tilde{\rho}_{m,e}} \tag{3.30}$$

where $C^H_{ijkl} = \left(E^H_{ijkl}\right)^{-1}$ is the homogenized compliance tensor.

Notice that the variables updated by the GCMMA are the unfiltered ones, i.e., $\boldsymbol{\rho}_1$ and $\boldsymbol{\rho}_2$. Therefore, the sensitivities w.r.t. $\boldsymbol{\rho}$ for each function f in the optimization problem stated in Eq. (3.27) are required as input by the optimizer and can be calculated using the chain rule:

$$\frac{\mathrm{d}f}{\mathrm{d}\rho_{m,e}} = \sum_{i\in N_e}\frac{\mathrm{d}f}{\mathrm{d}\tilde{\rho}_{m,i}}\frac{\mathrm{d}\tilde{\rho}_{m,i}}{\mathrm{d}\rho_{m,e}} = \sum_{i\in N_e}\frac{\mathrm{d}f}{\mathrm{d}\tilde{\rho}_{m,i}}\left[\frac{r_{min} - \|y_e - y_i\|}{\sum_{m\in N_i}\max\{0, r_{min} - \|y_e - y_i\|\}}\right] \tag{3.31}$$

In the case where the design variables are grouped together, to ensure material symmetries (recall Section 3.2.1), the derivative of the homogenized property is expressed as a summation of contributions of each element whose density has been grouped. The volume derivative w.r.t. $\tilde{\boldsymbol{\rho}}$, is equal to the element volume V_e and, since all elements of the UC are equal, such derivative is always the same. In the case where the elements densities are grouped as design variables, the volume derivative is simply multiplied by the number of

grouped elements, N_C. Here, $N_C = 4$ or 2 to reflect the symmetry conditions of Fig. 3.3a and Fig. 3.3b, respectively.

The derivatives of the remaining functions are easily obtained by derivation rules and are summarized in Table 3.1.

Table 3.1. – Sensitivities w.r.t. filtered densities $\tilde{\boldsymbol{\rho}}_m$ required to solve the optimization problem stated in Eq. (3.27).

Function	Derivative
f_v (Eq. 3.13)	$\frac{\mathrm{d}f_v}{\mathrm{d}\tilde{\rho}_{m,e}} = \frac{\mathrm{d}E^H_{1122}}{\mathrm{d}\tilde{\rho}_{m,e}} - \psi_1 0.8^i \left(\frac{\mathrm{d}E^H_{1111}}{\mathrm{d}\tilde{\rho}_{m,e}} + \frac{\mathrm{d}E^H_{2222}}{\mathrm{d}\tilde{\rho}_{m,e}}\right) - \psi_1 0.95^i \frac{\mathrm{d}E^H_{1212}}{\mathrm{d}\tilde{\rho}_{m,e}}$
f_α (Eq. 3.14)	$\frac{\mathrm{d}f_\alpha}{\mathrm{d}\tilde{\rho}_{m,e}} = \frac{\mathrm{d}\alpha^H_{11}}{\mathrm{d}\tilde{\rho}_{m,e}} + \frac{\mathrm{d}\alpha^H_{22}}{\mathrm{d}\tilde{\rho}_{m,e}}$
$V = \frac{1}{\lvert Y\rvert}\sum_{e=1}^{N} V_e \tilde{\rho}_{1,e}$	$\frac{\mathrm{d}V}{\mathrm{d}\tilde{\rho}_{m,e}} = \begin{cases} V_e, & if\ m = 1 \\ 0, & if\ m = 0 \end{cases}$
g_5 (Eq. 3.19)	$\frac{\mathrm{d}g_4}{\mathrm{d}\tilde{\rho}_{m,e}} = \frac{2}{E^1}\left(\frac{\mathrm{d}E^H_{1111}}{\mathrm{d}\tilde{\rho}_{m,e}} - \frac{\mathrm{d}E^H_{2222}}{\mathrm{d}\tilde{\rho}_{m,e}}\right)(E^H_{1111} - E^H_{2222})$
g_6 and g_7 (Eq. 3.20)	$\frac{\mathrm{d}g_6}{\mathrm{d}\tilde{\rho}_{m,e}} = \frac{\frac{\mathrm{d}E^H_{1111}}{\mathrm{d}\tilde{\rho}_{m,e}} E_{2222} - E_{1111}\frac{\mathrm{d}E^H_{2222}}{\mathrm{d}\tilde{\rho}_{m,e}}}{\epsilon_2^+ {E^H_{2222}}^2}; \frac{\mathrm{d}g_7}{\mathrm{d}\tilde{\rho}_{m,e}} = -\frac{\mathrm{d}g_6}{\mathrm{d}\tilde{\rho}_{m,e}}$
g_8 (Eq. 3.21)	$\frac{\mathrm{d}g_8}{\mathrm{d}\tilde{\rho}_{m,e}} = \frac{2}{\alpha^1}\left(\frac{\mathrm{d}\alpha^H_{11}}{\mathrm{d}\tilde{\rho}_{m,e}} - \frac{\mathrm{d}\alpha^H_{22}}{\mathrm{d}\tilde{\rho}_{m,e}}\right)(\alpha^H_{11} - \alpha^H_{22})$
g_9 (Eq. 3.22)	$\frac{\mathrm{d}g_5}{\mathrm{d}\tilde{\rho}_{m,e}} = \frac{2}{\epsilon_3^2}\frac{\mathrm{d}\alpha^H_{12}}{\mathrm{d}\tilde{\rho}_{m,e}}\alpha^H_{12}$

3.2.4 Scale-Size Effects

In practical applications, the hypothesis considered in the homogenization methods may not be met. This raises awareness about the importance of studying scale-size effects on the effective thermoelastic properties of periodic metamaterials. For this purpose, the composite material is tested with a finite number of repetitions of the UC, to evaluate to what extent the properties calculated by the homogenization theory compare with the simulations of the finite composite.

The Representative Volume Element (RVE) method allows for full-size characterization of composite materials, avoiding the need for geometric periodicity when the RVE is

sufficiently large [91,92]. Homogeneous BCs are then applied to the resulting sample, now seen as periodically finite. Either a displacement field rendering uniform strain (Dirichlet-type BCs) or distributed forces rendering uniform stress (Neumann-type BCs) is applied. From such micromechanical standard tests, the strain energy of the RVE is computed, and consequently, the apparent properties of the equivalent homogeneous material, can be obtained. Scale-size effects on the predicted properties likely appear due to boundary effects, depending on the number of UC's repeated inside the RVE. When the periodic composite material can be replaced by a homogeneous medium, it implies that each body average in Eq. (3.32) is equal to the equivalent homogeneous medium and the RVE [91,110]:

$$\bar{\sigma}_{ij} = \frac{1}{|\Psi|}\int_{\Psi} \sigma_{ij}^{0} \mathrm{d}\Psi \,; \bar{\varepsilon}_{ij} = \frac{1}{|\Psi|}\int_{\Psi} \varepsilon_{ij}^{0} \mathrm{d}\Psi \,; \tag{3.32}$$

In Eq. (3.32), $|\Psi|$ denotes the RVE's domain volume (area in 2D), the superscript $\bar{}$ stands for the body average of stresses and strains. Furthermore, σ_{ij}^{0} and ε_{ij}^{0} are the uniform stresses and strains in the RVE domain Ψ, respectively. When the RVE domain is discretized, these values are assumed constant at each element.

Unlike the homogenization techniques, based on rigorous mathematical theory, the estimates through the RVE method are based upon numerical simulations, to investigate how the apparent properties converge to homogenization, with an increasing scale factor n. This factor is defined as $n = D/d$ [93], and considering the dimension D as unitary, i.e., $|\Psi| = 1$, n can be interpreted as the number of repetitions of the UC included in the RVE, as showed in Fig. 3.5. Recall that the effective properties in Eq. (3.8) and Eq. (3.9) are computed when $n \to +\infty$. Hence, it is predictable that the results will be more accurate toward homogenization, as the scale factor increases. Furthermore, instead of computing the average in the RVE domain (i.e., outer dashed line), $|\Psi|$ can be replaced by the volume of the UC itself, $|Y|$, and then the averaging in Eq. (3.32) is done only in the UC located at the center of the RVE, i.e., enclosed by the inner fine dotted line box seen in Fig. 3.5. This will mitigate the boundary effects and the corresponding results will converge faster to the homogenization predictions.

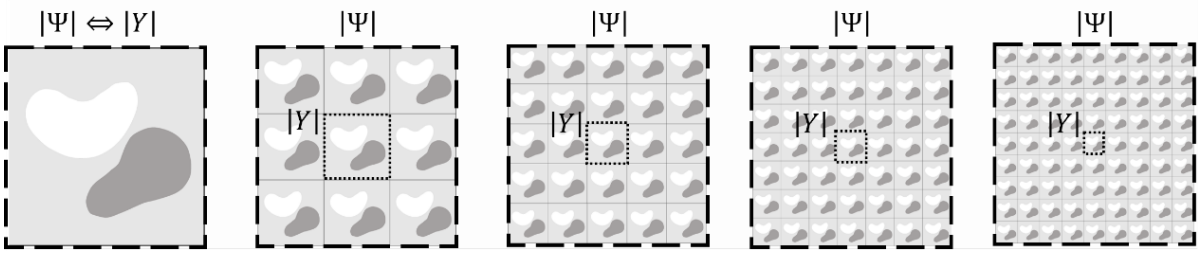

Figure 3.5. – RVE containing n×n UCs (n ranges from 1 to 9, only considering odd numbers).

It is shown in Coelho et al. [94] that the Neumann-type BCs underestimates the apparent properties of porous materials as result of applying forces on void modelled regions of very low stiffness, placed at outer boundaries. Hence, only Dirichlet-type BCs will be considered here, as it suffices to illustrate the convergence of properties in the RVE method, by applying a standard numerical procedure based on constant strain [159]. The numerical simulations described below are used to investigate how the apparent properties converge with an increasing scale factor n.

Consider the Dirichlet-type BCs, defined as:

$$\mathbf{u}(\mathbf{x})|_{\partial\Psi} = \varepsilon_{ij}^{0(i)}\mathbf{x}|_{\partial\Psi} \tag{3.33}$$

where $\mathbf{u}$ is the displacement vector in the RVE domain Ψ, $\partial\Psi$ is the RVE boundary, ε_{ij}^{0} is the specific unit strain and $\mathbf{x}$ is the spatial position vector. The superscript i is used to denote the application of three-unit test strains (two normal and one shear mechanical test). To estimate the thermoelastic properties an additional thermal load case is considered, i.e., a unit thermal load ($\Delta\mathrm{T} = 1$) corresponding to a thermal strain $\bar{\varepsilon}_{ij}{}^{th} = \alpha_{ij}\Delta\mathrm{T}$.

The average stress and strain of the homogeneous thermoelastic medium follow the Hooke's law for thermoelasticity, given by Eq. (3.34).

$$\bar{\sigma}_{ij} = E_{ijkl}^{RVE}\bar{\varepsilon}_{ij}{}^{m} = E_{ijkl}^{RVE}\left(\bar{\varepsilon}_{kl} - \bar{\varepsilon}_{kl}{}^{th}\right) = E_{ijkl}^{RVE}\bar{\varepsilon}_{kl} - \beta_{ij}^{RVE}\Delta\mathrm{T} \tag{3.34}$$

where the superscripts m and th denotes the mechanical and thermal part of the total strain, respectively. E_{ijkl}^{RVE} and β_{ij}^{RVE} are the stiffness and thermal stress tensors, computed through the RVE method, respectively. The constitutive constants in these tensors, E_{ijkl}^{*} and β_{ij}^{*}, are computed resorting to the following relation between averaged stresses and strains:

$$\begin{Bmatrix}\bar{\sigma}_{11}\\ \bar{\sigma}_{22}\\ \bar{\sigma}_{12}\end{Bmatrix} = \begin{bmatrix}E_{1111}^{*} & E_{1122}^{*} & E_{1112}^{*}\\ E_{2211}^{*} & E_{2222}^{*} & E_{2212}^{*}\\ E_{1211}^{*} & E_{1222}^{*} & E_{1212}^{*}\end{bmatrix}\begin{Bmatrix}\bar{\varepsilon}_{11}\\ \bar{\varepsilon}_{22}\\ \bar{\varepsilon}_{12}\end{Bmatrix} - \begin{bmatrix}\beta_{11}^{*}\\ \beta_{22}^{*}\\ \beta_{12}^{*}\end{bmatrix}\Delta\mathrm{T} \tag{3.35}$$

The fundamental three-unit tests considered in Eq. (3.33) can provide full characterization of the elastic tensor. Let us consider, e.g., the first load case, $\bar{\varepsilon}_{ij} = [1\ 0\ 0]^{\mathrm{T}}$. Using commercial software (e.g. ANSYS®), the averages stresses, i.e., $\bar{\sigma}_{ij}$, are computed and the first row of coefficients in Eq. (3.35) is calculated. The same reasoning is applied for the remaining elastic components.

To predict the thermoelastic properties, the average strain on the microstructure is evaluated through the application of a unitary temperature differential, $\Delta\mathrm{T} = 1$, keeping the domain fully constrained or clamped, i.e., $\bar{\varepsilon}_{ij} = [0\ 0\ 0]$. This way, the thermal stress coefficients can be straightforwardly obtained from the resulting relationship $\bar{\sigma}_{ij} = -\beta_{ij}^{RVE}$.

3.3 Truss Topology Optimization Framework

Several studies found in the literature refer to materials as "lattice", "frame-like cellular", "truss" among other similar terms when, in fact, the design domain is being discretized with continuum-like elements, considering low relative density. Here, the discretization of a truss-like microstructure based on the Ground Structure (GS) approach is investigated. The advantage of considering truss-like microstructure lies in the fact that auxetic metamaterials usually present mechanism-like behaviour, better captured by a discrete discretization. Moreover, this type of discretization enables the ribs (in this case, bars) to be composed of a single material, rather than combining two interlaced materials within the same rib, which simplifies the fabrication process. To that purpose, in addition to the extensions applied in the commercial codes mentioned in the Section 3.2, a truss-like discretization of the UC was implemented in the context of this thesis.

The standard homogenization formulas (recall Section 2.3) were derived for continuum structures. Therefore, it is necessary to consider the modelling of trusses within a continuum framework. For that purpose, each bar member in the GS is treated as a two-node continuum element that only have stiffness in the longitudinal direction and that have zero shear stiffness. In this way, the bar element follows the usual stress-strain for an elastic material.

Consider an arbitrary bar element represented in Fig. 3.6, in the local coordinate system $y_1' y_2'$, defined between node i and j, with length L and rotated θ degrees w.r.t the global coordinate system $y_1 y_2$. Note that here, the superscript $'$ represents the quantities expressed in the local coordinate system.

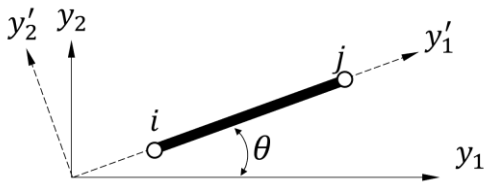

Figure 3.6. – Arbitrary bar element in the local coordinate system.

To solve the homogenization Eqs. (3.3)-(3.9), the strain-displacement matrix, $\mathbf{B}_e$ and the stiffness matrix in the global coordinate system, $\mathbf{E}_e$, must be defined. The shape functions, N_i, with $i = 1,2$ of the bar element are given by Eq. (3.36).

$$N_1 = \frac{L - {y_1}'}{L}; N_2 = \frac{{y_1}'}{L} \tag{3.36}$$

where ${y_1}'$ is the position on the horizontal axe of the local coordinate system, and $0 \leq y_1' \leq L$. Since the local CS of the bar is not aligned with the global CS, the shape functions N_i are functions of θ. The derivatives of the shape functions w.r.t. the global CS are given by Eq. (3.37).

$$\begin{cases} \dfrac{\partial N_1}{\partial y_1} = -\dfrac{\cos(\theta)}{L}; \dfrac{\partial N_1}{\partial y_2} = -\dfrac{\sin(\theta)}{L} \\ \dfrac{\partial N_2}{\partial y_1} = \dfrac{\cos(\theta)}{L}; \dfrac{\partial N_2}{\partial y_2} = \dfrac{\sin(\theta)}{L} \end{cases} \tag{3.37}$$

Following the detailed formulation of FE found in [160], the strain-displacement matrix, $\mathbf{B}_e$, and the transformation matrix $\mathbf{T}_e$ are given by Eqs. (3.38) and (3.39), respectively. The transformation matrix relates strain and stress expressed in the global CS with the local CS, i.e., $\boldsymbol{\varepsilon} = \mathbf{T}\boldsymbol{\varepsilon}'; \boldsymbol{\varepsilon}' = \mathbf{T}^{-}\boldsymbol{\varepsilon}$ and $\boldsymbol{\sigma} = \mathbf{T}^{T}\boldsymbol{\sigma}'$; $\boldsymbol{\sigma}' = \mathbf{T}^{-T}\boldsymbol{\sigma}$.

$$\mathbf{B}_e = \frac{1}{L}\begin{bmatrix} -c & 0 & c & 0 \\ 0 & -s & 0 & s \\ -s & -\mathrm{c} & s & \mathrm{c} \end{bmatrix} \tag{3.38}$$

$$\mathbf{T}_e = \begin{bmatrix} c^2 & s^2 & cs \\ s^2 & c^2 & -cs \\ -2cs & 2cs & c^2 - s^2 \end{bmatrix} \tag{3.39}$$

where $c = \cos(\theta), s = \sin(\theta)$.

Note that the matrix given in Eq. (3.39) is a particular form valid in two dimensions, for a plane stress state and for Cartesian coordinates. Also, the transformation of strains and

stresses can be represented graphically by the Mohr circles. A more detailed information can be found in [160].

The constitutive matrix of a bar element in the local CS (aligned with the bar) is given by Eq. (3.40), which corresponds to a material with stiffness in only one direction.

$$\mathbf{E}'_e = \begin{bmatrix} E & 0 & 0 \\ 0 & 0 & 0 \\ 0 & 0 & 0 \end{bmatrix} \tag{3.40}$$

where E is the Young Modulus of the material, considered to be isotropic.

Finally, the stiffness tensor for any arbitrary bar FE is given by Eq. (3.41), and the 2-node bar element can easily be treated as a continuum setting and implemented in the homogenization formulation described in Section 2.3.

$$\mathbf{E}_e = \mathbf{T}^T \mathbf{E}'_e \mathbf{T} \tag{3.41}$$

Note that when the microstructure is discretized using bar elements, the volume $|Y|$ of the microstructure is considered as the area of the UC. This arises because, although the dimensions within the UC tend asymptotically to zero, the relative density of the UC remains constant, as the volume occupied by the bars is proportional to the area of the UC [161].

For the truss-like metamaterials, the UC domain is discretized with bar FE, shown in Fig. 3.7. This represents a considerable reduction in the number of FE compared to the continuum discretization. A multimaterial setting is considered as well, with two design variables per each design FE, i.e., $\rho_{1,e}$ and $\rho_{2,e}$. The cross-sectional area of the bar elements is added as a design variable, however, to prevent the problem from being dimensional dependent, a scale factor S_A is considered. Therefore, the area of the bar is $A_e = S_A a_e$, where a_e is a dimensional design variable and varies in the same range as the artificial density variables, i.e., $a_e \in [10^{-3}, 1]$. Finally, in the truss-like discretization, there are three design variables per each element, $\rho_{1,e}$, $\rho_{2,e}$ and a_e. The material interpolation in each FE is done following the exact same reasoning as the continuous discretization, using the extended SIMP scheme defined in Eq. (3.1) and (3.2). Note that in this case it is not required a density filter, as each element corresponds to one of the three material phases. Furthermore, PBCs were considered here as well.

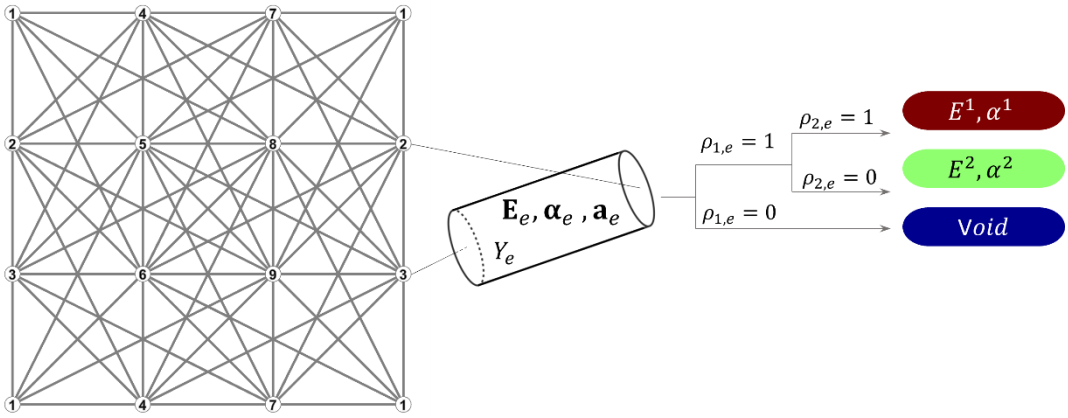

Figure 3.7 – Microscale material model considering a multimaterial truss-like periodic microstructure.

For the truss-like discretization, the formulated problem was more simplified, with the objective focused on designing a microstructure that exhibits both NPR and NTE, without a multiobjective approach or a Pareto-based investigation. Also bear in mind that the reduction of design variables also limits the design space. Finally, the optimization problem can be stated as follows:

$$\begin{aligned} &\min_{\rho_{min} \leq \rho_{m,e}, a_e \leq 1} f \\ &\text{s.t.} \quad \frac{\sum_{e=1}^{N} L_e \tilde{\rho}_{1,e} A_e}{V_i V^+} - 1 \leq 0 \end{aligned} \tag{3.42}$$

where L_e is the length of the bar element e and V_i represents the total volume of the ground structure. In this context, the volume fraction V^+ represents a percentage of the total volume, and the volume constraints in Eq. (3.42) suffice to generate an anepectic microstructure with connectivity. Similar to the continuum problem, the objective function, f, in Eq. (3.42) is defined resorting to the weight sum method, recall Eq. (3.24).

3.4 Results and Discussion

The results from the microscale topology optimization are presented for continuum-like microstructures in Section 3.4.1 and for truss-like microstructures in Section 3.4.2. In Section 3.4.1.1, the influence of different material combinations on the optimal design of thermoelastic metamaterials, specifically focusing on the NTE property, is investigated. Section 3.4.1.2 presents, in the Pareto setting, the conflicting design criteria of NPR and NTE. In Section 3.4.1.3, representative design solutions from Section 3.4.1.2 are used to investigate scale-size effects resorting to the RVE method. In Section 3.4.2 a truss-like metamaterial with both

NPR and NTE is designed to demonstrate the application of this methodology to a UC discretized using the GS approach.

3.4.1 Continuum-like Microstructures

Examples of anepectic metamaterials are presented, featuring varying material volume fractions, microstructural stiffness orientations (bulk- or shear-dominated), and different material symmetries. The main goal is to investigate, for each example, the competition between NPR and NTE when these performances are simultaneously minimized, according to the optimization problem formulations summarized in Table 3.2. Each example has a different initial design, and it was chosen to end up in an auxetic (when only PR is minimized) known from the literature, for the sake of comparison or validation purposes. Therefore, six examples are considered, and named as follows: (A) Star-shaped re-entrant; (B) Chiral cubic; (C) Re-entrant honeycomb; (D) Chiral anisotropic; (E) Arrowhead-shaped 1; (F) Arrowhead-shaped 2. The anepectic metamaterial designs for examples C, E, and F can be regarded as rather novel because they are systematically obtained for the first time in the present work. Previous related works presented only a direct (empirical or analytical) design approach [42,50,162]. In examples C and F, structural responses depend on direction, i.e., the desired counterintuitive effect (say contraction) along the horizontal direction is prevailing under vertical mechanical loading (say compression) or heating. Example D results in a chiral anisotropic metamaterial design, which had been reported in the literature for auxetic behavior alone [107] and never for combined NPR and NTE, as done here. Although examples A and B have been covered before in terms of systematic design [79], they were never studied in the Pareto sense.

In Table 3.2, the examples are organized according to Bulk-driven (star-shaped re-entrant, chiral cubic, re-entrant honeycomb, and chiral) and Shear-driven (arrowhead-shaped 1 and 2). As regards the elasticity tensor, three distinct symmetries are analyzed: cubic, orthotropic, and anisotropic. As regards the thermoelastic property tensor, it is considered either isotropic or orthotropic. For all examples, the UC volume is unitary and meshed with 100×100 unitary four-node isoparametric quadrilateral FEs (Q4). Since each FE has two density variables, there is a total of 20000 design variables, but such total only applies to example D because it is reduced to a quarter in examples A-C, or to a half in E and F (see Table 3.2 along with Fig. 3.3). The proposed MMTO problem is highly non-linear, so the gradient-based optimizer chosen (GCMMA) gets easily stuck in local minima. As an attempt to

escape local minima, the optimization problems are solved considering different combinations of p_1 and p_2 values, see Eqs. (3.1) and (3.2). The seven combinations covered are $p_1 = 3$ with $p_2 = 1, 2, 3$, and $p_1 = 4$ with $p_2 = 1, 2, 3, 4$. Since these combinations penalize intermediate density values such that the iterative design process ends up on 0 and 1 densities, the objective and constraint values obtained with the different combinations can be comparable. Regarding the initial designs, the material selection design variable is considered uniform across the design domain, $\boldsymbol{\rho}_2^0 = 0.5$, in all examples. The topology design variable is initialized differently across the domain, depending on the example, see Table 3.2, such that $\boldsymbol{\rho}_1^0 = V^+ - 0.2$ (in the faded green regions shown) and $\boldsymbol{\rho}_1^0 = V^+ + 0.2$ (in the vivid green regions). The optimization stopping criterion can be either the maximum number of iterations (500) or the design variable change between consecutive iterations less than 1%, i.e., $\max\left|\boldsymbol{\rho}^{i+1} - \boldsymbol{\rho}^i\right| < 0.01$, whichever comes first. However, to ensure that the continuation approaches, described below, are fully applied, and premature convergence is avoided, the optimization never stops before 150 iterations. For each example, the problem formulation detailing the constraints applied (recall Section 3.2.1), as well as the parameters used in the objective functions and constraints, are summarized in Table 3.2 for comprehension.

Continuation approaches for the parameters ϕ_1 and ϕ_2 (related to bulk and shear stiffness constraints, respectively, see Eqs. (3.17) and (3.18)) are applied during the first 50 design iterations. The parameter ϕ_1 gradually decreases from 18 to 1.8 during the first 20 iterations, and then from 1.8 to 1.1, over the 30 iterations that follow. Afterwards, it remains constant and equal to 1.1, meaning that NTE and NPR oriented designs eventually differ 10% maximum in bulk stiffness. The parameter ϕ_2 gradually increases from 0.01 to 0.07, being the respective constraint active, which then means that the shear stiffness of optimal designs is 7% of the shear modulus of the stiffest base material. The continuation approach set for the filter radius, in examples C, E, and F, starts after iteration 50 and the radius linearly decreases until iteration 100, remaining constant afterwards. This helps avoiding fine geometric details and premature convergence of microstructural layouts, making design interpretation easier and more comparable to what is found in the literature [42,50,162].

Table 3.2 – Summary of the initial designs, problem formulation, problem parameters and material symmetries for examples A to F. Green highlighted regions help to identify the imposed symmetries, and the different green tones mean higher and lower initial ρ_1 densities.

		Initial design	Problem formulation	Problem parameters	Material symmetries
Bulk-driven	A	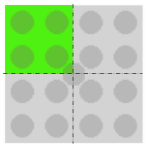	$\min_{\rho_{min}\leq\rho_{m,e}\leq 1} f$ $s.t.\ g_1, g_2, g_3, g_5, g_8 \leq 0$	$\psi_1 = 1; \psi_2 = 0$ $m = 2$ $V^+ = 0.5$ $r_{min} = 1.9$ $\phi_1 = 18 \rightarrow 1.1$	$\mathbf{E}^H$: Cubic $\boldsymbol{\alpha}^H$: Isotropic
	B	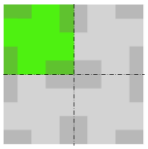			
	C	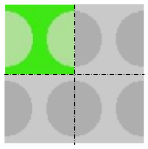	$\min_{\rho_{min}\leq\rho_{m,e}\leq 1} f$ $s.t.\ g_1, g_2, g_3, g_6, g_7, g_{10} \leq 0$	$\psi_1 = 1; \psi_2 = 0$ $m = 1$ $V^+ = 0.35$ $r_{min} = 4.9 \rightarrow 1.9$ $\phi_1 = 18 \rightarrow 1.1$	$\mathbf{E}^H, \boldsymbol{\alpha}^H$: Orthotropic
	D		$\min_{\rho_{min}\leq\rho_{m,e}\leq 1} f$ $s.t.\ g_1, g_2, g_3, g_8, g_9 \leq 0$	$\psi_1 = 1; \psi_2 = 0$ $m = 2$ $V^+ = 0.5$ $r_{min} = 1.9$ $\phi_1 = 18 \rightarrow 1.1$	$\mathbf{E}^H$: Anisotropic $\boldsymbol{\alpha}^H$: Isotropic
Shear-driven	E	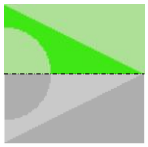	$\min_{\rho_{min}\leq\rho_{m,e}\leq 1} f$ $s.t.\ g_1, g_4, g_5, g_8 \leq 0$	$\psi_1 = 0; \psi_2 = 1$ $m = 2$ $V^+ = 0.35$ $r_{min} = 4.9 \rightarrow 1.9$ $\phi_2 = 0.01 \rightarrow 0.07$	$\mathbf{E}^H$: Cubic $\boldsymbol{\alpha}^H$: Isotropic
	F		$\min_{\rho_{min}\leq\rho_{m,e}\leq 1} f$ $s.t.\ g_1, g_4, g_5, g_{10} \leq 0$	$\psi_1 = 0; \psi_2 = 1$ $m = 1$ $V^+ = 0.35$ $r_{min} = 4.9 \rightarrow 1.9$ $\phi_2 = 0.01 \rightarrow 0.07$	$\mathbf{E}^H$: Cubic $\boldsymbol{\alpha}^H$: Orthotropic

Fig. 3.8 presents the color map related to densities distributions and thus adopted to identify the two distinct material phases and to distinguish solid from void. The white color represents the void phase, whereas the dark red and green colors identify material phases 1

and 2, respectively. A few transient colors show up in final designs due to intermediate densities left by the filter with a minimum radius.

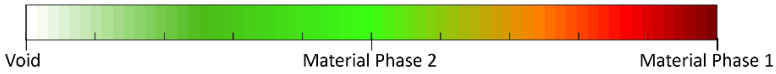

Figure 3.8 – Colour representation of the density distribution within the microstructure.

3.4.1.1 Influence of material ratios on effective thermoelastic properties

To understand how the Young's Moduli or CTEs ratios, between two pre-selected base materials, influence the metamaterial optimal design and performance, the four material combinations presented in Table 3.3 are considered to conduct this study. The problem solved is the minimization of f_α, recall Eq. (3.14), with a normalization factor of $\alpha^* = 10$ (see Section 3.2.2). The polymer combination (PVA-Nylon) is particularly interesting due to the dissimilar and high CTEs [32]. However, polymers' properties are more temperature-dependent, comparing to metals or their alloys, which may hinder their applications. This justifies here the second and third metal combinations, reported in Table 3.3 [39]. The last row shows hypothetical material combinations with different CTE ratios serving the purpose of a merely theoretical study (see also, e.g.,[77,78]).

Table 3.3 – Physical properties and ratios of different material combinations: PVA-Nylon [32], Ti-Al, Ni-Iv [39], and hypothetical material combinations.

Combinations	Young's modulus [GPa]	Ratio $\frac{E^1}{E^2}$	CTE [ppm°C^{-1}]	Ratio $\frac{\alpha^1}{\alpha^2}$
PVA – Nylon	2.329 – 0.889	2.6187	21 – 166	0.1265
Ti 6Al4V – Al 6061	113.8 – 68.9	1.6517	8.6 – 23.2	0.3707
Nickel – Invar	200 – 150	1.3333	13.14 – 1.44	9.1250
Hypothetical	1	1	[1/4; 1/2; 1/1.75; 1/1.5; 1/1.25; 1; 1.25; 1.5; 1.75; 2; 4]	

PVA-Nylon and Ti-Al are combinations where the stiffest material is the one that thermally expands the least, i.e., $E^1 > E^2$ and $\alpha^1 < \alpha^2$. The Ni-Iv case differs, as the stiffest material expands more, i.e., $E^1 > E^2$ and $\alpha^1 > \alpha^2$. The hypothetical combination case has equal Young's moduli ($E^1 = E^2 = 1$). However, several CTE ratios (α^1/α^2) are explored, ranging from 0.25 to 4, assuming $\alpha^2 = 1$. The listed α^1/α^2 ratios below 1 are simply the in-

verse of those above 1. This way it is possible to draw conclusions about the CTE influence in both relative and absolute terms.

Table 3.4 presents the optimal designs obtained for the first three material combinations, for each example. The exponent p values that rendered the best results are tabulated, as well as the effective coefficients of thermal expansion, α_{ij}^H, in ppm°C^{-1}. The results shown below may help to identify potential suitable material combinations or combination trends to attain the desired NTE metamaterials.

Table 3.4 – Results of the CTE minimization problem (with $\omega = 0$ and $\alpha^* = 10$) solved for examples A-F and PVA-Nylon, Ti-Al, and Ni-Iv material combinations. The bi-material design is shown along with the respective tensor $\boldsymbol{\alpha}^H$, and PR, ν_{12}^H.

	PVA-Nylon		Ti-Al		Ni-Iv	
	UC	α_{ij}^H, ν_{12}^H	UC	α_{ij}^H, ν_{12}^H	UC	α_{ij}^H, ν_{12}^H
A	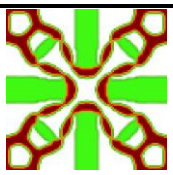	$\begin{bmatrix}-216.67\\-214.55\\0\end{bmatrix}$ 0.165	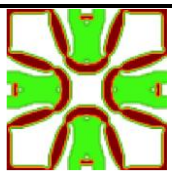	$\begin{bmatrix}-19.62\\-19.62\\0\end{bmatrix}$ 0.003	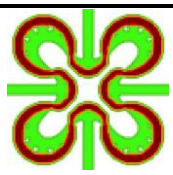	$\begin{bmatrix}-22.77\\-23.00\\0\end{bmatrix}$ 0.322
B	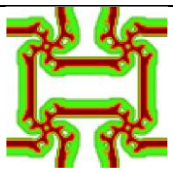	$\begin{bmatrix}-208.81\\-209.22\\0\end{bmatrix}$ −0.670	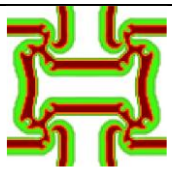	$\begin{bmatrix}-18.26\\-18.42\\0\end{bmatrix}$ −0.590	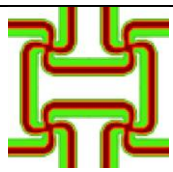	$\begin{bmatrix}-21.17\\-21.14\\0\end{bmatrix}$ −0.617
C	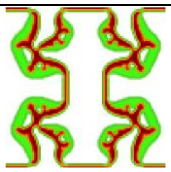	$\begin{bmatrix}-425.81\\21.00\\0\end{bmatrix}$ 1.450	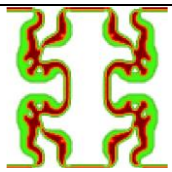	$\begin{bmatrix}-41.84\\8.60\\0\end{bmatrix}$ 1.465	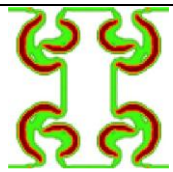	$\begin{bmatrix}-42.11\\1.44\\0\end{bmatrix}$ 1.440
D	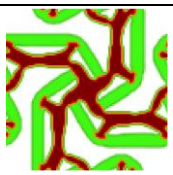	$\begin{bmatrix}-238.00\\-240.41\\1.00\end{bmatrix}$ −0.178	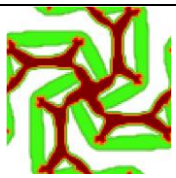	$\begin{bmatrix}-21.52\\-21.74\\1.00\end{bmatrix}$ −0.136	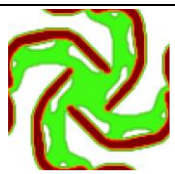	$\begin{bmatrix}-23.83\\-23.59\\-1.00\end{bmatrix}$ −0.242
E	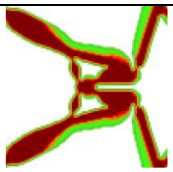	$\begin{bmatrix}-88.53\\-88.93\\0\end{bmatrix}$ 0.472	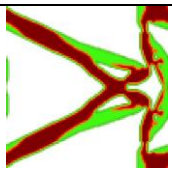	$\begin{bmatrix}-3.90\\-3.75\\0\end{bmatrix}$ −0.481	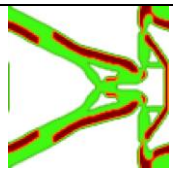	$\begin{bmatrix}-7.57\\-7.53\\0\end{bmatrix}$ −0.448
F	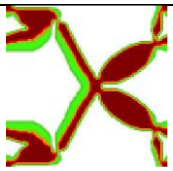	$\begin{bmatrix}-181.79\\21.00\\0\end{bmatrix}$ 0.602	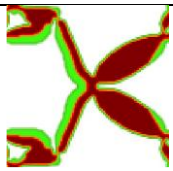	$\begin{bmatrix}-12.33\\8.60\\0\end{bmatrix}$ 0.562	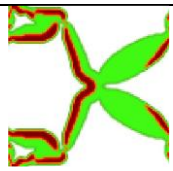	$\begin{bmatrix}-13.40\\1.44\\0\end{bmatrix}$ 0.539

As seen in Table 3.4, the material combination that leads to the most negative homogenized CTE, α_{ij}^{H}, for all examples, is the PVA-Nylon, as it includes a base material with a comparatively much higher CTE (see Table 3.3). Furthermore, the highest base CTE values in Ti-Al ($\alpha^{Al} = 23.2\ \text{ppm°C}^{-1}$) and Ni-Iv ($\alpha^{Ni} = 13.14\ \text{ppm°C}^{-1}$) have the same order of magnitude. However, the Ni-Iv combination leads to a slightly more negative homogenized CTE because the difference between the base CTE's is greater than the one verified for the Ti-Al combination. For examples B to F, the design solutions look similar between PVA-Nylon and Ti-Al combinations, where the lowest base CTE is linked to the first phase (red one). For Ni-Iv combination, the lowest base CTE is linked to the second phase (green), which justifies that the material phases appear reversed in a comparatively similar topology. In example A, consistency in optimal layouts among all material combinations is less evident. Even though, PVA-Nylon and Ti-Al layouts look quite similar.

For examples C and F, where an orthotropic CTE tensor is considered, the response in the horizontal direction is significantly higher than in the vertical direction. The value of α_{22}^{H} is equal to the lowest base CTE, as a result of constraint g_9 being active. In other words, prioritizing the minimization of the CTE in one spatial direction (say horizontal) compromises the performance in the orthogonal direction. This is evident when comparing examples E and F that only differ in the imposed symmetry in $\boldsymbol{\alpha}^{H}$, orthotropic or isotropic. Being isotropy a more restrictive symmetry, the negative CTE value in the horizontal direction, α_{11}^{H}, for example E, is approximately one order of magnitude lower than the one for example F (orthotropic). However, the vertical CTE, α_{22}^{H}, is negative in example E, as imposed by symmetry, whereas it is positive in example F, equaling the material 1 CTE.

Furthermore, it is observed that the optimized property of CTE depends mostly on the material combination and constraints considered in the optimization problem. For example, for bulk-oriented examples A, B and D, the CTE tensor is isotropic. The CTE remains within a relatively small range ($\sim 210 - 240\ \text{ppm°C}^{-1}$, for PVA-Nylon; $\sim 18 - 22\ \text{ppm°C}^{-1}$, for Ti-Al; and $\sim 21 - 24\ \text{ppm°C}^{-1}$, for Ni-Iv), regardless of the UC configurations. When the problem is shear-oriented, the CTE tends to be slightly less negative. This is evident in example E, where the CTE is isotropic and around 3 times lower in magnitude than examples A, B, and D. A similar trend can be observed when comparing the orthotropic CTE tensors of the bulk-oriented design (example C) and the shear-oriented design (example F), with example F exhibiting values around 3 times lower than example C for α_{11}^{H}.

Regarding the effective PR values (recall that the optimization problem addressed in this section aims exclusively at minimizing the CTE), almost all solutions exhibit positive PR values, except for examples B and D, whose optimal chiral topologies, obtained from CTE minimization, already display negative PR (as will later be shown in Table 5), as well as example E for the Ti-Al and Ni-Iv material combinations. It can be observed that the effective PR is mainly governed by the topology of the UC, as similar PR values are found across different material combinations in examples B, C, D, and F, where the topology remains nearly unchanged despite the variation in material properties. In contrast, in example A, the topology differs for each material combination, resulting in different PR values. A similar situation occurs in example E, where the topology for PVA-Nylon differs from those obtained for Ti-Al and Ni-Iv.

In summary, the effective PR is primarily determined by the microstructural topology, whereas the effective CTE is mainly influenced by the material properties. For instance, comparing examples A and B, both come from the same optimization problem (see Table 1), the CTE values are similar for each material combination, yet the PR values differ significantly due to differences in topology.

The results just presented, indicate that both absolute and relative CTE values are relevant to attain extreme NTE metamaterials. This is conceptually emphasized by investigating the last (hypothetical) material combination in Table 3.3. Consistently, the highest α^1/α^2 ratio, equal to 4, leads to the most negative metamaterial CTE (see Fig. 3.9). In contrast, for the ratio $\alpha^1/\alpha^2 = 1/4$, which means that material 1 expands comparatively four times less instead of 4 times more (reference is material 2), the CTE of the resulting metamaterial is also negative, as expected, but much less negative. For ratio α^1/α^2 =1 the metamaterial CTE equals the base material CTE (always positive) and in the vicinity of such ratio, say between 0.6 and 1.5 as observed in Fig. 3.9, no NTE metamaterials are obtained, which has no surprise as it means that $\alpha^1$and α^2 are not dissimilar enough.

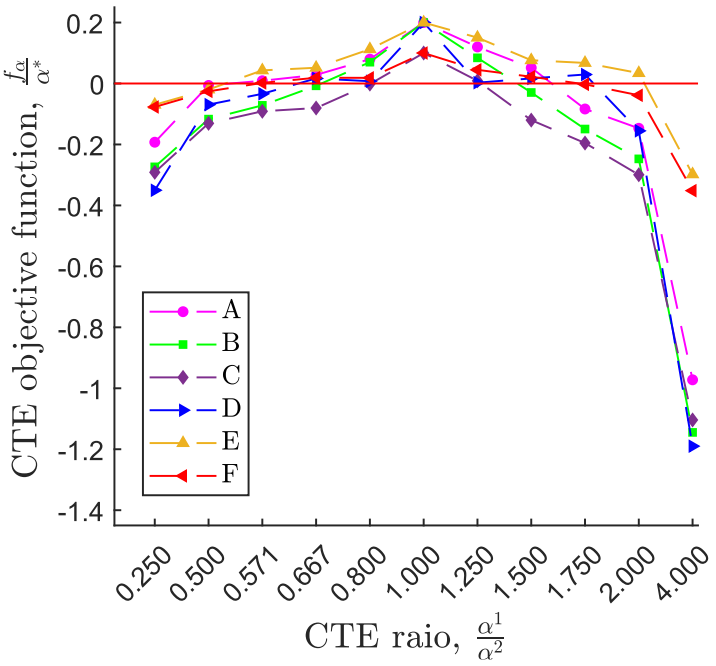

Figure 3.9 – CTE ratio influence on the effective thermoelastic property, based on hypothetical base materials.

3.4.1.2 Pareto front results

This subsection aims to illustrate the approximated Pareto fronts obtained from the solutions of the scalarized multiobjective problem stated in Eq. (3.27), for each example. This shows the competition between the PR-related and CTE objective functions when both are minimized to attain NPR and NTE. Results are here shown choosing the material combination of PVA-Nylon, see Table 3.3. Fig. 3.10 shows the obtained front for each example. The reading of each front, from left to right, can be interpreted as an increase of weight ω from 0 to 1 in 0.1 increments. Furthermore, as an attempt to escape local minima, seven combinations of penalizations p_1 and p_2 were considered when solving the optimization problem for each ω, which resulted in a total of 77 runs per example. Considering the volume of computations involved, the implementation was done in MATLAB® R2024b and running the respective script using the Parallel Computing toolbox on a shared-memory Workstation HP Z8 G4, 2 CPUs Intel Xeon 6242R 3.1 GHz 2933 MHz 20C, 256 GB RAM.

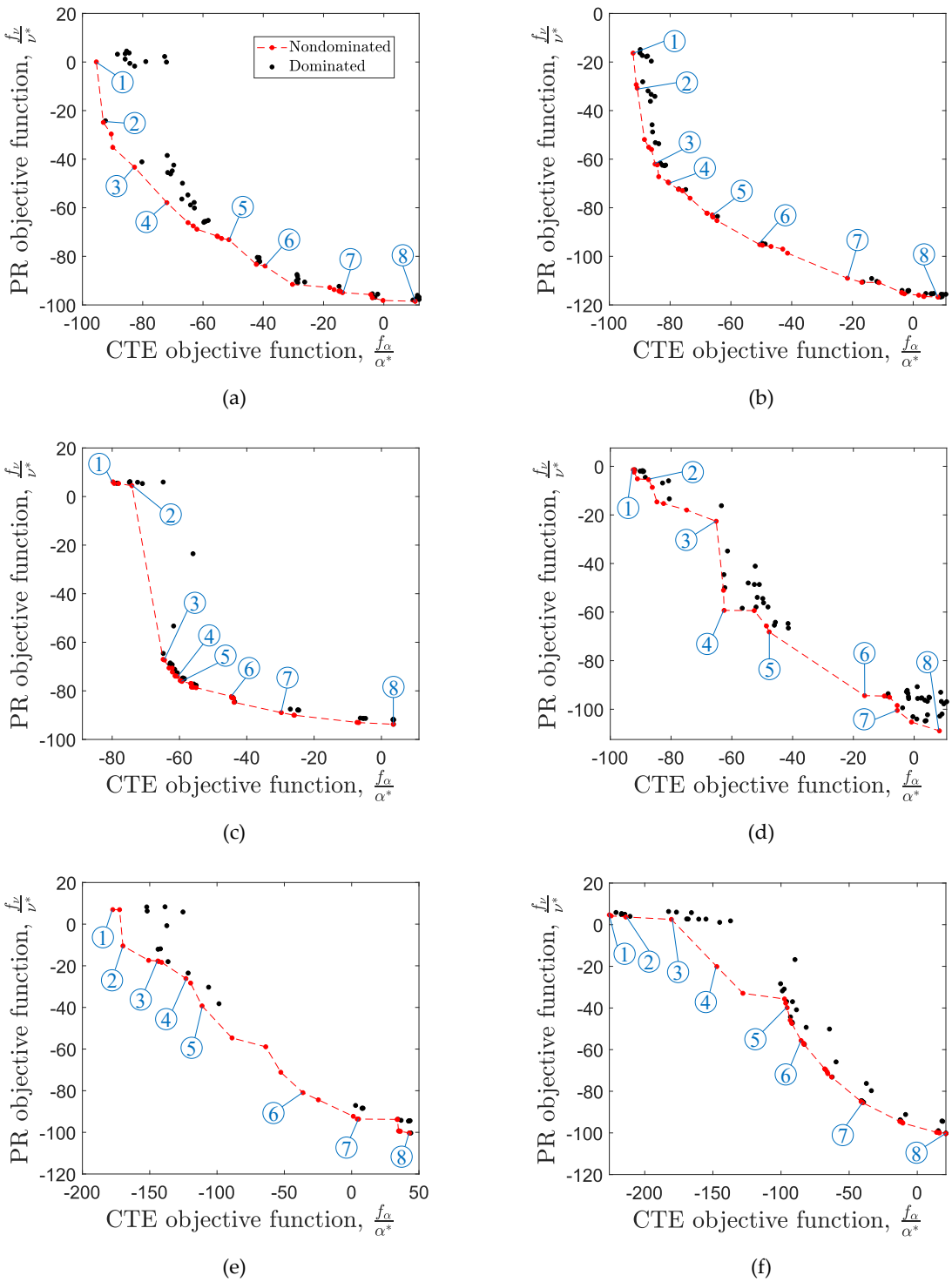

Figure 3.10 – Nondominated Pareto front solutions (red dots) as well as dominated solutions (black dots) in the space of design objectives: CTE and PR-related objective functions. Subset of 8 Pareto solutions is highlighted to further detail results. Pareto front for each example: (a) A; (b) B; (c) C; (d) D; (e) E, and (f) F

In Fig. 3.10, the set of nondominated solutions, among the 77 obtained, is highlighted resorting to red points. For examples A, B, C, D, E, and F are obtained 25, 34, 29, 22, 23, and 29 nondominated solutions, respectively. The remaining dominated solutions correspond to the scattered black points. A subset of 8 Pareto solutions, also highlighted in Fig. 3.10, are selected as representative solutions to further detail afterwards.

At every plot of the objective functions shown in Fig. 3.10, it can be recognized a competitive trend between the two design objectives to both become as much negative as possible. A rightward analysis of the Pareto front, i.e., as ω increases from 0 (left) to 1 (right), shows that, when the CTE is exclusively being minimized, the PR value becomes nearly zero, except for example B, where the solution that minimizes CTE also presents NPR. For intermediate values of ω, getting a more negative PR is always at the expense of CTE becoming less negative. For the extreme case where PR is exclusively minimized (right), the CTE becomes positive in all examples. This is because when only PR is minimized, a single material design solution is found (as shown below) and thus, the metamaterial CTE equals the base material CTE, i.e., $\boldsymbol{\alpha}^H = \boldsymbol{\alpha}^1$. This observation supports the claim that there is no mechanistic relationship between NPR and NTE, as one can be negative without the other, and vice-versa [5]. However, for both to be negative, a trade-off is required.

In Fig. 3.10a-d, the two normalized objective functions, f_α/α^* and f_ν/ν^*, roughly range from -100 to 0, as explained in Section 3.2.2. For the shear-driven examples, the proposed strategy of normalizing by the amplitude did not provide comparatively so good results, i.e., the CTE objective function would quickly lose its relative importance for $\omega > 0$, leading to solutions absolutely dominated by the PR-related minimization. Therefore, to ensure transparency regarding the cases in Fig. 3.10e and 3.10f, no normalization was applied to f_α (i.e., $\alpha^* = 1$), resulting in the CTE objective function ranging from -200 to 0.

For the first two examples, A and B, which differ solely in the initial design used (re-entrant or chiral-like, see Table 3.2), the Pareto fronts have a similar appearance. It can also be observed that when more importance is given to the CTE minimization (on the left side), i.e., $\omega \leq 0.5$, the solutions are more dependent on the penalty exponents, p_1 and p_2, resulting in a greater spread of dominated points. Conversely, in the other half of the weights' interval, where more importance is given to minimizing PR, the solution points are more clustered, meaning that for different exponents the final topology and material distribution is quite similar. For the re-entrant honeycomb, example C, the topology of the solutions is quite similar, regardless of the penalty exponents used, resulting in the clustering of solutions

clearly identifying an elbow of the Pareto front, see Fig. 3.10c. The anisotropic chiral case, example D, presents dominated points more widely spread. This is because this example offers the greatest design freedom, with no imposed symmetry conditions or grouping of design variables. The formulation of example E generates some solutions, for values of ω between 0.3 and 0.6 with $p_2 > 1$, that end up in designs with some 'grey' regions, making the design interpretation particularly challenging. Therefore, it was decided to exclude these solutions from the space of design objectives in Fig. 3.10e, which thus explains less plotted points and comparatively wider gaps among the dominated plotted points.

The UC optimal design and respective periodic microstructure (array of 3x3 UC's), for the 8 highlighted points, from each Pareto front in Fig. 3.10, are presented in Fig. 3.11. The design solutions seen for point 8, where only PR is minimized, correspond to well-established results in the literature [59,163,164]. In examples E and F, the solutions for point 8 are identical because only the $\boldsymbol{\alpha}^{\mathrm{H}}$ imposed symmetry, isotropic versus orthotropic, differs between them. This difference is gradually manifested in the design as one moves from point 7 to 1, in Fig. 3.11. The representative set of Pareto front solutions, from 1 to 8, gives a good overall idea on how substantially micro-architectures and material distributions differ for each example studied here. In all examples, solutions from 1 to 5 have been selected from $\omega \leq 0.5$ (CTE minimization prioritized) while the remaining, 6 to 8, correspond to $\omega > 0.5$ (PR minimization prioritized). The reasoning of having more selected solutions on the side of $\omega \leq 0.5$ is related to the fact that more variety in design is observed when more weight is given to CTE minimization.

By analyzing the 8 representative Pareto solutions, from left to right, it can be observed that the material 2 volume fraction (green) gradually decreases as ω increases. This general trend means that the metamaterial loses its NTE performance, as such effect is on account of bi-material design solutions. Although such a trend was expected, related design transitions may not be trivial, as observed in Fig. 3.11. Eventually, such transitions end up on a single material solution, which makes sense when only PR is minimized ($\omega = 1$, point 8). Notice that the green contour in point 8, along the solid-void interface, is due to the filtering technique and the color scheme used.

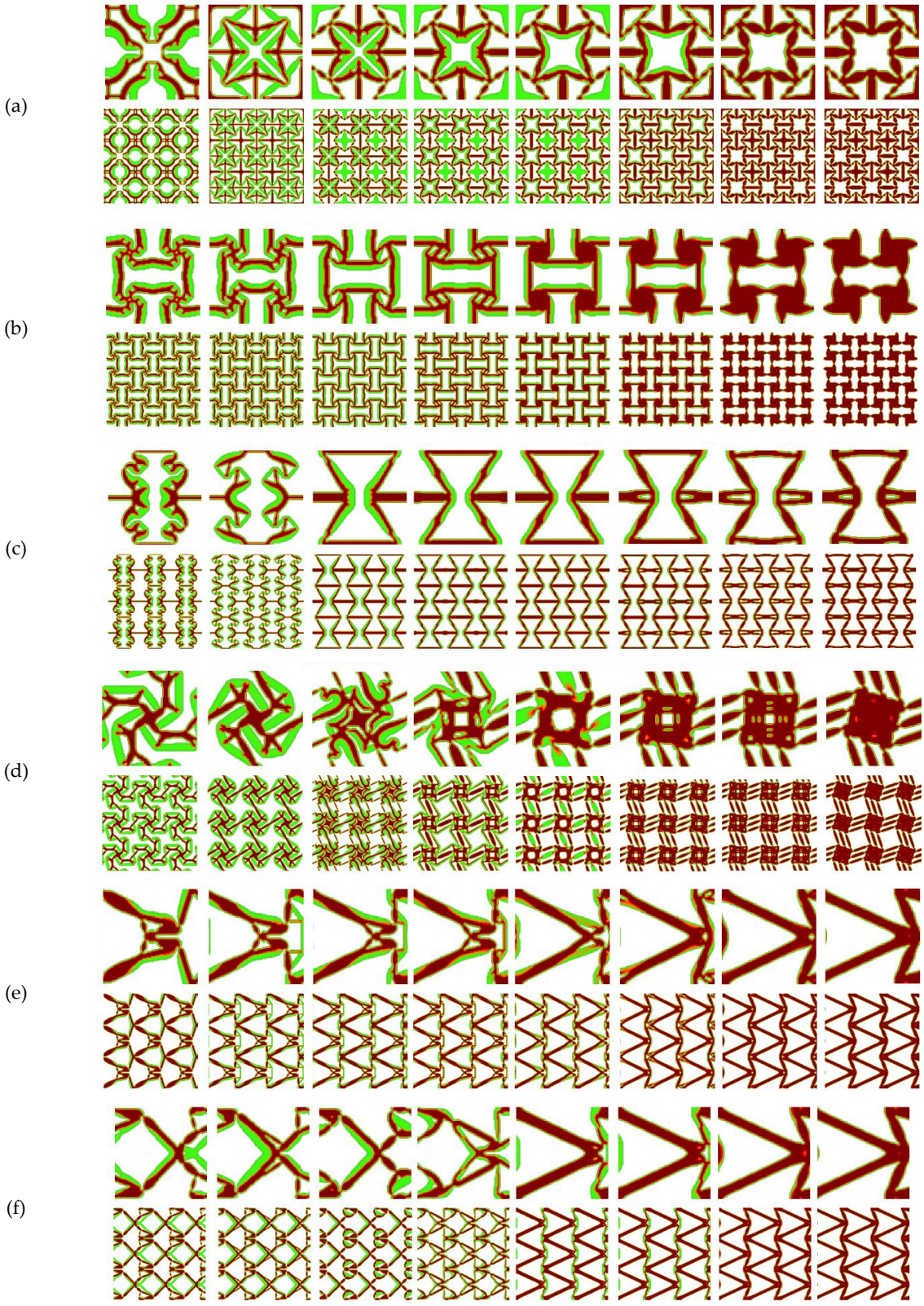

Figure 3.11 – Summary of the UC and respective microstructure (3x3 repetitions) for the 8 Pareto representative points (from left to right) highlighted in Fig. 3.10, for each example: (a) A; (b) B; (c) C; (d) D; (e) E, and (f) F.

Regarding the microstructure layouts in Fig. 3.11, for each example, the design is quite unique for point 1, except for example B where the topology is relatively consistent among the 8 points, varying then the distribution of the two materials. Apart from example B, the microstructures topologies only become quite similar above solution 2 in example C, above 4 in A and D, and above point 5 in E and F. Whereas layouts remain almost unchanged, material 2 presence changes. This evidences that the auxetic behavior is mostly determined by the UC architecture alone. To achieve NTE, not only the architecture, but also the distribution of the two base materials with positive CTE, plays a crucial role. Metamaterials for examples C and F, reasonably balancing NTE and NPR (focus on points 5 or 6), typically show green stripes (material 2) usually vertically oriented in zig-zag fashion, providing significant auxetic response in the horizontal direction, i.e., α_{11}^{H} is considerably negative. These design predictions may bring to mind previously reported lattice anepectic microstructures, as the auxetic-inspired honeycomb [162], the 2D double-V honeycomb structure [165] or the re-entrant triangular metamaterial [42]. In the past, these designs were proposed based on a direct design approach, relying on individual intuition and experience. Comparable re-entrant honeycomb or arrowhead-shaped structures are here systematically obtained for the first time. Novelty is also linked to example E, where roughly horizontally oriented "green" stripes are added, such that isotropic thermal auxeticity is attained. The anisotropic chiral metamaterial, as treated in example D, has no previous studies on bi-material solutions for both NTE and NPR, which also appears here as novel. Example A is probably the most seen anepectic design, already obtained in a systematic way [77–79,81]. However, no previous studies have unfolded design transitions toward NTE alone, moving from points 8 to 1, in Fig. 3.11a. Finally, example B solutions, roughly showing horizontal and vertical-oriented bi-material ribs, are original, although they may resemble previous solutions of two-dimensional bi-material anti-tetrachiral metamaterial, typically interpreted resorting to beam-like ribs, see [81,166,167].

From Fig. 3.11, it can be clearly seen that the topology that minimizes the CTE is not optimal for the PR minimization, since extreme designs are quite distinct and when thermal expansion gets negative, PR gets positive (or near zero), and vice-versa. In between extremes, design transitions clearly demonstrate the required trade-off in terms of layout and the presence of two materials, to balance between NTE and NPR, which highlights the competing nature of improving these performances concurrently.

Fig. 3.11 may offer an invaluable visual critical analysis on how the bi-material design changes along the front. However, room is left to better quantify the individual material volume fractions, which can be regarded as a distinguished optimization result, compared to prior works that simply fixed such fractions. Therefore, Fig. 3.12 provides, for each example, the obtained optimal values of individual material volume fractions (red and green colors refer to material 1 and 2, respectively) along with the stiffness (bulk or shear modulus) of each microstructure.

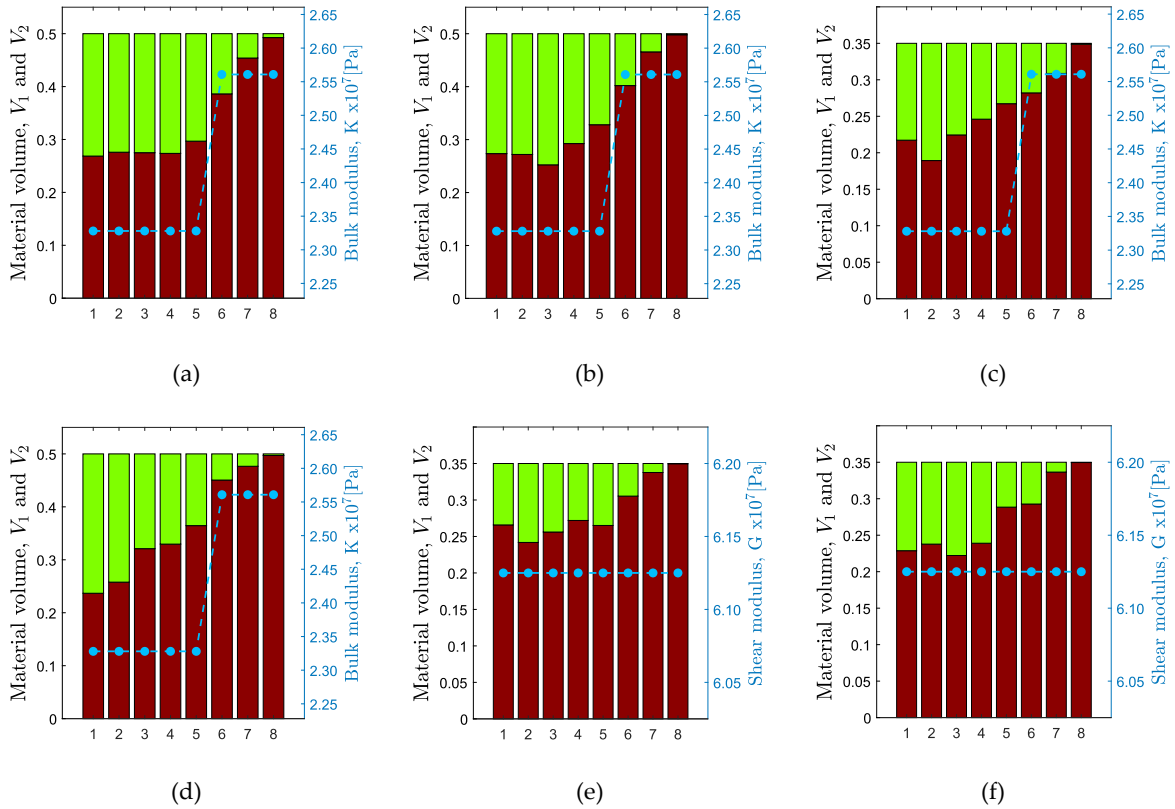

Figure 3.12 – Volume of material phase 1 (red bars) and 2 (green bars) and stiffness for the 8 Pareto representative points highlighted for each example: (a) A; (b) B; (c) C; (d) D; (e) E, and (f) F.

As seen in Fig. 3.12, around the first three or four representative points out of 8, depending on the example, the individual volume fractions may present an irregular progression. That can be justified by the fact that it happens when the optimal topologies mostly differ among themselves. For the remaining points, up to 8, optimal topologies look almost the same and regular progression on individual volume fractions is seen, i.e., material 1 increases as material 2 decreases. This observation further stresses the importance of letting design freedom extended to individual material volume fractions. In practice, the materials proportions are hardly known a priori and tend to be highly problem dependent.

Regarding the stiffness values given in Fig. 3.12, the bulk-oriented designs (examples A-D) present the following trend. For $\omega \leq 0.5$ (points 1 to 5) the metamaterials have the minimum allowed stiffness, indicating that lowering stiffness is in favor of getting CTE further negative. For $\omega > 0.5$ the upper bound is active, as the objective function for PR-related minimization, Eq. (3.13), inherently maximizes stiffness, i.e., $E^H_{1111} + E^H_{2222}$. Based on extensive testing and analysis of the problem, it was verified that the PR may come less negative with no upper bound, because a too high longitudinal elastic coefficient, either E^H_{1111} or E^H_{2222}, means increasing overmuch the denominator in the PR definition (recall Section 2.2). Therefore, bear in mind the limitation of Eq. (3.13), as it only allows a PR-related minimization, i.e., not the minimization of PR itself. However, by imposing these stiffness bounds, the approximated Pareto solutions are closer to the exact PR property and more comparable with one another, as shown next section. As for the shear-based designs (examples E and F), regardless of the weight ω considered, the constraint imposing lower bound on shear stiffness is always active, indicating that as long as both CTE and PR would become more negative, that stiffness (homogenized shear modulus) would be further reduced. The analysis of microstructural stiffness will be further complemented using polar plots in the next subsection (see Table 3.6).

3.4.1.3 Effective properties: Results and discussion

The underlying mechanisms behind NPR and NTE can be distinguished, respectively, as follows: (1) deformation mechanisms from rotating rigid units, re-entrant or chiral single-material microstructures; (2) the interplay of solids with dissimilar thermal expansion, arranged in different directions at structural level. Accordingly, the "green" material in the rib-like structures in Fig. 3.11 (left) expands more than the "red" one under temperature increase, inducing bending or rotation in the ribs that contract the overall structure, whereas the mechanism-like deformation of single-material microstructures for NPR hinders NTE (point 8). However, similarities between bending and stretching mechanisms of NPR and NTE can be verified in some cases.

The optimal results presented in the previous section come from weighing differently the normalized objective functions f_ν and f_α, see Eq. (3.24). However, f_ν defined in Eq. (3.13), is not directly aligned with the PR definition given in Section 2.2. Regarding the objective f_α, it is the effective property of CTE itself. Therefore, in the dual objective functions' spaces shown in Fig. 3.10, the presented solutions can be considered reliable in the case of CTE but need to be post-processed to obtain the exact PR value, due to the stated discrepancy be-

tween the objective used and the effective property itself. This section intends to pick up such solutions, in order to calculate the respective PR's by definition, and replot solutions in the space of true effective properties.

In Table 3.5, the effective properties of the 8 representative Pareto points highlighted in Fig. 3.10 are presented. Note that the auxeticity of the metamaterials in examples C and F is direction dependent. The response in the horizontal direction is significantly higher than the vertical one. Therefore, for these couple of examples, the effective properties presented in Table 3.5 correspond to the higher PR, ν_{12}^H, and higher CTE, α_{11}^H, characterizing the optimized metamaterial. As for the remaining examples, where the response is the same in both directions, there is a unique PR and CTE.

Table 3.5 – Effective properties (homogenized PR, ν_{12}^H, and homogenized CTE, in ppm°C^{-1}, α_{11}^H) for the 8 Pareto representative points highlighted in Fig. 3.10.

Property	Example	Representative Pareto point							
		1	2	3	4	5	6	7	8
PR, ν_{12}^H	A	0.003	-0.706	-0.714	-0.848	-0.876	-0.881	-0.893	-0.913
	B	-0.656	-0.774	-0.873	-0.890	-0.895	-0.903	-0.924	-0.929
	C	0.566	0.343	-1.485	-1.508	-1.514	-1.510	-1.474	-1.485
	D	-0.167	-0.418	-0.721	-0.897	-0.900	-0.921	-0.925	-0.931
	E	0.472	-0.310	-0.393	-0.397	-0.540	-0.650	-0.651	-0.670
	F	0.373	0.520	0.139	-0.551	-0.573	-0.630	-0.650	-0.670
CTE, α_{11}^H	A	-232.9	-226.1	-202.0	-174.9	-124.9	-95.8	-33.3	25.5
	B	-214.7	-211.6	-197.4	-187.4	-154.0	-117.3	-50.4	19.0
	C	-447.2	-415.6	-361.4	-339.8	-332.4	-249.6	-166.7	19.7
	D	-240.0	-236.5	-194.4	-162.4	-126.1	-42.3	-14.4	21.5
	E	-88.9	-85.1	-72.2	-71.9	-55.8	-18.3	2.4	21.0
	F	-226.0	-224.6	-180.4	-147.1	-95.5	-85.3	-10.9	21.0

As expected, example C exhibits the most extreme properties, both in PR and CTE, as the optimization was directional, with both tensors $\mathbf{E}^H$ and $\boldsymbol{\alpha}^H$ orthotropic. However, as pointed before, improving performance in one direction is at the expense of compromising it along the orthogonal direction. For example, for point 1, the value of the CTE in the vertical direction is $\alpha_{22}^H = 21$ ppm°C^{-1}, due to the imposition of constraint g_9, whereas along the hor-

izontal direction it is quite expressive, $\alpha_{11}^{H} = -447.2\ \text{ppm°C}^{-1}$. For point 8, the metamaterial when loaded horizontally responds vertically according to a PR that is $\nu_{21}^{H} = -0.61$, whereas the other PR is approximately 2.5 times more negative, i.e., $\nu_{12}^{H} = -1.485$. A similar comment applies to example F in terms of CTE. As seen from Table 3.5, its horizontal CTE, $\alpha_{11}^{H} = -226\ \text{ppm°C}^{-1}$, is quite expressive when compared to the arrowhead-shaped with isotropic thermal expansion, example E, with $\alpha_{11}^{H} = -88.9\ \text{ppm°C}^{-1}$. However, in the vertical direction, example E has NTE performance with $\alpha_{22}^{H} = -88.9\ \text{ppm°C}^{-1}$, whereas example F has positive CTE, $\alpha_{22}^{H} = 21\ \text{ppm°C}^{-1}$. These observations suggest that it is not possible to further improve the response in one direction without compromising it in the other. Depending on the intended metamaterial application, this trade-off awareness and its quantification can be quite advantageous. Finally, for the arrow-type examples, E and F, point 8 represents the same solution, as the difference between these examples lies on the thermoelasticity tensor symmetry. This point 8 solution (for E and F) is comparable to the one previously obtained in the literature [59,164], with a PR of $\nu_{12}^{H} = -0.67$. Comparing the remaining examples, the chiral anisotropic metamaterial (example D) exhibits slightly superior negative properties of unique PR and CTE, as it is the one generated with comparatively greater design freedom. Between examples A and B, the cubic chiral metamaterial presents a slightly more negative PR throughout the ω range, as well as a more negative CTE from point 4 onward. This superior performance of the cubic chiral design was also previously demonstrated in [79], where the authors achieved PRs of -0.79 and -0.88 for the cubic chiral metamaterial, and -0.55, -0.57, and -0.59 for the star-shaped re-entrant design. In the present work, metamaterials with even more negative PR values were obtained, i.e., between -0.71 and -0.91 for the star-shaped re-entrant design, and between -0.77 and -0.93 for the cubic chiral. In terms of the CTE, a direct comparison is not possible with the previous works, as the materials used here differ, and the materials choice significantly influences the CTE performances, as stated in Section 3.4.1.1.

The conclusions drawn here are consistent with those presented in Section 3.4.1.1. In the first half of the interval ω, where CTE minimization dominates, the CTE values remain similar across comparable optimization problems, regardless of the underlying topology. This is particularly evident for bulk-driven and isotropic-CTE cases, such as examples A, B, and D. For shear-driven problems, the CTE tends to be lower in magnitude compared to their bulk-driven counterparts; for instance, example F (shear-driven) shows lower CTE values than example C (bulk-driven), despite both exhibiting orthotropic behaviour. Likewise,

example E presents lower isotropic CTE values compared to the other isotropic cases. In the second half of the interval, where PR minimization becomes dominant (mostly from point 6 up to 8), the PR varies only slightly within each example, as the topology remains nearly unchanged and only minor adjustments occur in the material phase distribution.

Among the 8 points in Table 3.5, it is observed, in connection with example C, a slightly inconsistent progression of PR negative values, as one moves from selected points 1 to 8. This happens here as the objective function used to approximate Pareto fronts is PR-related and not the PR value itself. Although such inconsistency is only visible in Table 3.5 for example C, within the set of 8 points, it can show up more when calculating the effective properties to include all the nondominated solutions plotted in Fig. 3.10. For a comprehensive overview of what happens in the dual space of effective properties, the effective PR and CTE values of all design solutions seen in Fig. 3.10 are plotted in Fig. 3.13. To help interpretation, this last plot resembles an Ashby chart, where each example (A-F) has its own colorful shaded region, embracing a cluster of points, to facilitate the reading about the range of properties. The results spread along the third quadrant of effective properties where both are negative. Comprehensively, not every nondominated solution in Fig. 3.10 plots as such in Fig. 3.13, but the resulting perturbations can be considered small, allowing one to observe clear enough trends to infer a competition between NPR and NTE. Some overlapping can be seen among examples A, B, and D, i.e., designs differ but performances are quite equivalent. Example C excels in performance while examples E and F present the lowest auxeticity, because their shear resistance is higher.

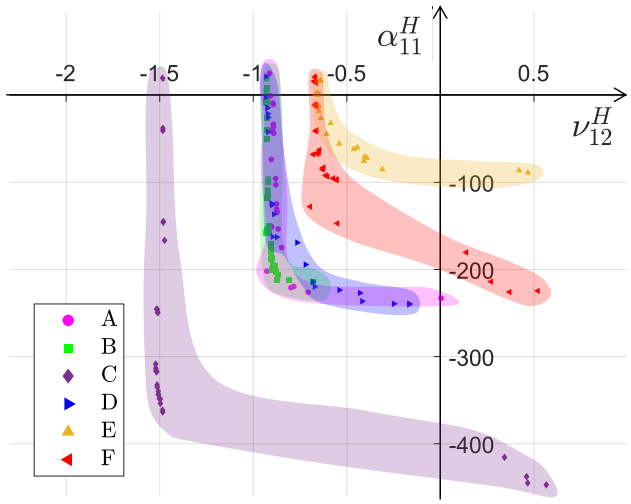

Figure 3.13 – Effective properties (homogenized PR, ν_{12}^H, and homogenized CTE in ppm°C^{-1}, α_{11}^H) for the points in the Pareto fronts plotted in Fig. 3.10 in a fashion resembling Ashby chart

Finally, it can be observed in Fig. 3.13 that, from a certain point onward, there is almost a vertical alignment of points, i.e., the effective PR values remain nearly the same among solutions. In fact, to render considerable NPR, the optimal topology remains quite unchanged at each example, as NPR depends strongly on geometry, instead of two materials coexisting. Therefore, design differences become more evident on the side of NTE, as it depends not only on geometry but also on how different materials are distributed within that geometry.

3.4.1.4 Scale-size effects on thermoelastic properties

In this subsection, the composite is treated as the finite repetition of the UC inside a RVE, an odd number of times, generating periodic patterns from 3 × 3 to 11 × 11 (recall Fig. 3.5). The RVE method, explained in Section 3.2.4, is then used to evaluate the thermoelastic properties, which are compared to the homogenization predictions to conclude about scale-size effects. For the sake of example and to keep the presentation concise, the designs from Fig. 3.11, corresponding to point 5, are selected to conduct this study. Table 3.6 presents the elastic and thermoelastic coefficients of the composite, comprising 11×11 UCs, computed by the RVE method, along with the predictions from the AH method. The averaging of stresses and strains is performed in the central UC, and not over the full RVE's domain, so that the boundary effects are mitigated, leading to better convergence toward homogenization predictions. A polar plot of the horizontal stiffness based on the rotation of the compliance tensor, $(\mathbf{E}^H)^{-1}$, representing the material anisotropy, as described in [94], is also provided in Table 3.6.

Analyzing the stiffness directionality by looking at the polar plots in Table 3.6, the difference between the bulk-driven and the shear-driven designs are evident. While the bulk-driven designs are stiffer along the horizontal and vertical principal directions, the shear-driven ones are comparatively stiffer along the ±45° directions. Interestingly, plots for examples E and F are nearly isotropic, as also verified in [59], where these arrowhead-shaped microstructures were first designed by targeting an isotropic tensor. These examples, E and F, also present comparatively higher bulk stiffness, reducing auxeticity. Additionally, one highlights in example C the comparatively much lower stiffness along the horizontal direction, resulting in greater horizontal auxeticity. Finally, the polar plots are symmetric with respect to horizontal and vertical axis, except for example D. This last one is comparatively slightly twisted, thus reflecting the respective stiffness tensor small anisotropy.

Table 3.6 – Elastic and thermoelastic coefficients, E_{ijkl} and β_{ij}, of metamaterials corresponding to point 5 of Table 4, computed with the AH and the RVE method, considering the composite comprising 11×11 UCs.

Example	Elastic coefficients, E_{ijkl} [$\times 10^7$ Pa]		Stiffness polar plot [$\times 10^7$ Pa]	Thermoelastic coefficients, β_{ij} [$\times 10^9$Pa. ppm°C^{-1}]	
	AH	$\text{RVE}_{11\times11}$		AH	$\text{RVE}_{11\times11}$
A	$\begin{bmatrix} 9.39 & -8.23 & 0 \\ & 9.39 & 0 \\ sym & & 0.17 \end{bmatrix}$	$\begin{bmatrix} 9.24 & -8.06 & 0 \\ & 9.24 & 0 \\ sym & & 0.17 \end{bmatrix}$	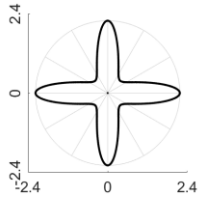	$\begin{bmatrix} -1.45 \\ -1.45 \\ 0 \end{bmatrix}$	$\begin{bmatrix} -1.42 \\ -1.42 \\ 0 \end{bmatrix}$
B	$\begin{bmatrix} 11.07 & -9.98 & 0 \\ & 11.21 & 0 \\ sym & & 0.37 \end{bmatrix}$	$\begin{bmatrix} 11.00 & -9.95 & 0 \\ & 11.19 & 0 \\ sym & & 0.37 \end{bmatrix}$	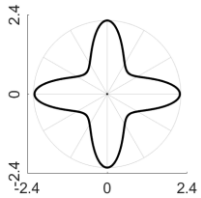	$\begin{bmatrix} -2.09 \\ -2.26 \\ 0 \end{bmatrix}$	$\begin{bmatrix} -2.14 \\ -2.20 \\ 0 \end{bmatrix}$
C	$\begin{bmatrix} 4.34 & -6.57 & 0 \\ & 11.13 & 0 \\ sym & & 0.09 \end{bmatrix}$	$\begin{bmatrix} 4.13 & -6.58 & 0 \\ & 11.14 & 0 \\ sym & & 0.09 \end{bmatrix}$	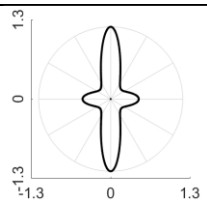	$\begin{bmatrix} -4.70 \\ 5.36 \\ 0 \end{bmatrix}$	$\begin{bmatrix} -4.83 \\ 5.58 \\ 0 \end{bmatrix}$
D	$\begin{bmatrix} 11.55 & -10.37 & 4.25 \\ & 11.51 & -4.25 \\ sym & & 1.75 \end{bmatrix}$	$\begin{bmatrix} 11.20 & -9.97 & 4.26 \\ & 11.16 & -4.26 \\ sym & & 1.75 \end{bmatrix}$	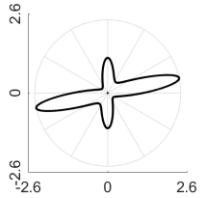	$\begin{bmatrix} -1.49 \\ -1.44 \\ -0.01 \end{bmatrix}$	$\begin{bmatrix} -1.45 \\ -1.38 \\ -0.01 \end{bmatrix}$
E	$\begin{bmatrix} 4.94 & -2.67 & 0 \\ & 4.99 & 0 \\ sym & & 6.13 \end{bmatrix}$	$\begin{bmatrix} 4.99 & -2.48 & 0 \\ & 4.90 & 0 \\ sym & & 6.14 \end{bmatrix}$	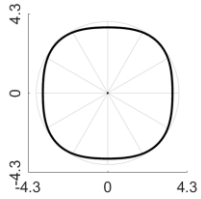	$\begin{bmatrix} -1.28 \\ -1.27 \\ 0 \end{bmatrix}$	$\begin{bmatrix} -1.00 \\ -1.43 \\ 0 \end{bmatrix}$
F	$\begin{bmatrix} 4.73 & -2.71 & 0 \\ & 4.78 & 0 \\ sym & & 6.13 \end{bmatrix}$	$\begin{bmatrix} 4.79 & -2.55 & 0 \\ & 4.69 & 0 \\ sym & & 6.14 \end{bmatrix}$	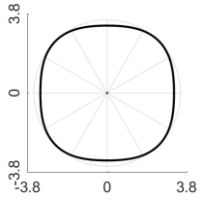	$\begin{bmatrix} -4.87 \\ 3.22 \\ 0 \end{bmatrix}$	$\begin{bmatrix} -4.65 \\ 3.08 \\ 0 \end{bmatrix}$

In the scale-size effect analysis the thermal stress tensor, $\boldsymbol{\beta}^H$, is used instead of the CTE tensor, as it is directly obtained through the RVE method, see Eq. (3.35). The percent deviation toward homogenization predictions, for each non-zero coefficient of the homogenized thermal stress tensor and stiffness tensor, for each example A-F, can be seen in Fig. 3.14

and Fig. 3.15. The bars in different colors represent the various scale factors, n, ranging from 3 (dark blue) to 11 (white). When a single UC is evaluated by the RVE method, the results significantly differ from homogenization since the applied Dirichlet BCs do not replicate the theoretical periodic BCs. Besides that, the composite is periodic and thus a unique UC is never an RVE. Therefore, the case 1×1 is omitted in Fig. 3.14. The deviation of the tensor components is calculated as $\left(\beta_{ij}^{*} - \beta_{ij}^{H}\right)/\beta_{ij}^{H} \times 100$. The reference value, β_{ij}^{H}, stands for the result given by the AH method, whereas β_{ij}^{*} is the coefficient value given by the RVE method. A similar scale-size effects analysis for the stiffness tensor was previously conducted, see e.g. [94].

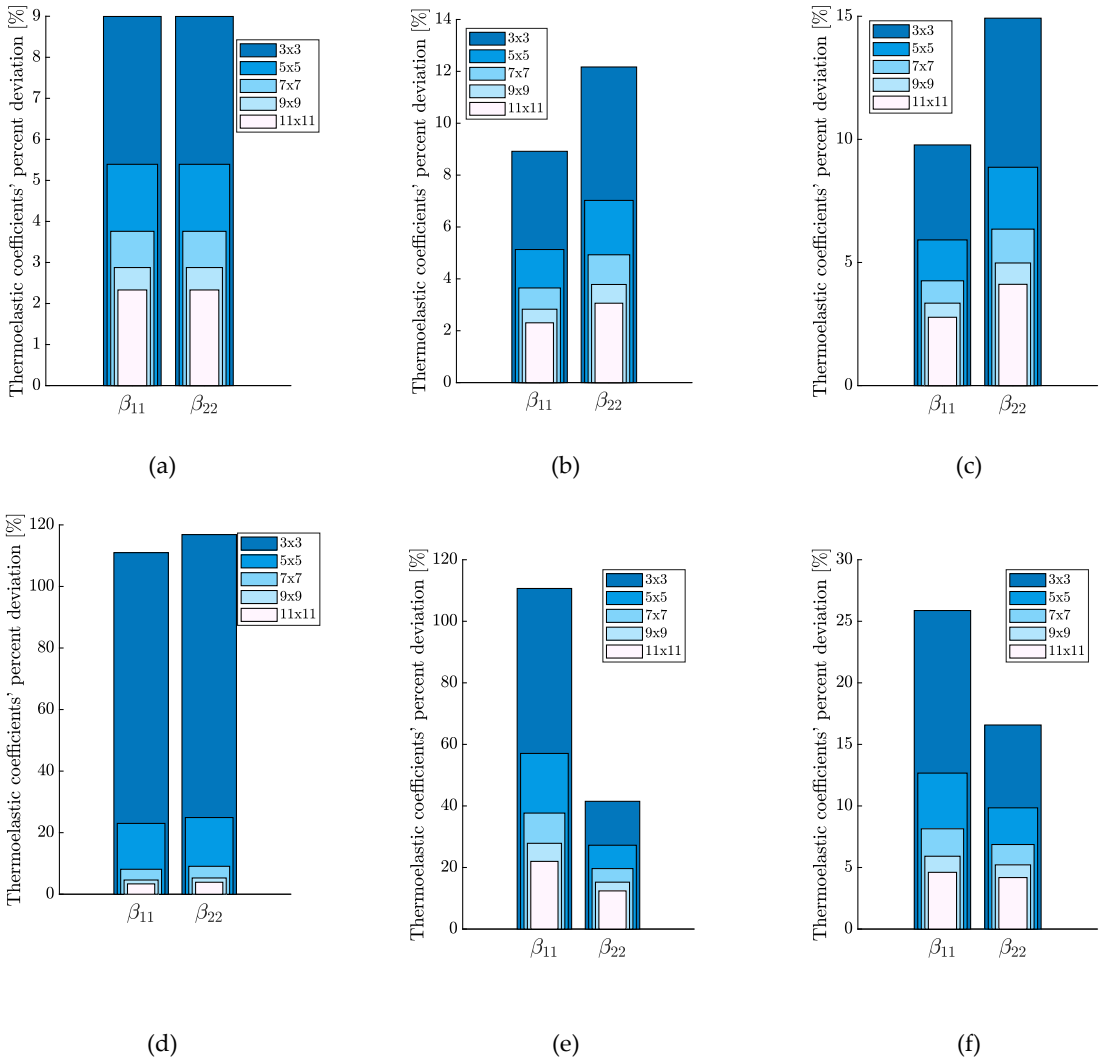

Figure 3.14 – Scale-size effects analysis for the fifth representative point of each example A-F. Percent deviation for the components of β_{ij}^{H}, for example: (a) A; (b) B; (c) C; (d) D; (e) E, and (f) F.

For the examples A to F, with 11×11 UCs, the deviation towards the homogenization, for components β_{11} and β_{22}, respectively, are as follows (extracted from the results in Fig. 3.14): 2.3% for both β's in example A; 2.3% and 3.1% for B; 2.8% and 4.1% for C; 3.4% and 3.9% for D; 21.9% and 12.4% for E; 4.6% and 4.2% for F. Except for example E, all deviations are below 5%, demonstrating remarkably convergence towards the homogenization predictions. In fact, when only considering 3×3 UCs, the β_{11} and β_{22} deviations are already relatively low, between 9% and 15% among examples A-C. On the contrary, for the anisotropic chiral case (D) and arrow-type (E), the deviations considering 3×3 UCs are higher than 100%. However, as more repetitions of the UC are considered, such high deviations rapidly drop.

Regarding the coefficients of the stiffness tensor, repeating 11×11 UCs, on one hand, the largest deviation is verified for the elastic coefficient E_{1122} for all examples, except E, and its values are: 2.0%, 0.9%, 5.6%, 3.8% and 2.1%, respectively. For example E the largest deviation is 1.8%, for the coefficient E_{2222}. On the other hand, the lowest deviation is verified for the component E_{1212}, and is 0.02%, 0.1%, 0.1%, 0.2%, and 0.3%, for each example A, B, D, E and F, respectively. For example C, the lowest deviation is 0.03%, for the component E_{2222}. Therefore, for the elasticity tensor, the convergence of the effective properties toward homogenization is remarkable, with maximum deviations below 6%.

For both the stiffness and thermal stress tensor coefficients, the deviation rapidly decreases as n increases, and the convergence is consistent and quite notable when more than 7×7 UCs are considered, for all examples. Although not every metamaterial solution is here studied regarding scale-size effects, the selected cases can be representative, covering material solutions characterized by orthotropic and isotropic thermal stress tensors and by cubic, orthotropic and anisotropic stiffness tensors.

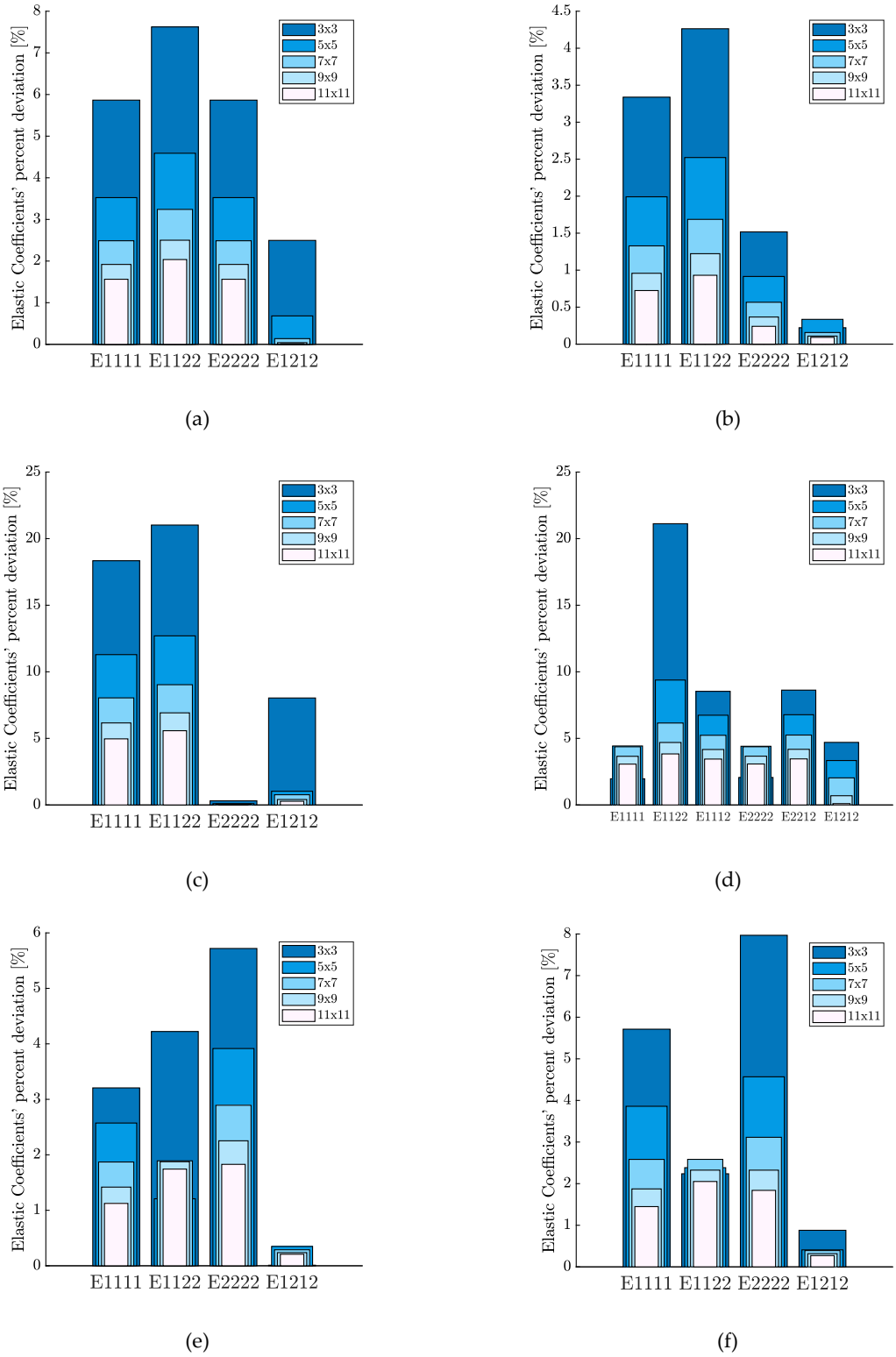

Figure 3.15 – Scale-size effects analysis for the fifth representative point of each example A-F. Percent deviation for the components of E^H_{ijkl}, for example: (a) A; (b) B; (c) C; (d) D; (e) E, and (f) F

3.4.2 Truss-like Microstructures

The optimization problem stated in Eq. (3.42) is solved considering two different initial designs, a 3 × 3 and a 4 × 4 GS, presented in Fig. 3.16a and Fig. 3.16b. The GSs are constructed with full node connectivity, resulting in 66 and 120 potential bar members, for each of the respective discretizations. The penalty parameters of Eq. (3.1) and Eq. (3.2), set in both examples, are $p_1 = 4$ and $p_2 = 2$. The design variables are initialized by setting $\boldsymbol{\rho}_1^0$ as 0.5 and $\boldsymbol{\rho}_2^0$ as 1, whereas $\mathbf{a}_e^0$ is set as 1, in all elements. The weight is set as $\omega = 0.2$ in the objetive function and the volume fraction is set to 0.3 (or 30%). The length of the UC is 3 (Fig. 3.16a) or 4 (Fig. 3.16b), as the length of the horizontal and vertical elements is unitary. The maximum cross-sectional area of the bar FE is set around 2% of the length of the UC, as recommended in [59], meaning that the area of the FE can change between 2.8 mm^2 and 2800 mm^2 for the first case, and between 5 mm^2 and 5000 mm^2 for the second case. The optimization stopping criterion is the maximum number of iterations, set to 150. The chosen material combination is Nylon-PVA (see Table 3.3).

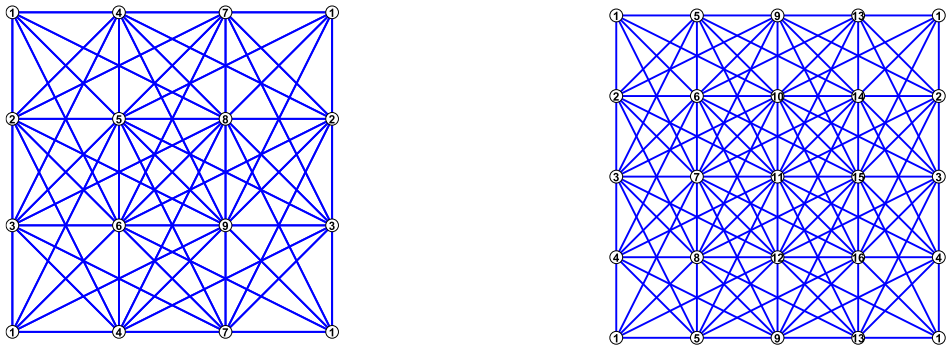

(a) (b)

Figure 3.16 – Initial designs for the truss-like optimization problem, with (a) 3 × 3 and (b) 4 × 4 nodes GS.

The optimized microstructure is presented in Fig. 3.17 for each GS considered. The optimized metamaterial solutions obtained using a truss-like discretized microstructure based on bar elements revealed some important limitations. Since no stiffness criterion was included in the formulation, the resulting designs exhibit low overall stiffness. More critically, the structures possess zero shear stiffness, which would lead them to collapse through a mechanism-like motion under shear loading. Additionally, from a manufacturing perspective, the presence of overlapping bars lacks physical interpretation and would render the design non-manufacturable in practice. This highlights the need to incorporate geometric constraints into the optimization formulation to prevent such overlaps and ensure manufac-

turable designs. Furthermore, stiffness constraints should also be considered in the problem formulation.

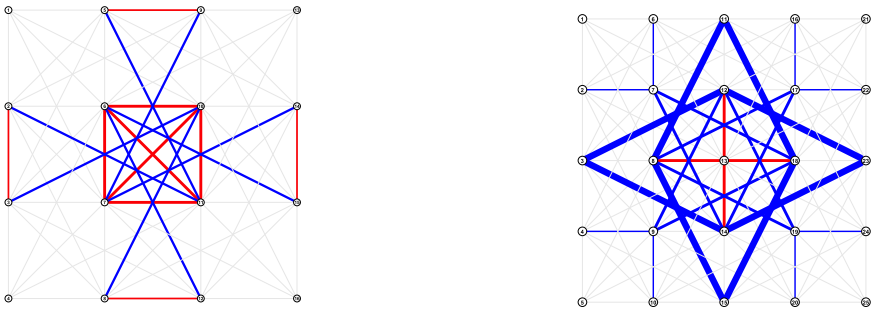

(a) (b)

Figure 3.17 – Optimal microstructure for the (a) 3 × 3 and (b) 4 × 4 nodes GS.

In Table 3.7 is presented, for each example, the periodic material, considering 3 × 3 repetitions of the UC, and the respective homogenized property tensors.

Table 3.7 – Optimal topology and corresponding effective thermoelastic properties of the metamaterials obtained from solving the optimization problem stated in Eq. (3.42).

	3 × 3	4 × 4
Periodic material	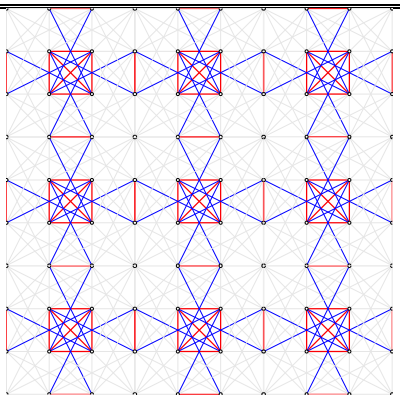	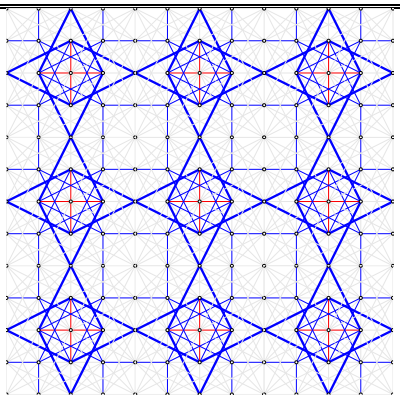
Homogenized properties	$E^H_{ijkl} = \begin{bmatrix} 5.941 & -0.794 & \sim 0 \\ & 5.941 & \sim 0 \\ sym & & \sim 0 \end{bmatrix} \times 10^6 \text{Pa}$	$E^H_{ijkl} = \begin{bmatrix} 7.933 & -2.933 & \sim 0 \\ & 7.933 & \sim 0 \\ sym & & \sim 0 \end{bmatrix} \times 10^4 \text{Pa}$
	$\beta^H_{ij} = \begin{bmatrix} -3.895 \\ -3.895 \\ \sim 0 \end{bmatrix} \times 10^8 \text{ppm°C}^{-1}\text{Pa}$	$\beta^H_{ij} = \begin{bmatrix} -8.381 \\ -8.381 \\ \sim 0 \end{bmatrix} \times 10^5 \text{ppm°C}^{-1}\text{Pa}$
	$\alpha^H_{ij} = \begin{bmatrix} -75.667 \\ -75.667 \\ \sim 0 \end{bmatrix} \text{ppm°C}^{-1}$	$\alpha^H_{ij} = \begin{bmatrix} -16.76 \\ -16.76 \\ \sim 0 \end{bmatrix} \text{ppm°C}^{-1}$

3.5 Conclusions

The microscale optimization problem is here formulated using the weighted sum method, imposing only a total volume constraint, for the sake of design freedom. Since the two objective functions differ much in order of magnitude, weighting them requires careful normalization. It is proposed an amplitude-based normalization as well as scaling objective function values to be between 1 and 100 to meet the GCMMA recommendations. To avoid local minima, for each starting point, seven combinations of penalizations, used in the density-based interpolation laws, are explored along with continuation approaches. This strategy proves to be successful in getting sharp multi-material designs, populating an approximated Pareto front. This quite unfolds PR and CTE as competing design criteria which is an innovative aspect of this work.

The macroscopic (equivalent) thermoelastic behavior of composites is predicted using homogenization theory. While both the AH and EBH methods are equivalent, EBH is more practical as it directly applies boundary conditions in finite element models. This work revisits these methods in the context of inverse homogenization and critically analyses their differences. For gradient-based optimization, only the AH method can compute sensitivities. Additionally, as homogenization hypothesis of infinite periodicity does not hold in practice, a scale-size effect analysis is conducted to compare the homogenization predictions of the effective thermoelastic properties with the mechanical responses of the composite obtained using the RVE method. Similar previous studies had been focused only on elastic properties.

The proposed framework successfully designs bi-material re-entrant and chiral like metamaterials to attain different optimal levels of thermoauxetic or anepectic performance, depending on the relative importance of design objectives. It is then up to the designer preferences or engineering applications to pick one of the attained solutions. Furthermore, both bulk- and shear-driven designs are explored by adapting the objective function and incorporating bulk or shear stiffness constraints. During extensive numerical testing it was verified that the highly non-linear problem of thermoelastic TO generally leads to poor microstructural connectivity. That motivated the implementation of the different material symmetry constraints, namely orthotropy and isotropy on the CTE tensor and cubic symmetry, orthotropy and anisotropy in the stiffness tensor. This way, various examples are presented to explore a broader range of microstructures. Before addressing the multiobjective problem, four material combinations were considered when minimizing the CTE, to gain insight into

the influence of the base materials on achieving a negative CTE. The material combination that leads to a more negative value of CTE was selected to conduct the multiobjective optimization. It was shown, by means of approximated Pareto fronts, that both indexes (CTE and PR) are indeed competing. Improving one index necessarily worsens the other, and vice-versa, due to the shifting optimization paradigm based on the weight assigned to each function. When CTE minimization is prioritized, the resulting microstructures typically exhibit lower stiffness and incorporate both material phases. Conversely, for the PR minimization, the microstructures become stiffer and single material. Furthermore, it was concluded that the auxetic behaviour relies solely on microstructure architecture, whereas CTE depends heavily on material distribution. Finally, scale-size effects were analysed for one preselected solutions of each example. The corresponding UCs are repeated an increasingly number of times, from 3×3 to 11×11. From the present work, it can be concluded that in practice the deviations toward homogenization predictions become quite low by repeating the UC only a few times. For an 11×11 RVE, deviations typically less than 8% and 5% are achieved for the stiffness and thermal stress tensor, respectively.

In terms of the truss-like topology optimization, the problem formulated using bar FE to discretize the UC has demonstrated the capability to optimize truss-like metamaterials exhibiting both NPR and NTE. One significant advantage of this approach is the reduction in the number of finite elements required, which results in lower computational costs and, consequently, improved optimization efficiency. However, there are several challenges that need to be addressed when modelling the microstructure using bar elements. Firstly, while the truss-like discretization effectively captures mechanism-like behavior, which is often expected in metamaterials with extreme properties, it inherently leads to low stiffness. This could limit the performance of the optimized metamaterial, requiring this to be considered in the problem formulation. Additionally, manufacturability considerations must be incorporated at the formulation level, as the ground structure discretization allows for the presence of overlapping bars, which are not feasible to manufacture in practice. Moreover, a truss-like structure modelled with bar FE assumes pinned connections between the bars, a simplification that does not accurately reflect the physical behavior of real materials.

For this reason, to optimize metamaterials with truss-like discretization in a way that reflects more realistic physical characteristics and moves beyond purely conceptual designs, further constraints and considerations must be integrated into the formulation of the optimi-

zation problem. These adjustments will help ensure that the optimized structures are not only theoretically sound but also practically manufacturable and mechanically robust.

Finally, the double-negative index metamaterials covered in this work, impossible to obtain from conventional counterparts, may provide opportunities for forefront engineering applications. However, their applicability still requires further investigation. For example, to prevent failure in service, the thermoelastic design problem should appropriately include fatigue resistance or strength-oriented design criteria. Extensions to three-dimensions and non-linear material behaviour (e.g., dependence on temperature) could be also addressed. In order to allow the additive manufacture of the proposed designs, more research in processing polymers and mainly dissimilar metals is demanded. Experimental characterization and testing are also needed, to validate the computational designs and their predicted performances. The full potential of systematic design is explored here, resulting in the development of metamaterials with negative indexes. This accomplishment highlights the ability of the developed framework to effectively address multiple objectives and constraints, ensuring structural stiffness.

4

MULTISCALE OPTIMIZATION APPROACH

This chapter addresses the multimaterial topology optimization of metamaterials from a multiscale perspective. The advantage of a multiscale model is that it allows the consideration of realistic boundary conditions and therefore designing to a specific structural application, e.g., thermal actuators [101]. In the works outlined in Section 2.1, Fig. 2.3, as well as in the previous chapter, the composite material was treated as an equivalent homogeneous medium, where the macroscopic elastic behaviour is computed through homogenization methods, by analysing the microscale. The thermoauxetic behaviour is thus achieved by manipulating the components of the thermoelastic properties tensor to the desired objective (i.e., PR minimization and CTE minimization). Therefore, the resulting metamaterials are only optimal in terms of equivalent mechanical properties, which may not perform optimally in real structural applications. The development of the thermoelastic macrostructural behavior was published on the scientific paper "Topology optimization of thermoelastic structures with single and functionally graded materials exploring energy and stress-based formulations", published in Structural and Multidisciplinary Optimization in 2025 [168], and it can be regarded as the foundations for the multiscale approach presented in this chapter.

In microscale optimization, the concept of an auxetic material is relatively straightforward, as the focus lies in tailoring the properties of a given material to achieve NPR. However, in a multiscale setting, the interpretation becomes less obvious. Rather than designing purely auxetic material, we must now consider the emergence of auxetic behavior at the structural level and not only reasoning at the material level, i.e., how the arrangement of

the material within a structure of a given shape can lead to an overall auxetic structural response. This raises the key question: what does it mean for a structure to be auxetic? A way to interpret this is to consider the response of a structure under compression in a preferential direction: if the structure contracts laterally (i.e., in the transverse direction), it can be considered to exhibit auxetic behavior. It is important to note, however, that this interpretation relies on the existence of a preferential loading direction, and it cannot be extended to arbitrary loading conditions.

In a pursuit to better understand the unexplored work of thermoauxetic structures, the present chapter addresses the following matters: The general multiscale material model and formulation is presented in Section 4.1, along with FE analysis to better comprehend and validate the multiscale formulation. In Section 4.2 the general concurrent topology optimization problem is formulated, with the respective sensitivity analysis. In Section 4.3, four distinct case studies are presented to demonstrate and evaluate the proposed multiscale framework: (1) design of anisotropic auxetic metamaterials; (2) revisiting the multiobjective optimization problem from Section 3.2.2 and adapting it to the multiscale design setting, to validate the methodology and obtain Pareto fronts in the space of effective properties; (3) investigation of how macroscale features, particularly load changes, influence the material design process; and (4) a benchmark problem of a beam under pure bending, displaying auxetic behavior. Additionally, Section 4.4 presents a computational cost analysis, providing insight into the numerical effort associated with multiscale optimization. Finally, the conclusions regarding the multiscale optimization approach are drawn in Section 4.5.

4.1 Material Model and Proof-of-Concept

4.1.1 Multiscale Material Model

The material model considered here comprises two length scales: the macroscale and the microscale, where the microstructure design domain, Y, corresponds to the UC, and the macroscale design domain Ω, corresponds to the structure. The effective properties of the microscale are computed using the AH method (see section 2.3.1), and the macroscopic behavior (i.e., strains or stress) depends on these homogenized properties. The macroscale material model, represented in Fig. 4.1, is defined by an arbitrary domain Ω, discretized with FE, with applied boundary conditions (e.g., displacement $\mathbf{u}$, forces $\mathbf{F}$ and temperature $\boldsymbol{\Delta T}$). The structure is assumed to be composed of a heterogeneous composite material, and therefore, each

point (or FE) in the macrostructure is associated with a microstructure. Regarding the design parameterization of the macroscale, the microstructure can be uniform throughout the macroscopic domain, or it can differ element-wise or instead it can be the same in subdomains, e.g., layer-wise solutions [128]. These different parameterizations will be further detailed in the following sections.

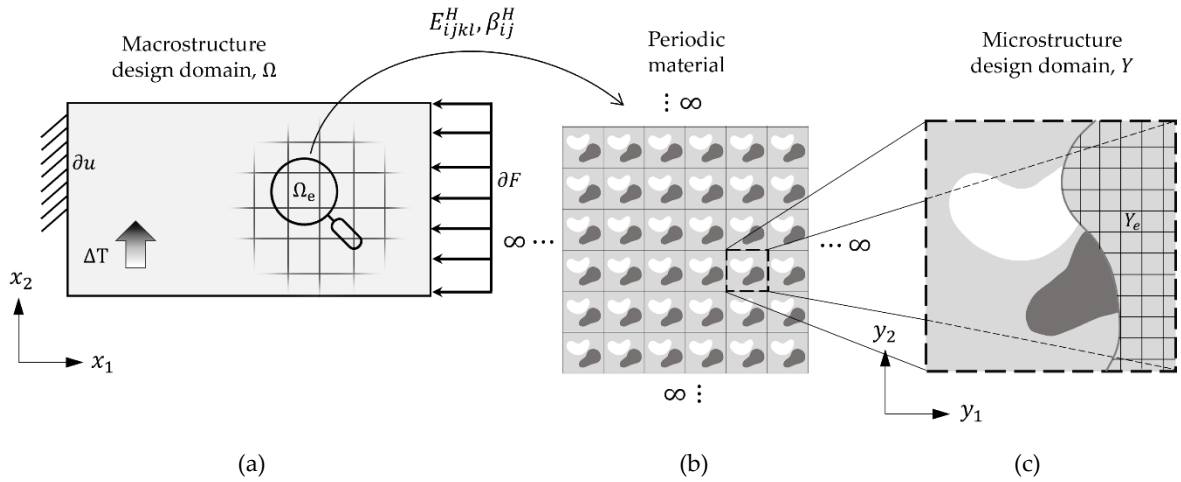

Figure 4.1 – Multiscale material model: (a) Structure (macro) design domain composed of (b) composite material, with (c) periodic microstructure (UC).

Recall the stress-strain relation for a classical linear thermoelastic problem, given by the generalized Hooke's law, defined in Eq. (4.1).

$$\sigma_{ij} = E_{ijkl}\varepsilon_{kl} - \beta_{ij}\Delta\mathrm{T} \tag{4.1}$$

As each point in the macrostructure is associated with a material that has a heterogeneous microstructure, the stiffness and thermal stress tensors, E_{ijkl} and β_{ij}, depend directly on the homogenized quantities:

$$E_{ijkl} = E^H_{ijkl} = \begin{bmatrix} E^H_{1111} & E^H_{1122} & E^H_{1112} \\ & E^H_{2222} & E^H_{2212} \\ sym & & E^H_{1212} \end{bmatrix} \tag{4.2}$$

$$\beta_{ij} = \beta^H_{ij} = \begin{bmatrix} \beta^H_{11} \\ \beta^H_{22} \\ \beta^H_{12} \end{bmatrix} \tag{4.3}$$

These tensors are computed through the homogenization method, where the UC associated with each macroscopic point (see Fig. 4.1c) is discretized using the same reasoning introduced in the previous chapter.

The linear static equilibrium equation of the macrostructure, for a thermoelastic problem is $\mathbf{KU} = \mathbf{F}$, where the load vector includes both mechanical and thermal loads, i.e., $\mathbf{F} = \mathbf{F}^m + \mathbf{F}^{th}$. Consequently, the displacements are solution of applying both thermal and mechanical loads, i.e., $\mathbf{U} = \mathbf{U}^m + \mathbf{U}^{th}$. Note that the thermal and mechanical problems are decoupled such that the equilibrium problem, $\mathbf{K}(\mathbf{U}^m + \mathbf{U}^{th}) = \mathbf{F}^m + \mathbf{F}^{th}$, can be considered individually as $\mathbf{KU}^m = \mathbf{F}^m$ and $\mathbf{KU}^{th} = \mathbf{F}^{th}$. The global structural stiffness matrix of the macroscale, $\mathbf{K}$, is given by Eq. (4.4):

$$\mathbf{K} = \sum_{e^M=1}^{N^M} \int_{V_{e^M}} \mathbf{B}_{e^M}^{\mathrm{T}} \mathbf{E}_{e^M}^{H} \mathbf{B}_{e^M} \mathrm{d}V_{e^M} \tag{4.4}$$

where N^M is the number of macro FE, $\mathbf{B}_{e^M}$ denotes the strain-displacement matrix of the macro FE, $\mathbf{E}_{e^M}^{H}$ is the stiffness tensor of the macro FE, considering the heterogeneity of the microscale (see Eq. 4.2) and V_{e^M} is the macro FE volume.

The mechanical load vector, $\mathbf{F}^m$, is design-independent and accounts for all the externally applied macroscopic mechanical loads. The thermal load vector is design dependent, as it arises from the temperature field applied to the macrostructure, as defined in Eq. (4.5):

$$\mathbf{F}^{th} = \sum_{e^M=1}^{N^M} \int_{V_{e^M}} \mathbf{B}_{e^M}^{\mathrm{T}} \boldsymbol{\beta}_{e^M}^{H} \Delta \mathrm{T} \mathrm{d}V_{e^M} \tag{4.5}$$

where $\boldsymbol{\beta}_{e^M}^{H}$ is the thermal stress tensor of the macroscale, depending on the microscale, see Eq. (4.3), and ΔT the applied macroscopic temperature.

The equilibrium equation is solved at the macroscale, considering that the structure is composed of a heterogeneous composite material. The relation between both scales is thus given by the stiffness matrix (Eq. 4.4) and the thermal load vector (Eq. 4.5). Therefore, a multiscale problem is solved, where the macroscale quantities, used in the problem formulation, depend on the microscopic material lay-outs.

The strain in each macro element Ω_{e^M} is assumed uniform and computed as an area average (in 2D problems) of the strain components ε_{ij} computed at each Gauss point of the FE, i.e.,

$$\varepsilon_{ij}^{e^M} = \frac{1}{\Omega_{e^M}} \int_{\Omega_{e^M}} \varepsilon_{ij}^{GP} \, \mathrm{d}\Omega_e \tag{4.6}$$

where ε_{ij}^{GP} is the strain in each Gauss point and Ω_e is the macro element's domain. Each element has a total of four (2 × 2) Gauss points. Using a FE formulation to solve the equilibrium equations, the macroscopic element strain is obtained from the displacement field according to Eq. (4.7).

$$\boldsymbol{\varepsilon} = \mathbf{B}\mathbf{U} \tag{4.7}$$

where both thermal and mechanical effects are included in the total displacement, i.e., $\mathbf{U} = \mathbf{U}^m + \mathbf{U}^{th}$, and so, $\boldsymbol{\varepsilon} = \boldsymbol{\varepsilon}^m + \boldsymbol{\varepsilon}^{th}$.

The discretized thermal stress tensor is given by Eq. (4.8).

$$\boldsymbol{\varepsilon}^{th} = \boldsymbol{\alpha}^H \Delta \mathrm{T} \tag{4.8}$$

Since the structure is discretized into multiple FEs, its overall strain is evaluated as a volumetric average of the local strain values associated with each macroscopic finite element, according to Eq. (4.9).

$$\bar{\varepsilon}_{ij} = \frac{1}{\Omega}\int_{\Omega} \varepsilon_{ij}^{e^M} \, \mathrm{d}\Omega \tag{4.9}$$

where $\bar{\varepsilon}_{ij}$ is the average strain of the structure, the element strain, $\varepsilon_{ij}^{e^M}$ is computed according to Eq. (4.6), for each macro element and Ω is the macro domain. The reasoning is the same for both mechanical and thermal average strain. This approach is relevant in the multiscale context, where the goal is to understand how a structure can exhibit material-like behavior, i.e., auxeticity. Therefore, the global response of a structure must be interpreted in terms of average quantities.

One of the main advantages of considering the multiscale model is that it allows for the computation of real properties of PR and CTE, instead of using the homogenized coefficients. The PR is, by definition, the ratio of transverse strain deformation to longitudinal strain deformation under tension/compression, i.e., $\nu_{long} = \varepsilon_{trans}/\varepsilon_{long}$. For a structure to exhibit NPR, it should expand in the lateral direction when stretched axially and contract laterally when compressed. The CTE describes how much the structure's size (say strain) changes per unit change in temperature, expressed as $\boldsymbol{\alpha} = \boldsymbol{\varepsilon}/\Delta \mathrm{T}$. A material exhibiting NTE contracts when heated and expands when cooled. Therefore, using a multiscale material model, allows to directly compute the PR and the CTE properties, based on the structure deformation, by Eq. (4.10) and Eq. (4.11), respectively:

$$\bar{\nu}_{21} = -\frac{\bar{\varepsilon}_{22}^{m}}{\bar{\varepsilon}_{11}^{m}};\ \bar{\nu}_{12} = -\frac{\bar{\varepsilon}_{11}^{m}}{\bar{\varepsilon}_{22}^{m}} \tag{4.10}$$

$$\bar{\alpha}_{11} = \bar{\varepsilon}_{11}^{th}/\Delta T;\ \bar{\alpha}_{22} = \bar{\varepsilon}_{22}^{th}/\Delta T \tag{4.11}$$

where $\bar{\varepsilon}_{ij}^{m}$ and $\bar{\varepsilon}_{ij}^{th}$ are the averaged macroscopic mechanical and thermal strain, respectively.

4.1.2 Proof-of-concept

Here, a simplified macroscopic material model is considered, in which the entire structural domain is composed of a spatially uniform heterogeneous material. FE simulations are performed to evaluate the mechanical response of the macrostructure (strain distribution and mechanical properties). The numerical implementation of Eqs. (4.4)-(4.9) was done in MATLAB® R2024b and the results are compared with those obtained using the commercial software Ansys Mechanical APDL®, to validate the proposed framework.

Two load cases of compression in both vertical and horizontal directions are considered, with a force of $F = 1$ kN as well as a thermal load case, with $\Delta T = 100$, see Fig. 4.2a, 4.2b and 4.2c, respectively. From the loading conditions in Fig 4.2a and 4.2b, ν_{21} and ν_{12} are computed, respectively, according to Eq. (4.10). The thermal load case in Fig. 4.2c allows to compute the CTE in both directions, as stated in Eq. (4.11).

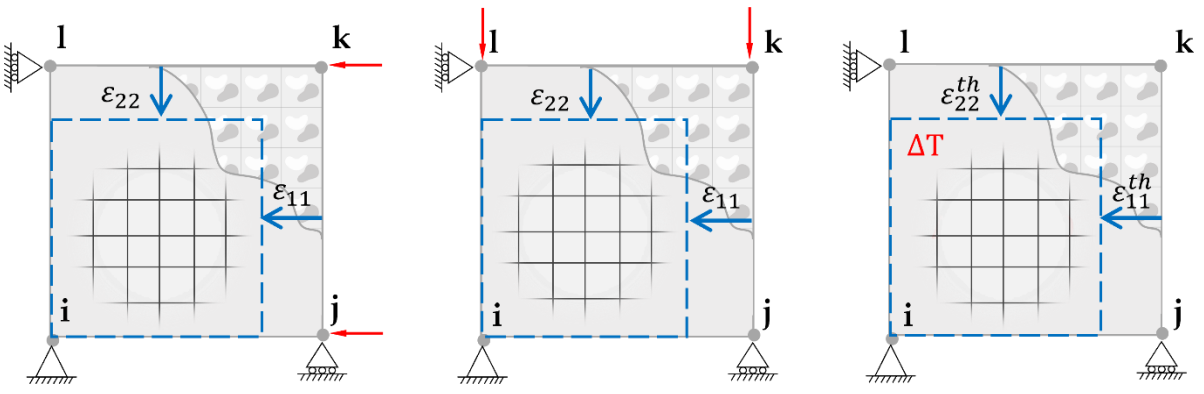

(a) (b) (c)

Figure 4.2. – Schematic BCs for the multiscale topology optimization framework, considering a square structure design domain. (a) Horizontal compression; (b) vertical compression and (c) uniform thermal load.

Recalling the results from Section 3.5.1, the microstructures A, C, D and F are used here to define the structure's material and solve the equilibrium equations. These examples are chosen here to cover a range of tensor symmetries. For the elasticity tensor, the considered cases include cubic symmetry (A and F), orthotropic (C), and anisotropic (D). Regarding the

thermoelastic tensor, C and F exhibit orthotropic symmetry, while A and D are isotropic. The tensors for the respective examples are presented in Table 3.6.

In all cases except D, the macrostructure is discretized using a single macro FE, i.e., $N^M = 1$, with unitary dimensions. This simplification is justified by the orthotropic nature of the stiffness tensor, which ensures that, under uniaxial loading, the deformation of the structure remains orthogonal, that is, the initial edges at right angles of the structure remain so after the deformation. Therefore, a single element is sufficient to capture the global mechanical response. However, in the anisotropic case D, this orthogonality is no longer preserved. To capture this behavior, different discretizations of the macrostructure are explored, namely 1×1, 5×5, 10×10 and 100×100 2D unitary quadrilateral element (Q4) grid meshes. In fact, the BCs used are not ideal for anisotropic materials, as the deformation under compression is not expected to align orthogonally with the global axes, i.e., horizontal and vertical direction. These constraints introduce reaction forces that result in a non-uniform stress distribution across the macrostructure, which should be kept in mind when interpreting the results of the anisotropic case. Yet, the applied BCs do not invalidate the findings and are consistently applied to all examples in this section.

Finally, the PR and CTE properties are computed by both the microscale model, i.e., $\nu_{21} = E^H_{1122}/E^H_{2222}$, $\nu_{12} = E^H_{1122}/E^H_{1111}$, $\alpha_{11} = \alpha^H_{11}$ and $\alpha_{22} = \alpha^H_{22}$, and macroscale model through Eq. (4.10) and (4.11). This way it is possible to find out to what extent the measures based on the homogenized quantities differ from the real properties. For the cases A, C and E, as the elastic tensor is orthotropic, both measurements (micro and macro) are expected to give the exact same results (recall Section 2.2). However, for the anisotropic case (D), the measurement represents an approximate measure of the deformation ratio in the principal directions [107], and therefore it is expected that an error is associated with this case. The results obtained for cases A, C and F are summarized in Table 4.1. The error between both predictions is calculated as $(\nu_{12}^{Macro} - \nu_{12}^{micro})/\nu_{12}^{micro} \times 100$ (for all properties).

For the cases with an orthotropic stiffness tensor, both the microscale and macroscale models yield the same result, confirming the consistency and accuracy of the homogenization predictions in these cases. This consistency was already expected, as the predictions of the properties computed from the microscale model (i.e., ratio between homogenized coefficients), derive directly from the real definition of PR (i.e., ratio between strains).

Table 4.1 – Comparison of effective properties of PR and CTE computed through homogenization (micro) and structural analysis (macro), for different orthotropic microstructures.

Microstructure		Property	Micro	Macro	Error %
A	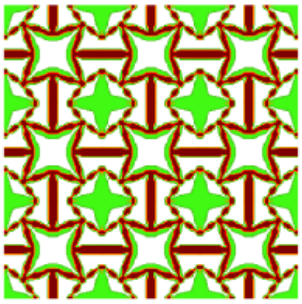	ν_{21}	-0,876	-0,876	0,00%
		ν_{12}	-0,876	-0,876	0,00%
		α_{11}	-124,886	-124,886	0,00%
		α_{22}	-124,886	-124,886	0,00%
C		ν_{21}	-0,591	-0,591	0,00%
		ν_{12}	-1,514	-1,514	0,00%
		α_{11}	-332,420	-332,420	0,00%
		α_{22}	-148,108	-148,108	0,00%
F	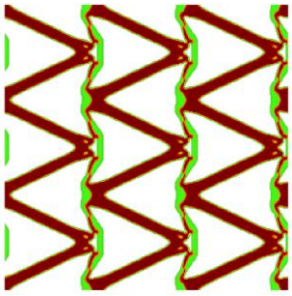	ν_{21}	-0,568	-0,568	0,00%
		ν_{12}	-0,573	-0,573	0,00%
		α_{11}	-95,498	-95,498	0,00%
		α_{22}	13,124	13,124	0,00%

The deformed configurations for Examples A and C are shown in Fig 4.3. A scale factor of 3 is used to illustrate the elastic deformation under the boundary conditions (BCs) illustrated in Fig. 4.2a and Fig. 4.2b, while a scale factor of 10 is used to visualize the thermal deformation (BCs in Fig. 4.2c). The black dashed line represents the undeformed configuration of the macrostructure.

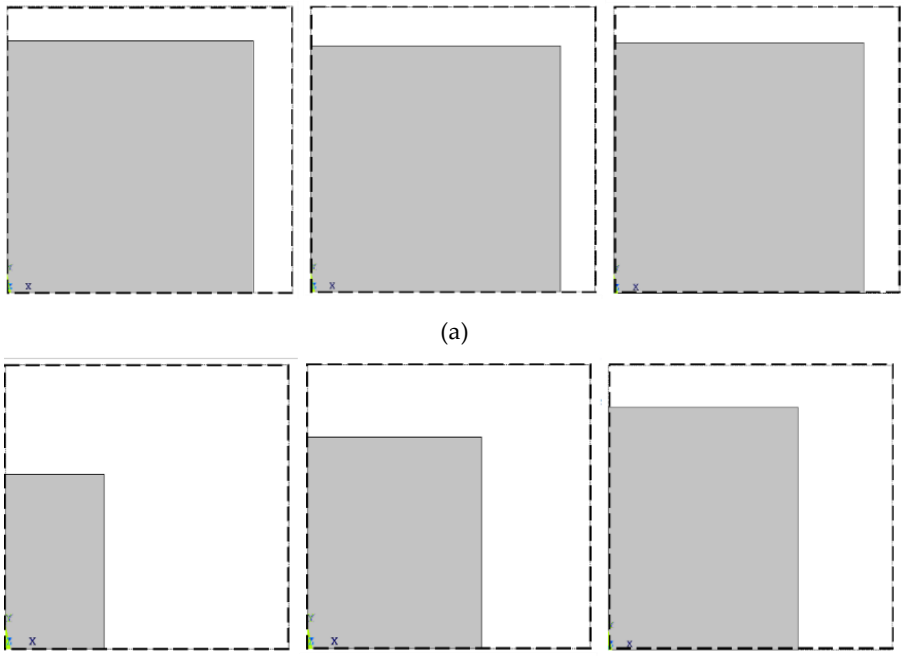

(a)

(b)

Figure 4.3 – Deformed configurations for example (a) A and (b) C, for the three BCs illustrated in Fig. 4.2, reading from left to right.

As illustrated by the polar plots presented in Table 3.6, example C exhibits lower stiffness along the principal directions compared to example A, explaining the higher deformation observed in this case. For case A, due to the cubic symmetry of the elastic tensor, both elastic BCs render the same result. In contrast, case C shows a directional dependence on its mechanical response. Regarding thermal deformation, example A yields equal thermal strain in both vertical and horizontal directions, whereas example C displays different thermal strains in each direction due to the orthotropic nature of its CTE tensor.

A detailed analysis of the mechanical behavior of the anisotropic case, D, is presented below. The mechanical properties computed from both micro and macro models, for the four different discretizations of the macro structure, are presented in Table 4.2. The macroscopic property used for error calculation corresponds to the most refined discretization, which is 100×100, as it provides the highest level of accuracy in the structural analysis.

Table 4.2 – Comparison of effective properties of PR and CTE computed through homogenization (micro) and structural analysis (macro), for anisotropic microstructure, with different discretizations.

Microstructure		Micro	Macro				Error %
			1	5	10	100	
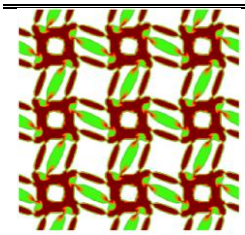	ν_{21}	-0,900	-0,834	-0.498	-0.389	-0.316	64.88%
	ν_{12}	-0,898	-0,832	-0.497	-0.390	-0.315	64.86%
	α_{11}	-126,188	-126,169	-126.174	-126.176	-126.177	0.01%
	α_{22}	-126,075	-126,094	-126.089	-126.086	-126.085	0.01%

In the anisotropic case (D), a relative error of approximately 65% is observed when comparing the microscale-based prediction with the macroscale results. Unlike the orthotropic cases, the homogenized PR in this setting should be interpreted as an approximate measure, i.e., so-called quasi-effective PR [107]. However, as the mesh of the macrostructure is refined, the discrepancy between the microscale prediction and the actual macroscopic response becomes more pronounced. This discrepancy highlights a critical limitation: employing a homogenized microscale model to represent anisotropic metamaterials may lead to significant deviations from the actual structural response, and therefore the multiscale design model must be pursued.

The elastic deformed configurations for example D, for the 1×1, 5×5, 10×10 and 100×100 discretizations are shown in Fig. 4.4. The thermal deformation remains orthogonal as the CTE tensor is isotropic (similar to the deformation in example A), and therefore will not be shown here, for the sake of brevity. A scale factor of 3 is used here as well to represent the elastic deformation under the BCs illustrated in Fig. 4.2a and Fig. 4.2b.

As the discretization of the macrostructure becomes more refined, the deformation reveals angular distortions that are not captured when using a single finite element. With a discretization of 10×10 elements, the mechanical response is already well approximated. The observed trend of the PR becoming less negative with increasing mesh refinement is consistent with the physical behavior, as the transverse displacements (along the top edge in the first deformation case and the left edge in the second) begin to exhibit both positive and negative values. Finally, note that the average strain measurement used to evaluate the effective PR corresponds to a volumetric average over the entire structure, see Eq. (4.10). As such, the resulting value should be interpreted as an estimate of the overall structural response, rather than an exact material property.

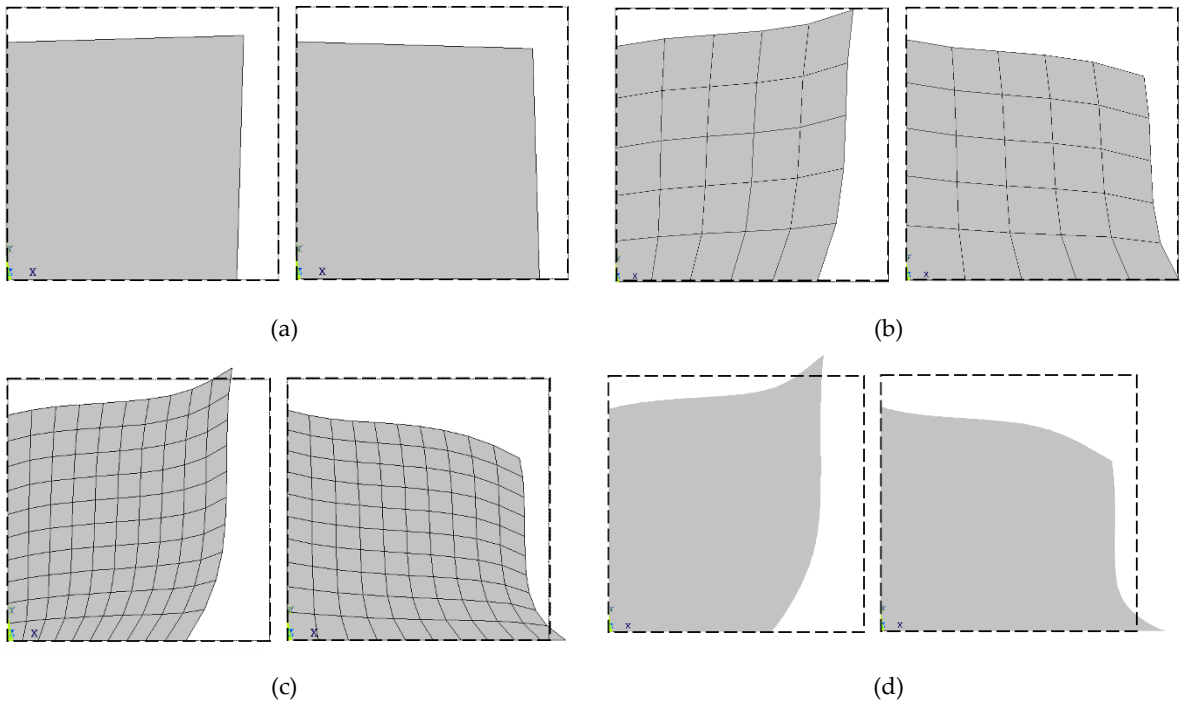

Figure 4.4 – Deformed configurations for example D, under the BCs illustrated in Fig. 4.2a and Fig.4.2b, for the macrostructure discretized with (a) 1 × 1, (b) 5 × 5, (c) 10 × 10 and (d) 100 × 100 elements.

4.2 Topology Optimization Framework

By reformulating the problem in terms of strains, it becomes possible to accurately address the PR and CTE in the objective function as true measures of the structural response, unlike the microstructural optimization problem where homogenized coefficients are manipulated. The optimization problem to achieve negative indexes can thus be posed as a strain-related minimization problem. Different algorithmic strategies and design parameterizations can be used to solve this problem, but here the so-called implicit strategy is adopted, as it assumes that the macro density is implicitly computed through the micro density distribution [128]. This allows the micro problems to be all solved at once, which results in a more straightforward algorithm implementation and generally it exhibits fewer convergence issues. However, a major drawback is its parallel implementation not being straightforward. Therefore, a serial run, can easily lead to a high computational cost, as it will be addressed in Section 4.4.

Regarding the design parameterizations, the microstructure can be optimized either considering it constant throughout the entire macroscopic domain, in a layer-wise fashion or considering the macrostructure varying point-wisely. As the PR is a measure that depends on a load direction, and to facilitate the interpretation of results, as well as reducing the computational costs, only a uniform and layer-wise approach [100,140] are investigated in

this chapter, paving the way for addressing future challenges within the multiscale approach. The material model considered in the multiscale optimization problem is represented in Fig. 4.5.

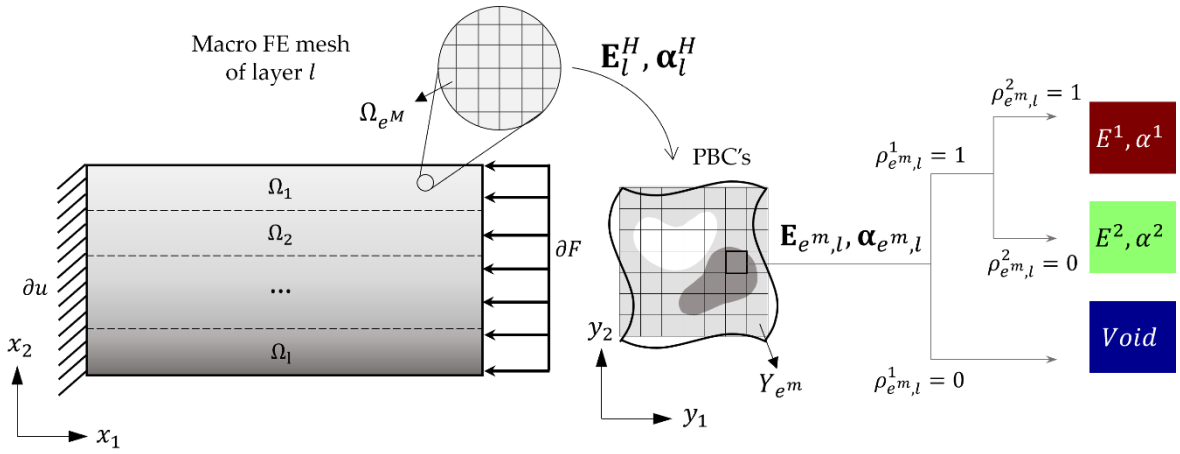

Figure 4.5 – Multiscale material model considering a multimaterial periodic microstructure in each macro subdomain, layer-wise design parameterizations.

The structural design macro domain is divided into nl smaller design subdomains, here referred to as *layer*, Ω_l, with $l \in [1 \dots nl]$ and $\sum\Omega_l \equiv \Omega$. In the uniform case, a single material microstructure is required everywhere, which means using $nl = 1$ in this model. Each layer can be discretized using the desired mesh resolution (more or less refined), with N^M 2D plane macro FE (Q4), and $\sum\Omega_{e^M} \equiv \Omega_l$, where Ω_{e^M} is the domain of each macro element. All macro elements in the same layer have the same homogenized properties. For each layer there is a corresponding microstructure, discretized with a square grid mesh of N^m micro FE. For the sake of consistency between the multiscale and microscale formulation, the micro-design variables are here denoted as $\rho^t_{e^m,l}$, where the superscript t is either 1, meaning that the variable is topological or 2, for the material selection design variable. The subscript e^m refers to the micro FE $e^m \in [1 \dots N^m]$ of the microstructural material of layer l. The interpolation of the material properties at the microscale level is done in the same manner as previously shown through Eq. (3.1) and (3.2). The design variables are only the microscale density variables. It is assumed that the macrostructure topology basically remains unchanged, i.e., macro domain is completely occupied by composite layers of microstructures. However, the volume of each layer is dependent on the distribution of the microstructure density design variable, i.e., $V_l = \int_Y \rho^1_{e^m,l} dY$. Therefore, even without macro design variables, the problem

is still a multiscale topology optimization problem, as the volume of the different layers is not fixed *a priori* and depend on the microscale topology.

In the implicit strategy the design variables are optimized at the same time by the optimizer, in this case, the MMA or GCMMA [16,117]. The design variables vector is constructed the following way: firstly, the micro density design variables of all N^m FE of layer 1 are stored, then those from layer 2 and so forth until layer nl. Then all the micro material selection design variables are stored in the same way. Therefore, the total number of design variables is $2 \times nl \times N^m$ and the vector of the design variables is filled the following:

$$\boldsymbol{\rho} = \left[\rho^1_{1,1} \dots \rho^1_{N^m,1}\, \rho^1_{1,2} \dots \rho^1_{N^m,2} \dots \rho^1_{N^m,nl}\, \rho^2_{1,1} \dots \rho^2_{N^m,nl}\right] \tag{4.12}$$

To solve the multiscale optimization problem, an algorithm implementation is carried out resorting to Matlab® language, which integrate the previous developed microscale optimization procedures. The general multiscale optimization methodology proposed in this chapter is given by the flowchart shown in Fig. 4.6.

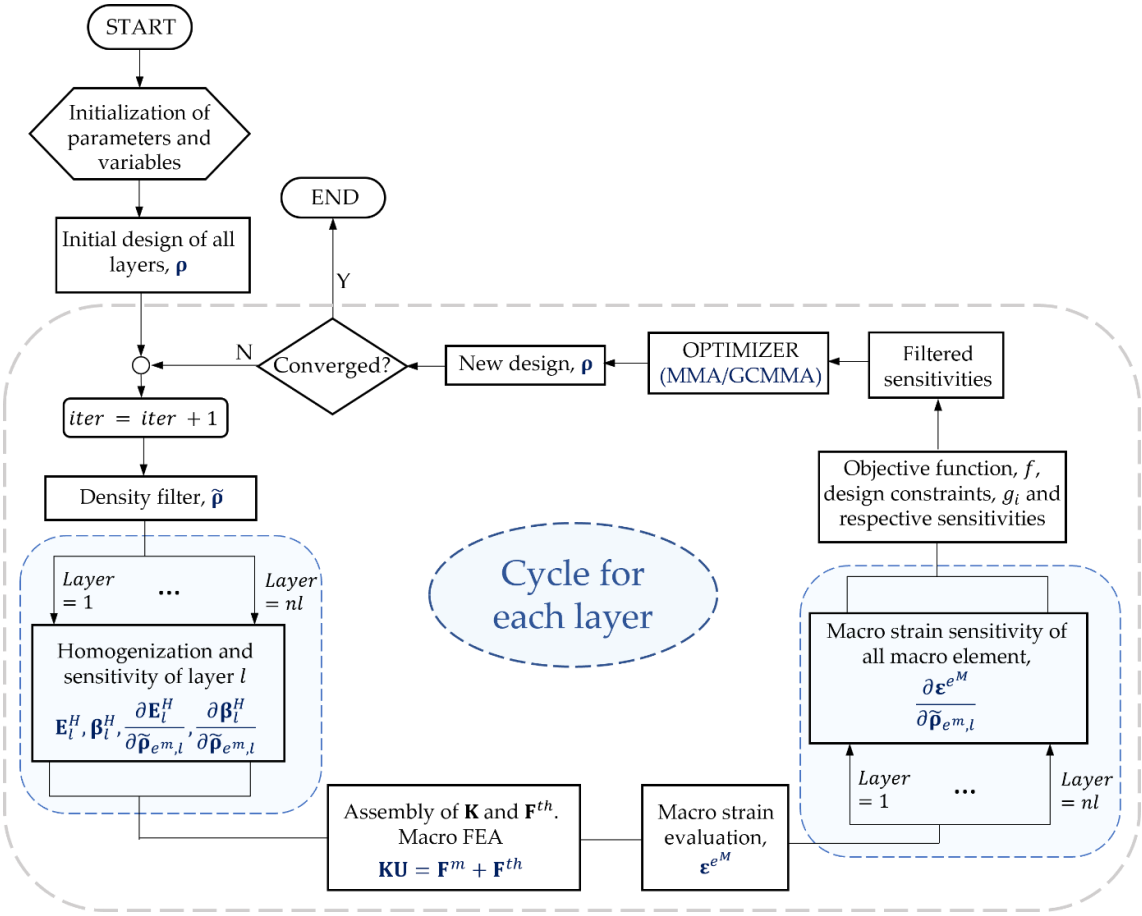

Figure 4.6 – Flowchart illustrating the optimization algorithm for multiscale topology optimization.

First, the design variables are initialized according to the chosen initial design and then filtered using a density filter. The effective properties and corresponding sensitivity analysis are computed for each layer, depending on its microscopic material. Next, the macroscopic stiffness matrix, Eq. (4.4), and thermal load vector, Eq. (4.5), are assembled, allowing for the finite element analysis at the macroscale. From this analysis, the average strain in each macro element is calculated, along with its sensitivity. The objective and constraint functions are then evaluated, and their sensitivities filtered. Finally, the optimization problem is solved, and the unfiltered design variables, Eq. (4.12), are updated. This cycle repeats until convergence is achieved or the maximum number of iterations is reached.

4.2.1 Strain Evaluation and Sensitivity Analysis

The main advantage of the multiscale model is that instead of using an objective function that simply handles homogenized coefficients to minimize (indirectly) the PR and CTE, it deals directly with the definition of PR and overall auxetic structure response, recall Eq. (4.10) and (4.11). Therefore, the objective function to minimize PR and CTE can be defined directly from strains, respectively, by Eq. (4.13) and Eq. (4.14).

$$f_\nu = \bar{\nu}_{12} + \bar{\nu}_{21} = -\frac{\bar{\varepsilon}^m_{11}}{\bar{\varepsilon}^m_{22}} - \frac{\bar{\varepsilon}^m_{22}}{\bar{\varepsilon}^m_{11}} \tag{4.13}$$

$$f_\alpha = \bar{\alpha}_{11} + \bar{\alpha}_{22} = \bar{\varepsilon}^{th}_{11} + \bar{\varepsilon}^{th}_{22} \tag{4.14}$$

where the average mechanical strain $\bar{\boldsymbol{\varepsilon}}^m$ is computed by applying the load cases descripted in Fig. 4.2a e 4.2b, guaranteeing that the PR in both directions is optimized. The average thermal strain $\bar{\boldsymbol{\varepsilon}}^{th}$ is computed by applying a constant temperature of $\Delta T = 100℃$, corresponding to the load case in Fig. 4.2c. Note that the objective functions do not necessarily need to be the sum of the properties in both directions, and can be adapted for a specific target, e.g., enhancing the mechanical response in a given direction.

The sensitivity of the objective function w.r.t. the design variables is given by the derivative of the average strain. Recall that the average strain of a macrostructure is given by Eq. (4.9). This strain is computed by solving the equilibrium equations, and so it is function of the displacement, i.e., $\varepsilon_{ij}^{e^M}\left(\mathbf{U}_{e^M}\right)$. The derivative of the strain of each macro element, w.r.t the filtered densities, is given by:

$$\frac{\mathrm{d}\varepsilon_{ij}^{e^M}}{\mathrm{d}\tilde{\rho}_{e^m,l}^{t}} = \frac{\mathrm{d}\varepsilon_{ij}^{e^M}}{\mathrm{d}\tilde{\rho}_{e^m,l}^{t}} + \frac{\partial\varepsilon_{ij}^{e^M}}{\partial\mathbf{U}_{e^M}}\frac{\partial\mathbf{U}_{e^M}}{\partial\tilde{\rho}_{e^m,l}^{t}} \tag{4.15}$$

where the first term of Eq. (4.15) is null. The derivative of the strain in order to the element displacement is simply the derivative of Eq. (4.7):

$$\frac{\partial\varepsilon_{ij}^{e^M}}{\partial\mathbf{U}_{e^M}} = \mathbf{B}_{e^M} \tag{4.16}$$

Note that if the macro-FE mesh is made of a regular mesh with all FE with the same geometry, this derivative only needs to be computed once, and it's the same for all elements. As for the derivative of the displacement in order to the design variables, the adjoint method is used (recall Section 2.4.5.1), and the derivative is given by Eq. (4.17):

$$\frac{\partial\mathbf{U}_{e^M}}{\partial\tilde{\rho}_{e^m,l}^{t}} = \mathbf{K}^{-1}\left[\frac{\partial\mathbf{F}}{\partial\tilde{\rho}_{e^m,l}^{t}} - \frac{\partial\mathbf{K}}{\partial\tilde{\rho}_{e^m,l}^{t}}\mathbf{U}\right] \tag{4.17}$$

Now, replacing both Eq. (4.16) and (4.17) into (4.15), yields:

$$\frac{\mathrm{d}\varepsilon_{ij}^{e^M}}{\mathrm{d}\tilde{\rho}_{e^m,l}^{t}} = \boldsymbol{\lambda}^{\mathrm{T}}\left[\frac{\partial\mathbf{F}}{\partial\tilde{\rho}_{e^m,l}^{t}} - \frac{\partial\mathbf{K}}{\partial\tilde{\rho}_{e^m,l}^{t}}\mathbf{U}\right] \tag{4.18}$$

From Eq. (4.18) it comes that the adjoint problem is given by:

$$\mathbf{K}\boldsymbol{\lambda} = \left(\mathbf{B}'_{e^M}\right)^{\mathbf{T}} \tag{4.19}$$

Now note that the dimensions of the matrixes in Eq. (4.18) and Eq. (4.19) depends on the total number of degrees of freedom (dofs) of the structure, $ndof$, as the adjoint problem is solved at the global level for the entire structure, i.e., for the equilibrium problem $\mathbf{KU} = \mathbf{F}$. Therefore, to solve Eq. (4.19), the variable $\mathbf{B}'_{e^M}$ is in fact the strain-displacement matrix, assembled in the global dimension. That is, the dimension of $\mathbf{B}'_{e^M}$ is $3 \times ndof$, with null columns in the dofs that don't correspond to the dofs of the element e^M, and it is equal to $\mathbf{B}_{e^M}$ in the dofs of the element (i.e., strain-displacement matrix of the macro FE, with dimension 3×8). If the macro mesh is regular, the matrix $\mathbf{B}_{e^M}$ is the same for all elements. For each macro element, the adjoint problem in Eq. (4.19) is solved only once, as it depends solely on the macro element itself and not on the specific microscale design variable with respect to which the sensitivity is being computed.

The derivative of the stiffness matrix and the thermal stress tensor, in Eq. (4.4) and (4.5), are given by Eq. (4.20) and Eq. (4.21), respectively:

$$\frac{\partial \mathbf{K}}{\partial \tilde{\rho}^{t}_{e^{m},l}} = \sum_{e^{M}=1}^{N^{M}} \int_{V_{e^{M}}} \mathbf{B}^{\mathrm{T}}_{e^{M}} \frac{\partial \mathbf{E}^{H}_{e^{M}}}{\partial \tilde{\rho}^{t}_{e^{m},l}} \mathbf{B}_{e^{M}} \mathrm{d}V_{e^{M}} \tag{4.20}$$

$$\frac{\partial \mathbf{F}^{th}}{\partial \tilde{\rho}^{t}_{e^{m},l}} = \sum_{e^{M}=1}^{N^{M}} \int_{V_{e^{M}}} \mathbf{B}^{\mathrm{T}}_{e^{M}} \frac{\partial \boldsymbol{\beta}^{H}_{e^{M}}}{\partial \tilde{\rho}^{t}_{e^{m},l}} \Delta \mathrm{T} \mathrm{d}V_{e^{M}} \tag{4.21}$$

In this case, the homogenized stiffness tensor of the element e^{M}, $\mathbf{E}^{H}_{e^{M}}$, depends solely on the micro density of the layer l where the macro element is located. This means that the derivative is only non-zero when $e^{M} \in l$. For example, if the macro element is in the first layer, and the derivative of its strain is being computed in order to the micro design variables of the second layer, the derivative of the homogenized stiffness tensor is null, i.e.,

$$\frac{\partial \mathbf{E}^{H}_{e^{M}}}{\partial \tilde{\rho}^{t}_{e^{m},l}} = \begin{cases} \text{Eq. (3.28)}, & if\ e^{M} \in l \\ \mathbf{0}_{3\times 3}, & if\ e^{M} \notin l \end{cases} \tag{4.22}$$

The exact same reasoning is applied to the derivative of the thermal stress tensor, where $\partial \boldsymbol{\beta}^{H}_{e^{M}} / \partial \tilde{\rho}^{t}_{e^{m},l}$ is given by:

$$\frac{\partial \boldsymbol{\beta}^{H}_{e^{M}}}{\partial \tilde{\rho}^{t}_{e^{m},l}} = \begin{cases} \text{Eq. (3.29)}, & if\ e^{M} \in l \\ \mathbf{0}_{3\times 1}, & if\ e^{M} \notin l \end{cases} \tag{4.23}$$

Furthermore, within each layer, the microstructure is assumed to be uniform. As a result, the local (microscale) problem for computing the homogenized properties only needs to be solved once per layer, regardless of the number of macro finite elements used to model it. Consequently, the derivatives in Eqs. (4.22) and (4.23) are also computed just once per layer.

As the strain is not a global measure, but instead a local one, the derivative of the strain of each element must be computed in order to all micro design variables, to be able to compute the volume average in Eq. (4.9). This means that as the macro-FE mesh refinement increases, so does the computational time, at it will be discussed in Section 4.4, and the implicit strategy becomes infeasible, as it does not favor parallelization. However, for the sake of the examples presented in this chapter, the implicit strategy is implemented.

4.2.2 Microscopic Stress Evaluation

In the context of a multiscale analysis, it makes sense to evaluate not only the microscopic strain but also the stress distribution across the microstructure domain, since it is now inserted in a macro structure externally loaded. The stress in the microstructure is computed for each element, $\boldsymbol{\sigma}$, using the thermal stress equation in (4.24). For convenience, the subscript e^M is omitted bellow, but all variables are assumed to refer to element quantities.

$$\boldsymbol{\sigma} = \mathbf{E}\boldsymbol{\varepsilon} - \mathbf{E}\boldsymbol{\alpha}\Delta\mathrm{T} \tag{4.24}$$

where $\mathbf{E}$ and $\boldsymbol{\alpha}$ are the stiffness and CTE tensors of the micro element, respectively given by Eqs. (3.1) and (3.2), ΔT is the change in the assumed uniformly distributed temperature and $\boldsymbol{\varepsilon}$ is the total strain in the element.

The element strain field is, in fact, the combination of the average macroscopic applied strain tensor $\bar{\boldsymbol{\varepsilon}}$, and the local fluctuating displacement fields, elastic, $\boldsymbol{\varepsilon}^*$, and thermal, $\boldsymbol{\varepsilon}^{*\alpha}$, which are solution of the local homogenization problems. That is, $\boldsymbol{\varepsilon} = \bar{\boldsymbol{\varepsilon}} - \boldsymbol{\varepsilon}^* + \boldsymbol{\varepsilon}^{*\alpha}$. Replacing the strain in (4.24) with the elastic and thermal displacement fields that are obtained from the homogenization analyses, the thermoelastic stress in the microstructure is given by:

$$\boldsymbol{\sigma} = \mathbf{E}(\mathbf{I} - \mathbf{B}\boldsymbol{\chi})\bar{\boldsymbol{\varepsilon}} - \mathbf{E}(\boldsymbol{\alpha} - \mathbf{B}\boldsymbol{\Upsilon})\Delta\mathrm{T} \tag{4.25}$$

where $\mathbf{B}$ is the element strain-displacement matrix, $\boldsymbol{\chi}$ and $\boldsymbol{\Upsilon}$ are the elastic and thermal displacement vectors, and $\mathbf{I}$ is a 3×3 identity matrix representing the three-unit macroscopic strain cases, from the homogenization analysis. The full development of Eq. (4.25) is here omitted for brevity but can be found in [73].

Again, the solution A and D from the previous chapter are revisited here, to evaluate the stress in the microstructure, and validate Eq. (4.25). To this end, the strategy proposed in [73] is adopted, where a macroscopic model, i.e., a RVE with 5 repetitions of the microstructure (recall Section 3.2.4), is analysed in ANSYS MAPDL®. This allows the evaluation of microstructural stresses either through a homogenization-based stress analysis (using a single UC with PBCs and computing stresses according to Eq. (4.25)) or by standard macroscopic mechanical analysis, in which the entire macrostructure is modelled. To guarantee that the microstructure being analysed is equivalent between both models, the UC is defined in ANSYS by assigning a different material model for each element, preserving the filtering information. Displacements were applied to the boundaries of the RVE, equivalent to a macroscopic strain of $\bar{\boldsymbol{\varepsilon}} = [0 \quad -0.001 \quad 0]^{\mathrm{T}}$ and a uniform thermal change of $\Delta\mathrm{T} = 100℃$ is applied.

The von-Mises stress, σ^{VM}, in each micro element is given by a volume average of the values computed at each Gauss point in the FE analysis, given by Eq. (4.26):

$$\sigma^{VM} = \frac{1}{Y_{e^m}} \int_{Y_{e^m}} \sqrt{\frac{1}{2}[(\sigma_{11} - \sigma_{22})^2 + (\sigma_{22})^2] + 3(\sigma_{12})^2} \mathrm{d}Y_{e^m} \tag{4.26}$$

where Y_{e^m} is the micro FE area, and σ_{ij} the components of $\boldsymbol{\sigma}$, computed in Eq. (4.25).

Fig. 4.7 shows the von-Mises stress distribution in the microstructure for examples A and D, also analysed in Section 4.1.2. Although the standard macroscopic mechanical analysis was performed in ANSYS Mechanical APDL®, both macro and micro stress results are plotted in the same environment for consistency.

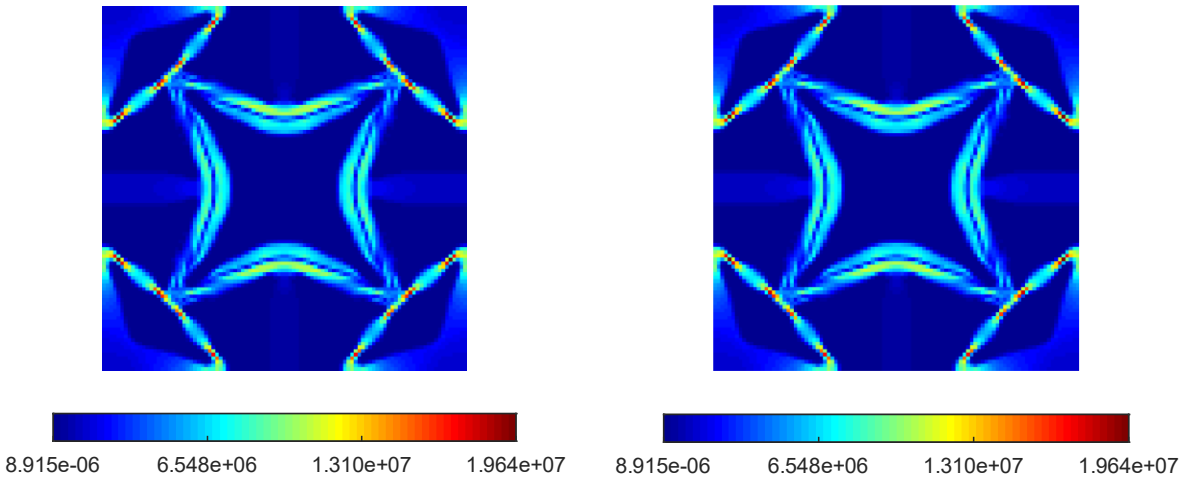

(a)

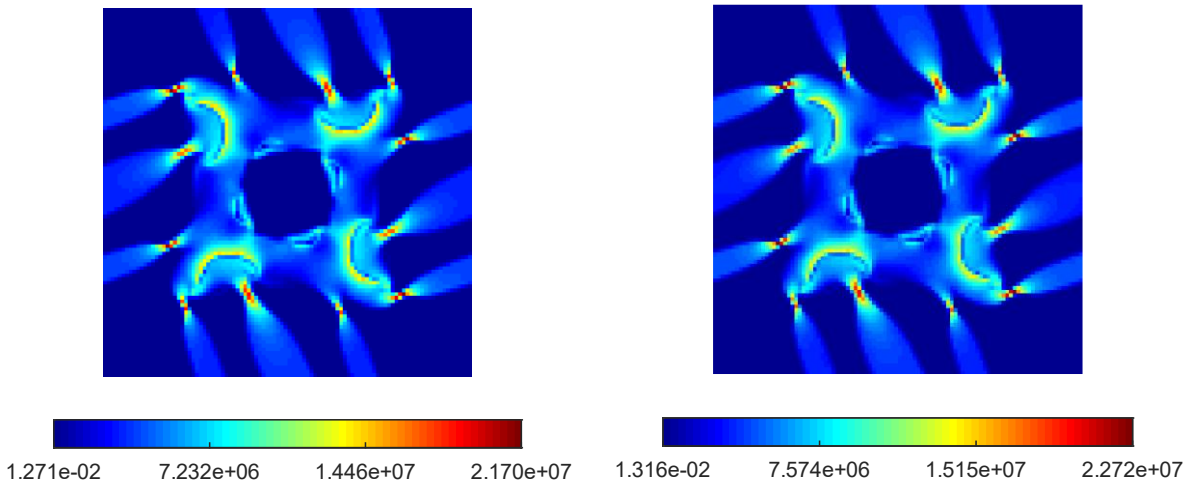

(b)

Figure 4.7 – Von Mises stress (Pa) distribution in the microstructure, computed through macroscale structural analysis (left) and homogenization-based analysis (right) for example (a) A and (b) D.

Both measurements are very accurate, with a deviation of approximately 4,6% for the maximum stress in example D, due to the anisotropic of the elastic tensor. Nonetheless, the results are accurate and satisfactory, validating the accuracy of the microscopic stress calculated using Eq. (4.25). The maximum von Mises stress is observed at regions of geometric discontinuity, such as the corners and the transitions between different material phases. Stress concentrations are also clearly observed in the narrowest regions of the microstructure, particularly at the hinges or connections, where the structural dimension is reduced. These effects are further amplified by the zigzag or jagged nature of the material distribution inherent to the density-based approach. Although a filtering technique is applied to smooth the material field and mitigate abrupt transitions between solid and void phases, residual stress concentrations can still occur in areas where the material gradient changes sharply.

4.3 Optimization Case Studies

To investigate the performance and versatility of the proposed multiscale optimization framework, a series of case studies is presented in this section. These examples aim to explore different aspects of the methodology, from its ability to generate auxetic anisotropic metamaterials to its performance in more realistic engineering contexts.

4.3.1 Anisotropic Auxetic Metamaterials

As observed in Section 4.1.2, using a single macro design finite element to model the structure, leads to an error in the PR measure for an anisotropic metamaterial which raises the need for macro FE mesh convergence analysis. Moreover, in the previous chapter, the anisotropic metamaterial under analysis was optimized exclusively at the microscopic level, not being influenced at all by the structure design domain and its BCs. This raises the question of how the macroscale FE mesh discretization influences the design of auxetic metamaterials, and whether it leads to different results.

To assess the impact of the macroscale on the auxetic behavior of anisotropic materials, the PR minimization problem is revisited here, considering different discretizations of the square structure at macroscale, as follows: A) 1×1; B) 3×3; C) 5×5 and D) 10×10 elements, see Fig. 4.8. Each FE is unitary, i.e., $|\Omega_e| = 1$, and therefore the size of macrostructure is scaled according to the number of elements. As the compliance of the macrostructure is constrained in the optimization problem, the applied loads are scaled such that the loading

conditions are the same, despite the resolution of the macrostructure. The displacement-based BCs are the rollers imposed along two edges to prevent rigid body motions. For each discretization, seven different combinations of p_1 and p_2 are covered, $p_1 = 3$ with $p_2 = 1, \dots, 3$ and $p_1 = 4$ with $p_2 = 1, \dots, 4$. The combination that leads to the better solution in terms of property and material definition is presented here.

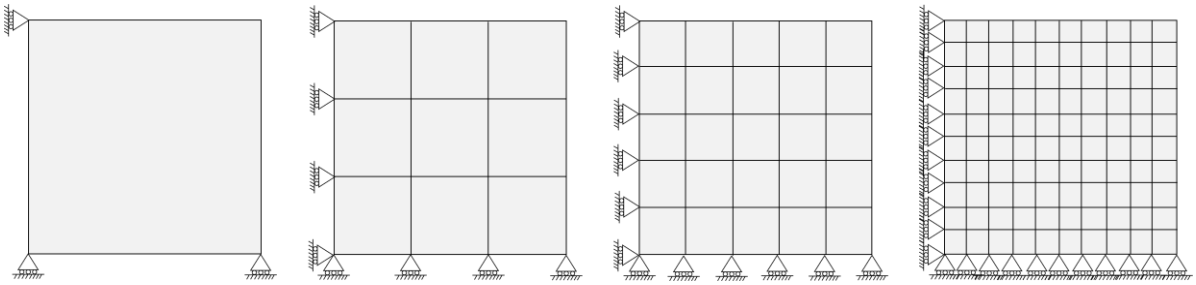

(a) (b) (c) (d)

Figure 4.8 – Different FE discretizations of the macroscale (squared structure domain) in the optimization problem: (a) Example A: 1 × 1; (b) Example B: 3 × 3; (c) Example C: 5 × 5 and (d) Example D: 10 × 10.

The initial design considered is shown in Fig. 4.9. Note that the anisotropy arises naturally from starting from a chiral and anisotropic initial design. This not only highlights how the inherent geometric features of the UC, such as chirality, can drive the emergence of anisotropic behavior as an optimal response, but it also emphasizes the strong dependency of the optimization outcome on the initial design.

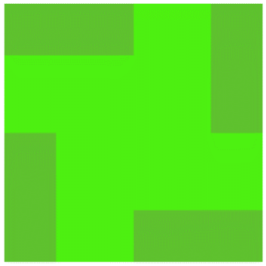

Figure 4.9 – Chiral initial design, with $\rho_1 = 0.3$ in vivid green elements and $\rho_1 = 0.7$ in darker green elements, whereas $\rho_2 = 0.5$ in all elements.

The microstructure is considered uniform in the macroscale's domain. The formulation of the optimization problem is presented in Eq. (4.27).

$$\min_{\rho^t_{e^m,l}} f_v$$

$$s.t.: \begin{cases} g_1 = \dfrac{V^{mi}}{V^+} - 1 \leq 0 \\ g_2 = \dfrac{C}{C^+} - 1 \leq 0 \\ g_3 = \left(\dfrac{E^H_{1111}/E^H_{2222} - 1}{\epsilon_1} \right)^2 - 1 \leq 0 \\ \rho_{min} \leq \rho^t_{e^m,l} \leq 1 \qquad t = 1,2;\ e^m = 1, 2, \dots, N^m; \rho_{min} = 10^{-3}; l = 1 \end{cases} \tag{4.27}$$

where f_v is the objective function that minimizes the PR in both directions. V^{mi} is the total material volume within the microstructure design domain, and V^+ the upper bound on that volume, set here as 0.5. The compliance of the macrostructure, C, is given by $C = 0.5\mathbf{U}^{\mathrm{T}}\mathbf{K}\mathbf{U}$ [169], calculated for a bulk-type loading case (superposition of the loading conditions in Fig. 4.2a and Fig. 4.2b). The upper bound on the compliance is set as $C^+ = 1.8 \times 10^5$ J, and it is in line with the stiffness previously considered in the corresponding microscale optimization problem. The constraint g_3 ensures that the coefficients E^H_{1111} and E^H_{2222} differ by a maximum percentage, by adjusting the parameters ϵ_1. This prevents the structure from having stiffness in only one direction. Here $\epsilon_1 = 0.01$, which allows a difference of 1% between both coefficients.

Solving the optimization problem stated in Eq. (4.27), for each discretization of the macroscale shown in Fig. 4.8, leads to a different optimal microstructure, that is presented in Table 4.3, with 3 repetitions of the UC to better visualize the resulting periodic pattern. The deformed configuration of each solution, introduced in a macrostructure discretized with 100×100 elements, is shown in Table 4.3 for the two different load cases presented in Fig. 4.2a and 4.2b, along with the stiffness polar plots. The combination of penalization used was $p_1 = 4$ for all examples, while $p_2 = 2$ for examples A and B, and $p_2 = 1$ in examples C and D.

Interestingly, in example A, when the macrostructure is discretized using a single finite element, the minimization of the PR is interpreted as minimizing both horizontal and vertical displacements of that single element. As a result, the algorithm converges to a **chiral** metamaterial with **orthotropic** behavior, as reflected in both the stiffness polar plot and the deformed shape of the structure. The optimization algorithm, although starting from an initial anisotropic tensor (see Fig. 4.9), is capable of identifying an optimal chiral microstructure while achieving orthotropy. This solution minimizes strain in both directions and preserves

orthogonal displacements, in contrast to the domain distortions (observed in Table 4.3, examples B - D), typical of anisotropic chiral designs.

Table 4.3 – Optimal results of material microstructures using 3 × 3 UC to ease interpretation, obtained from solving the PR minimization problem stated in Eq. (4.27), for different FE discretizations of the macrostructure in Fig. 4.8.

Example	Microstructure	Stiffness polar plots	Deformed shape running analysis on a macro-domain 100 × 100 ν_{21}	ν_{12}
A	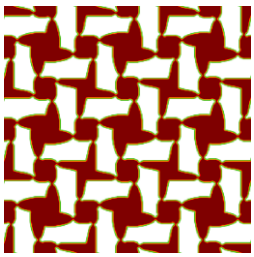	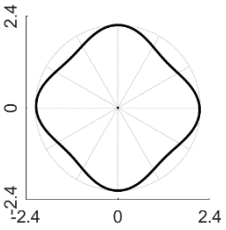	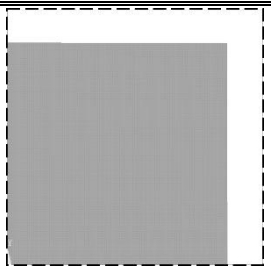	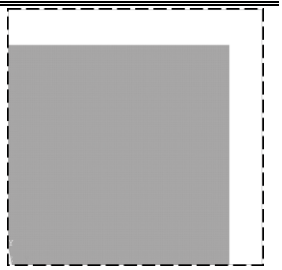
B		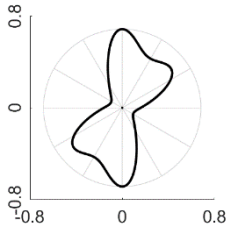	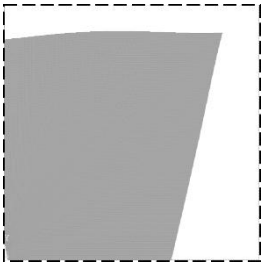	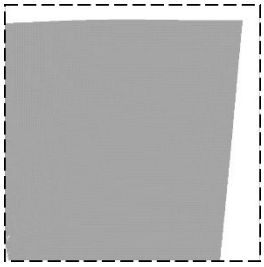
C		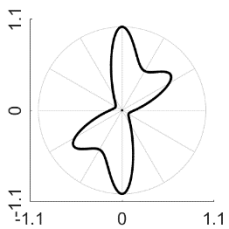	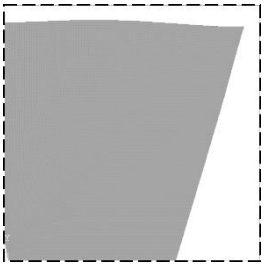	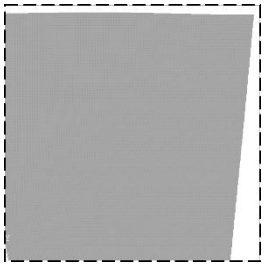
D		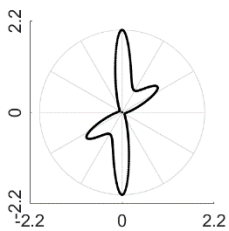	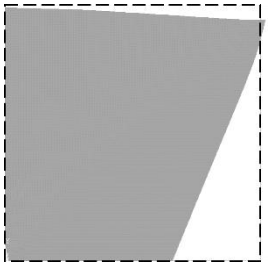	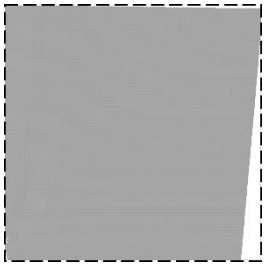

In the remaining cases (B – D), the optimized stiffness tensors maintain a certain degree of anisotropy, as observed in their respective polar plots and macrostructural deformations in Table 4.3, and also seen in Table 4.4. However, as desired, these solutions produce nega-

tive displacements in both vertical and horizontal directions, unlike the structural response obtained from a chiral metamaterial optimized exclusively at the microscale framework (see Fig. 4.4). This suggests that the multiscale design approach unveils aspects of auxecticity otherwise overlooked while performing microstructural design alone. This highlights the importance of optimizing metamaterials using a multiscale approach, as it tailors the material design to the structural context and to its intended mechanical function.

To gain deeper insight into the structural response of the optimized material, the same strategy from Section 4.1.2 is used here, where a finite element analysis is performed for each obtained solution. For each macroscale FE discretization used during the multiscale optimization process, a distinct microstructure is generated. Each of these microstructures, characterized by its own topology and effective stiffness tensor, is then embedded into macrostructures with various FE discretizations as shown in Table 4.4, regardless of the FE discretization used during optimization, although they may coincide at some point as highlighted in bold in Table 4.4. This allows evaluating the PR of the optimized material when subjected to different macroscale FE resolutions. For example, it allows to see how the material optimized for a macrostructure discretized with a specific mesh responds when inserted into a macrostructure with a higher FE mesh resolution.

Table 4.4 – Stiffness tensor of the optimized microstructures and comparative analysis between the micro-PR predictions in line with chapter 3 and the macro-PR computed with different FE discretizations of the macrostructure, for the chiral microstructures in examples A – D.

Example	Elastic coefficients, E^H_{ijkl} [$\times 10^8$ Pa]	Property	Micro	Different macro FE mesh resolutions for PR analysis				
				1×1	3×3	5×5	10×10	100×100
A	$\begin{bmatrix} 1.670 & -1.568 & -0.062 \\ & 1.687 & 0.060 \\ & & 0.218 \end{bmatrix}$	ν_{21}	-0.929	**-0.929**	-0.928	-0.928	-0.928	-0.928
		ν_{12}	-0.939	**-0.938**	-0.938	-0.938	-0.938	-0.938
B	$\begin{bmatrix} 0.612 & -0.398 & 0.477 \\ & 0.612 & -0.136 \\ & & 0.477 \end{bmatrix}$	ν_{21}	-0.648	-0.522	**-0.477**	-0.468	-0.462	-0.457
		ν_{12}	-0.648	-1.042	**-1.476**	-1.620	-1.742	-1.869
C	$\begin{bmatrix} 0.665 & -0.350 & 0.485 \\ & 0.665 & -0.107 \\ & & 0.412 \end{bmatrix}$	ν_{21}	-0.526	-0.418	-0.375	**-0.366**	-0.360	-0.355
		ν_{12}	-0.527	-0.887	-1.422	**-1.658**	-1.878	-2.133
D	$\begin{bmatrix} 1.019 & -0.132 & 0.791 \\ & 1.020 & 0.077 \\ & & 0.634 \end{bmatrix}$	ν_{21}	-0.129	-0.186	-0.210	-0.215	**-0.219**	-0.221
		ν_{12}	-0.129	-0.430	-1.133	-1.585	**-2.128**	-2.740

As expected, only in the first example shown in Table 4.4 are the micro and macro scale measurements equivalent, as the stiffness tensor is nearly orthotropic. In the remaining examples, the out of diagonal elastic coefficients, E_{1112} and E_{2212} (recall Eq. 4.2), of the stiffness tensor have the same order of magnitude as the main diagonal terms. While the micro-PR remains the same in both directions, as it does not take into account the E_{1112} and E_{2212} components, the "real" PR obtained through structural analysis reveals differences between directions. These differences become more pronounced as the macrostructure discretization changes, confirming that purely microstructural design for PR minimization may lead to quite unreal results. Interestingly, in the first example, the analysis reveals that chirality is not necessarily linked to anisotropy, as using a macrostructure discretized with a single element led to the design of an orthotropic chiral metamaterial.

4.3.2 Multiobjective Optimization

In this subsection, the multimaterial and multiobjective topology optimization problem introduced in Section 3.2.2 is revisited from a multiscale perspective. To keep the problems equivalent, and therefore verify that anepectic metamaterials can be designed through multiscale TO, the macroscale is considered to have only one layer, i.e., the microstructure is constant throughout the macro domain, which can be interpretated as a square plate made from a thermoauxetic composite material. The macro domain is discretized using a single FE, however, it should be noted that, in the case of a chiral-type solution, this design simplification at macroscale may yield misleading results as pointed out in the precious section while investigating material anisotropy effects.

Two examples from the previous chapter are revisited here, namely the star-shaped reentrant and the chiral, whose initial designs are presented as case A and D in Table 3.2. Regarding the constraints used here, it is verified that the upper bound on the bulk modulus used in connection with the objective function defined in Eq. (3.13), due to stiffness artificially increased during the first design iterations, is not needed here, as the objective function is now defined from strains instead of elastic coefficients, recall Eq. (4.13) and (4.14). Therefore, only the lower bound on the stiffness is necessary to prevent structure absence (constraint g_2 in Eq. (3.17)). However, to require a minimum stiffness to the structure, minimizing the compliance, rather than constraining the bulk modulus, would be more meaningful in the multiscale approach, as compliance is a global measure of structure response whereas the bulk modulus has to do more with material design. However, this approach is not yet

adopted here to keep both problem formulations (microscale and multiscale optimization) as much equivalent as possible. The volume constraint, Eq. (3.16), as well as the constraints assuring a cubic symmetry and isotropic CTE, Eq. (3.19), Eq. (3.21) and Eq. (3.22), are used here as well. The normalization used for the multiobjective method is presented in Section 3.2.2. For each weight factor ω, seven combinations of penalizations p_1 and p_2 where used. Essentially, the optimization problem is kept as similar as the microscale optimization problem as possible, to compare both formulations. Therefore, the multiscale topology optimization problem is stated as follows:

$$\begin{aligned} &\min_{\rho_{e^m}^t} f = \omega \frac{f_\nu}{\nu^*} + (1-\omega)\frac{f_\alpha}{\alpha^*} \\ &s.t.: \begin{cases} g_i \leq 0, & \text{with } i = 1,2,5,8,9 \\ \rho_{min} \leq \rho_{e^m,l}^t \leq 1 & t = 1,2;\ e^m = 1,2,\dots,N^m; \rho_{min} = 10^{-3}; l = 1 \end{cases} \end{aligned} \tag{4.28}$$

Fig. 4.10 presents the results from solving the optimization problem stated in Eq. (4.28), for the star-shaped re-entrant example, with 20 nondominated solutions. The first point highlighted in the Pareto front, corresponding to $\omega = 0.2$, exceeds in performance in CTE compared to the solutions for $\omega = 0$ and $\omega = 0.1$, which are local minima. However, as these weights are not included in the nondominated solutions, the topology of all Pareto solutions is quite similar, see Fig. 4.10c, resulting in a small variation in terms of PR value, from $\nu_{21} = -0.73$, in point 1, to $\nu_{21} = -0.90$ in point 6, while the CTE value varies from $\alpha_{11} = -221.15$ ppm°C^{-1} to $\alpha_{11} = 28.60$ ppm°C^{-1}. As more importance is given to the PR minimization, the CTE value increases. However, only when $\omega = 1$, does the solution becomes single material and therefore, the CTE becomes positive. In fact, as can be seen in Fig. 4.10b), the CTE value of solution point 6 is approximately the same as the base material ($\alpha^{PVA} = 21$ ppm°C^{-1}).

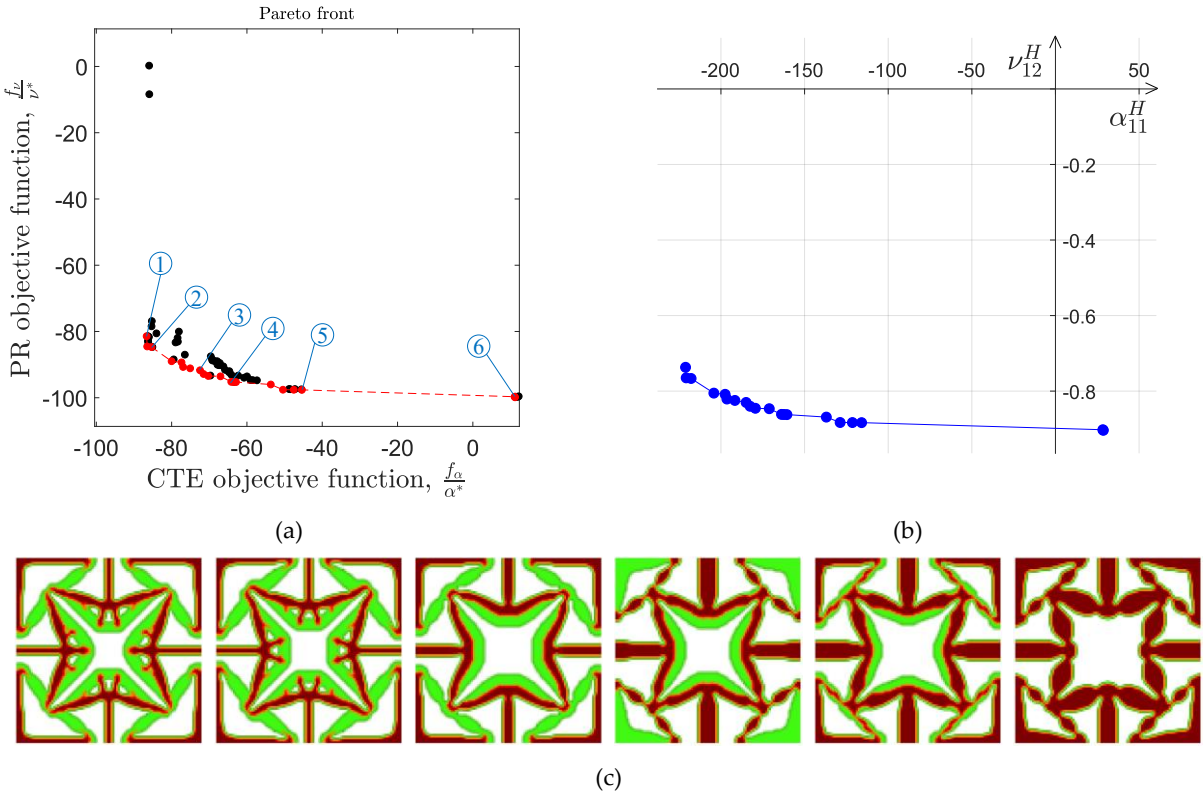

Figure 4.10 – Multiscale optimization results for the star-shaped re-entrant example: (a) Nondominated (red dots) and dominated (black dots) Pareto front solutions for CTE and PR objective function; (b) Effective properties (PR, ν_{21}, and CTE in ppm°C^{-1}, α_{11}) for the points in the Pareto front; (c) UC of the periodic microstructure corresponding to solution points 1 to 6.

Fig. 4.11 presents the results from solving the optimization problem stated in Eq. (4.28), for the chiral cubic example. For the chiral example, 22 nondominated solutions are obtained. Here, contrary to the previous case, the solutions for $\omega = 0$ are nondominated, and the microstructure is similar to the microstructural optimization. However, as the weight evolve from 0 to 1, the microstructure becomes quite distinct, contrary to the star-shaped re-entrant case where the topology differs less across the Pareto design solutions, for the PR minimization, when comparing the multiscale and microscale design solutions. This happens because, in the case of an orthotropic stiffness tensor, the elastic coefficients ratio corresponds to the strains ratio. Although the objective function in the microscale optimization is not explicitly defined as the homogenized property, minimizing the coefficient E_{1212}, while maximizing E_{1111} and E_{2222}, is equivalent to minimizing the PR, making the problems closely related. However, for the chiral, and thus, allowing anisotropy, the elastic coefficients ratio is no longer equivalent to the strains ratio. As a result, the two formulations of the optimiza-

tion problem diverge, and the multiscale approach accurately captures the structural response.

Similar to the re-entrant case, for $\omega = 1$, when the PR is exclusively minimized, the PR has a value of $\nu_{21} = -0.93$, and the CTE value is around the CTE of the base material, with $\alpha_{11} = 21.95$ ppm°C^{-1}. For the first solution point, with $\omega = 0$, the values of the properties are $\nu_{21} = -0.07$ and $\alpha_{11} = -246.028$ ppm°C^{-1}.

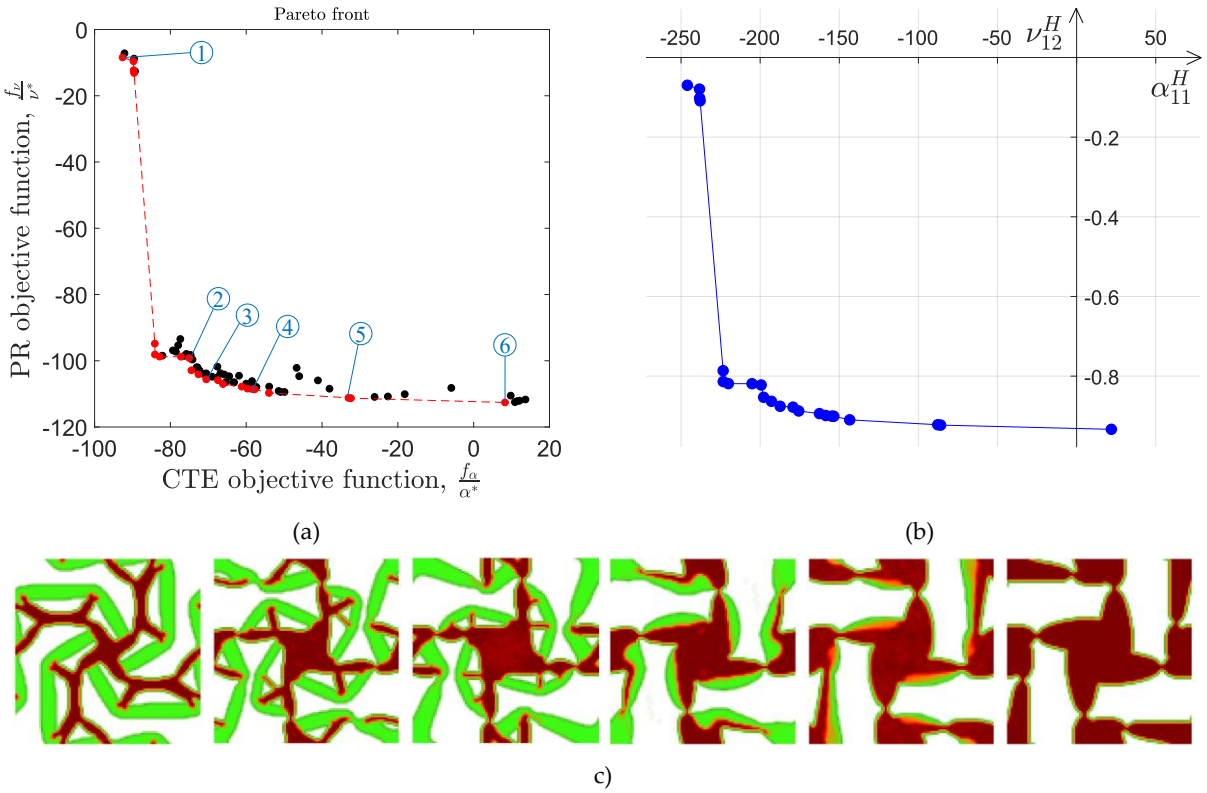

Figure 4.11 – Multiscale optimization results for the chiral example: (a) Nondominated (red dots) and dominated (black dots) Pareto front solutions for CTE and PR objective function; (b) Effective properties (PR, ν_{21}, and CTE in ppm°C^{-1}, α_{11}) for the points in the Pareto front; (c) UC of the periodic microstructure corresponding to solution points 1 to 6.

In the microscale topology optimization problem, the Pareto front solutions do not necessarily correspond to nondominated solutions when plotted in the dual space of effective properties (see Fig. 3.13). In fact, without an upper bound on the stiffness, as the ω value approaches one, the PR tends to increase, even though the objective function defined in Eq. (3.13) decreases. This is because, in the microscale optimization, the PR is not directly minimized, and the objective function maximizes stiffness during the initial iterations. In the multiscale case, the correspondence between the objective function and the material property is direct (up to a scaling factor related to the normalization parameters ν^* and α^*, used in the

multiobjective formulation), since the optimization is performed in the property space itself, specifically targeting the effective NPR and NTE. The Pareto front solutions appear more clustered in the multiscale optimization compared to the microscale optimization Pareto fronts, for weights between 0.1 and 0.9. This behavior was expected, as a similar trend is observed in Fig. 3.13, where the PR remains relatively constant across this range. This verifies that the PR depends mostly on the topology of the UC, while the CTE property is also related to the material distribution, as it was also demonstrated in the previous chapter. In the multiscale formulation, as the objective function directly reflects the effective properties, this aspect is also reflected in the Pareto front.

These conclusions highlight the advantages of formulating the metamaterials design problem from a multiscale perspective, where the design process is explicitly guided through macroscopic structural response, rather than indirectly via homogenized tensor coefficient. This advantage is more noticeable for the anisotropic cases as far as discussed till now in this thesis, but further advantages are pointed out in the next sections. So far, this section demonstrates that the proposed multiscale formulation is robustly developed and implemented, providing a viable alternative to the typical microstructural topology optimization design approach.

4.3.3 Influence of Load Changes

This subsection investigates the impact of load changes on the structural auxetic performance, to assess how macroscale features (e.g., displacement and force-based BCs, void or solid non-design subdomains) influence the material microstructure design. To that purpose, instead of applying a uniformly distributed load, a linearly varying distributed load is considered, creating a controlled imbalance in the mechanical loading. This imbalanced load distribution is defined by a given percentage, as illustrated in Fig. 4.12.

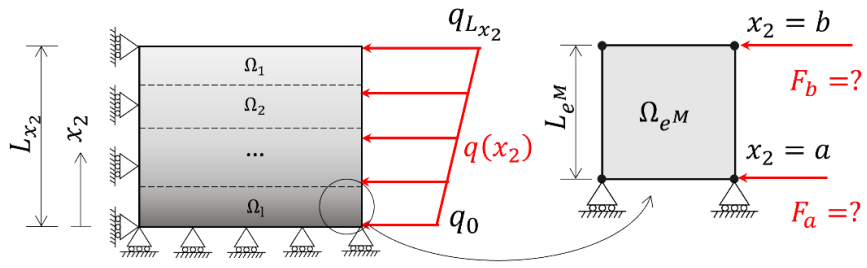

Figure 4.12 – Imbalanced load distribution, considering symmetry conditions on the macrostructure (left) and correspondence with the nodal force applied to a 4-node FE (right).

First, let us define the equivalence between distributed load applied along the structure's boundary and its corresponding nodal forces applied to the elements. For each element, the load vector applied to the nodes is given by Eq. (4.29), see [160].

$$\mathbf{F}_e = \int \mathbf{N}^{\mathrm{T}}\mathbf{b}\mathrm{dV} + \int \mathbf{N}^{\mathrm{T}}\mathbf{q}\mathrm{d}\Omega + \int \mathbf{B}^{\mathrm{T}}\mathbf{E}\boldsymbol{\varepsilon}_0\mathrm{d}\Omega + \int \mathbf{B}^{\mathrm{T}}\boldsymbol{\sigma}_0\mathrm{d}\Omega \tag{4.29}$$

where $\mathbf{b}$ is the body loads vector, $\mathbf{q}$ is the traction forces in the boundary $\partial\Omega$, and $\boldsymbol{\varepsilon}_0$ and $\boldsymbol{\sigma}_0$ are the initial strain and stress in the structure, respectively. Note that depending on the problem, some of the terms may be null in some elements.

In the case schematized in Fig. 4.12, only $\mathbf{q}$ is considered, and is applied on the elements on the right end of the structure, and therefore, Eq. (4.29) is simplified such that:

$$\mathbf{F}_e = \int \mathbf{N}^{\mathrm{T}}\mathbf{q}\mathrm{d}\Omega \tag{4.30}$$

More specifically, for a FE located at the border of the structure, see Fig. 4.12 (right), the loads in each node, a and b, are given by:

$$\begin{cases} F_{\boldsymbol{a}} = \int_a^b N_a(x_2)q(x_2)\mathrm{d}x_2 \\ F_{\boldsymbol{b}} = \int_a^b N_b(x_2)q(x_2)\mathrm{d}x_2 \end{cases} \tag{4.31}$$

Considering that the structure is discretized in such a way that $a = 0$, $b = 1$ and $L_{x_2} = 1$ in every FE. The shape functions in each node are $N_a = 1 - x_2$ and $N_b = x_2$, and the distributed load, $\mathrm{q}(x_2)$, is given by Eq. (4.32):

$$q(x_2) = q_0 + \frac{q_{L_{x_2}} - q_0}{L_{x_2}}x_2; \quad x_2 \in [0 \quad L_{x_2}] \tag{4.32}$$

where q_0 and $q_{L_{x_2}}$ are the values of the load in the coordinates, $x_2 = 0$ and $x_2 = L_{x_2}$, respectively.

By solving the integral in Eq. (4.31), with the load expression defined in Eq. (4.32), where $q_a = q(a)$ and $q_b = q(b)$, the resulting nodal forces are obtained as:

$$\begin{cases} F_{\boldsymbol{a}} = \frac{1}{2}q_a + \frac{1}{6}(q_b - q_a) \\ F_{\boldsymbol{b}} = \frac{1}{2}q_a + \frac{1}{3}(q_b - q_a) \end{cases} \tag{4.33}$$

From here the equivalence between the imbalanced distributed load and the nodal forces is easily obtained, and generalized for any discretization of the macrostructure, as long as the finite elements are unitary.

Here $q_0 = 1$ MPa and the value of $q_{L_{x_2}}$ varies depending on the generated imbalance of the distributed load. Both the uniform and the layer-wise approach are explored, for the optimization problem of obtaining auxetic structures (only mechanical loads are considered). In the microscopic framework, stiffness is ensured by imposing a lower bound on the bulk modulus, but in the multiscale approach, it is more meaningful to work directly with the structural stiffness or compliance, as it directly reflects the structural response. Therefore, here the structural compliance is directly minimized in the objective function using a weight sum method, since a compliance bound may be difficult to define for use as a constraint. Furthermore, in this context, the weight sum method serves to guide the optimization rather than balance multiple objectives, since the focus remains on minimizing the PR alone, and so the weights do not carry the same meaning as in the previous section. Here the compliance is calculated when the structure is subjected to a bulk-type loading case.

Finally, the optimization problem to minimize the structural PR is stated in Eq. (4.34).

$$\min_{\rho^t_{e^m,l}} f = \frac{\overline{\nu}_{21}}{\nu^*} + ca\frac{C}{C^*}$$
$$s.t.: \begin{cases} g_1 = \dfrac{V^{mi}}{V^+} - 1 \leq 0 \\ g_2^l = \left(\dfrac{E^H_{1111}/E^H_{2222} - 1}{\epsilon_1}\right)^2 - 1 \leq 0 \\ \rho_{min} \leq \rho^t_{e^m,l} \leq 1 \qquad t = 1,2;\ e^m = 1,2,\dots,N^m; \rho_{min} = 10^{-3}; l = 1,\dots,nl \end{cases} \tag{4.34}$$

where ν^* and C^* are used here to normalize the objective function and are the values for PR and Compliance in the first design iteration, respectively. The continuation approach parameter ca is applied in the first 20 iterations and gradually increases from 0 to 0.2. As the structural stiffness is ensured by incorporating the compliance in the objective function, only two constraints are used. The first is the volume fraction constraint, set to 50% in all examples presented below. As the PR is only being minimized in one direction, the tendency of the problem is to differ both PRs as much as possible, and the constraint g_2^l ensures that the components E_{1111} and E_{2222}, within each layer l, do not differ from one another more than a given percentage ϵ_1. This constraint is applied independently to each layer, as each one is associated with its own material and thus its own homogenized elasticity tensor, $\mathbf{E}^H$.

In all examples, the macrostructure is discretized using a 3 × 3 element grid, and the microstructure is either assumed to be uniform throughout de macroscale or defined in a layer-wise manner. The applied BCs and discretization scheme are illustrated in Fig. 4.13.

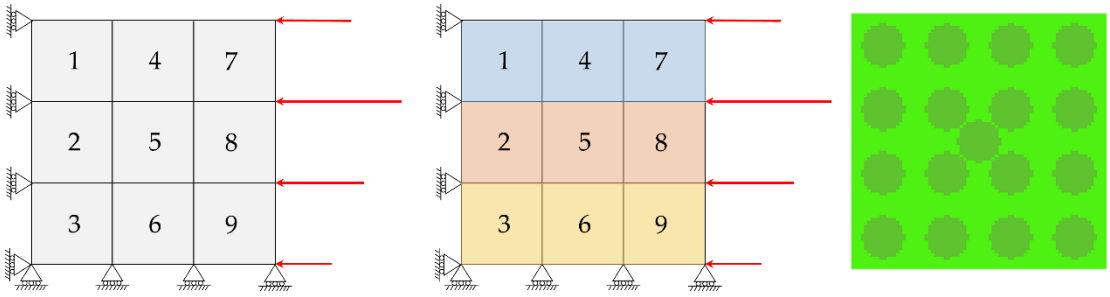

(a) (b) (c)

Figure 4.13 – BCs for the PR minimization problem with non-uniform load influence for a macrostructure with (a) uniform material microstructure and (b) layer-wise material distribution; (c) initial design.

The value $q_{L_{x_2}}$ for the distributed load is given as $q_{L_{x_2}} = \delta q_0$, where δ is the percentage parameter to set the load imbalance considered. Four cases are investigated: $\delta = 1$, $\delta = 1.2$, $\delta = 1.4$ and $\delta = 1.5$, corresponding to a perturbation of 10%, 20%, 40% and 50% of the compression load. For each loading case, three different relations between the parameters E_{1111} and E_{2222} are considered, by setting the parameter ϵ_1 in the g_2 as $\epsilon_1 = 0.05$, $\epsilon_1 = 0.2$ and $\epsilon_1 = 1$. The optimization problem was solved for the seven combinations of penalization parameters p_1 and p_2, but it was verified that, in this problem, the parameter $p_1 = 4$ resulted in superior solutions in terms of design definition, properties and symmetry (when expected). The initial design used for the UC consists of an 80 × 80 microelement grid, see Fig. 4.13c, and a density filter with radius $r_{min} = 3$ is applied. Although this discretization is slightly coarser than that used before, it remains sufficiently detailed to generate well-defined microstructures. The slightly larger filter radius helps avoiding overly intricate geometries. In the microstructure plots, the green transition layer visible between solid and void regions is thus due to the filtering radius.

4.3.3.1 Uniform Approach

For the structure composed of a uniform material, the optimal microstructures corresponding to each combination of δ and ϵ_1 are presented in Table 4.5. Although the illustrations show 3 × 3 repetitions of the UC, the actual macrostructure should be interpreted as a domain with an infinite periodic repetition of the UC.

Table 4.5 – Optimized microstructure topologies for increasing load imbalance and relaxation of the constraint g_2.

	$\delta = 1$	$\delta = 1.2$	$\delta = 1.4$	$\delta = 1.5$
$\epsilon_1 = 0.05$		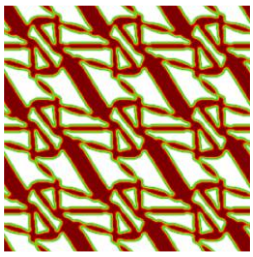	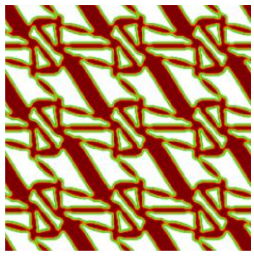	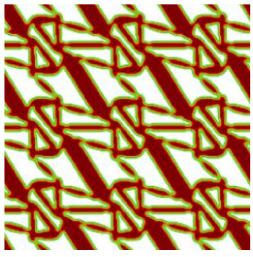
$\epsilon_1 = 0.50$		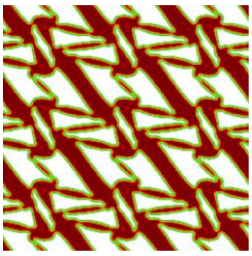	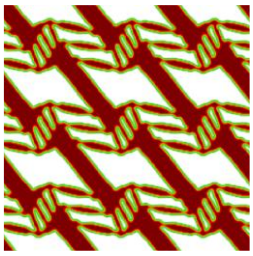	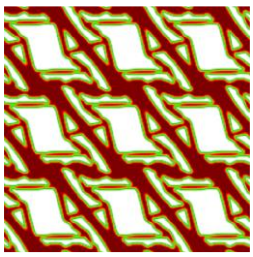
$\epsilon_1 = 1.00$	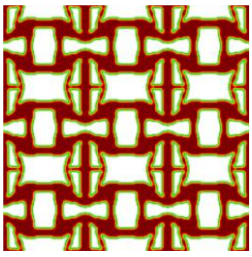	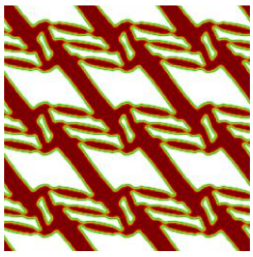	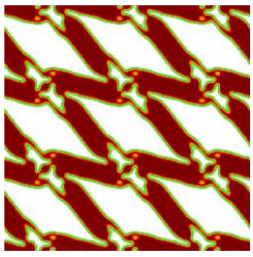	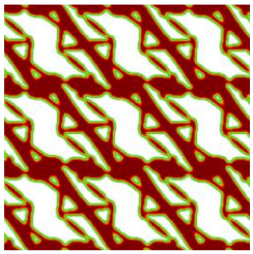

As observed in the topologies of the UCs, when the constraint that enforces similarity between E^H_{1111} and E^H_{2222} is active (i.e., for the lower value of ϵ_1), the resulting microstructure for $\delta = 1$ is nearly identical in both directions. For all the other values of δ, regardless of the load perturbation, the microstructure is identical, but no longer symmetrical in both directions. For the load case with $\delta = 1$, this symmetry arises because the optimization is forced to preserve similar stiffness in both principal directions. However, as ϵ increases and the constraint is progressively relaxed, the topology becomes increasingly sensitive to the load perturbation. In other words, when the material is allowed to be more anisotropic, the design adapts more clearly to the load changes, as can be seen in the microstructures along the first column on Table 4.5. It is also important to note that the algorithm may progressively lose symmetry during the optimization process, which can promote the emergence of anisotropic microstructural features. Once such asymmetries arise, they tend to be amplified in subsequent iterations, influencing the final optimized design.

Notably, when $\epsilon_1 = 0.05$, meaning the stiffness components can only differ by up to 5%, the topology remains practically unchanged even as the load imbalance parameter δ varies. In contrast, for $\epsilon_1 = 1$, where the constraint is more relaxed, the differences between the two directions become pronounced as the algorithm concentrates the optimization effort on minimizing the PR in one direction, even at the expense of worsening that ratio in the other direction. This leads to clearly asymmetric topologies, especially under increased slope in load application.

Table 4.6 presents the mechanical properties (PR and compliance values), for different parameter combinations, allowing a direct comparison between the geometry changes of the microstructure, illustrated in Table 4.5, and mechanical performance.

Table 4.6 – Effective properties of the solutions for increasing load imbalance and relaxation of the constraint g_2.

	Macroscale property	$\delta = 1$	$\delta = 1.2$	$\delta = 1.4$	$\delta = 1.5$
$\epsilon_1 = 0.05$	$\bar{\nu}_{21}$	-0.714	-1.719	-1.760	-1.766
	C [J × 10^4]	1.171	3.497	3.527	3.510
$\epsilon_1 = 0.50$	$\bar{\nu}_{21}$	-0.874	-2.142	-2.295	-2.200
	C [J × 10^4]	1.336	4.105	4.145	4.018
$\epsilon_1 = 1.00$	$\bar{\nu}_{21}$	-1.100	-2.521	-2.344	-2.396
	C [J × 10^4]	1.380	3.991	4.604	4.067

From Table 4.6 it can be observed that relaxing the constraint that imposes a relation between the stiffness components E^H_{1111} and E^H_{2222} leads to more negative values of PR, but at the expense of increased compliance. This was expected, as more negative values of PR are associated with less stiff structures due to the mechanism-like deformation behavior of auxetics. Additionally, when the applied load changes from a uniform distribution to an imbalanced one, the PR becomes more negative in all cases. Interestingly, for $\delta = 1.5$ with $\epsilon_1 = 0.5$, and for $\delta = 1.4$ and $\delta = 1.5$ with $\epsilon_1 = 1$, the PR remains nearly unchanged or even slightly decreases. This suggests a limit beyond which further perturbations in the load may influence the topology but have little influence on the auxetic response. In fact, as the load becomes more imbalanced, the principal strain directions also become less aligned with the coordinate system main directions involved in the PR calculation, which is calculated as a ratio of horizontal to transverse strains measured in the structure coordinate system.

To analyze the anisotropy level of each solution, the stiffness polar plots are shown in Table 4.7.

Table 4.7 – Stiffness polar plots [$\times 10^7$ Pa] of the solutions for increasing load imbalance and relaxation of the constraint g_2.

	$\delta = 1$	$\delta = 1.2$	$\delta = 1.4$	$\delta = 1.5$
$\epsilon_1 = 0.05$	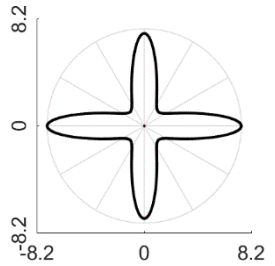	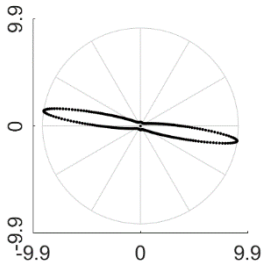	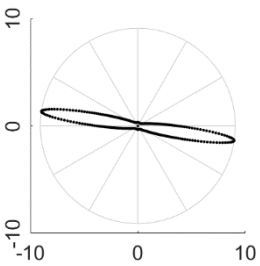	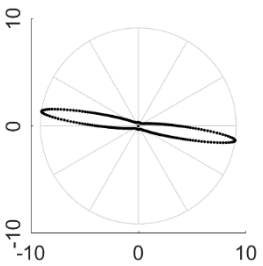
$\epsilon_1 = 0.50$	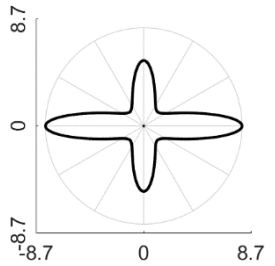	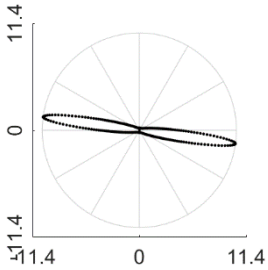	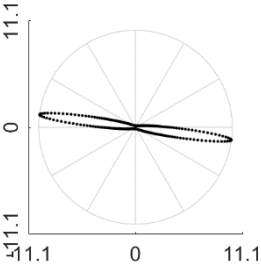	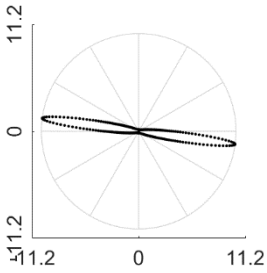
$\epsilon_1 = 1.00$	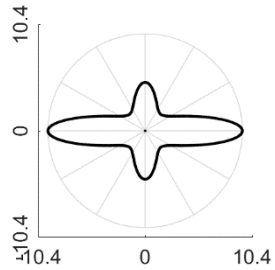	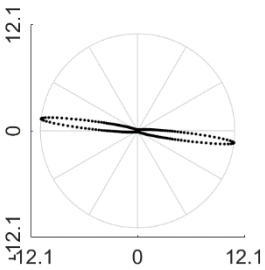	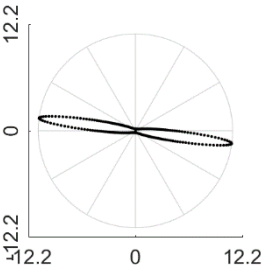	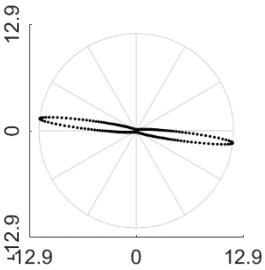

The stiffness polar plots graphically represent the trend already observed in Table 4.6. For $\delta = 1$, as the parameter ϵ increases so does the directional response of the metamaterial. While stiffness increases slightly in the horizontal direction (the loading direction), it decreases significantly in the vertical one. This asymmetry contributes directly to the observed increase in the PR value, since the PR that is being minimized is ν_{21}, that measures the vertical (transverse) strain response to horizontal loading. For $\delta > 1$, all solutions become quite similar, exhibiting strong directional stiffness, emphasizing the anisotropic nature of the optimized designs, even in the first case where $\epsilon_1 = 0.05$.

4.3.3.2 Layer-wise Approach

For the structure composed of a layer-wise material, the optimal microstructures corresponding to each combination of δ and ϵ_1 are presented in Table 4.8. Although the illustrations

show 1×3 repetitions of the UC in each layer, the actual macrostructure should be interpreted as a domain with an infinite periodic repetition of the UC.

Table 4.8 – Optimized microstructure topologies of each layer for increasing load imbalance and relaxation of the constraint g_2.

	$\delta = 1$	$\delta = 1.2$	$\delta = 1.4$	$\delta = 1.5$
$\epsilon_1 = 0.05$	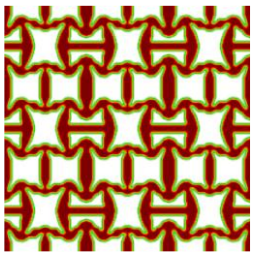	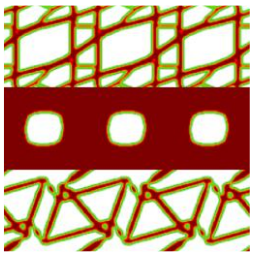	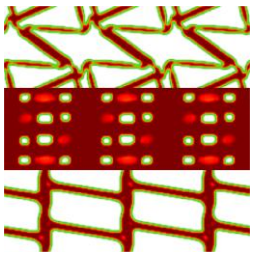	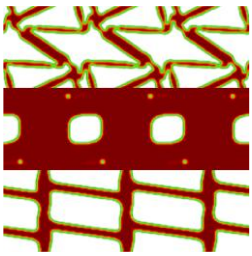
$\epsilon_1 = 0.50$	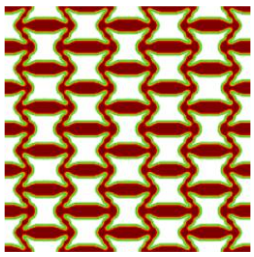	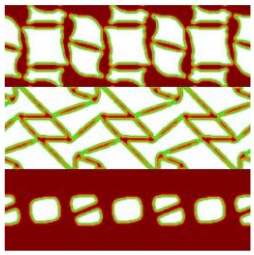	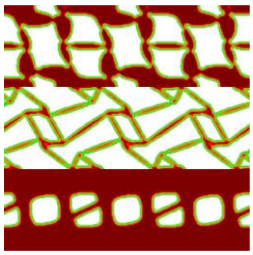	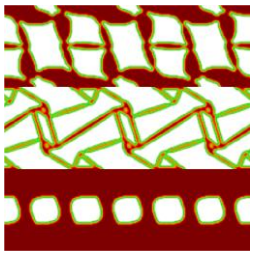
$\epsilon_1 = 1.00$	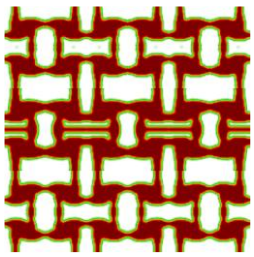	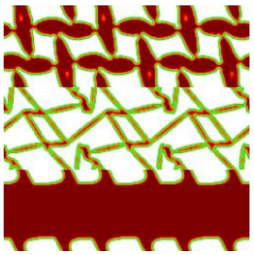		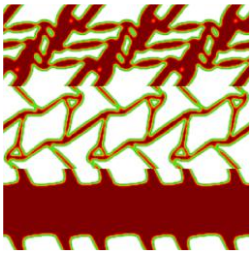

As observed from the microstructures in the Table 4.8, there is no connectivity between the microstructures of adjacent layers in the layer-wise designs. While this represents a significant manufacturing limitation, there are strategies to address it, such as introducing non-design boundary connections between layers [170]. However, this aspect was not accounted for in the current study, as the problem is still being explored at a fundamental stage.

The optimization problem was formulated to not be so restrictive, imposing the volume constraint globally, i.e., imposing the average volume across all microstructures. This allows each microstructure to have its own volume, leading to different regions of the macrostructure exhibiting varying levels of porosity. The topology of the microstructures shown in Table 4.8 allow us to graphically see the evolution of the microstructure with the

imbalance of the load, and in Table 4.9 the corresponding mechanical properties (PR and compliance) of the macrostructure are presented. For the imbalanced load, $\delta = 1$, the microstructure is the same in all layers, except when $\epsilon_1 = 1$, where the middle layer is slightly different from the others. However, symmetry is still preserved as expected for a uniform load. For increasing values of load imbalance ($\delta > 1$), the microstructures across the layers begin to differ more significantly, particularly for relaxed stiffness coefficient constraints (higher ϵ_1). This behavior reflects the asymmetry in the strain field induced by the perturbed load. In the cases where $\epsilon_1 = 0.5$ and $\epsilon_1 = 1.0$, the top and bottom layers develop distinct topologies, tailored to accommodate different strain levels, where the bottom layer presents higher volume, while the middle layer remains as a transition zone. On the contrary, when $\epsilon_1 = 0.05$, it is the middle layer that has the greatest volume.

Table 4.9 – Effective properties of the solutions for increasing load imbalance and relaxation of the constraint g_2.

	Macroscale property	$\delta = 1$	$\delta = 1.2$	$\delta = 1.4$	$\delta = 1.5$
$\epsilon_1 = 0.05$	$\bar{\nu}_{21}$	-0.783	-4.658	-4.468	-4.603
	C [$\times 10^4$ J]	1.179	10.565	8.620	8.783
$\epsilon_1 = 0.50$	$\bar{\nu}_{21}$	-0.873	-6.920	-6.386	-6.878
	C [$\times 10^4$ J]	1.383	18.847	16.877	18.644
$\epsilon_1 = 1.00$	$\bar{\nu}_{21}$	-1.144	-6.624	-2.798	-2.883
	C [$\times 10^4$ J]	1.348	17.298	4.289	4.367

Here the PR and compliance show the same trend as the previous example, where a more negative PR is associated with higher compliance. However, the overall PR of the structure is significantly more negative compared to the homogeneous case, with $\overline{\nu}_{21} = -6.878$ for the layer-wise approach and $\overline{\nu}_{21} = -2.200$ for the uniform design (comparing the optimization problem with $\epsilon_1 = 0.5$ and $\delta = 1.5$). For the uniform load ($\delta = 1$) the structural performance is nearly the same for both approaches. Interestingly, the only case where no improvement in properties is observed is for $\epsilon_1 = 1$ and $\delta = 1.4$ and $\delta = 1.5$, but this may be related to the optimizer converging to a local minimum, as this is the least constricted case.

Note that the mechanical properties, such as PR and compliance, reflect global measures at the macroscale. In contrast, the stiffness polar plots are represented for each layer, as it depends on the stiffness tensor ($\mathbf{E}^H$) of each microstructure. To assess the level of anisotropy in each solution, the corresponding polar plots of stiffness are shown in Table 4.10.

Table 4.10 – Stiffness polar plots [$\times 10^7$ Pa] of the solutions for increasing load imbalance and relaxation of the constraint g_2.

	$\delta = 1$	$\delta = 1.2$	$\delta = 1.4$	$\delta = 1.5$
$\epsilon_1 = 0.05$	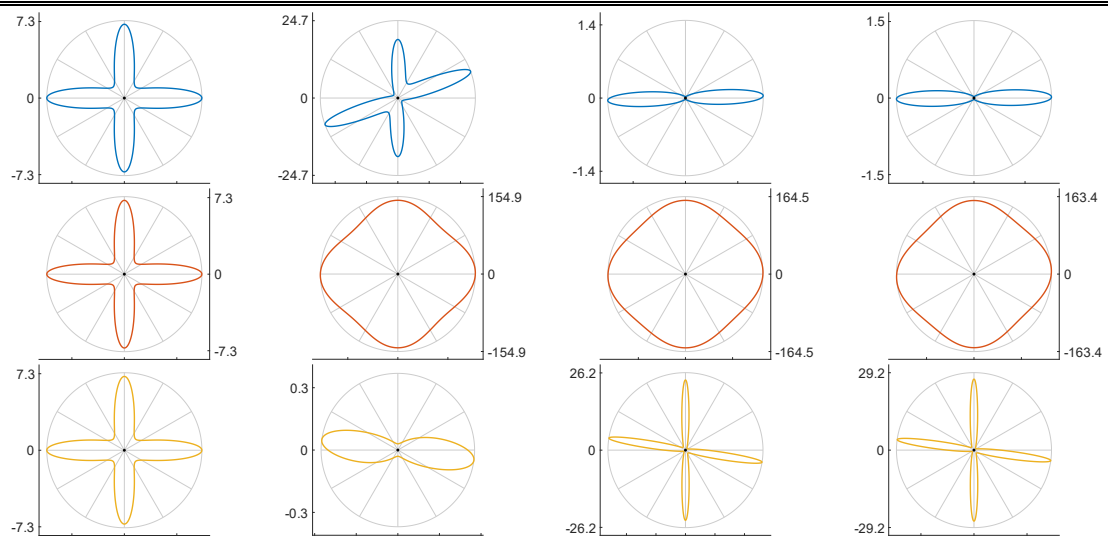			
$\epsilon_1 = 0.50$	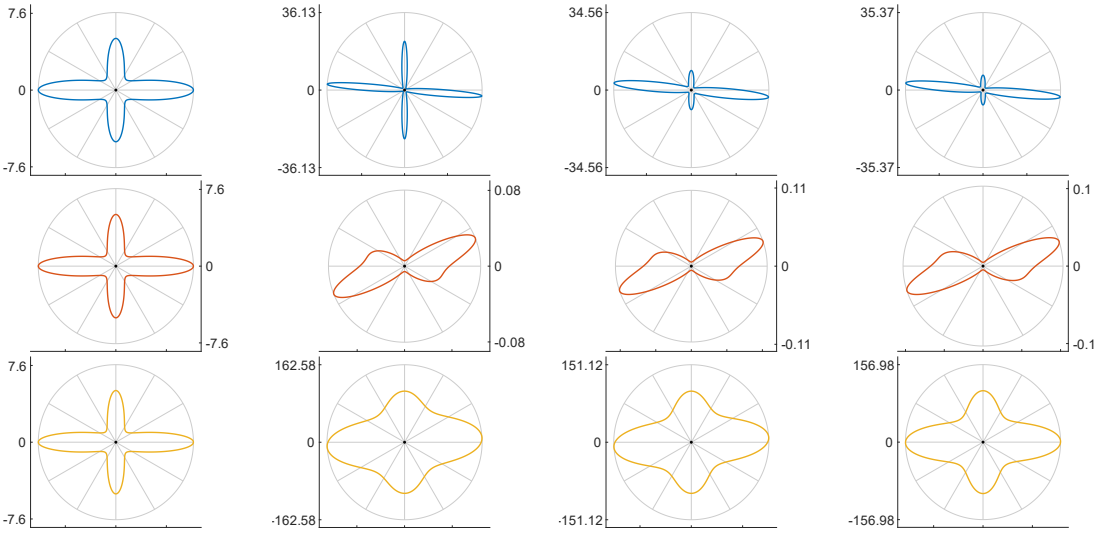			
$\epsilon_1 = 1.00$	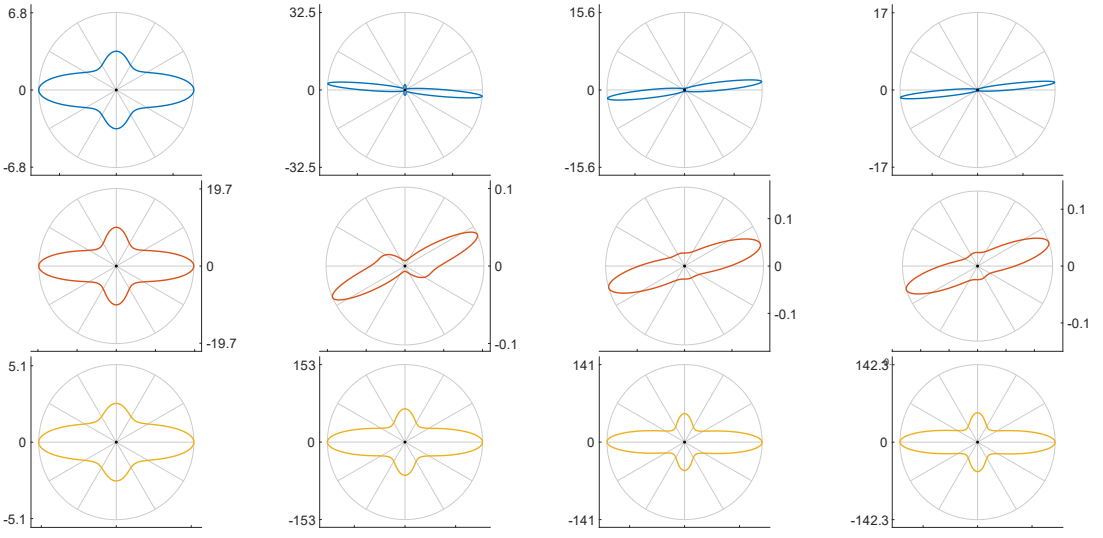			

The stiffness polar plots shown in Table 4.10 provide a graphical interpretation of the structural behavior of each microstructure. For the uniform load case ($\delta = 1$), all layers display an orthotropic response, with symmetry axes aligned with the principal directions. As ϵ increases, this orthotropy becomes progressively more directional, favoring stiffness along the horizontal axis. This trend was already observed in the uniform strategy. When the load becomes imbalanced ($\delta > 1$), a noticeable contrast emerges among layers: the stiffest layer, typically the one with higher volume fraction, tends to exhibit an orthotropic response, while the remaining layers exhibit increased anisotropy. This difference becomes more evident as ϵ_1 increases. It is also verified that, as in the uniform case, for $\delta = 1.4$ and $\delta = 1.5$ the response is similar, suggesting that further perturbations in the load become less meaningful, as the load is no longer aligned with the strain principal directions. As a result, the computed $\overline{\nu}_{21}$ may not fully capture the transversal response.

4.3.4 Beam Under Pure Bending

To analyse the multiscale problem in a more practical and meaningful example, a classical beam under bending BCs, inspired from the work in [171] is analysed here, see Fig. 4.14. In the macroscale FE model a linearly distributed load is applied at the free end of the beam to induce a bending moment, and symmetry is imposed as shown Fig. 4.14b.

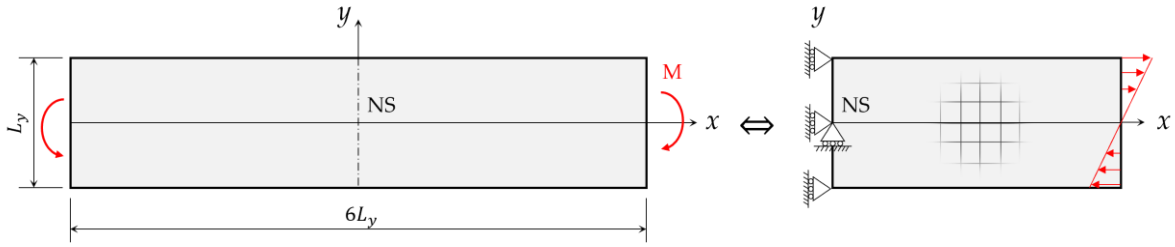

(a) (b)

Figure 4.14 – Bending beam example: (a) benchmark, inspired from [171]; (b) FE model simplified by symmetry.

This proof-of-concept of auxeticity in pure bending thus involves a linear distribution of strains along the vertical axis of the beam but their sign is reversed crossing the beam neutral surface. This example is particularly relevant because, given that the strain is constant along the horizontal direction, only one element per layer is needed to represent the average strain in each horizontal row of elements, which reduces the computational cost of the problem. Additionally, the symmetry of the absolute strain values distribution toward the neutral surface motivates the coupling of opposite layers into the same auxetic material when using a layer-wise beam parameterization while performing optimization, which further reduces

the computational cost. However, to maintain this linear strain distribution, the microstructure must be considered orthotropic. To guarantee this, a symmetric UC is adopted in the optimization, and coupling between micro design variables is enforced, recall Fig. 3.3a.

Let us start by analysing the expected behaviour of a beam under bending, for a material with positive PR (PPR) versus a material with NPR. For that purpose, the following fictional isotropic material properties (see [59]) are considered: Young modulus of $E = 1$ GPa, and PR of $\nu^{PPR} = 0.5$ or $\nu^{NPR} = -0.5$. As can be seen in the strain distribution map in Fig. 4.15, the horizontal strain distribution remains the same for either positive or negative PR, see Fig. 4.15a. However, in the case where the beam is made of a material with NPR, the transverse strain distribution becomes reversed compared to a material with PPR. That is, above the neutral axis the strain becomes positive, and below it becomes negative. This is consistent with the expected behavior of NPR materials, as under the bending moment shown, the top half of the beam experiences traction and the bottom compression, and due to the auxetic response, the transverse strains follow this reversed pattern.

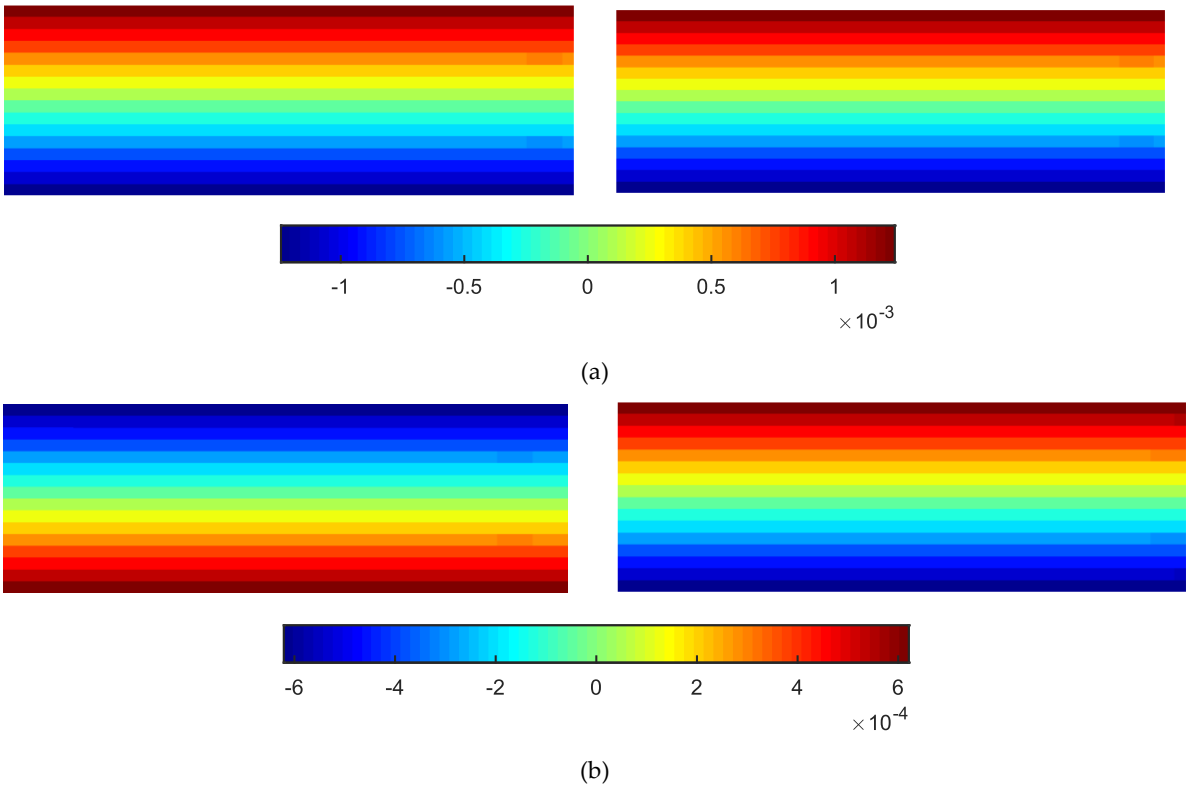

Figure 4.15 – Strain distribution for a beam in bending: (a) horizontal strain distribution, ε_{11}, for PPR (left) and NPR (right); (b) vertical strain distribution, ε_{22}, for PPR (left) and NPR (right).

For either the uniform and layer-wise approach, the macroscale is discretized using a 24×8 unitary FE (Q4) mesh, a re-entrant initial design is considered, with 80×80 micro-

elements, see Fig. 4.13c, and a density filter radius of $r_{min} = 3$ is applied. To simulate a pure bending moment, a linearly varying normal load is applied across the height of the beam: the top edge is subjected to a tensile stress of 1 MPa, decreasing linearly to 0 MPa at the neutral surface, see Fig. 4.14b. The applied BCs and discretization schemes are illustrated in Fig. 4.16.

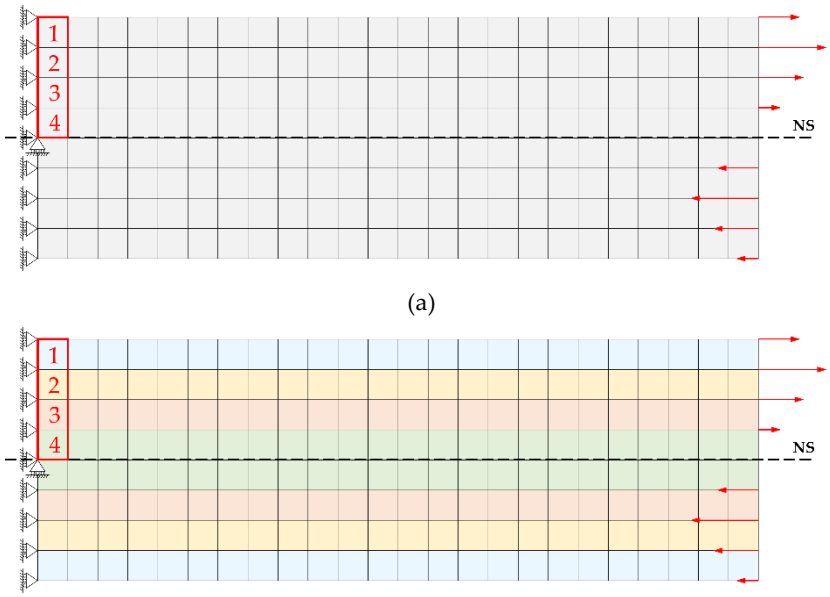

Figure 4.16 – Boundary conditions for the bending beam problem, discretized with 24 × 8 unitary Q4 FE, with (a) uniform material and (b) layer-wise material distribution.

The average PR ($\overline{\nu}_{21}$) of the structure is computed using only the first four elements, highlighted Fig. 4.16, as they suffice to represent the average strain, and thus the PR, across the entire structure, due to the strain being constant along the horizontal direction. This significantly reduces the computational cost since strain sensitivity is only required for four out of the 192 macro elements. Nonetheless, the entire macroscale structure is accounted for in the optimization problem through the sensitivity of the stiffness matrix in Eq. (4.20). Moreover, in the uniform approach, the four highlighted elements share the same microstructure, whereas in the layer-wise approach, each element has its own distinct microstructure and design variable. As a result, the number of variables to which the strain sensitivity must be computed increases four times in the layer-wise case, further impacting the computational effort.

Finally, the optimization problem is stated in Eq. (4.35).

$$\min_{\rho^t_{e^m,l}} f = \frac{\overline{\nu}_{21}}{\nu^*} + ca\frac{C}{C^*}$$
$$s.t.: \begin{cases} g_1^l = \dfrac{V^{mi}}{V^+} - 1 \leq 0 \\ g_2^l = \left(\dfrac{E^H_{1111}/E^H_{2222} - 1}{\epsilon_1}\right)^2 - 1 \leq 0 \\ \rho_{min} \leq \rho^t_{e^m,l} \leq 1 \qquad t = 1{,}2;\ e^m = 1, 2, \dots, N^m; \rho_{min} = 10^{-3}, l = 1, \dots, nl \end{cases} \tag{4.35}$$

where ν^* and C^* are used here to normalize the objective function and are the values for PR and compliance in the first iteration, respectively. The continuation approach parameter ca is applied in the first 20 iterations and gradually increases from 0 to 0.2, allowing the problem to find an anepectic solution without stiffness influence.

Here, contrary to the previous case studies, where structural compliance was evaluated under a bulk-type loading condition, the compliance is measured for the specific forces at the beam end shown in Fig. 4.16. Applying a bulk load case would result in a non-uniform strain distribution along the horizontal axis, invalidating the simplifications considered in this example, i.e., using only four elements to compute the structure's average PR. Because of this, a volume constraint is imposed on each individual layer rather than globally, ensuring material presence throughout the entire structure. This means that the optimization problem in the uniform approach only have two constraints, as $nl = 1$, and eight constraints in the layer-wise approach, as $nl = 4$.

For both the uniform and layer-wise approach, the following penalization parameters are considered: $p_1 = 4$ and $p_2 = 3$. The volume fraction is set as 50%. A value of $\epsilon_1 = 5$ was considered here. As proven in the previous section a larger separation between the coefficients E_{1111} and E_{2222} typically leads to more negative PR and was used here to illustrate a different scenario and solution set. It is noteworthy that, despite the applied load being non-uniform, the microstructure maintains orthotropic behavior due to the imposed symmetry in the UC, which ensure a linear strain distribution.

4.3.4.1 Uniform Approach

The following results correspond to the case study of the beam under pure bending with uniform microstructure across the beam's domain. The microstructure's UC and respective beam domain are shown in Fig. 4.17. Note that a single UC is represented in each macro element, but must be interpreted as a periodic composite material, within each macroscopic point.

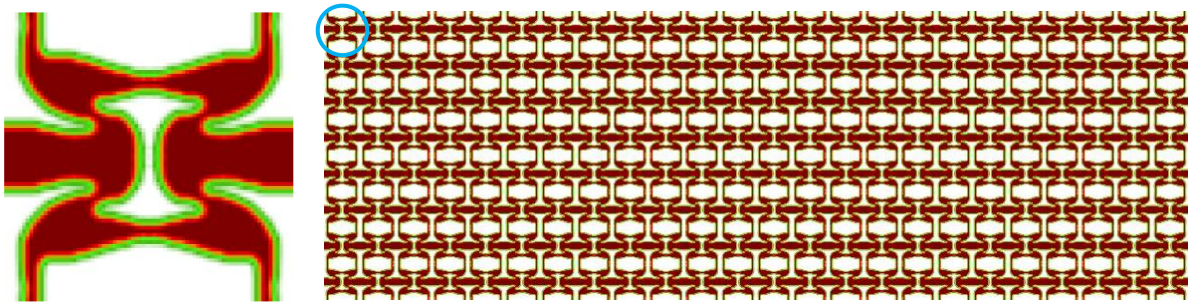

Figure 4.17 – UC of the optimized microstructure (left) and corresponding periodic pattern within the macroscopic beam domain (right).

The optimized UC is orthotropic, exhibiting distinct directional behavior. It shows significantly higher stiffness in the horizontal direction, which results in the PR $\overline{\nu}_{21}$ being much more negative than $\overline{\nu}_{12}$, although both remain negative, with $\overline{\nu}_{21} = -2.185$ and $\overline{\nu}_{12} = -0.364$. This outcome is expected, as the objective function specifically minimizes the PR in the vertical direction, for the pure bending load.

The horizontal, ε_{11}, and vertical, ε_{22} strain distribution along the beam are shown in Fig. 4.18a and 4.18b, respectively. The horizontal strain, ε_{11}, distribution along the beam remains uniform in the horizontal direction and reaches its maximum at the top fiber (i.e., the upper surface of the beam in the positive y-direction). Along the vertical direction, the strain varies linearly, which is consistent with classical bending theory. As for the vertical strain distribution, ε_{22}, the same uniformity is observed in the horizontal direction, and the same liner variation is observed in the vertical direction. The vertical strain is higher at the vertical layer, and positive in the upper half of the beam. This observation confirms the behavior previously reported for a uniform auxetic material, as shown in Fig. 4.15a, as the upper section of the beam is under traction, resulting in an expansion in the transversal direction, and vice-versa for the lower half of the beam.

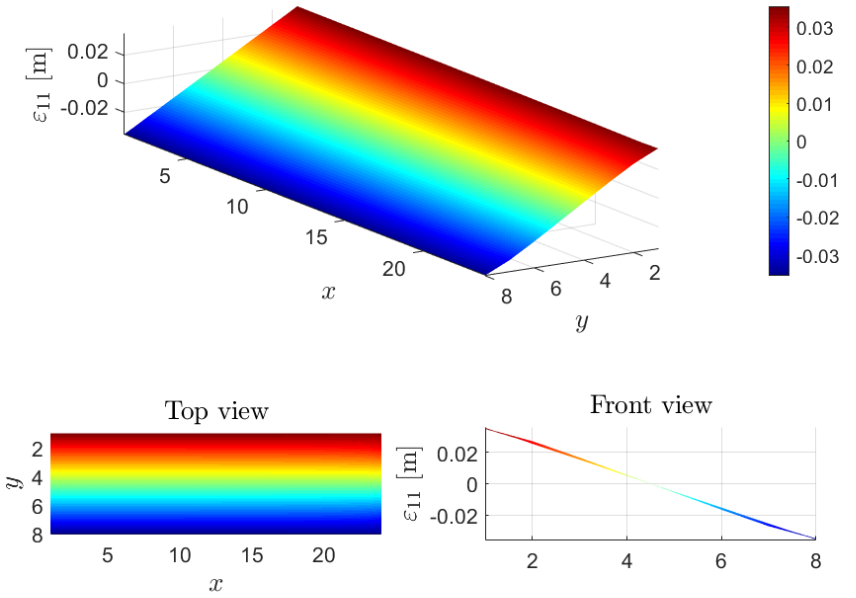

(a)

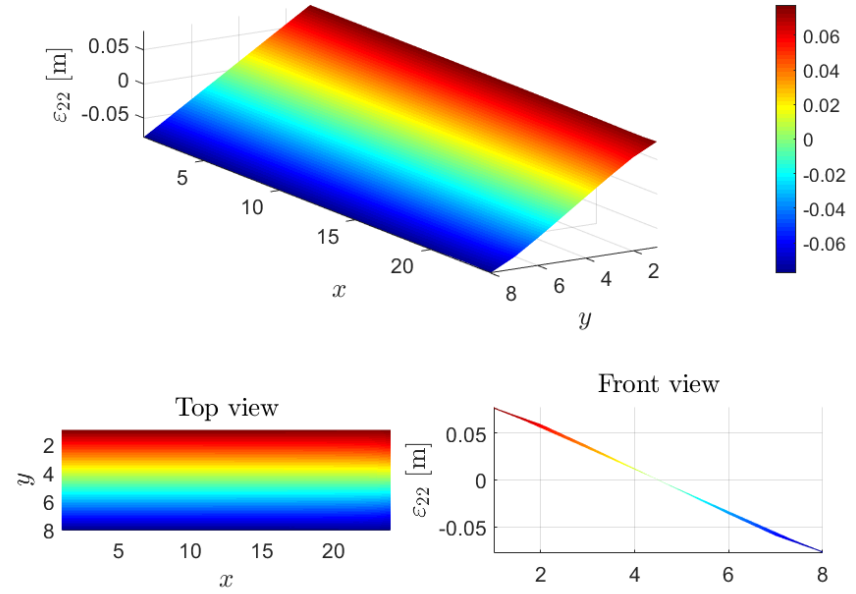

(a)

Figure 4.18 – Strain distribution in the optimized beam under pure bending with a uniform microstructure. (a) Horizontal strain distribution, ε_{11} and (b) vertical strain distribution, ε_{22}.

4.3.4.1 Layer-wise Approach

The results for the case study of the beam under pure bending with a layer-wise parameterization are presented below. The microstructure's UC of each layer and respective beam domain are shown in Fig. 4.19.

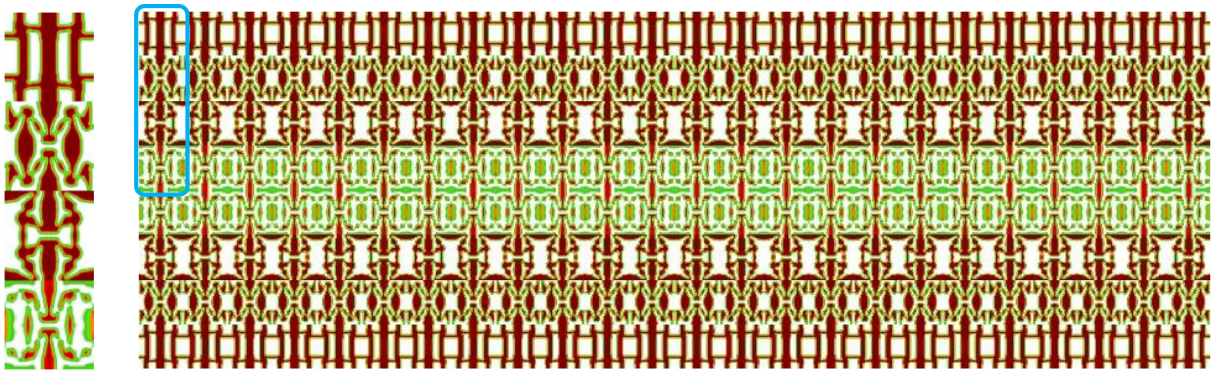

Figure 4.19 – UC of the optimized microstructure of each layer (left) and corresponding periodic pattern within the macroscopic beam domain (right).

The optimized microstructures exhibit stiffness quite oriented as each layer shows stiffness around 6 times higher along the horizontal direction. As a result, the average PR $\overline{\nu}_{21}$ is more negative than $\overline{\nu}_{12}$, although both remain negative, with $\overline{\nu}_{21} = -2.232$ and $\overline{\nu}_{12} = -0.443$. Compared to the previous case study, in Section 4.3.3, the improvement in $\overline{\nu}_{21}$ achieved by adopting the layer-wise approach is less pronounced. This is mainly due to the more constrained optimization problem, where the volume constraint is applied individually to each layer, rather than globally. Such restriction prevents the emergence of (excessive) porosity gradients across the macrostructure. Furthermore, the microstructure in the last layer exhibits noticeably lower stiffness compared to the other layers, with a volume fraction of only 0.34 (the respective local volume fraction constraint is inactive). In fact, it contains nearly disconnected regions, and the material phase is not clearly defined, compromising both stiffness and structural integrity. Notably, this layer is also where the applied strain due to pure bending is the lowest. To mitigate such behavior, alternative constraint formulations could be considered, for example, by enforcing a minimum stiffness or connectivity threshold per layer, introducing regularization terms that penalize disconnected patterns. These strategies remain an interesting avenue for future work.

Fig. 4.20a and 4.20b present the distribution of horizontal, ε_{11}, and vertical, ε_{22} strains along the beam, respectively. One of the first observations is that, in contrast with the beam composed of a uniform material, the strain distribution along the y-direction is no longer linear, although it remains continuous. Nevertheless, both the horizontal (ε_{11}) and vertical (ε_{22}) strains follow a similar pattern: in the upper half of the beam, where the horizontal strain is positive, the vertical strain is also positive. This behavior is expected, as all layers exhibit NPR. However, since the material stiffness varies now between layers, the applied pure bending load considered, which varies linearly with the beam's height, is no longer

consistent with the strain distribution (not linear) at the beam midspan, i.e., far enough from the applied load at the beam end. It is also observed that, although the strain distribution (both ε_{11} and ε_{22}) remains nearly uniform along the x-direction, there is a slight perturbation near the beam's end where the load is applied. According to Saint-Venant's principle, the localized effects of the applied load diminish with distance from the loaded end. Therefore, it is reasonable to focus on the strain distribution further into the beam domain (midspan), where the first few elements already capture the representative behavior along the horizontal direction, validating the adopted modeling strategy.

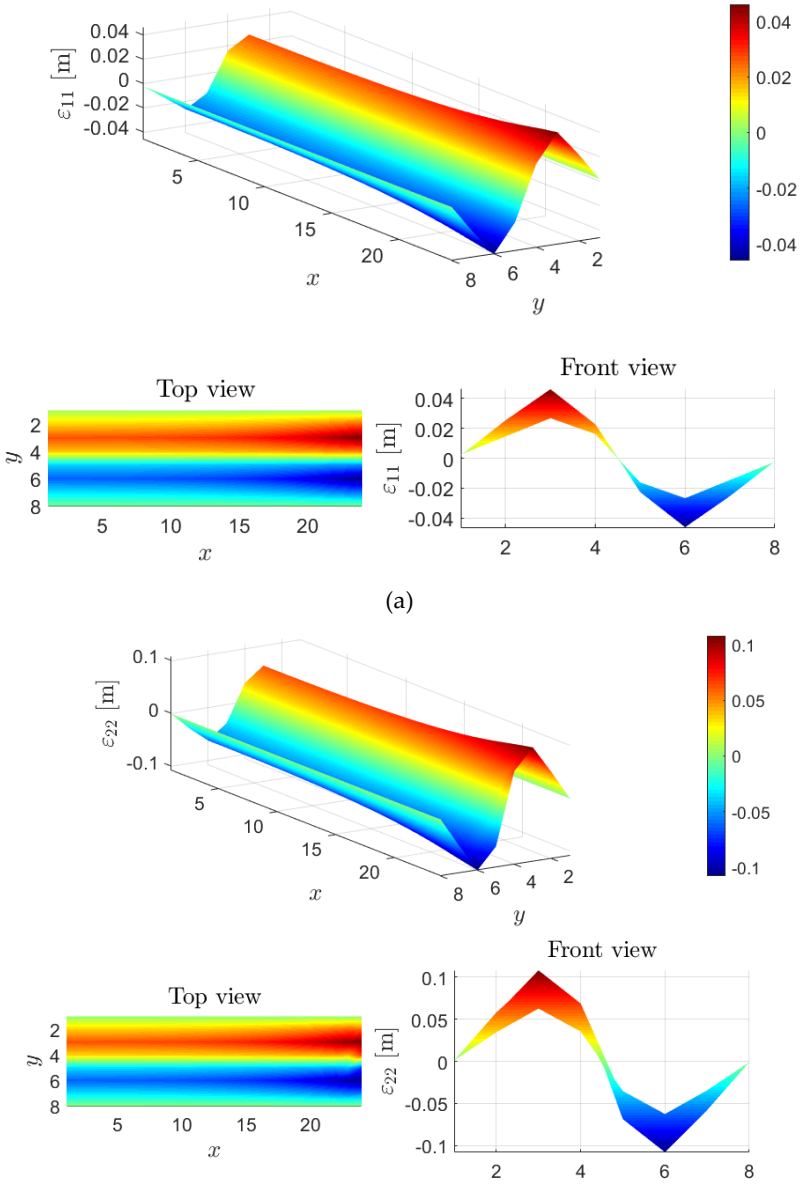

Figure 4.20 – Strain distribution in the optimized beam under pure bending with layer-wise microstructure. (a) Horizontal strain distribution, ε_{11}, and (b) vertical strain distribution, ε_{22}.

4.4 Computational Cost of Multiscale Analysis

To illustrate the computational cost of the multiscale optimization framework, an extra analysis is carried out here using the case study of the beam under pure bending. However, the insights and conclusions from this analysis can be extended to all optimization problems discussed in this chapter. In order to compute the average PR (Eq. 4.10) or the average CTE (Eq. 4.11), it is necessary to evaluate the strain field in each macrostructural element, and to solve the optimization problem, and the respective sensitivity of the strain must be computed (Eq. 4.18).

This analysis considers three discretizations of the macrostructure: 6×4, 12×8 and 24×16, corresponding to $N^M = 24$, $N^M = 96$ and $N^M = 384$ macro elements. For each macroscale discretization, four levels of microstructure resolution are evaluated: 40×40, 60×60, 80×80 and 100×100 microelements, corresponding to $N^m = 1600$, $N^m = 3600$, $N^m = 6400$ and $N^m = 10000$, respectively. The microstructure design is assumed uniform in all macro elements, without any symmetry conditions.

For each combination of macro- and micro-discretization, the following computational times are measured:

- t^{mi}: Time spent solving the microscale finite element problem and computing the homogenized properties (Eqs. (3.3)–(3.9)).
- t^{MA}: Time spent in the macroscale finite element analysis, including stiffness matrix assembly, Eq. (4.4), thermal load vector construction, Eq. (4.5), and solving the equilibrium equations.
- t^{ε}: Time required to compute the strain field in each macro element, Eq. (4.7).
- $t^{\partial\varepsilon}$: Time needed to compute the sensitivity of strain in each macro element with respect to all design variables, Eq. (4.18).

As an example, in the least expensive configuration (40×40 microelements and 6×4 macrostructure) there are $N^m = 1600$ microelements, which corresponds to $n = 2 \times N^m = 3200$ design variables (for the two-phase case), and $N^M = 24$ macro elements. Consequently, the sensitivity analysis in Eq. (4.18) must be performed $n \times N^M = 76.800$ times. In contrast, for the most computationally expensive scenario, this number increases for 7.680.000 times, i.e., 100 times more. This exponential increase highlights the importance of carefully selecting discretization levels to balance solution accuracy with computational load.

This computational time evaluation was done in MATLAB® R2024b, running the respective script using the Parallel Computing toolbox on a shared-memory Workstation HP Z8 G4, 2 CPUs Intel Xeon 6242R 3.1 GHz 2933 MHz 20C, 256 GB RAM. The computational times are shown in Fig. 4.21.

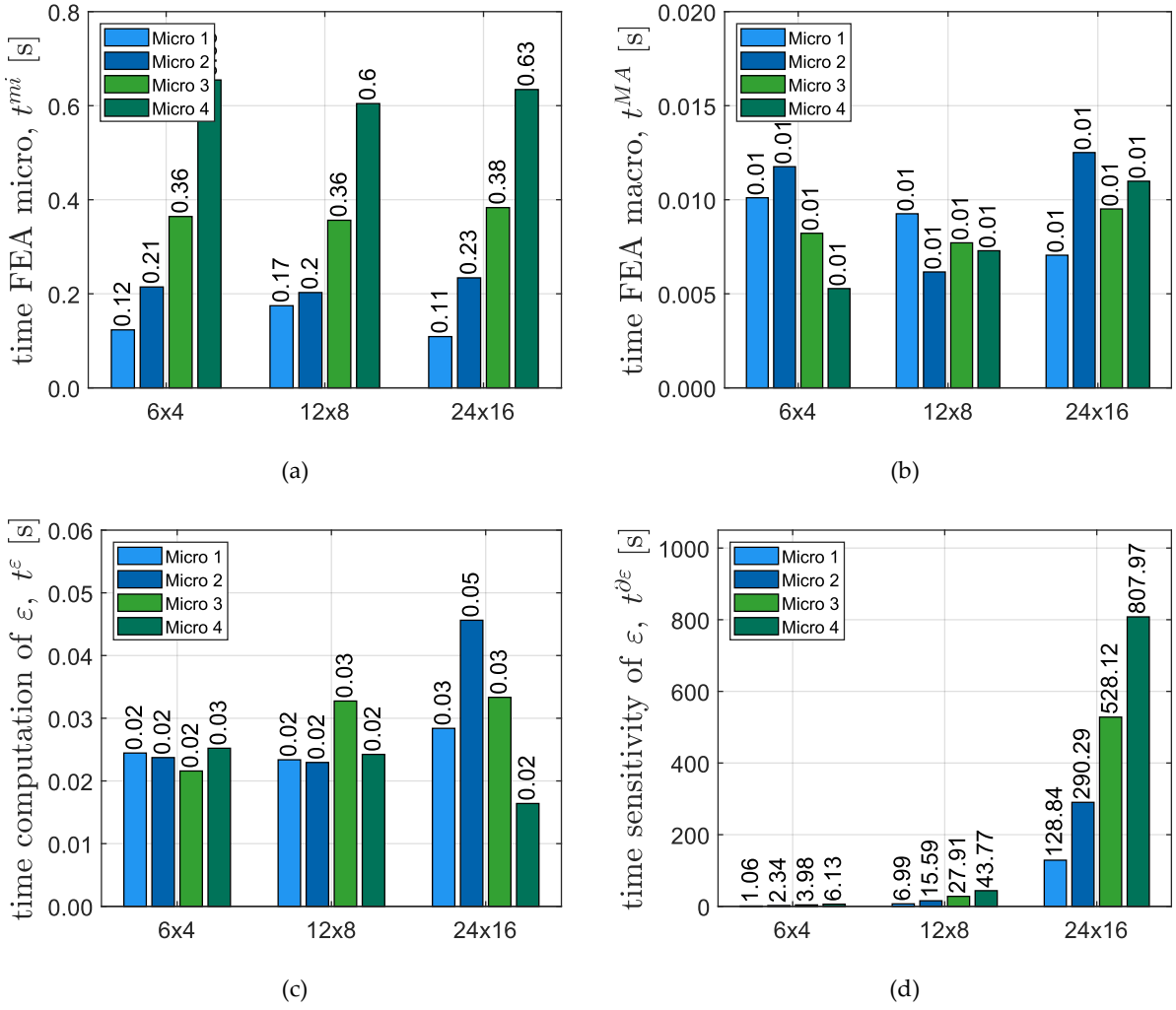

Figure 4.21 – Computational time breakdown for each step of the multiscale optimization process, for different combinations of macro and microstructure discretizations: (a) Microscale homogenization time, t^{mi}; (b) macroscale FEA time, t^{MA}; (c) strain computation time, t^{ε} and (d) sensitivity analysis time, $t^{\partial\varepsilon}$.

The time spent by the program solving the homogenization equations tends to grow quasi-exponentially with the refinement of the microstructure discretization, which is expected given the rapid increase in the number of microelements. This step is independent of the macroscale discretization, as the homogenization equations regard only the UC. On the other hand, the time required for the macroscale equilibrium analysis and strain evaluation

remains consistently negligible across all configurations. Minor fluctuations observed in these timings are likely due to system-level factors such as memory allocation, caching, and parallel processing behavior in MATLAB.

In contrast, the sensitivity analysis time shows a strong dependency on both the micro- and macroscale sizes. It increases significantly as the number of macro elements and microstructure design variables grows, especially in the most refined configurations. The time required for the most computationally expensive case is nearly 760 times greater than that of the simplest one, highlighting the substantial impact of scaling the FE meshes on optimization time costs.

4.5 Conclusions

The multiscale optimization framework developed in this chapter offers a powerful and realistic approach to designing architected materials by embedding the microstructure directly into the structural context. Rather than optimizing a material in terms of equivalent properties, this methodology allows to design the microstructures, accounting for their role within a larger structural system. This guarantees that the metamaterials are optimal not only in terms of material properties but also in terms of structural performance.

In particular, the concept of an *auxetic structure* was introduced and explored here. The goal was to extrapolate a behavior traditionally associated with material response, both NPR and NTE, to the scale of a structure, and ultimately design anepectic metamaterials by using the structural response in the optimization problem, specifically, the effective strain. This methodology proved successful, as anepectic metamaterials were achieved by tailoring the structural-level behavior to reproduce the response of auxetic materials. Furthermore, two different paradigms were considered regarding the formulation of the problem: The material is distributed within the structure either in a uniform or in a layer-wise fashion. This allows for the macrostructure to have different porosity levels, as the microstructure of each layer can have different volume fractions. This becomes particularly relevant when the structure is subjected to non-uniform loads, as the material distribution can benefit from locally tailored microstructures.

To investigate the proposed multiscale framework, four case studies are presented here: (1) TO of anisotropic auxetic metamaterials; (2) multiobjective MMTO to investigate the

influence of the effective properties; (3) influence of the load change in the auxetic behavior, for both uniform and layer-wise strategies and (4) auxetic beam under pure loading.

Although anisotropic auxetic materials have been previously reported in the literature, their effective PR is often measured using ratios between effective stiffness properties, that do not accurately reflect the global structural response. In contrast, the present methodology captures the true macroscopic behavior by computing the PR as the ratio between transverse and axial strains of the overall structure. The proposed multiscale framework proved to be especially relevant in the anisotropic context, where the ratio between effective properties is not equivalent to the ratio between strains. Using this approach, a chiral orthotropic metamaterial was obtained even with a single macro element, indicating that chirality does not inherently require anisotropy. However, as the number of macro elements increases and the macrostructure discretization is more refined, the optimizer naturally converges toward anisotropic chiral architectures.

Furthermore, the multimaterial, multiobjective problem introduced in Chapter 3 was revisited using the multiscale optimization framework. This methodology proved capable of successfully designing metamaterials that simultaneously exhibit NPR and NTE. One of the key advantages of this approach lies in the ability of directly controlling the effective properties, rather than relying on objective functions that only implicitly minimize the property (the PR) as shown in Chapter 3. As a result, the generated Pareto fronts in Chapter 4 offer a more accurate and meaningful representation of the trade-off between the two competing indices. This direct formulation highlights here as well the conflicting nature of NPR and NTE.

The impact of load changes on the auxetic behavior of optimized structures was investigated here as well. Allowing the macrostructure to exhibit varying porosities, by using microstructures with different volume fractions across layers, enabled improved minimization of the effective PR. Additionally, when subjected to non-uniform loading, the resulting microstructures naturally exhibited anisotropic characteristics, revealing the strong interplay between load variations and optimal material architecture.

The developed methodology was also applied to a more practical example of a bending beam, with either uniform or layer-wise material distribution. This example is particularly interesting in this context due to the well known linear strain distribution, that allows for meaningful optimization results with reduced computational cost. The algorithm successfully designed a material distribution that resulted in an auxetic beam under pure bending conditions. Unlike conventional beams, this structure expands in the regions under traction

and contracts in those under compression. This auxetic behavior was observed both for a uniform microstructure throughout the domain and for a layer-wise material distribution. Nevertheless, this problem offers further potential for exploration, which is left for future work.

Although the proposed multiscale topology optimization approach provides a more realistic representation of the material-structure interaction, it also introduces significant computational challenges. The evaluation of local strain in each macro element and, especially, the sensitivity analysis with respect to all design variables, is computationally expensive. As shown in the time breakdown analysis, this cost increases sharply with the refinement of both the macro and micro FE discretizations. Therefore, a trade-off between mesh refinements and computational costs is essential to unlock designs that could not be achieved otherwise.

5

METAMATERIALS: FROM DESIGN TO FABRICATION

This chapter presents the workflow developed to bridge design and fabrication of the metamaterials that are obtained employing the design methodologies presented in the previous chapters. The advanced in design methods such as optimization allowed the achievement of more complex and demanding structures. These developments in optimization techniques became impactful with the simultaneous innovation of manufacturing techniques. However, it is essential to develop a workflow that translates the numerical (or *in silico*) results to manufacturable prototypes. In the previous sections, several optimal metamaterials were designed using the density-based method, resulting in fine scale geometric features and jagged boundaries, that are impractical and senseless to be fabricated. Moreover, thermoauxetic solutions involve two materials and void, and the transition between material phases is not only jagged at the material–void interface, but also between the two solid material phases. Therefore, to fabricate these solutions a workflow that smooths interfaces between material phases, either material-void or material-material, is developed. This is a step forward in processing *in silico* data, with a view to experimentally producing parts. The workflow developed in this chapter is part of the work presented in the scientific paper "Functionally graded materials and structures: a unified approach by optimal design, metal additive manufacturing and image-based characterization", published in Materials, 2024 [15].

5.1 Data Processing Workflow

Before developing the workflow that enables the transformation of digital data from TO into a manufacturable STL file, it was essential to understand the nature of this data. This subchapter describes the necessary steps to convert the optimization data into a smoothed, printable geometry, including interpretation of the design variables, boundary reconstruction, file format conversion, and preparation for additive manufacturing.

Density-based TO approaches work upon a square grid, where an artificial density variable is attributed to each "square" (or finite element). This artificial density will define whether an element is solid or void. In the bi-material design case, two artificial density design variables are associated to each FE, one for topology definition and another for material selection. Therefore, jagged boundaries appear during the optimization process not only between solid and void phases, but also at the interfaces between two solids. These jagged boundaries require post processing such that the metamaterial be properly fabricated and functional.

The workflow presented in Fig. 5.1 comprises six main stages and a synergy between the following commercial software: ANSYS Mechanical APDL®, ANSYS Workbench® and Blender®.

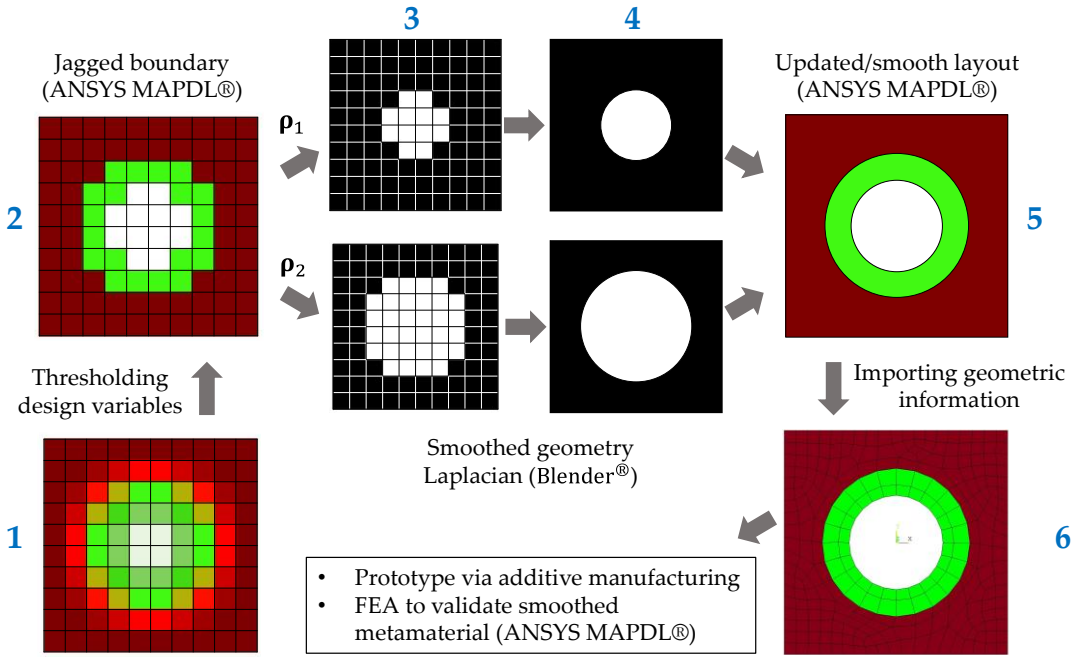

Figure 5.1 – Digital workflow converting digital data from TO to AM.

Although the output of the optimization process consists of a Boolean distribution of design variables (e.g., 0 or 1), the use of a density filter introduces intermediate density values in the material phase transitions. This creates somehow virtual smoothing of the material boundaries, as it prevents the transition between material phases from being sharp while maintaining the zigzagged discretization of the microstructure. However, these intermediate densities have no interpretation from a manufacturing perspective, as they represent a virtual or artificial transition between material phases. As the metamaterials being optimized here are composed of discrete material phases, to transfer the original data to the smoothed structure, and subsequently for manufacturing, it must be clearly identified where each base material is located within the structure domain.

Th first stage of the smoothing process consists of transferring the optimization data to a square-grid mesh of plane elements in ANSYS® Mechanical APDL, defining the stepwise distribution of $\boldsymbol{\rho}_1$ and $\boldsymbol{\rho}_2$ densities (see Fig. 5.1 left). In the second stage, a threshold of 0.5 is applied to the density distribution, identifying the following possible cases:

(1) Void, when $\rho_1 < 0.5$ (see Fig. 5.1, top center, white elements). For all elements that have $\rho_1 \geq 0.5$ (see Fig. 5.1, top center, black elements), the element is solid phase, and it is the variable ρ_2 that decides whether the solid is material phase 1 or 2.
(2) Material 1 when $\rho_2 \geq 0.5$.
(3) Material 2 when $\rho_2 < 0.5$.

In the third stage, after applying the threshold to both density fields, the solid parts of both fields, i.e., the parts corresponding to $\rho_1 = 1$ and $\rho_2 = 1$ (black elements), are saved in a CDB file. This file format is a text-based database file used to store finite element analysis data, including geometry, mesh, material properties, etc. The geometry is transferred to ANSYS Workbench®, where the FE model can then be saved in an STL format to be exported to Blender® for further processing. Here, ANSYS Workbench® bridges the ANSYS Mechanical APDL® and Blender® environments [15].

Once both density fields are imported into Blender®, the jagged boundaries are smoothed using the smooth Laplacian modifier (stage 4 in Fig. 5.1). This modifier allows for reducing noise on a mesh while preventing its shape integrity by adjusting the following parameters: *lambda factor*, *lambda border* and *repeat*. The modifier must be carefully applied, as the microstructure being smoothed corresponds, in fact to a UC of a periodic structure, and thus, its outer (square) boundary must remain unchanged so as not to compromise periodicity and continuity. When using the modifier, it is possible to select sub-groups of nodes, which is particularly useful for independently smoothing different geometric details and

leaving the outer boundary square shape preserved. The smaller and more localized the geometric feature, the more effectively the modifier performs. For instance, in a UC with two circles of significantly different sizes, applying the modifier to both simultaneously lead to inconsistent and less accurate results. Smoothing each boundary individually produces better outcome, as maintaining the volume of each circle. This, along with the need to fine-tune the modifier's parameters, makes the Blender® processing stage problem dependent. However, this tailored approach yields more accurate geometries than adopting a one-size-fits-all strategy.

After smoothing the boundary, the geometric data of both density fields is exported from Blender®, in STL format, and reimported into ANSYS Workbench®, where the 2D structure is now represented as two reshaped domains. At this stage, only geometric entities, such as areas, lines, and keypoints, remain. Up to this point, the strategy implemented here resembles the one developed in [15], where the structure is modeled as a Functionally Graded Material (FGM). However, this thesis extends the methodology to a bi-material microstructure, addressing the interface between distinct material phases. To represent the different materials, both smoothed regions, corresponding to $\boldsymbol{\rho}_1$ and $\boldsymbol{\rho}_2$, are considered. Note that the area corresponding to $\boldsymbol{\rho}_2 = 1$ is always included within the solid region, where $\boldsymbol{\rho}_1 = 1$. Thus, by overlaying both smoothed regions, the boundary smoothing is performed not only between solid material and void (through the smoothed boundary of $\boldsymbol{\rho}_1$), but also between the two material phases, through the smoothed boundary of $\boldsymbol{\rho}_2$. For that purpose, smoothed geometry is exported from ANSYS Workbench® in IGS format and imported into ANSYS Mechanical APDL® (see stage 5 in Fig. 5.1).

Before manufacturing any prototype, it is important to verify that the smoothing process applied to the boundary of the microstructure does not compromise its thermoelastic structural performance, and therefore a new finite element analysis must be conducted and compared with the original optimized results. For that purpose, the smoothed geometry is meshed using quadrilateral elements. If the equivalence between both designs is verified, then the geometric information of each material phase is exported to an STL file to be manufactured by 3D printing.

5.2 Preservation of Thermoelastic Properties

A comparative study between the original optimized UC and its smoothed counterpart is conducted here, to verify the preservation of thermoelastic properties of the design materials after the smoothing process. The methodology adopted follows the RVE method described in Section 3.2.4, where the thermoelastic effective properties of the material are evaluated by modeling a RVE with a finite number of UC repetitions in ANSYS®. As previously demonstrated, using more than five UC repetitions ensures that the homogenized properties converge with acceptable accuracy to those obtained in the optimization (see results in Section 3.4.1.3). In this study, a 5×5 repetition pattern is used to evaluate both configurations. By comparing the effective thermoelastic properties before and after smoothing, this analysis aims to confirm that digital data-conversion to go from design to fabrication preserves the key material behaviors necessary for functional performance.

Dirichlet-type BCs are considered, and three-unit elastic test strains and one thermal test strain are applied as shown in Fig. 5.2. These BCs correspond to the displacement vector defined in Eq. (3.33).

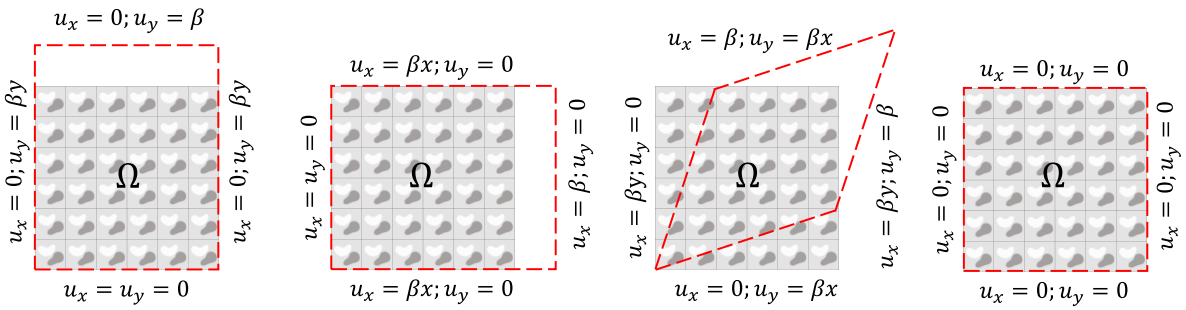

Figure 5.2 – Numerical tests (2D representation of RVE). Dirichlet-type conditions: (a) vertical normal test; (b) horizontal normal test; (c) shear test; (d) thermal test.

The star-shaped re-entrant design solution resulting from the optimization problem stated in Eq. (3.27), with $\omega = 0.3$, $p_1 = 3$ and $p_2 = 3$, is used here to conduct the intended analysis. The optimized and smoothed microstructure are shown in Fig. 5.3a and 5.3b, respectively. The smoothed structure is generated after applying the process described in the previous section. The BCs illustrated in Fig. 5.2 are applied to the RVE, which is then used to evaluate the material's effective properties, following the procedure described in Section 3.2.4. Note that the smoothed UC is not discretized using a regular square grid, and therefore

the application of the BCs in Fig. 5.2 as well as the computation of the body averages in the RVE domain, must be carefully carried out to account for the irregular mesh.

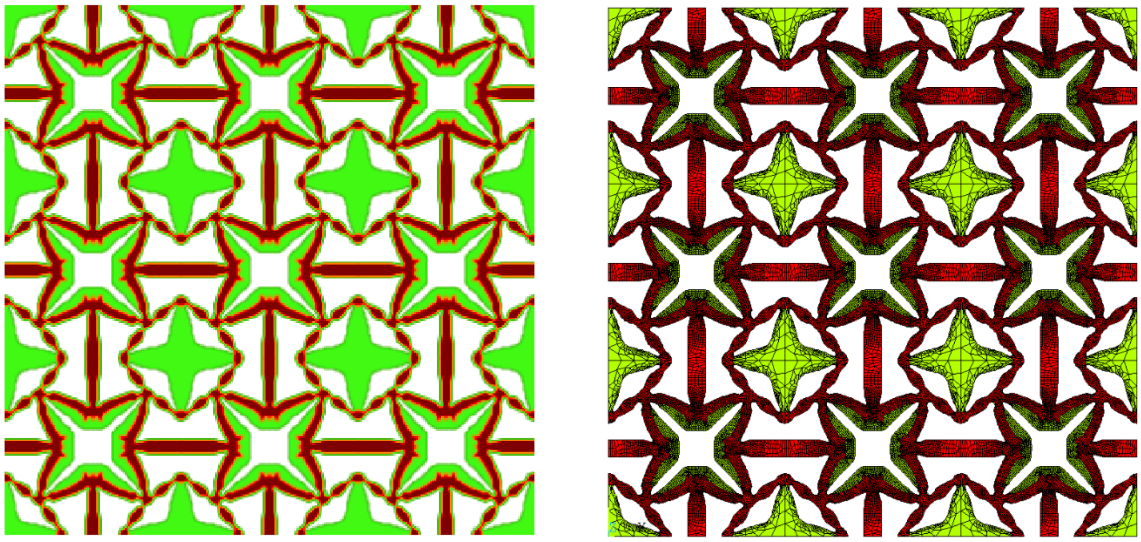

(a) (b)

Figure 5.3 – Anepectic microstructure (a) before and (b) after boundary smoothing. For visualization purposes of the smoothed structure defined in ANSYS®, only the elements corresponding to materials 1 and 2 are shown; void elements are not represented.

Table 5.1 presents the effective thermoelastic properties of the microstructure before and after smoothing, and the relative error introduced by the smoothing procedure. The relative error is calculated as $\left(E^S_{ijkl} - E^H_{ijkl}\right)/E^H_{ijkl} \times 100$, for both the stiffness tensor and the thermal stress tensor. The null components are skip here. The superscript S stands for the effective properties of the smoothed structure.

Table 5.1 – Effective properties of a microstructure before and after the smoothing procedure.

	Elastic properties [$\times 10^7$ Pa]				Thermoelastic properties [$\times 10^9$ ppm°C^{-1}Pa]	
	E_{1111}	E_{1122}	E_{2222}	E_{1212}	β_{11}	β_{22}
Optimal structure	7.323	-5.699	7.323	0.069	-2.555	-2.555
Smoothed structure	9.568	-6.979	9.574	0.224	-2.666	-2.674
Error [%]	30.66	22.47	30.74	225.55	4.37	4.66

The results show that, for the normal stiffness components E_{1111} and E_{2222}, the smoothing process introduces an error of approximately 30%, while the coupling term E_{1122}

deviates by around 22%. Thermal components show minimal deviation, with an average error of $4-5\%$. However, a significantly larger error is observed for the shear component E_{1212}, which increases by nearly 200% after smoothing. This discrepancy may result from the fact that shear behavior is particularly sensitive to geometric changes in the boundary region, especially when fine zig-zag features are removed or altered during smoothing. Additionally, as illustrated in Fig. 5.3, the optimal structure (before boundary smoothing) exhibits more compliant hinge regions, particularly in areas where fine geometrical features are present and filtered, appearing as green transition zones between solid (red) and void (white) regions. These thin joints tend to behave almost like mechanical hinges, allowing local rotations that reduce the overall stiffness. The smoothed structure, Fig. 5.3b, have a volume fraction of 0.56 (instead of 0.5 as in the optimal microstructure) which leads to the hinges loosening some of their fine detail. As a result, these joints behave more rigidly, which can contribute to the observed increase in stiffness in the smoothed microstructure. This effect is especially relevant under Dirichlet-type shear tests, where the difference in hinge flexibility between the two configurations may become more pronounced and contribute to the significant variation observed in the shear modulus E_{1212}.

5.3 Experimental Characterization of Auxetic Behavior

To demonstrate the manufacturability and practical feasibility of the proposed designs, physical prototypes were produced based on the smoothed computational models presented in Fig. 5.4a-c, corresponding to three different material volume fractions: 0.20, 0.35, and 0.50; the respective samples are referred to as mesh #1, mesh #2 and mesh #3. The first and last meshes result from solving the optimization problem starting from the star-shaped reentrant initial design, with different volume fractions (recall Table 3.2). Mesh #2 arises from the inverted honeycomb initial design. Both bi-material and single-material versions were fabricated, illustrating different strategies to obtain the optimized geometries. These prototypes serve as a first step towards experimental validation and provide insight into the geometric complexity and material distribution challenges that may arise in real-world applications.

The homogenized PR, of the optimized microstructures prior to smoothing, corresponds to the output of the multiscale optimization framework. Before any post-processing steps for manufacturability are applied, the following PR values are obtained. The PR of the microstructures in Fig. 5.4a-c, is $\nu_{12} = -0.667$, $\nu_{21} = -0.579$ and $\nu_{12} = -0.864$, respectively.

These values serve as reference for assessing the mechanical response of the prototypes. However, bear in mind that the smoothing process may introduce geometric changes leading to slight variations in the effective properties.

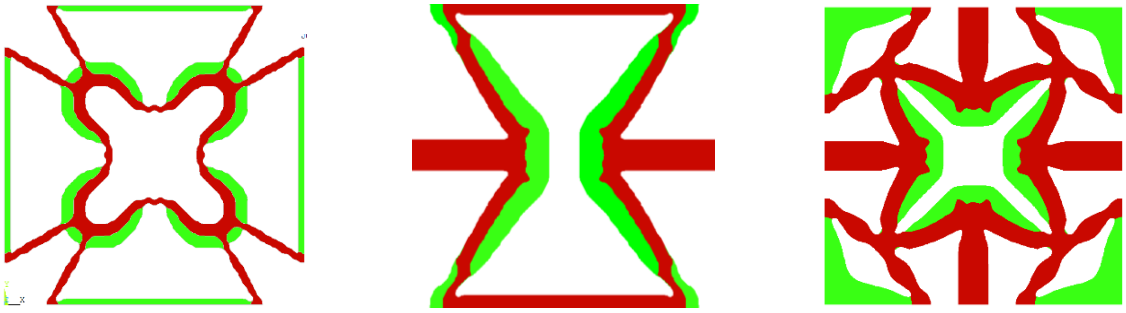

(a) (b) (c)

Figure 5.4 – Smoothed computational models of the unit cells used for prototyping different samples: (a) mesh #1, (b) mesh #2, and (c) mesh #3.

5.3.1 Prototypes

Additive manufacturing (AM), commonly known as 3D printing, enables the fabrication of complex geometries by depositing material layer by layer, based on a digital 3D model. Fused Filled Filament (FFF), also known as Fused Deposition Modelling (FDM®), belongs to a subcategory of Material Extrusion AM, where a polymer filament, in its fused state, is dispensed through a nozzle, as outlined in Fig. 5.5a. The advances in 3D printing and other AM techniques are particularly advantageous for manufacturing metamaterials, which are usually characterized by intricate microstructural features and multimaterial compositions that would otherwise be impossible to fabricate using conventional subtractive methods such as CNC machining [172,173].

The prototypes were printed using FFF technology, on an Ultimaker 3 3D printer, seen in Fig. 5.5b, processing the digital files via the Ultimaker Cura software, with both PVA and Nylon for the bi-material samples and Nylon for the single-material samples. All layers were printed uniformly to prevent gradient effects and the brim was removed to ensure clean boundaries. The following printing settings were adopted:

- 0.4 mm nozzle and a layer height of 0.1 mm and width of 0.4 mm;
- Extrusion temperature of 255°C for Nylon and 215°C for PVA;
- Build plate temperature of 60°C;
- Printing speed of 70 mm/s for Nylon and 35 mm/s for PVA.

For the dual-material samples, the appropriate material profiles and toolpath switching were managed via Ultimaker Cura's multi-material settings. These parameters were selected to ensure optimal layer adhesion, dimensional accuracy, and mechanical performance.

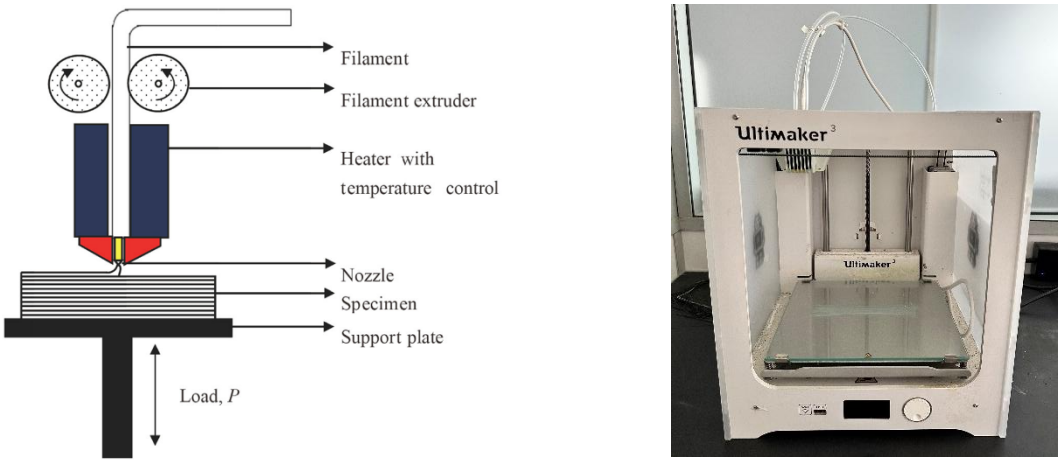

(a) (b)

Figure 5.5 – (a) Schematic representation of FFF process [173]. (b) 3D printer (Ultimaker 3) used for fabricating the prototypes via FFF technology.

5.3.1.1 Bi-material Prototypes

The production of the bi-material prototypes, presented in Fig. 5.6, involved the extrusion of two thermoplastic filaments through separate nozzles, PVA (white) and Nylon (black), whose mechanical properties are listed in Table 3.3, allowing the spatial distribution of different materials as designed by the computational model procedure previously presented. The printing settings used are the same as previously described.

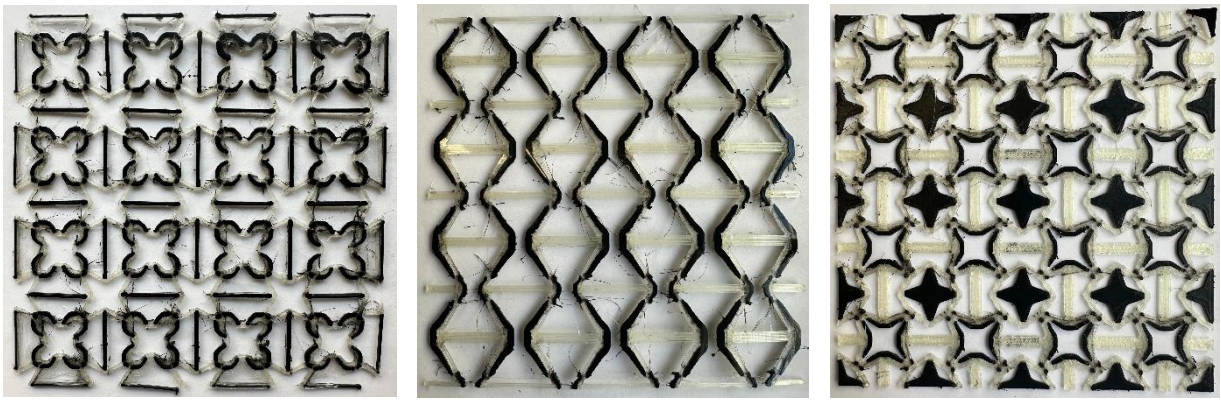

(a) (b) (c)

Figure 5.6 – Bi-material prototypes manufactured using Fused Filament Fabrication (FFF) technology. Samples with 4 × 4 repetitions of the UC: (a) mesh #1, (b) mesh #2, and (c) mesh #3.

The bi-material prototypes were printed with four repetitions of the unit-cell in each spatial direction, horizontal and vertical, resulting in a total sample size of 120 mm × 120 mm. As observed, the samples still exhibit some residual filament strands, commonly referred to as "stringing", a typical occurrence in FFF processes, especially when printing with multiple materials. Additionally, in the first example, it is visible that there was no adhesion at the interface between the two materials, in the bottom edge of the sample, indicating a lack of proper adhesion during printing. These imperfections suggest that the manufacturing process can still be optimized to improve the quality and reliability of the prototypes.

5.3.1.2 Single-material Prototypes

The single-material prototypes, shown in Fig. 5.7, were manufactured using Nylon. These prototypes include circular supports designed to enable mechanical testing following the procedure described in [9] for measuring the PR. Although this testing could, in principle, be extended to bi-material samples, single-material prototypes offer a more straightforward and reliable fabrication route for preliminary experimental validation. Work is still ongoing to refine the bi-material prototypes and ensure their suitability for mechanical testing.

Note that the microstructure in Fig. 5.7b is rotated 90° when compared to the configuration presented in Fig. 5.4b, meaning that the test is measuring the PR ν_{21} instead of ν_{12}, as done for the other microstructures. Recall that ν_{21} is derived from an applied horizontal load, which is equivalent to a vertical test when the structure is rotated by 90°. This microstructure exhibits different responses along the two principal directions due to its orthotropic behavior, which makes it interesting for future testing under loading in both orientations.

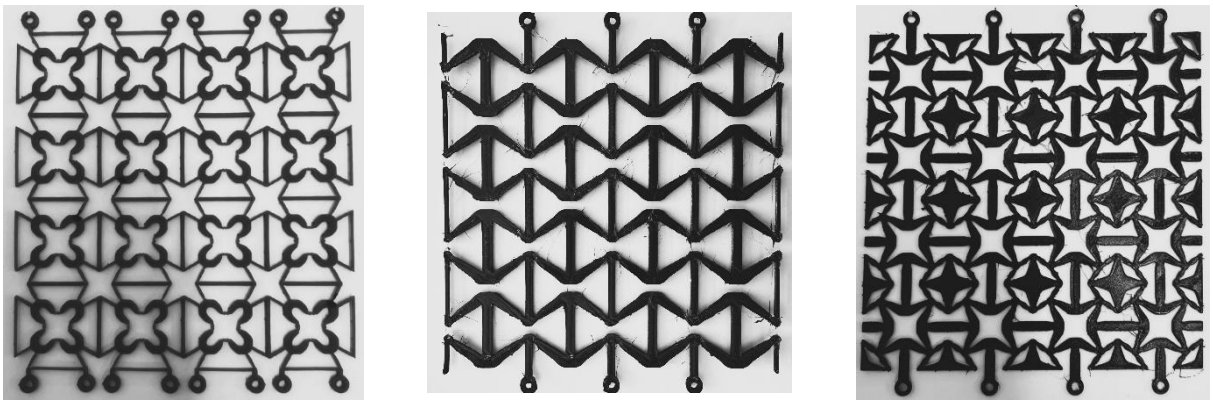

(a) (b) (c)

Figure 5.7 – Single-material prototypes manufactured using Fused Filament Fabrication (FFF) technology, with supports for testing. Samples with 4 × 4 repetitions of the UC: (a) mesh #1, (b) mesh #2, and (c) mesh #3.

5.3.2 Experimental Setup

All mechanical tests were carried out using a Shimadzu AG-50kN G universal testing machine, see Fig. 5.8a, equipped with a 50 kN load cell and operated via the proprietary TRAPEZIUM 2 software. Due to the buckling tendency of 2D mesh-like structures under compressive loading, the samples were tested under uniaxial tension instead, using custom-designed metal grips equipped with hook-shaped fixtures specifically developed for this application, to prevent restricted horizontal displacements, see Fig. 5.8b. To determine the PR, the deformation was recorded using a camera positioned to capture displacement along two orthogonal directions. Special care was taken to minimize parallax error and to maintain a constant distance between the camera lens and the specimen. The camera setup is presented in Fig. 5.8b. All tests were performed at a constant displacement rate of 1 mm/min.

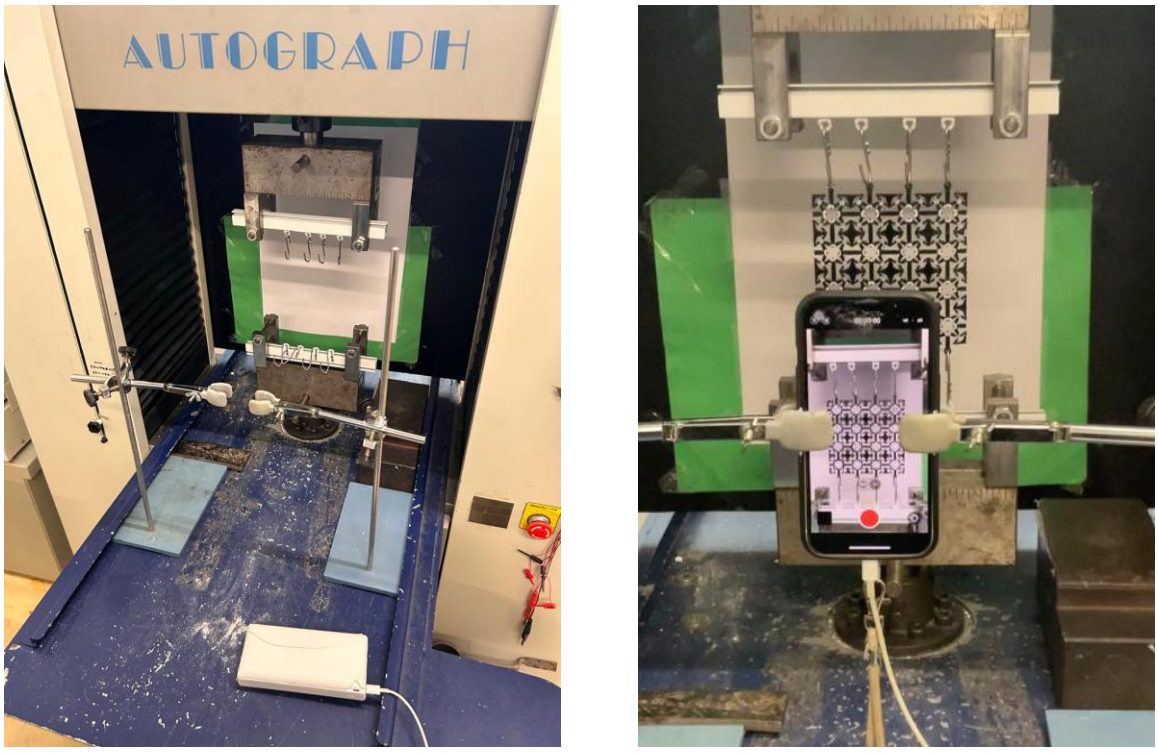

(a) (b)

Figure 5.8 – (a) Shimadzu AG-50kN G universal testing machine used for the tensile tests. (b) Experimental setup showing the camera positioning used to capture in-plane deformations for PR measurements.

The deformation was later analyzed with ImageJ software. The microstructure was previously marked with reference points, and the corresponding deformations were measured at the final deformed state, as presented in Fig. 5.9.

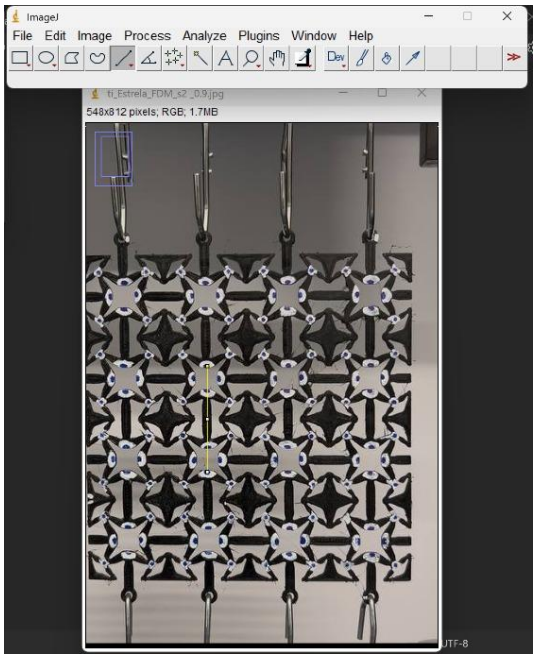

Figure 5.9 – ImageJ interface used to measure the deformation of the samples during the tensile tests. Representative straight line used to determine dimensional changes between the initial and deformed configurations, with reference points (white with blue dots).

The UCs located at the sample boundaries were excluded from the deformation measurements, as they are more susceptible to edge effects that can lead to non-representative displacements and compromise the accuracy of the analysis. As in the computational scale size effect study, only the central UCs were used to ensure that the measured deformation closely reflects the periodic behavior of the microstructure. With the image open, the "Straight" tool was used to draw a straight line across 2 or 3 inner UCs of the structure in both the horizontal and vertical directions. Then, the "Analyze > Measure" function was used to record the corresponding lengths (width and height), which were later entered into an Excel sheet to compute the PR, according to the following expression:

$$\nu = -\frac{\varepsilon_{trans}}{\varepsilon_{long}} = -\frac{\Delta L_{width}/L_{width}}{\Delta L_{height}/L_{height}} \tag{5.1}$$

Although the entire computational framework was developed assuming a purely two-dimensional formulation, in practice, the structure thickness may influence the mechanical response. For this reason, each sample in Fig. 5.7 was fabricated with two different thickness, 0.9 mm and 1.8 mm. Furthermore, each sample is printed three times, allowing for three in-

dependent tests per microstructure. This repetition enabled the calculation of the PR as an average value, helping to mitigate experimental errors and variability. The results are presented in Table 5.2.

Table 5.2 – Comparison between homogenized and experimental average PR values for printed samples mesh #1, mesh #2 and mesh #3.

Sample	Thickness [mm]	Experimental PR	Optimized PR	Deviation [%]
Mesh #1	0.9	–	-0.667	-
	1.8	-0.723		8.5
Mesh #2	0.9	-0.133	-0.579	77.0
	1.8	-0.276		52.3
Mesh #3	0.9	-0.690	-0.864	20.0
	1.8	-0.549		36.4

Regarding the results obtained from the mechanical testing, it is worth noting that for mesh #1, which corresponds to the lowest volume fraction (0.20), it was not feasible to print the sample with a thickness of 0.9 mm. The structure exhibited excessive stringing and was too fragile in certain areas, making it impractical for testing. Therefore, only the 1.8 mm thick version was fabricated. Interestingly, this microstructure is the one that shows the smallest deviation, less than 10% from the homogenized value. In contrast, mesh #2 presented the highest deviation among the three cases. During testing, the sample exhibited noticeable out-of-plane deformation, which likely compromised the accuracy of the strain measurements and, consequently, the PR estimation. Finally, mesh #3 showed a deviation of approximately 20% for the 0.9 mm sample and 36% for the 1.8 mm version, both underestimating the expected PR. This underestimation is aligned with the previous observations (see Section 5.2), where the smoothed version of the microstructure was found to be stiffer than the original topology, due to the increase in the volume fraction after the smoothing process. Also, bear in mind that the optimized PR value are computed for the bi-material structures, and the samples are single material. Although the PR value is mostly insensitive to the material distribution and depends solely on the topology of the microstructure, it is also reasonable to think that in practice this change may translate into a small perturbance of the PR value.

Furthermore, another aspect that can significantly impact the results is the number of support points used in each sample. Mesh #1 has a total of 8 supports, while mesh #2 and #3 only have 3 and 4 supports, respectively. In both samples #2 and #3 the edge effects where

more evident, and in the case of mesh #2 the lack of support points lead to out-of-plane deformation, as can be seen in Fig. 5.10.

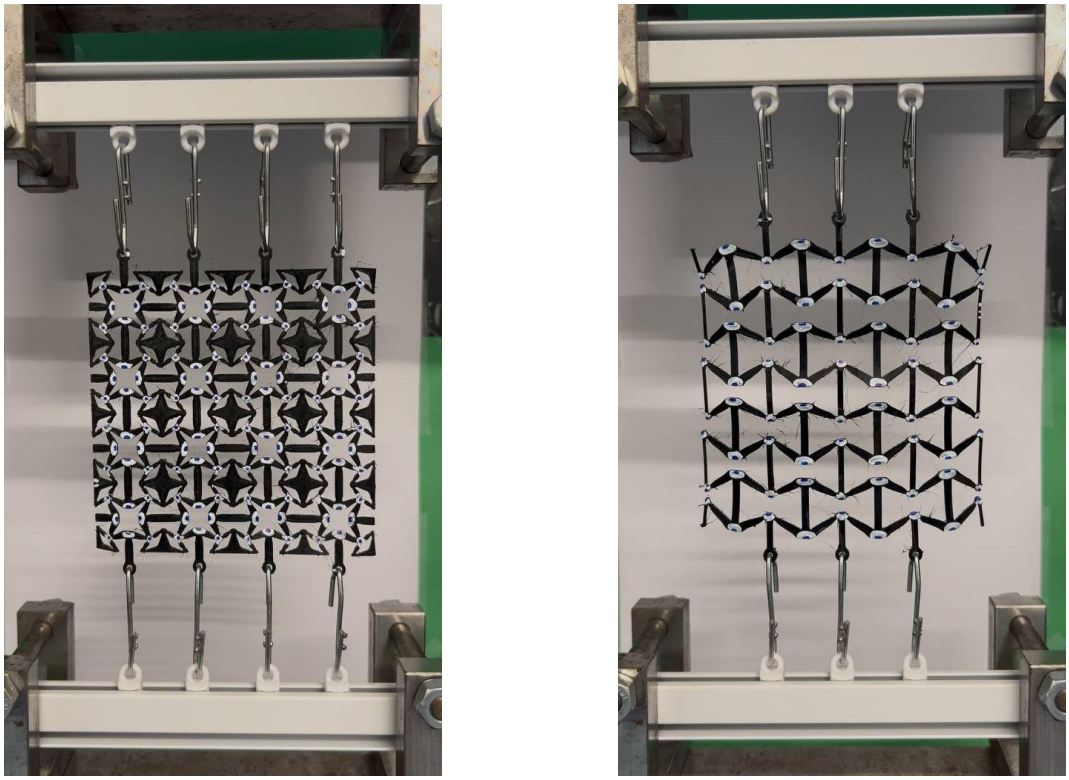

Figure 5.10 – Edge effects and out-of-plane deformations of mesh #2 and mesh #3.

These results highlight that there is still room for improvement, particularly in refining the clamping/support system to enhance testing reliability, and in improving the smoothing process to avoid inadvertently increasing the structure's volume fraction. This is part of an ongoing work, which also includes the implementation of thermal tests to validate the thermo-auxetic behavior of the designed microstructures. Nevertheless, the outcomes obtained for mesh #1 and mesh #3 are promising and serve as an interesting validation of the computational predictions, demonstrating the feasibility of using such optimized structures for achieving NPR in practice.

6

FINAL REMARKS AND FUTURE WORKS

6.1 Summary and Conclusions

The aim of this thesis was to conceptualize and develop a computational tool to assist in the systematic design of functional metamaterials, focusing on the simultaneous achievement of negative Poisson's ratio (NPR) and negative thermal expansion (NTE). By incorporating advanced topology optimization techniques, including multimaterial, multiobjective, and multiscale formulations, this work extends the state-of-the-art on material design. The primary contribution lies in the development of a methodology that not only tailors effective properties at the microscale but also ensures their successful integration into macroscale structures, enabling enhanced overall mechanical performance.

In particular, the thesis introduces and validates novel strategies to systematically design auxetic and anepectic metamaterials, where the desired effective behavior emerges from the geometric layout and spatial distribution of multiple materials. The integration of homogenization techniques with optimization enables a robust and flexible design approach, with potential applications across engineering domains where lightweight, thermomechanical functional materials are required. Two complementary optimization strategies were explored: a microscale approach and a multiscale approach. The microscale strategy focuses primarily on the conflict between achieving NPR and NTE, presenting results for both continuum-like and truss-like discretized microstructures. In contrast, the multiscale strategy emphasizes the relationship between auxetic behavior and the structural context in which

the material is inserted, exploring how the macroscale geometry, and loading conditions influence the performance and distribution of the designed microstructures.

In the microscale optimization framework, a weighted-sum formulation was implemented to investigate the conflicting nature of NPR and NTE. The problem was formulated using the known inverse-homogenization method, where the effective properties of the material are computed through the homogenization method and then used in the objective function. It was demonstrated that a trade-off between these properties can be systematically explored. The NPR behavior was shown to be largely governed by microstructural geometry, whereas the NTE response was highly sensitive to material distribution. Several material behaviors were explored with different examples, such as anisotropic, orthotropic and cubic materials. A representative volume element (RVE) analysis confirmed that the optimized unit cells achieve their target behavior after only a few repetitions, supporting the assumption of scale separation in homogenization.

Still in the context of microstructural design optimization, a truss-like formulation based on bar elements was also explored. While capable of generating auxetic and NTE behavior with significantly lower computational cost, this approach introduced simplifications that limit its physical practicality, particularly due to idealized hinges and overlapping bars. Nevertheless, it proved valuable as a conceptual tool to explore truss-like discretizations, which are way less explored in the literature.

At the multiscale level, a novel optimization framework was developed that integrates the microstructure directly into a structure, moving beyond the traditional approach of optimizing equivalent properties, introducing the concept of an auxetic structure. By using effective strain as the objective function, the framework allows the design of microstructures tailored to their structural response, e.g., PR, through average strain ratio. Several case studies demonstrated the ability to extrapolate NPR and NTE behavior to the structural scale, validating the concept of auxetic and thermoauxetic structures whose effective behavior emerges from structural deformation directly.

Four case studies were conducted regarding the multiscale optimization framework: (1) optimization of anisotropic auxetic metamaterials, (2) multiobjective, multimaterial optimization to explore NPR-NTE trade-offs, (3) the impact of load change on auxetic behavior under both uniform and layer-wise strategies, and (4) an auxetic bending beam example under pure bending. These studies confirmed the flexibility of the framework and the relevance

of microstructural tailoring, particularly inserted in a structural system, i.e., considering the structure geometry and loading conditions.

The proposed methodologies contribute to the advancement of systematic material design, introducing novel mechanisms to achieve complex elastic and thermoelastic effective behavior. The microstructural optimization framework successfully explores the competition between NPR and NTE, aided by problem normalization. The findings emphasize that NPR and NTE, though often discussed together, rely on different physical mechanisms: the former on geometry, the latter on material layout.

The truss-like discretization offered a fast and interpretable way to identify structural principles behind auxetic and NTE behavior, but it is limited by its simplifications. Its reliance on idealized joints and bar overlaps can hinder physical feasibility, indicating the need for more refined modeling for manufacturable designs.

The multiscale formulation represents a conceptual change in metamaterial design, embedding the microstructure within its functional structural environment. This enables the design of materials that perform optimally under realistic loads and boundary conditions. However, the approach is computationally demanding, particularly due to the sensitivity analysis and local strain evaluations in each macro element. The balance between computational cost and mesh resolution becomes critical, especially in large-scale applications. However, despite these limitations, the ability to directly control effective structural response, rather than optimizing effective properties, marks a substantial methodological advancement.

Finally, a computational workflow was developed to convert the optimized microstructures into smoothed geometries, enabling their physical fabrication, and contributing to the development of an engineering cycle for additive manufacturing. It was verified that, although the overall material distribution is preserved, the smoothed microstructure is slightly stiffer due to a slight increase in the volume fraction. Even so, three different meshes with different volume fractions are selected, to fabricate both single-material and bi-material prototypes, and to assess the manufacturability and practical implementation of the proposed designs. Mechanical tests were performed on the single-material samples to determine their effective PR. The results showed good agreement with the computational predictions, particularly for the microstructures with lower volume fractions. Despite some limitations, such as out-of-plane deformation and sensitivity to boundary conditions, the tests confirmed

the feasibility of the optimized designs, with mesh #1 and mesh #3 showing especially promising performance.

The methodologies developed open pathways for the design of next-generation materials tailored to specific functions, loads, and environments. By integrating material design, structural performance, and functional optimization into a unified computational framework, this work lays the groundwork for a new era of architected materials.

6.2 Future Work

The developments presented in this thesis provide a solid foundation for the systematic design of metamaterials with tailored mechanical and thermal responses. However, several avenues for future research are identified to address the challenges and limitations discussed throughout this work.

In the case of the truss-like discretization, while it effectively captures key mechanisms behind auxetic and NTE behavior with reduced computational cost, it remains limited in terms of structural feasibility. The assumption of pinned connections and presence of overlapping bars in the final designs results in unfeasible solutions to fabricate. Future work should focus on extending this framework to incorporate manufacturing constraints. This would improve the physical realism and applicability of the truss-based optimization approach.

For the multiscale optimization formulation, which represents a shift towards the inclusion of microstructural design within functional structural systems, further development is also necessary. Modeling challenges become more significant when dealing with anisotropic materials, where the structural response is less intuitive and more sensitive to directional effects. Addressing this will require more robust and unbiased modeling strategies that can fully capture anisotropic behavior without compromising the structural fidelity at the macro scale. In addition, while the present work focuses on the auxetic performance of the optimized structures under linear thermoelastic assumptions, future studies should consider more general thermo-mechanical analyses, including temperature-dependent loading conditions and transient thermal effects at the macroscale, in order to fully characterize and optimize the thermoauxetic response. Finally, although the multiscale approach offers a powerful tool for integrated design, its high computational cost remains a barrier to practical application. Future research should explore algorithmic improvements, such as advanced

solvers, model order reduction techniques, or parallelization strategies, to make this approach more scalable for large and complex systems.

Despite the fundamentally computational nature of this thesis, experimental validation remains a key step to validate the optimized solutions. While some single-material prototypes have been fabricated and tested, future work should prioritize the use of multi-material additive manufacturing to fabricate and test selected designs, to confirm the predicted auxetic and thermoauxetic behavior. Additionally, improvements are needed in the mechanical testing setup, particularly in the design of the support fixtures, to avoid undesired effects such as out-of-plane deformations. Enhancing the print quality and interface adhesion of the bi-material samples is also a crucial step toward obtaining reliable prototypes allowing to extend the experimental testing to include thermal loading, in order to evaluate the effective thermal properties and further validate the thermoelastic predictions from the numerical framework.

Finally, all the proposed designs are evaluated under idealized loading and boundary conditions. Real-world applications, particularly in aerospace, biomedical, or energy sectors, would require consideration of nonlinearities, fatigue, manufacturing constraints, and robustness to uncertainties, factors that are currently outside the scope of this work. Additionally, the material models used throughout the thesis are also idealized. Linear elastic and isotropic behaviors are assumed in the base material phases, which may not reflect the full complexity of real-world materials, especially those produced via additive manufacturing, where anisotropy and thermal gradients are prevalent. Furthermore, the current formulations are limited to 2D. Extending the framework to 3D will enable the design of more application-relevant architectures and explore spatial interactions between NPR and NTE in full-scale components.

BIBLIOGRAPHY

[1] Cadman JE, Zhou S, Chen Y, Li Q. On design of multi-functional microstructural materials. J Mater Sci 2013;48:51–66. https://doi.org/10.1007/s10853-012-6643-4.

[2] Lu C, Hsieh M, Huang Z, Zhang C, Lin Y, Shen Q, et al. Architectural Design and Additive Manufacturing of Mechanical Metamaterials: A Review. Engineering 2022;17:44–63. https://doi.org/10.1016/j.eng.2021.12.023.

[3] Huang C, Chen L. Negative Poisson's Ratio in Modern Functional Materials. Advanced Materials 2016;28:8079–96. https://doi.org/10.1002/adma.201601363.

[4] Ren X, Das R, Tran P, Ngo TD, Xie YM. Auxetic metamaterials and structures: A review. Smart Mater Struct 2018;27:023001. https://doi.org/10.1088/1361-665X/aaa61c.

[5] Sigmund O, Torquato S. Design of materials with extreme thermal expansion using a three-phase topology optimization method. J Mech Phys Solids 1997;45:1037–67. https://doi.org/https://doi.org/10.1016/S0022-5096(96)00114-7.

[6] Hassani B, Hinton E. A review of homogenization and topology optimization I - homogenization theory for media with periodic structure. Comput Struct 1998;69:707–17. https://doi.org/https://doi.org/10.1016/S0045-7949(98)00131-X.

[7] Guedes JM, Kikuchi N. Preprocessing and postprocessing for materials based on the homogenization method with adaptive finite element methods. Computer Methods in Applied Mechanics and Engineering 1990;83:143–98. https://doi.org/https://doi.org/10.1016/0045-7825(90)90148-F.

[8] Allaire G. A brief introduction to homogenization and miscellaneous applications. ESAIM: Proceedings 2012;37:1–49. https://doi.org/10.1051/proc/201237001.

[9] Almeida CJ, Cardoso JO, Coelho PG, Velhinho AC, Xavier J. Architectured and additively manufactured double-negative index metamaterials. eccomas2022, 8th European Congress on Computational Methods in Applied Sciences and Engineering, Oslo, Norway, vol. 52, 2022. https://doi.org/10.23967/eccomas.2022.056.

[10] Sigmund O. Materials with prescribed constitutive parameters an inverse homogenization problem. Int J Solids Struct 1994;31:2313–29. https://doi.org/https://doi.org/10.1016/0020-7683(94)90154-6.

[11] Liu L, Yan J, Cheng G. Optimum structure with homogeneous optimum truss-like material. Comput Struct 2008;86:1417–25. https://doi.org/10.1016/j.compstruc.2007.04.030.

[12] Thompson MK, Moroni G, Vaneker T, Fadel G, Campbell RI, Gibson I, et al. Design for Additive Manufacturing: Trends, opportunities, considerations, and constraints. CIRP Ann Manuf Technol 2016;65:737–60. https://doi.org/10.1016/j.cirp.2016.05.004.

[13] Wu X, Su Y, Shi J. Perspective of additive manufacturing for metamaterials development. Smart Mater Struct 2019;28. https://doi.org/10.1088/1361-665X/ab2eb6.

[14] Plocher J, Panesar A. Review on design and structural optimisation in additive manufacturing: Towards next-generation lightweight structures. Mater Des 2019;183:108164. https://doi.org/10.1016/j.matdes.2019.108164.

[15] Silva RF, Coelho PG, Gustavo C V., Almeida CJ, Farias FWC, Duarte VR, et al. Functionally Graded Materials and Structures: Unified Approach by Optimal Design, Metal Additive Manufacturing, and Image-Based Characterization. Materials 2024;17. https://doi.org/10.3390/ma17184545.

[16] Svanberg K. A class of globally convergent optimization methods based on conservative convex separable approximations. SIAM Journal on Optimization 2002;12:555–73. https://doi.org/https://doi.org/10.1137/S1052623499362822.

[17] Ye M, Gao L, Li H. A design framework for gradually stiffer mechanical metamaterial induced by negative Poisson's ratio property. Mater Des 2020;192:108751. https://doi.org/10.1016/j.matdes.2020.108751.

[18] Coelho PG, Rodrigues HC. Hierarchical topology optimization addressing material design constraints and application to sandwich-type structures. Structural and Multidisciplinary Optimization 2015;52:91–104. https://doi.org/10.1007/s00158-014-1220-x.

[19] R.S. Kshetrimayum. A brief intro to metamaterials. IEEE Potentials 2004;23:44–6. https://doi.org/10.1109/MP.2005.1368916.

[20] Lakes R. Cellular solid structures with unbounded thermal expansion. J Mater Sci Lett 1996;15:475–7. https://doi.org/10.1007/bf00275406.

[21] Evans KE, Nkansah MA, Hutchinson IJ, Rogers SC. Molecular network design. Nature 1991;353:124–124.

[22] Lakes R. Foam Structures with a Negative Poisson's Ratio. American Association for the Advancement of Science 1987;235:1038–40.

[23] Prall D, Lakes RS. Properties of a chiral honeycomb with a Poisson's ratio of -1. Int J Mech Sci 1997;39:305–14.

[24] Under Armor. Https://AboutUnderarmourCom/En-Us/Stories/2019/06/Aj-and-Ua-Evolutionize-Boxing-from-the-Ground-upHtml 2025.

[25] Wang Y, Wang L, Ma Z, Wang T. A negative Poisson ' s ratio suspension jounce bumper. JMADE 2016;103:90–9. https://doi.org/10.1016/j.matdes.2016.04.041.

[26] Liu Q. Literature Review : Materials with Negative Poisson's Ratios and Potential Applications to Aerospace and Defence. Defence Science Technology Organisation 2006.

[27] Scarpa F. Auxetic materials for bioprostheses. IEEE Signal Process Mag 2008;25:128–126. https://doi.org/10.1109/MSP.2008.926663.

[28] Alderson KL, Fitzgerald A, Evans KE. The strain dependent indentation resilience of auxetic microporous polyethylene. J Mater Sci 2000;35:4039–47. https://doi.org/https://doi.org/10.1023/A:1004830103411.

[29] Argatov II, Guinovart-Díaz R, Sabina FJ. On local indentation and impact compliance of isotropic auxetic materials from the continuum mechanics viewpoint. Int J Eng Sci 2012;54:42–57. https://doi.org/10.1016/j.ijengsci.2012.01.010.

[30] Choi JB, Lakes RS. Fracture toughness of re-entrant foam materials with a negative Poisson's ratio: experiment and analysis. Int J Fract 1996;80:73–83. https://doi.org/https://doi.org/10.1007/BF00036481.

[31] Hou W, Yang X, Zhang W, Xia Y. Design of energy-dissipating structure with functionally graded auxetic cellular material. International Journal of Crashworthiness 2018;23:366–76. https://doi.org/10.1080/13588265.2017.1328764.

[32] Raminhos JS, Borges JP, Velhinho A. Development of polymeric anepectic meshes: Auxetic metamaterials with negative thermal expansion. Smart Mater Struct 2019;28:045010. https://doi.org/10.1088/1361-665X/ab034b.

[33] Yamamoto N, Gdoutos E, Toda R, White V, Manohara H, Daraio C. Thin films with ultra-low thermal expansion. Advanced Materials 2014;26:3076–80. https://doi.org/10.1002/adma.201304997.

[34] Xu H, Pasini D. Structurally efficient three-dimensional metamaterials with controllable thermal expansion. Sci Rep 2016;6. https://doi.org/10.1038/srep34924.

[35] Takenaka K. Negative thermal expansion materials: technological key for control of thermal expansion. Sci Technol Adv Mater 2012;13:013001. https://doi.org/10.1088/1468-6996/13/1/013001.

[36] Ai L, Gao X. Three-dimensional metamaterials with a negative Poisson's ratio and a non-positive coefficient of thermal expansion. Int J Mech Sci 2018;135:101–13. https://doi.org/10.1016/j.ijmecsci.2017.10.042.

[37] Miller W, Smith CW, Mackenzie DS, Evans E. Negative thermal expansion: a review. J Mater Sci 2009;44:5441–51. https://doi.org/10.1007/s10853-009-3692-4.

[38] Takezawa A, Kobashi M, Kitamura M. Porous composite with negative thermal expansion obtained by photopolymer additive manufacturing. APL Mater 2015;3:076103. https://doi.org/10.1063/1.4926759.

[39] Li Z, Gao W, Kessissoglou N, Oberst S, Wang MY, Luo Z. Multifunctional mechanical metamaterials with tunable double-negative isotropic properties. Mater Des 2023;232:112146. https://doi.org/10.1016/j.matdes.2023.112146.

[40] Grima JN, Farrugia P-S, Gatt R, Zammit V. Connected Triangles Exhibiting Negative Poisson's Ratios and Negative Thermal Expansion. J Physical Soc Japan 2007;76:025001.

[41] Ha CS, Hestekin E, Li J, Plesha ME, Lakes RS. Controllable thermal expansion of large magnitude in chiral negative Poisson's ratio lattices. Basic Solid State Physics 2015;252:1431–4. https://doi.org/10.1002/pssb.201552158.

[42] Ng CK, Saxena KK, Das R, Saavedra Flores EI. On the anisotropic and negative thermal expansion from dual-material re-entrant-type cellular metamaterials. J Mater Sci 2017;52:899–912. https://doi.org/10.1007/s10853-016-0385-7.

[43] Ai L, Gao X. Metamaterials with negative Poisson's ratio and non-positive thermal expansion. Compos Struct 2017;162:70–84. https://doi.org/10.1016/j.compstruct.2016.11.056.

[44] Wei K, Peng Y, Qu Z, Pei Y, Fang D. A cellular metastructure incorporating coupled negative thermal expansion and negative Poisson's ratio. Int J Solids Struct 2018;150:255–67. https://doi.org/10.1016/j.ijsolstr.2018.06.018.

[45] Peng Y, Wei K, Mei M, Yang X, Fang D. Simultaneously program thermal expansion and Poisson's ratio in three dimensional mechanical metamaterial. Compos Struct 2021;262. https://doi.org/10.1016/j.compstruct.2020.113365.

[46] Li X, Gao L, Zhou W, Wang Y, Lu Y. Novel 2D metamaterials with negative Poisson's ratio and negative thermal expansion. Extreme Mech Lett 2019;30:100498. https://doi.org/10.1016/j.eml.2019.100498.

[47] Fong E, Omairey SL, Dunning PD. Design of multifunctional metamaterials using optimization. ArXiv 2020:1–15.

[48] Fu M, Huang J, Zheng B, Chen Y. Three-dimensional auxetic materials with controllable thermal expansion. Smart Mater Struct 2020;29:085034.

[49] Peng XL, Bargmann S. A novel hybrid-honeycomb structure: Enhanced stiffness, tunable auxeticity and negative thermal expansion. Int J Mech Sci 2021;190:106021. https://doi.org/10.1016/j.ijmecsci.2020.106021.

[50] Li J, Yang Q, Wei Y, Huang N, Tao R. A synergistic design of composite metamaterial with drastically tailorable thermal expansion and Poisson's ratio. Compos Struct 2021;275. https://doi.org/10.1016/j.compstruct.2021.114446.

[51] Tian J, Yang J, Zhao Y. Metamaterial with synergistically controllable Poisson's ratio and thermal expansion coefficient. Int J Mech Sci 2023;256:108488. https://doi.org/10.1016/j.ijmecsci.2023.108488.

[52] Dong Y, Li Q, Cui F, Bai L, Xu W. Impact resistance analysis of a dual-constituent negative Poisson's ratio lattice metamaterial with tailorable coefficient of thermal expansion. Phys Scr 2024;99:065903. https://doi.org/10.1088/1402-4896/ad4009.

[53] Liu KJ, Liu HT, Zhen D. Mechanical and bandgap properties of 3D bi-material triangle re-entrant honeycomb. Int J Mech Sci 2024;261:108664. https://doi.org/10.1016/j.ijmecsci.2023.108664.

[54] Wang LY, Liu HT. 3D novel zero Poisson's ratio metamaterials with programmable thermal expansion and Young's modulus. Mater Today Commun 2024;39:109179. https://doi.org/10.1016/j.mtcomm.2024.109179.

[55] Sigmund O. Systematic design of metamaterials by topology optimization. IUTAM Symposium on Modelling Nanomaterials and Nanosystems: Proceedings of the IUTAM Symposium held in Aalborg, Denmark, 19–22 May 2008 , Dordrecht: Springer Netherlands; 2009, p. 151–9. https://doi.org/https://doi.org/10.1007/978-1-4020-9557-3_16.

[56] Bendsøe MP. Optimal shape design as a material distribution problem. Structural and Multidisciplinary OptimizationOptimization 1989;1:193–202. https://doi.org/10.1007/BF01650949.

[57] Bendsøe MP, Sigmund O. Material interpolation schemes in topology optimization. Archive of Applied Mechanics 1999;69:635–54. https://doi.org/https://doi.org/10.1007/s004190050248.

[58] Rodrigues H, Fernandes P. A material based model for topology optimization of thermoelastic structures. Int J Numer Methods Eng 1995;38:1951–65. https://doi.org/https://doi.org/10.1002/nme.1620381202.

[59] Sigmund O. Design of Material Structures Using Topology Optimization. Technical University of Denmark., 1994.

[60] Zhang W, Wang F, Dai G, Sun S. Topology optimal design of material microstructures using strain energy-based method. Chinese Journal of Aeronautics 2007;20:320–6. https://doi.org/10.1016/S1000-9361(07)60050-8.

[61] Zhang W, Dai G, Wang F, Sun S, Bassir H. Using strain energy-based prediction of effective elastic properties in topology optimization of material microstructures. Acta Mechanica Sinica/Lixue Xuebao 2007;23:77–89. https://doi.org/10.1007/s10409-006-0045-2.

[62] Xia L, Breitkopf P. Design of materials using topology optimization and energy-based homogenization approach in Matlab. Structural and Multidisciplinary Optimization 2015;52:1229–41. https://doi.org/10.1007/s00158-015-1294-0.

[63] Bensoussan A, Lions JL, Papanicolaou G. Asymptotic analysis for periodic structures. vol. 374. American Mathematical Soc..; 2011.

[64] Guo Y, Wang H, Wang W, Chen C, Wang Y. Topology optimization for metamaterials with negative thermal expansion coefficients using energy-based homogenization. Advances in Engineering Software 2024;198. https://doi.org/10.1016/j.advengsoft.2024.103794.

[65] Gibiansky L V, Sigmund O. Multiphase composites with extremal bulk modulus. J Mech Phys Solids 2000;48:461–98. https://doi.org/https://doi.org/10.1016/S0022-5096(99)00043-5.

[66] Hashin Z, Shtrikman S. A variational approach to the theory of the elastic behaviour of multiphase materials. J Mech Phys Solids 1963;11:127–40.

[67] Andreassen E, Andreasen CS. How to determine composite material properties using numerical homogenization. Comput Mater Sci 2014;83:488–95. https://doi.org/10.1016/j.commatsci.2013.09.006.

[68] Chatterjee T, Chakraborty S, Goswami S, Adhikari S, Friswell MI. Robust topological designs for extreme metamaterial micro-structures. Sci Rep 2021;11:15221. https://doi.org/10.1038/s41598-021-94520-x.

[69] Clausen A, Wang F, Jensen JS, Sigmund O, Lewis JA. Topology Optimized Architectures with Programmable Poisson's Ratio over Large Deformations. Advanced Materials 2015;27:5523–7. https://doi.org/10.1002/adma.201502485.

[70] Wang Y, Luo Z, Zhang N, Kang Z. Topological shape optimization of microstructural metamaterials using a level set method. Comput Mater Sci 2014;87:178–86. https://doi.org/10.1016/j.commatsci.2014.02.006.

[71] Agnelli F, Constantinescu A, Nika G. Design and testing of 3D-printed micro-architectured polymer materials exhibiting a negative Poisson's ratio. Continuum Mechanics and Thermodynamics 2020;32:433–49. https://doi.org/10.1007/s00161-019-00851-6.

[72] Agrawal G, Gupta A, Chowdhury R, Chakrabarti A. Robust topology optimization of negative Poisson's ratio metamaterials under material uncertainty. Finite Elements in Analysis and Design 2022;198:103649. https://doi.org/10.1016/j.finel.2021.103649.

[73] Alacoque L, Watkins RT, Tamijani AY. Stress-based and robust topology optimization for thermoelastic multi-material periodic microstructures. Comput Methods Appl Mech Eng 2021;379:113749. https://doi.org/10.1016/j.cma.2021.113749.

[74] Zhang X, Ye H, Wei N, Tao R, Luo Z. Design optimization of multifunctional metamaterials with tunable thermal expansion and phononic bandgap. Mater Des 2021;209:109990. https://doi.org/10.1016/j.matdes.2021.109990.

[75] Li Z, Gao W, Yu Wang M, Luo Z. Design of multi-material isotropic auxetic microlattices with zero thermal expansion. Mater Des 2022;222:111051. https://doi.org/10.1016/j.matdes.2022.111051.

[76] Li H, Li H, Xiao M, Zhang Y, Fu J, Gao L. Robust topology optimization of thermoelastic metamaterials considering hybrid uncertainties of material property. Compos Struct 2020;248:112477. https://doi.org/10.1016/j.compstruct.2020.112477.

[77] Wang Y, Gao J, Luo Z, Brown T, Zhang N. Level-set topology optimization for multimaterial and multifunctional mechanical metamaterials. Engineering Optimization 2017;49:22–42. https://doi.org/10.1080/0305215X.2016.1164853.

[78] Vineyard E, Gao XL. Topology and shape optimization of 2-d and 3-d micro-architectured thermoelastic metamaterials using a parametric level setmethod. CMES - Computer Modeling in Engineering and Sciences 2021;127:819–54. https://doi.org/10.32604/cmes.2021.015688.

[79] Han Z, Wei K. Multi-material topology optimization and additive manufacturing for metamaterials incorporating double negative indexes of Poisson's ratio and thermal expansion. Addit Manuf 2022;54:102742. https://doi.org/10.1016/j.addma.2022.102742.

[80] Han Z, Xiao X, Chen J, Wei K, Wang Z, Yang X, et al. Bifunctional metamaterials incorporating unusual geminations of Poisson's ratio and coefficient of thermal expansion. ACS Appl Mater Interfaces 2022;14:50068–78. https://doi.org/10.1021/acsami.2c11702.

[81] Han Z, Wang Z, Wei K. Shape morphing structures inspired by multi-material topology optimized bi-functional metamaterials. Compos Struct 2022;300:116135. https://doi.org/10.1016/j.compstruct.2022.116135.

[82] Jia Z, Liu F, Jiang X, Wang L. Engineering lattice metamaterials for extreme property, programmability, and multifunctionality. J Appl Phys 2020;127. https://doi.org/10.1063/5.0004724.

[83] Xue X, Lin C, Wu F, Li Z, Liao J. Lattice structures with negative Poisson's ratio: A review. Mater Today Commun 2023;34:105132. https://doi.org/10.1016/j.mtcomm.2022.105132.

[84] Arabnejad S, Pasini D. Mechanical properties of lattice materials via asymptotic homogenization and comparison with alternative homogenization methods. Int J Mech Sci 2013;77:249–62. https://doi.org/10.1016/j.ijmecsci.2013.10.003.

[85] Theerakittayakorn K, Nanakorn P, Sam P, Suttakul P. Exact forms of effective elastic properties of frame-like periodic cellular solids. Archive of Applied Mechanics 2016;86:1465–82. https://doi.org/10.1007/s00419-016-1129-5.

[86] Hirota M, Kanno Y. Optimal design of periodic frame structures with negative thermal expansion via mixed integer programming. Optimization and Engineering 2015:767–809. https://doi.org/10.1007/s11081-015-9276-z.

[87] Muñoz-Rojas PA, Carniel TA, Silva ECN, Öchsner A. Optimization of a unit periodic cell in lattice block materials aimed at thermo-mechanical applications. Advanced Structured Materials 2011;2:301–45. https://doi.org/10.1007/8611_2010_32.

[88] Li Z, Luo Z, Zhang LC, Wang CH. Topological design of pentamode lattice metamaterials using a ground structure method. Mater Des 2021;202:109523. https://doi.org/10.1016/j.matdes.2021.109523.

[89] Li Z, Gao W, Yu Wang M, Wang CH, Luo Z. Three-dimensional metamaterials exhibiting extreme isotropy and negative Poisson's ratio. Int J Mech Sci 2023;259:108617. https://doi.org/10.1016/j.ijmecsci.2023.108617.

[90] Yang Z, Zhang Y, Wu Z, Liu S. Multifunctional design of lattice metamaterial with desired thermal expansion behaviors using topology optimization. Mechanics of Materials 2024;197. https://doi.org/10.1016/j.mechmat.2024.105070.

[91] Terada K, Hori M, Kyoya T, Kikuchi N. Simulation of the multi-scale convergence in computational homogenization approaches. Int J Solids Struct 2000;37:2285–311. https://doi.org/https://doi.org/10.1016/S0020-7683(98)00341-2.

[92] Kanit T, Forest S, Galliet I, Mounoury V, Jeulin D. Determination of the size of the representative volume element for random composites: Statistical and numerical approach. Int J Solids Struct 2003;40:3647–79. https://doi.org/10.1016/S0020-7683(03)00143-4.

[93] Pecullan S, Gibiansky V, Torquato S. Scale effects on the elastic behavior of periodic andhierarchical two-dimensional composites. J Mech Phys Solids 1999;47:1509–42. https://doi.org/https://doi.org/10.1016/S0022-5096(98)00111-2.

[94] Coelho PG, Amiano LD, Guedes JM, Rodrigues HC. Scale-size effects analysis of optimal periodic material microstructures designed by the inverse homogenization method. Comput Struct 2016;174:21–32. https://doi.org/10.1016/j.compstruc.2015.10.001.

[95] Wang F, Sigmund O, Jensen JS. Design of materials with prescribed nonlinear properties. J Mech Phys Solids 2014;69:156–74. https://doi.org/10.1016/j.jmps.2014.05.003.

[96] Yan J, Guo X, Cheng G. Multi-scale concurrent material and structural design under mechanical and thermal loads. Comput Mech 2016;57:437–46. https://doi.org/10.1007/s00466-015-1255-x.

[97] Oliver J, Ferrer A, Cante JC, Giusti SM, Lloberas-Valls O, López MM, et al. On multi-scale computational design of structural materials using the topological derivative. Advances in Computational Plasticity: A Book in Honour of D. Roger J. Owen, 2018, p. 289–308.

[98] Yan J, Sui Q, Fan Z, Duan Z, Yu T. Clustering-based multiscale topology optimization of thermoelastic lattice structures. Comput Mech 2020;66:979–1002. https://doi.org/10.1007/s00466-020-01892-4.

[99] Zhang G, Khandelwal K. Computational design of finite strain auxetic metamaterials via topology optimization and nonlinear homogenization. Comput Methods Appl Mech Eng 2019;356:490–527. https://doi.org/10.1016/j.cma.2019.07.027.

[100] Li H, Luo Z, Gao L, Walker P. Topology optimization for functionally graded cellular composites with metamaterials by level sets. Comput Methods Appl Mech Eng 2018;328:340–64. https://doi.org/10.1016/j.cma.2017.09.008.

[101] Qiu Z, Li Q, Liu S. Sensitivity clustering-based multi-scale topology optimization method for metamaterial thermal actuators. Structural and Multidisciplinary Optimization 2024;67. https://doi.org/10.1007/s00158-023-03729-z.

[102] Kurioka H, Nakayama N, Furuta K, Noguchi Y, Izui K, Yamada T, et al. Multiscale optimal design method of acoustic metamaterials using topology optimization. Int J Numer Methods Eng 2023;124:2995–3024. https://doi.org/10.1002/nme.7237.

[103] Lu Y, Tong L. Concurrent multiscale topology optimization of metamaterials for mechanical cloak. Comput Methods Appl Mech Eng 2023;409. https://doi.org/10.1016/j.cma.2023.115966.

[104] Lee D, Chen W, Wang L, Chan YC, Chen W. Data-Driven Design for Metamaterials and Multiscale Systems: A Review. Advanced Materials 2024;36. https://doi.org/10.1002/adma.202305254.

[105] Kochmann DM, Hopkins JB, Valdevit L. Multiscale modeling and optimization of the mechanics of hierarchical metamaterials. MRS Bull 2019;44:773–81. https://doi.org/10.1557/mrs.2019.228.

[106] Huang X, Radman A, Xie YM. Topological design of microstructures of cellular materials for maximum bulk or shear modulus. Comput Mater Sci 2011;50:1861–70. https://doi.org/10.1016/j.commatsci.2011.01.030.

[107] Zhang H, Luo Y, Kang Z. Bi-material microstructural design of chiral auxetic metamaterials using topology optimization. Compos Struct 2018;195:232–48. https://doi.org/10.1016/j.compstruct.2018.04.058.

[108] Hassani B, Hinton E. A review of homogenization and topology opimization II - analytical and numerical solution of homogenization equations. Comput Struct 1998;69:719–38. https://doi.org/https://doi.org/10.1016/S0045-7949(98)00132-1.

[109] Hassani B, Hinton E. A review of homogenization and topology optimization III - topology optimization using optimality criteria. Comput Struct 1998;69:739–56. https://doi.org/https://doi.org/10.1016/S0045-7949(98)00133-3.

[110] Hashin Z. Analysis of Composite Materials-A Survey. Jornal of Applied Mechanics 1983;50:481–505. https://doi.org/https://doi.org/10.1115/1.3167081.

[111] Xia Z, Zhou C, Yong Q, Wang X. On selection of repeated unit cell model and application of unified periodic boundary conditions in micro-mechanical analysis of composites. Int J Solids Struct 2006;43:266–78. https://doi.org/10.1016/j.ijsolstr.2005.03.055.

[112] Maxwell JC. On reciprocal figures, frames and diagrams of forces. The Scientific Papers of James Clerk Maxwell 1890;2:175–7. https://doi.org/10.1017/CBO9780511710377.

[113] Michell AGM. The limit of economy of material in frame structures. Philosophical Magazine 1904;8:589–97.

[114] Courant R. Variational methods for the solution of problems of equilibrium and vibrations 1943;49:1–23.

[115] Clough RW. The Finite Element Method in Plane Stress Analysis, 1960.

[116] Schittkowski K. NLPQL: A fortran subroutine solving constrained nonlinear programming problems. Ann Oper Res 1986;5:485–500.

[117] Svanberg K. The method of moving asymptotes - a new method for structural optimization. Int J Numer Methods Eng 1987;24:359–73.

[118] Glover F. Future paths for integer programming and links to artificial intelligence. Comput Oper Res 1986;13:533–49.

[119] Silva R. Otimização topológica baseada na tensão de estruturas com gradiente de funcionalidade. Universidade NOVA de Lisboa, 2022.

[120] Dorn W, Gomory R, Greenberg M. Automatic design of optimal structures. J Mec 1964;3:25–52.

[121] Bendsoe MP, Sigmund O. Topology Optimization - Theory, Methods and Applications. 2004.

[122] Bendsoe MP, Kikuchi N. Generating optimal topologies in structural design using a homogenization method. Comput Methods Appl Mech Eng 1988;71:197–224.

[123] Stolpe M, Svanberg K. An alternative interpolation scheme for minimum compliance topology optimization. Structural and Multidisciplinary Optimization 2001;22:116–24.

[124] Wang MY, Wang X, Guo D. A level set method for structural topology optimization. Comput Methods Appl Mech Eng 2003;192:227–46.

[125] Sokolowski J, Zochowski A. On the Topological Derivative in Shape Optimization. SIAM J Control Optim 1999;37:1251–72.

[126] Deaton JD, Grandhi R V. A survey of structural and multidisciplinary continuum topology optimization: Post 2000. Structural and Multidisciplinary Optimization 2014;49:1–38. https://doi.org/10.1007/s00158-013-0956-z.

[127] Bruns TE, Tortorelli DA. Topology optimization of non-linear elastic structures and compliant mechanisms. Comput Methods Appl Mech Eng 2001;190:3443–59. https://doi.org/https://doi.org/10.1016/S0045-7825(00)00278-4.

[128] Conde F. Multiscale optimization of non-conventional composite structures for mproved mechanical response. NOVA University Lisbon, 2022.

[129] Li D, Kim IY. Multi-material topology optimization for practical lightweight design. Structural and Multidisciplinary Optimization 2018;58:1081–94.

[130] Lu S, Ma H, Xin L, Zuo W. Lightweight design of bus frames from multi-material topology optimization to cross-sectional size optimization. Engineering Optimization 2019;51:961–77.

[131] Jung Y, Lim S, Kim J, Min S. Lightweight design of electric bus roof structure using multi-material topology optimisation. Structural and Multidisciplinary Optimization 2020;61:1273–85. https://doi.org/10.1007/s00158-019-02410-8.

[132] Stegmann J. Analysis and Optimization of Laminated Composite Shell Structures. 2005.

[133] Lund E, Stegmann J. On structural optimization of composite shell structures using a discrete constitutive parametrization. Wind Energy 2005;8:109–24.

[134] Stegmann J, Lund E. Discrete material optimization of general composite shell structures. Int J Numer Methods Eng 2005;62:2009–27.

[135] Gao T, Zhang W. A mass constraint formulation for structural topology optimization with multiphase materials. Int J Numer Methods Eng 2011;88:774–96. https://doi.org/10.1002/nme.3197.

[136] Bruyneel M. SFP-a new parameterization based on shape functions for optimal material selection: Application to conventional composite plies. Structural and Multidisciplinary Optimization 2011;43:17–27.

[137] Wu J, Sigmund O, Groen JP. Topology optimization of multi-scale structures: a review. Structural and Multidisciplinary Optimization 2021;63:1455–80. https://doi.org/10.1007/s00158-021-02881-8.

[138] Rodrigues H, Guedes JM, Bendsoe MP. Hierarchical optimization of material and structure. Structural and Multidisciplinary Optimization 2002;24:1–10. https://doi.org/10.1007/s00158-002-0209-z.

[139] Coelho PG, Fernandes PR, Guedes JM, Rodrigues HC. A hierarchical model for concurrent material and topology optimisation of three-dimensional structures. Structural and Multidisciplinary Optimization 2008;35:107–15. https://doi.org/10.1007/s00158-007-0141-3.

[140] Conde FM, Coelho PG, Guedes JM. Multi-scale topology optimization of structures with multi-material microstructures using stiffness and mass design criteria. Advances in Engineering Software 2024;187. https://doi.org/10.1016/j.advengsoft.2023.103566.

[141] Deng J, Yan J, Cheng G. Multi-objective concurrent topology optimization of thermoelastic structures composed of homogeneous porous material. Structural and Multidisciplinary Optimization 2013;47:583–97. https://doi.org/10.1007/s00158-012-0849-6.

[142] Yan J, Yang S, Yang C. Multiscale analysis of thermal stress of lattice materials and its size effects. Journal of Thermal Stresses 2014;37:885–904. https://doi.org/10.1080/01495739.2014.912935.

[143] Yan J, Sui Q, Fan Z, Duan Z. Multi-Material and Multiscale Topology Design Optimization of Thermoelastic Lattice Structures. CMES - Computer Modeling in Engineering and Sciences 2022;130:967–86. https://doi.org/10.32604/cmes.2022.017708.

[144] Zhang Y, Li H, Xiao M, Gao L, Chu S, Zhang J. Concurrent topology optimization for cellular structures with nonuniform microstructures based on the kriging metamodel. Structural and Multidisciplinary Optimization 2019;59:1273–99. https://doi.org/10.1007/s00158-018-2130-0.

[145] Al Ali M, Shimoda M. Investigation of concurrent multiscale topology optimization for designing lightweight macrostructure with high thermal conductivity. International Journal of Thermal Sciences 2022;179. https://doi.org/10.1016/j.ijthermalsci.2022.107653.

[146] Kazakis G, Lagaros ND. Multi-Scale Concurrent Topology Optimization Based on BESO, Implemented in MATLAB. Applied Sciences (Switzerland) 2023;13. https://doi.org/10.3390/app131810545.

[147] Conde FM, Coelho PG, Guedes JM. Multi-scale topology optimization of structures with multi-material microstructures using stiffness and mass design criteria. Advances in Engineering Software 2024;187. https://doi.org/10.1016/j.advengsoft.2023.103566.

[148] Zhang W, Sun S. Scale-related topology optimization of cellular materials and structures. Int J Numer Methods Eng 2006;68:993–1011. https://doi.org/10.1002/nme.1743.

[149] Wu J, Aage N, Westermann R, Sigmund O. Infill Optimization for Additive Manufacturing-Approaching Bone-Like Porous Structures. IEEE Trans Vis Comput Graph 2018;24:1127–40. https://doi.org/10.1109/TVCG.2017.2655523.

[150] Wu J, Sigmund O, Groen JP. Topology optimization of multi-scale structures: a review. Structural and Multidisciplinary Optimization 2021;63:1455–80. https://doi.org/10.1007/s00158-021-02881-8.

[151] Svanberg K. The Method of Moving Asymptotes - Modelling aspects and solution schemes. Lecture Notes for the DCAMM Course Advaneecl Topies in Structural Optimization 1998:24.

[152] Svanberg K. A globally convergent version of MMA without linesearch. First World Congress of Structural and Multidiscipli-nary Optimization, 1995, p. 9–16.

[153] Haug E, Choi K, Komkov V. Design Sensitivity Analysis of Structural Systems. Academic Press, Inc,; 1986.

[154] Almeida C, Coelho P, Guedes JM, Custódio AL, Conde F, Velhinho A. Multiobjective topology optimization of metamaterials to analyse the conflicting nature of negative Poisson's ratio and negative thermal expansion. Structural and Multidisciplinary Optimization 2025;68. https://doi.org/10.1007/s00158-025-04131-7.

[155] Silva RF, Coelho PG, Conde FM, Almeida CJ, Custódio AL. Topology optimization of thermoelastic structures with single and functionally graded materials exploring energy and stress-based formulations. Structural and Multidisciplinary Optimization 2025;68. https://doi.org/10.1007/s00158-024-03929-1.

[156] Conde FM, Coelho PG, Guedes JM. Multi-material and strength-oriented microstructural topology optimization applied to discrete phase and functionally graded materials. Structural and Multidisciplinary Optimization 2022;65. https://doi.org/10.1007/s00158-022-03209-w.

[157] Marler RT, Arora JS. Survey of multi-objective optimization methods for engineering. Structural and Multidisciplinary Optimization 2004;26:369–95. https://doi.org/10.1007/s00158-003-0368-6.

[158] Conde FM, Coelho PG, Guedes JM. Multi-material and strength-oriented microstructural topology optimization applied to discrete phase and functionally graded materials. Structural and Multidisciplinary Optimization 2022;65:127. https://doi.org/10.1007/s00158-022-03209-w.

[159] Zohdi TI, Wriggers P. An Introduction to Computational Micromechanics. Springer Science & Business Media; 2008.

[160] Cook R D. Concepts and applications of finite element analysis. John wiley & sons; 2007.

[161] Jagiello E, Muñoz-Rojas PA. An extended multiscale finite element method (Emsfem) analysis of periodic truss metamaterials (ptmm) designed by asymptotic homogenization. Latin American Journal of Solids and Structures 2021;18. https://doi.org/10.1590/1679-78256240.

[162] Grima-Cornish JN, Attard D, Evans KE, Grima JN. Auxetic-Inspired Honeycomb Macrostructures With Anomalous Tailormade Thermal Expansion Properties Including "Negative" Heat-Shrinking Characteristics. Front Mater 2021;8:769879. https://doi.org/10.3389/fmats.2021.769879.

[163] Agnelli F, Constantinescu A, Nika G. Optimal design of auxetic, additively manufactured, polymeric structures. Hal 2018:01868830.

[164] Andreassen E, Lazarov BS, Sigmund O. Design of manufacturable 3D extremal elastic microstructure. Mechanics of Materials 2014;69:1–10. https://doi.org/10.1016/j.mechmat.2013.09.018.

[165] Yang H, Jiang W, Li M, Ma L. Multi-material 3D double-V metastructures with tailorable Poisson's ratio and thermal expansion. Int J Mech Sci 2021;210. https://doi.org/10.1016/j.ijmecsci.2021.106733.

[166] Yu H, Wu W, Zhang J, Chen J, Liao H, Fang D. Drastic tailorable thermal expansion chiral planar and cylindrical shell structures explored with finite element simulation. Compos Struct 2019;210:327–38. https://doi.org/10.1016/j.compstruct.2018.11.043.

[167] Wu L, Li B, Zhou J. Isotropic Negative Thermal Expansion Metamaterials. ACS Appl Mater Interfaces 2016;8:17721–7. https://doi.org/10.1021/acsami.6b05717.

[168] Silva RF, Coelho PG, Conde FM, Almeida CJ, Custódio AL. Topology optimization of thermoelastic structures with single and functionally graded materials exploring energy and stress-based formulations. Structural and Multidisciplinary Optimization 2025;68. https://doi.org/10.1007/s00158-024-03929-1.

[169] Zhang W, Yang J, Xu Y, Gao T. Topology optimization of thermoelastic structures: Mean compliance minimization or elastic strain energy minimization. Structural and Multidisciplinary Optimization 2014;49:417–29. https://doi.org/10.1007/s00158-013-0991-9.

[170] Zhou S, Li Q. Design of graded two-phase microstructures for tailored elasticity gradients. J Mater Sci 2008;43:5157–67. https://doi.org/10.1007/s10853-008-2722-y.

[171] Silva RF, Coelho PG, Conde FM, Santos BR, Oliveira JP. Minimizing the maximum von Mises stress of elastic continuum structures using topology optimization and additively manufactured functionally graded materials. Comput Struct 2024;301. https://doi.org/10.1016/j.compstruc.2024.107469.

[172] Sachs E, Cima M, Cornie J, Brancazio D, Bredt J, Curodeau A, et al. Three-Dimensional Printing: The Physics and Implications of Additive Manufacturing. CIRP Annals 1993;42:257–60.

[173] Joseph A, Mahesh V, Harursampath D. On the application of additive manufacturing methods for auxetic structures: a review. Adv Manuf 2021;9:342–68. https://doi.org/10.1007/s40436-021-00357-y.

A

SENSITIVITY ANALYSIS OF HOMOGENIZED COEFFICIENTS

The objective of design sensitivity analysis is to determine the total dependence of a given function in the design, i.e., to find $\mathrm{d}\Phi/\mathrm{d}\tilde{\rho}_{m,e}$, where Φ is any given function.

Let us recall the elastic and thermal local problems defined in Section 2.2, given, respectively, by (A.1) and (A.2).

$$\int_{¥} E_{ijpq} \frac{\partial \chi_p^{kl}}{\partial y_q} \frac{\partial v_i}{\partial y_j} \mathrm{d}Y = \int_{¥} E_{ijkl} \frac{\partial v_i}{\partial y_j} \mathrm{d}Y \tag{A.1}$$

$$\int_{¥} E_{ijpq} \frac{\partial \Upsilon_p}{\partial y_q} \frac{\partial v_i}{\partial y_j} \mathrm{d}Y = \int_{¥} \beta_{ij} \frac{\partial v_i}{\partial y_j} \mathrm{d}Y \tag{A.2}$$

The homogenized stiffness and thermal stress tensor in the symmetrical for are given by (A.3) and (A.4), respectively:

$$E_{ijkl}^H = \frac{1}{|Y|} \int_Y E_{rspq} \left(\delta_{pk}\delta_{ql} - \frac{\partial \chi_p^{kl}}{\partial y_q} \right) \left(\delta_{ir}\delta_{js} - \frac{\partial \chi_r^{ij}}{\partial \mathrm{y}_s} \right) dY \tag{A.3}$$

$$\beta_{ij}^H = \frac{1}{|Y|} \int_Y E_{rspq} \left(\alpha_{pq} - \frac{\partial \Upsilon_p}{\partial \mathrm{y}_\mathrm{q}} \right) \left(\delta_{ir}\delta_{js} - \frac{\partial \chi_r^{ij}}{\partial \mathrm{y}_s} \right) dY \tag{A.4}$$

The sensitivity of E_{ijkl}^H written in the symmetrical form, w.r.t the design variable $\tilde{\rho}_{m,e}$ is given by:

$$\frac{\mathrm{d}E^H_{ijkl}}{\mathrm{d}\tilde{\rho}_{m,e}} = \frac{1}{|Y|}\int_Y \frac{\partial E_{rspq}}{\partial \tilde{\rho}_{m,e}}\left(\delta_{pk}\delta_{ql} - \frac{\partial \chi_p^{kl}}{\partial y_q}\right)\left(\delta_{ir}\delta_{js} - \frac{\partial \chi_r^{ij}}{\partial \mathrm{y}_s}\right) dY$$
$$+ \frac{1}{|Y|}\int_Y E_{rspq}\frac{\partial\left(\delta_{pk}\delta_{ql} - \frac{\partial \chi_p^{kl}}{\partial y_q}\right)}{\partial \tilde{\rho}_{m,e}}\left(\delta_{ir}\delta_{js} - \frac{\partial \chi_r^{ij}}{\partial \mathrm{y}_s}\right) dY \tag{A.5}$$
$$+ \frac{1}{|Y|}\int_Y E_{rspq}\left(\delta_{pk}\delta_{ql} - \frac{\partial \chi_p^{kl}}{\partial y_q}\right)\frac{\partial\left(\delta_{ir}\delta_{js} - \frac{\partial \chi_r^{ij}}{\partial \mathrm{y}_s}\right)}{\partial \tilde{\rho}_{m,e}} dY$$

where:

$$\frac{\partial\left(\delta_{pk}\delta_{ql} - \frac{\partial \chi_p^{kl}}{\partial y_q}\right)}{\partial \tilde{\rho}_{m,e}} = -\frac{\partial}{\partial \tilde{\rho}_{m,e}}\left(\frac{\partial \chi_p^{kl}}{\partial \mathrm{y}_q}\right) \tag{A.6}$$

Considering Eq. (A.6), Eq. (A.5) simplifies to:

$$E^H_{ijkl} = \frac{1}{|Y|}\int_Y \frac{\partial E_{rspq}}{\partial \tilde{\rho}_{m,e}}\left(\delta_{pk}\delta_{ql} - \frac{\partial \chi_p^{kl}}{\partial y_q}\right)\left(\delta_{ir}\delta_{js} - \frac{\partial \chi_r^{ij}}{\partial \mathrm{y}_s}\right) dY$$
$$- \frac{1}{|Y|}\int_Y E_{rspq}\frac{\partial}{\partial \tilde{\rho}_{m,e}}\left(\frac{\partial \chi_p^{kl}}{\partial \mathrm{y}_q}\right)\left(\delta_{ir}\delta_{js} - \frac{\partial \chi_r^{ij}}{\partial \mathrm{y}_s}\right) dY \tag{A.7}$$
$$- \frac{1}{|Y|}\int_Y E_{rspq}\left(\delta_{pk}\delta_{ql} - \frac{\partial \chi_p^{kl}}{\partial y_q}\right)\frac{\partial}{\partial \tilde{\rho}_{m,e}}\left(\frac{\partial \chi_r^{ij}}{\partial \mathrm{y}_s}\right) dY$$

Choosing $\mathbf{v} \equiv \frac{\partial \boldsymbol{\chi}^{kl}}{\partial \tilde{\rho}_{m,e}}$ in the local elastic problem (A.1), and doing some index manipulation, it follows that:

$$\int_{¥} E_{rspq}\frac{\partial \chi_r^{ij}}{\partial y_s}\frac{\partial v_p}{\partial y_q}\mathrm{d}Y = \int_{¥} E_{pqij}\frac{\partial v_p}{\partial y_q}\mathrm{d}Y$$

$$\Leftrightarrow \int_{¥}\left(E_{rspq}\delta_{ir}\delta_{js} - E_{rspq}\frac{\partial \chi_r^{ij}}{\partial y_s}\right)\frac{\partial v_p}{\partial y_q}\mathrm{d}Y = 0 \tag{A.8}$$

$$\Leftrightarrow \int_{¥} E_{rspq}\left(\delta_{ir}\delta_{js} - \frac{\partial \chi_r^{ij}}{\partial y_s}\right)\frac{\partial}{\partial \tilde{\rho}_{m,e}}\left(\frac{\partial \chi_p^{kl}}{\partial \mathrm{y}_q}\right)\mathrm{d}Y = 0$$

Proving that the 2nd term of Eq. (A.7) is null. Following the same reasoning it is easily proved that the 3rd term of (A.7) is null as well.

Therefore, the sensitivity of E_{ijkl}^{H} in the symmetrical form w.r.t the design variable $\tilde{\rho}_{m,e}$ is given by Eq. (A.9):

$$\frac{\mathrm{d}E_{ijkl}^{H}}{\mathrm{d}\tilde{\rho}_{m,e}} = \frac{1}{|Y|}\int_{Y} \frac{\partial E_{rspq}}{\partial \tilde{\rho}_{m,e}}\left(\delta_{pk}\delta_{ql} - \frac{\partial \chi_{p}^{kl}}{\partial y_q}\right)\left(\delta_{ir}\delta_{js} - \frac{\partial \chi_{r}^{ij}}{\partial \mathrm{y}_s}\right) dY \tag{A.9}$$

Following the same reasoning as before, the sensitivity of β_{ij}^{H} w.r.t. the density of element e, $\tilde{\rho}_{m,e}$, $\frac{\mathrm{d}\beta_{ij}^{H}}{\mathrm{d}\tilde{\rho}_{m,e}}$, is given by (3.2).

$$\begin{aligned}\frac{\mathrm{d}\beta_{ij}^{H}}{\mathrm{d}\tilde{\rho}_{m,e}} = \frac{1}{|Y|}\int_{Y} & \frac{\partial E_{rspq}}{\partial \tilde{\rho}_{m,e}}\left(\alpha_{pq} - \frac{\partial \Upsilon_{p}}{\partial y_q}\right)\left(\delta_{ir}\delta_{js} - \frac{\partial \chi_{r}^{ij}}{\partial \mathrm{y}_s}\right) dY \\ & + \frac{1}{|Y|}\int_{Y} E_{rspq}\frac{\partial\left(\alpha_{pq} - \frac{\partial \Upsilon_{p}}{\partial y_q}\right)}{\partial \tilde{\rho}_{m,e}}\left(\delta_{ir}\delta_{js} - \frac{\partial \chi_{r}^{ij}}{\partial \mathrm{y}_s}\right) dY \\ & + \frac{1}{|Y|}\int_{Y} E_{rspq}\left(\alpha_{pq} - \frac{\partial \Upsilon_{p}}{\partial y_q}\right)\frac{\partial\left(\delta_{ir}\delta_{js} - \frac{\partial \chi_{r}^{ij}}{\partial \mathrm{y}_s}\right)}{\partial \tilde{\rho}_{m,e}} dY\end{aligned} \tag{A.10}$$

where:

$$\frac{\partial\left(\alpha_{pq} - \frac{\partial \Upsilon_{p}}{\partial y_q}\right)}{\partial \tilde{\rho}_{m,e}} = \frac{\partial \alpha_{pq}}{\partial \tilde{\rho}_{m,e}} - \frac{\partial}{\partial \tilde{\rho}_{m,e}}\left(\frac{\partial \Upsilon_{p}}{\partial y_q}\right) \tag{A.11}$$

and:

$$\frac{\partial\left(\delta_{ir}\delta_{js} - \frac{\partial \chi_{r}^{ij}}{\partial \mathrm{y}_s}\right)}{\partial \tilde{\rho}_{m,e}} = -\frac{\partial}{\partial \tilde{\rho}_{m,e}}\left(\frac{\partial \chi_{r}^{ij}}{\partial \mathrm{y}_s}\right) \tag{A.12}$$

Simplifying Eq. (A.10) with Eq. (A.11)-(A.12), results in Eq. (A.13):

$$\begin{aligned}\frac{\mathrm{d}\beta_{ij}^{H}}{\mathrm{d}\tilde{\rho}_{m,e}} = \frac{1}{|Y|}\int_{Y} & \frac{\partial E_{rspq}}{\partial\tilde{\rho}_{m,e}}\left(\alpha_{pq}-\frac{\partial\Upsilon_{p}}{\partial y_{q}}\right)\left(\delta_{ir}\delta_{js}-\frac{\partial\chi_{r}^{ij}}{\partial \mathrm{y}_{s}}\right)dY \\ & +\frac{1}{|Y|}\int_{Y} E_{rspq}\frac{\partial\alpha_{pq}}{\partial\tilde{\rho}_{m,e}}\left(\delta_{ir}\delta_{js}-\frac{\partial\chi_{r}^{ij}}{\partial \mathrm{y}_{s}}\right)dY \\ & -\frac{1}{|Y|}\int_{Y} E_{rspq}\frac{\partial}{\partial\tilde{\rho}_{m,e}}\left(\frac{\partial\Upsilon_{p}}{\partial y_{q}}\right)\left(\delta_{ir}\delta_{js}-\frac{\partial\chi_{r}^{ij}}{\partial \mathrm{y}_{s}}\right)dY \\ & -\frac{1}{|Y|}\int_{Y} E_{rspq}\left(\alpha_{pq}-\frac{\partial\Upsilon_{p}}{\partial y_{q}}\right)\frac{\partial}{\partial\tilde{\rho}_{m,e}}\left(\frac{\partial\chi_{r}^{ij}}{\partial \mathrm{y}_{s}}\right)dY\end{aligned} \tag{A.13}$$

Choosing $\mathbf{v} \equiv \frac{\partial \boldsymbol{\Upsilon}}{\partial\tilde{\rho}_{m,e}{}_{e}}$ in (A.1), and with some index manipulation, we have:

$$\int_{¥} E_{rspq}\frac{\partial\chi_{r}^{ij}}{\partial y_{s}}\frac{\partial v_{p}}{\partial y_{q}}\mathrm{d}Y = \int_{¥} E_{pqij}\frac{\partial v_{p}}{\partial y_{q}}\mathrm{d}Y$$

$$\Leftrightarrow \int_{¥}\left(E_{rspq}\delta_{ir}\delta_{js}-E_{rspq}\frac{\partial\chi_{r}^{ij}}{\partial y_{s}}\right)\frac{\partial v_{p}}{\partial y_{q}}\mathrm{d}Y = 0 \tag{A.14}$$

$$\Leftrightarrow \int_{¥} E_{rspq}\left(\delta_{ir}\delta_{js}-\frac{\partial\chi_{r}^{ij}}{\partial y_{s}}\right)\frac{\partial}{\partial\tilde{\rho}_{m,e}}\left(\frac{\partial\Upsilon_{p}}{\partial y_{q}}\right)\mathrm{d}Y = 0$$

This demonstrates that the third term of (A.13) is null. Now, choosing $\mathbf{v} \equiv \frac{\partial \boldsymbol{\chi}^{ij}}{\partial\tilde{\rho}_{m,e}}$ in (A.2), and with the same reasoning as before, it follows that:

$$\int_{¥} E_{rspq}\frac{\partial\Upsilon_{p}}{\partial y_{q}}\frac{\partial v_{r}}{\partial y_{s}}\mathrm{d}Y = \int_{¥} \beta_{rs}\frac{\partial v_{r}}{\partial y_{s}}\mathrm{d}Y$$

$$\Leftrightarrow \int_{¥}\left(\beta_{rs}-E_{rspq}\frac{\partial\Upsilon_{p}}{\partial y_{q}}\right)\frac{\partial v_{r}}{\partial y_{s}}\mathrm{d}Y = 0 \tag{A.15}$$

$$\Leftrightarrow \int_{¥} E_{rspq}\left(\alpha_{pq}-\frac{\partial\Upsilon_{p}}{\partial y_{q}}\right)\frac{\partial}{\partial\tilde{\rho}_{m,e}}\left(\frac{\partial\chi_{r}^{ij}}{\partial y_{s}}\right)\mathrm{d}Y = 0$$

Proving that the 4th term of (A.13) is null as well. Finally, the sensitivity of β_{ij}^{H} w.r.t. the design variable $\tilde{\rho}_{m,e}$ is given by (A.16):

$$\frac{\mathrm{d}\beta_{ij}^{H}}{\mathrm{d}\tilde{\rho}_{m,e}} = \frac{1}{|Y|}\int_{Y} \frac{\partial E_{rspq}}{\partial \tilde{\rho}_{m,e}}\left(\alpha_{pq} - \frac{\partial \Upsilon_{p}}{\partial y_{q}}\right)\left(\delta_{ir}\delta_{js} - \frac{\partial \chi_{r}^{ij}}{\partial \mathrm{y}_{s}}\right) dY + \frac{1}{|Y|}\int_{Y} E_{rspq}\frac{\partial \alpha_{pq}}{\partial \tilde{\rho}_{m,e}}\left(\delta_{ir}\delta_{js} - \frac{\partial \chi_{r}^{ij}}{\partial \mathrm{y}_{s}}\right) dY \tag{A.16}$$

2025

Cláudia Almeida

Methodologies for optimal design and additive manufacturing of metamaterials combining negative property indexes